Permeance based Modelling, Design and Optimization of Supercapacitor assisted Surge Absorber (SCASA)

A thesis submitted in fulfilment of the

requirements for the degree of

Doctor of Philosophy

in Electronic Engineering

at

The University of Waikato

by

Sadeeshvara Udayanga Silva Thotabaddadurage

THE UNIVERSITY OF
WAIKATO
Te Whare Wānanga o Waikato

April 2021

The University of Waikato

Abstract

Supercapacitor assisted (SCA) techniques are a unique set of circuit topologies designed to fulfil power conversion and protection tasks by circumventing the energy losses normally associated with *RC* based circuits. With million times larger capacitance compared to electrolytic type, supercapacitors (SCs) have shown a remarkable surge endurance as discovered by the University of Waikato (UoW) power electronics group. This thesis examines a patented SCA surge protector based on the novel use of SCs' surge withstanding capability, and investigates ways to optimize the present design based on the improvements made to circuit's magnetic components.

The supercapacitor assisted surge absorber (SCASA) developed at UoW incorporates a coupled-inductor wound to a specially selected magnetic material—powdered-iron—that absorbs transients. Despite its high performance, the circuit generates a secondary effect of a negative voltage-peak due to inductive energy release by the core. One aim of our study is to eliminate this undesirable voltage spike using air-gapped ferrite cores. We first identified coupled-inductor transformer action under contrasting voltage conditions. In predicting the SCASA operation under both 50 Hz AC and transient conditions, a permeance based model is used. Our model highlights non-ideal characteristics of the coupled-inductor such as leakage and magnetizing inductances, and provides theoretical predictions based on the permeance coefficients extracted from manufacturer specifications. Inductance measurements are taken over a range of kilohertz frequencies to confirm the accuracy of modelling work.

During initial investigations, we inserted air gaps to ferrite toroids to enhance surge energy storage capability and fringing losses associated with the core. Single- and double-gapped core approach we tested yielded positive test results showing a reduction in negative-surge effect. This encouraged us to develop circuit prototypes using commercially available (Magnetics Inc.) gapped cores of EER type which has an effective permeance comparable to original powdered-iron toroid. This new core configuration indicated improved performance under transient conditions while continually facilitating the passage of AC mains power. In particular, air-gapped cores resulted in optimizing SCASA performance by showing:

- 95% depletion of the negative-surge effect associated with the coupled-inductor
- ∼10% reduction of MOV clamping improving the load-side voltage characteristics
- improved surge endurance as per UL-1449 test standards
- minimized inductance tolerance and reduced manufacturing cost

To comprehend SCASA surge propagation, we applied a Laplace transform analysis to predict primary and secondary transient currents in the coupled-inductor. Compared to ideal transformer action, we quantify how the primary:secondary current ratio deviates from the turns ratio

due to magnetic reluctance of powdered-iron. LTSpice numerical simulations further confirm our analytical predictions.

All experimental procedures presented in this thesis are compliant with IEEE C62.41/IEC 61000-4-5 standards, and generated using a lightning surge simulator (Noiseken LSS-6230) coupled to 230 V, 50 Hz utility mains. Test results generated under these conditions were all within 10% of the predictions showing good consistency with the theorized models.

Dedication

This thesis is dedicated to the most
wonderful couple
I have known for ages
!!!!!!!!!!!!!!!!!!!!!!!!!!!
My Parents

Acknowledgement

It is a genuine pleasure to express deep sense of gratitude to my chief supervisor Nihal Kularatna for his support, patience and encouragement throughout. His unwavering enthusiasm for electronics kept motivating me to sail smoothly during the PhD journey passing challenging times. I would also like to owe a deep debt of gratitude to my co-supervisor Alistair Steyn-Ross who has imparted his knowledge on a wide range of subject matters to accomplish the research goals. His kind support and precious guidance empowered me in many ways to face the challenges and realise the strengths of mine.

My deep acknowledgement to Bradley M. Yourish, senior vice president of sales and marketing, Magnetics Inc. for providing magnetic core samples required for high performance circuit prototypes. I truly believe that his kind cooperation has helped in bringing colour to my research work.

IEEE Industrial Electronics Society (SYPA) is greatly appreciated for providing a travel grant which helped me to present my research findings at the 28th International Symposium on Industrial Electronics (ISIE-2019) Vancouver, Canada.

My sincere thanks to our former PhD student Jayathu Fernando for his valuable comments and suggestions during the early stages of my research.

I am also grateful to Mary Dalbeth, Natalie Shaw, Tanya Mete and Emma Juggins for their administrative support during my studies.

Finally, I extend wholehearted gratitude to my loving parents for giving me their fullest support in every imaginable way to achieve my dreams.

Contents

List of Figures

List of Tables

Acronyms and Abbreviations

AC	alternating current
ANSI	american national standards institute
BBD	bidirectional break-over diode
CM	common mode
CSV	comma separated values
DC	direct current
DM	differential mode
EMI	electromagnetic interference
ESR	equivalent series resistance
EC	electrochemical capacitor
EDLC	electric double-layer capacitor
EUT	equipment under test
GDT	gas discharge tube
HC	hybrid capacitor
IEC	international electrotechnical commission
IEEE	institute of electrical and electronics engineers
ITRS	international technology roadmap for semiconductors
KVL	Kirchoff's voltage law
KCL	Kirchoff's current law
LT	Laplace transform
LSS	lightning surge simulator
MATLAB	matrix laboratory
MPL	magnetic path length
MOV	metal oxide varistor
NASA	national aeronautics and space administration
PC	pseudo capacitor
SPD	surge protection device
SPICE	simulation program with integrated circuit emphasis
SC	supercapacitor
SCASA	supercapacitor-assisted surge absorber
TMOV	thermally protected metal oxide varistor
TVS	transient voltage suppressor
UC	ultra capacitor
RMS	root-mean square
UL	underwriters laboratories

Chapter 1

Introduction

1.1 Prelude

Transient-surge absorption capability of small/low cost supercapacitors (SCs) is already published. Supercapacitor assisted surge absorber (SCASA) is a patented technique that led to the development of a high performance commercial surge protector which adheres to UL-1449 3rd edition test protocols. The commercial implementation of SCASA known as SMART-TViQ comprises a coupled-inductor, two metal oxide varistors (MOVs) and a SC sub-circuit. The research work presented in this thesis aims at optimizing the present surge protector based on the improvements made to circuit's magnetic components.

1.2 Background and Motivation

Since the late 19th century to the present day, with the rapid developments in electronics industry, the need for processing and managing electricity has emerged as an essential requirement to get disturbance-free power. Based on the developments of international technology roadmap for semiconductors (ITRS) and its predictions, protection of modern-day electronic systems from

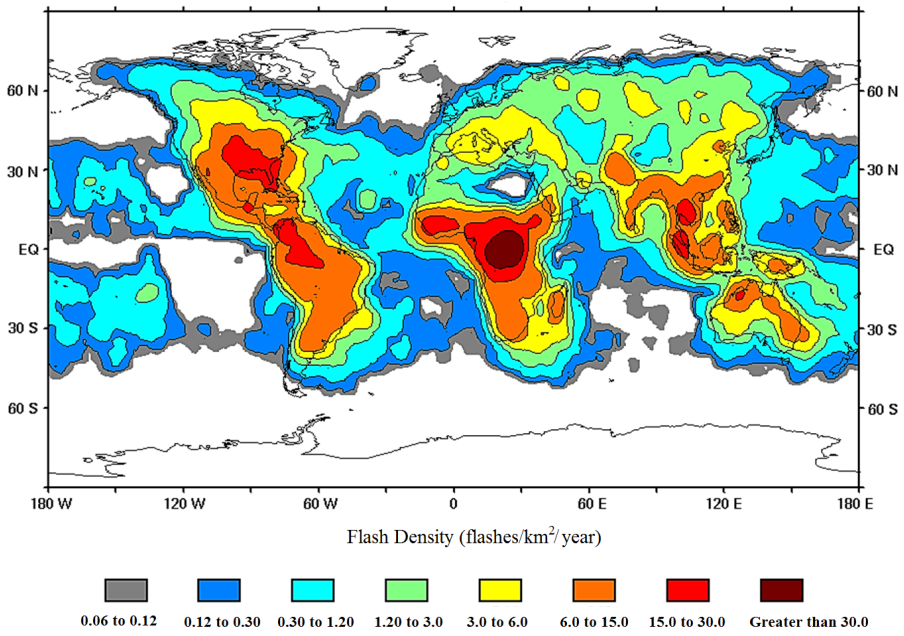

Figure 1.1: Distribution patterns for annual lightning flash density (Annual Lightning Climatology: NASA[1]) [1]

high voltage transients has become mandatory [2]. Today, more than 75% of the power generated across the world is processed by power electronics [3]. In a single- or three-phase utility main supply, it is expected that AC power delivers at a nominal RMS voltage with a minimum percentage tolerance of ±5–10% [4]. But, due to voltage disturbances such as RMS fluctuations, transients, noise and harmonics, utility power is downgraded (more information given in Chapter 2). Out of various power quality issues, transient surges are considered to have the greatest voltage stress in an electronic system [5].

According to the Lightning and Atmospheric Research Center[1] (NASA), lightning induced transients are the severest which cause most frequent damage [1, 6]. Specially due to the high probability of lightning flash occurrence (>30 flashes/km^2/year) around the equatorial belt (Figure 1.1), high transient rates are observed in North American, South American, African, Asian, and Oceanian countries [6]. According to a survey[2], on average, the New Zealand land region is estimated to receive ∼45,000 lightning strikes a year [7]. Due to this highly unpredictable nature and severity of transients, though 100% elimination is not possible, surge protector devices (SPDs) can be engineered to minimize the destructive impact.

A reliable surge protector can minimize transient effects by:

- limiting the surge energy passing to the protected load
- reducing faulty problems on various end user circuits
- avoiding distorted data transmissions in signal lines

Based on the voltage division principle [8], SPDs are designed using non-linear devices (NLDs) such as metal oxide varistors (MOVs), bi-directional break-over diodes (BBDs), series inductors and shunt capacitors to reduce transient stress as mentioned above (more details found in Chapter 2). While traditional SPDs are designed using NLDs and inductor-capacitor filter combinations [9], the use of supercapacitors (SCs) in surge protector circuits is a relatively new concept developed and tested by the power electronics research group at University of Waikato. According to the investigations summarised in [10], a SC based low-component count surge protector was developed as SCASA [11–13]. It is a patented technique which led to a commercial product SMART TViQ, developed and manufactured by Thor technologies, Australia in 2016 [14]. In developing this first product design, a coupled-inductor topology was used by adopting a powdered-iron toroid, where a SC sub-circuit is placed between the ends of inductor windings. The limitation of low DC rating of SCs is clearly addressed by the coupled-inductor as it maintains a low voltage difference across the SC sub-circuit under 230 V AC conditions (details found in Chapter 3). Given the success of this first commercial implementation, research goals of our study were formulated to develop an analytical model for the SCASA magnetic core and to optimize the existing design by incorporating high performance magnetic cores.

1.3 Goals and Objectives

Inspired by the original SCASA circuit configuration, this research is conducted with the aim of advancing the existing technique by improving surge absorption capability and ultimate surge

[1] https://ghrc.nsstc.nasa.gov/lightning/
[2] https://www.stats.govt.nz/

endurance. Theory development and experimental work are carried out during different phases of the research. Also, the simulation work conducted appear to corroborate experimental measurements and offer some explanation about possible measurement issues with the physical system. The work presented in this thesis is based on the following research objectives.

- During the early testing of first SCASA version, one major problem faced was the selection of magnetic core: commercially available ferrite cores did not perform well, while a powdered alloy such as 0077071A7 from Magnetics Inc. [13] was able to satisfactorily perform. Thus, as the initial goal of this research, I investigate magnetic properties of ferrites and powdered-iron based alloys with an special emphasis to hysteresis behaviour, magnetic permeability and energy storage capability of the two materials.
- While SCASA surge protector performs well according to UL-1449 test protocols [15], the next research target is to identify limitations of the present design. It is discovered that limitations are in two basic forms: the inductive energy release associated with the coupled-inductor, and the relatively high (>700 V) output clamping level under transients. To address the first, magnetic action of the two inductive coils is examined in detail.
- Development of a permeance based circuit model for the SCASA transformer to explain the non-ideal characteristics of the core. Based on the theorized concept, operational modes of the coupled-inductor is studied under contrasting voltage conditions. 230 V, 50 Hz AC steady state and the transient propagation state of the equivalent circuit model will be elucidated with experimental validations.
- With regard to the non-ideality of the core, research work is aimed at measuring leakage inductances of primary and secondary coupled windings, whereas permeance based analytical approach is expected to be applied in predicting the magnetic coupling between SCASA coils.
- As an initial optimization step, the use of air-gapped ferrite cores in SCASA will be investigated with the aim of improving surge endurance and transient energy absorption. In addition, the importance of leakage and fringing flux based losses are examined as applied to SPD development.
- Given the complexity in transient propagation, a detailed mathematical analysis will be carried out using Laplace transforms to predict the surge current propagation through coupled-inductor windings of SCASA magnetic core. Compared to 50 Hz RMS operation, the significance of inductive impedance is emphasized with regard to the high-frequency spectrum of a 1.2/50 μs surge pulse. Moreover, during this research phase, a numerical analysis will be conducted using LTSpice simulations to support the predictions of analytical work.
- As a final objective of this research, circuit modifications and further design optimizations of SCASA magnetic component will be experimented using surge immunity tests. In predicting the optimum core material and shape within the commercial price constraints, our selections will be based on permeance (inductance factor-A_{L}) of Kool μu, High Flux, X Flux and air-gapped EER core types. Overall, as the ultimate research output, a better version of the SCASA surge protector is expected to be developed with reduced clamping and greater surge endurance that is suitable for a low-cost commercial product.

1.4 Methodology

In achieving the research objectives, I followed a combination of theoretical, experimental and simulation methods during the course of this study. For the optimization of present SCASA surge protector, the need of an analytical model is identified to predict circuit's transformer action. Similarly, circuit prototypes designed using low-cost commercial magnetic toroids (selected on the basis of magnetizing permeance) are subjected to typical surge waveforms defined by IEC61000-4-5/IEEE C62.41.2 standards. In confirming our analytical and experimental approaches, numerical simulation methods are applied using LTSpice and MATLAB software tools. Figure 1.2 presents a summary of the research methodology adopted in this thesis.

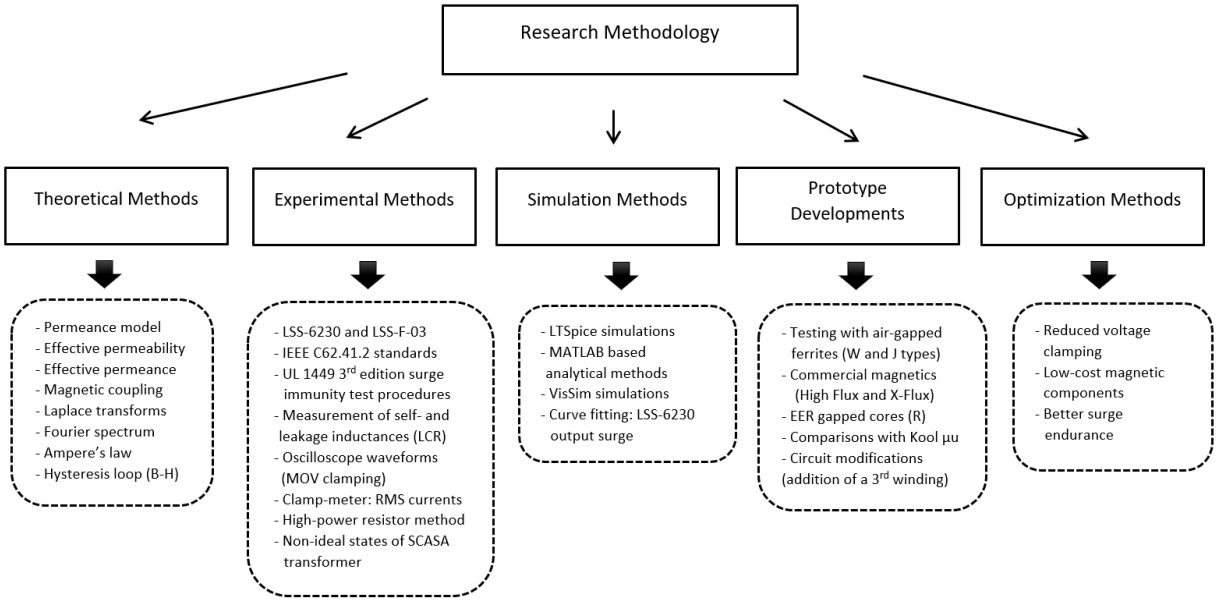

Figure 1.2: Summary of the research methodology

All surge immunity tests conducted during the experimental phase adhere to UL-1449 3rd edition standards, and they are performed by NoiseKen lightning surge simulators (LSS-6230 and LSS-F03). As UL-1449 test procedure verifies the safe operation of a SPD after being subjected to a series of transient surges, our destructive testing is evaluated on the basis of 6 kV/3 kA repetitive pulses. Furthermore, surge protector output waveforms (MOV clamping) are monitored using a digital oscilloscope with 100 MHz bandwidth and 1 GS/s sample rate (Tektronix-TPS2014). In validating operational states of SCASA transformer, Tektronix-A622 clamp meters are used to measure the RMS currents through the core windings, whereas high-power resistor blocks provided waveforms relating to transient current propagation. As illustrated by Figure 1.2, ultimate optimizations are achieved in three ways: reduced load clamping, low-cost magnetic components and better surge endurant prototypes are among the top outcomes of this research.

In the next section, I elucidate original contributions arising from this thesis, and discuss how research goals are met with the overall methodology emulated.

1.5 Original Contributions of the Thesis

This thesis establishes the following original contributions:

- Development of a permeance based model for the transformer core of SCASA surge protector, and theoretical prediction of different operational modes of the core under 230 V AC and transient conditions. Moreover, experimental validation of the theorized model based on the RMS and transient currents propagation through transformer windings.
- Investigation of magnetic component selection problem of SCASA design; this includes the testing and study of commercially available ferrite and powdered-iron toroids with regard to their hysteresis behaviour, magnetic permeability and energy storage capability.
- Proposing a new method of optimization on the basis of air-gapped ferrite cores for the SCASA magnetic core. Here, analytical models are developed for the effective permeability and permeance of a gapped toroid, whereas leakage and fringing energy losses associated with an air gap are also highlighted.
- Measurement of self-, leakage and mutual inductances of the SCASA transformer windings, while an analytical framework is established to study the magnetic coupling of powdered-iron and ferrite transformers.
- Mathematical analysis of surge propagation in SCASA coupled-inductor using Laplace transforms; this is further justified by numerical simulations conducted by LTSpice software tools. Frequency spectrum of a standard surge waveform is also validated using fast Fourier transform.
- Estimation of surge energy distribution among SCASA circuit components. Here, analytical predictions of Laplace method and LTSpice numerical techniques are applied to conduct a percentage analysis of energy absorptions/dissipations.
- Construction of high-performance SCASA circuit prototypes using Kool μu, High Flux, X Flux and air-gapped EER core types to meet the commercial price constraints. Selection of these magnetic materials and core geometry is determined in accordance with our permeance model.

1.6 Structure of the Thesis

Based on the literature survey and original contributions of the research, this thesis is structured into eight main chapters. Each chapter is sub-divided into sections and sub-sections to maintain a steady flow of the theoretical and experimental content presented. Furthermore, a brief introduction is included at the beginning of each chapter, while it ends with a concise summary and links firmly with next. Following is a description of the thesis contents presented in subsequent chapters; an overall summary is depicted in Figure 1.3.

In **Chapter 1**, the need for surge protection is introduced with a general background of lightning induced transients and SPD development. The motivation for this research is discussed here; hence, goals and objectives are also emphasized in relation to the methodology followed. An outline of the overall thesis contents is also included in this Chapter, while original contributions arising from this research are discussed with respective peer-reviewed publications.

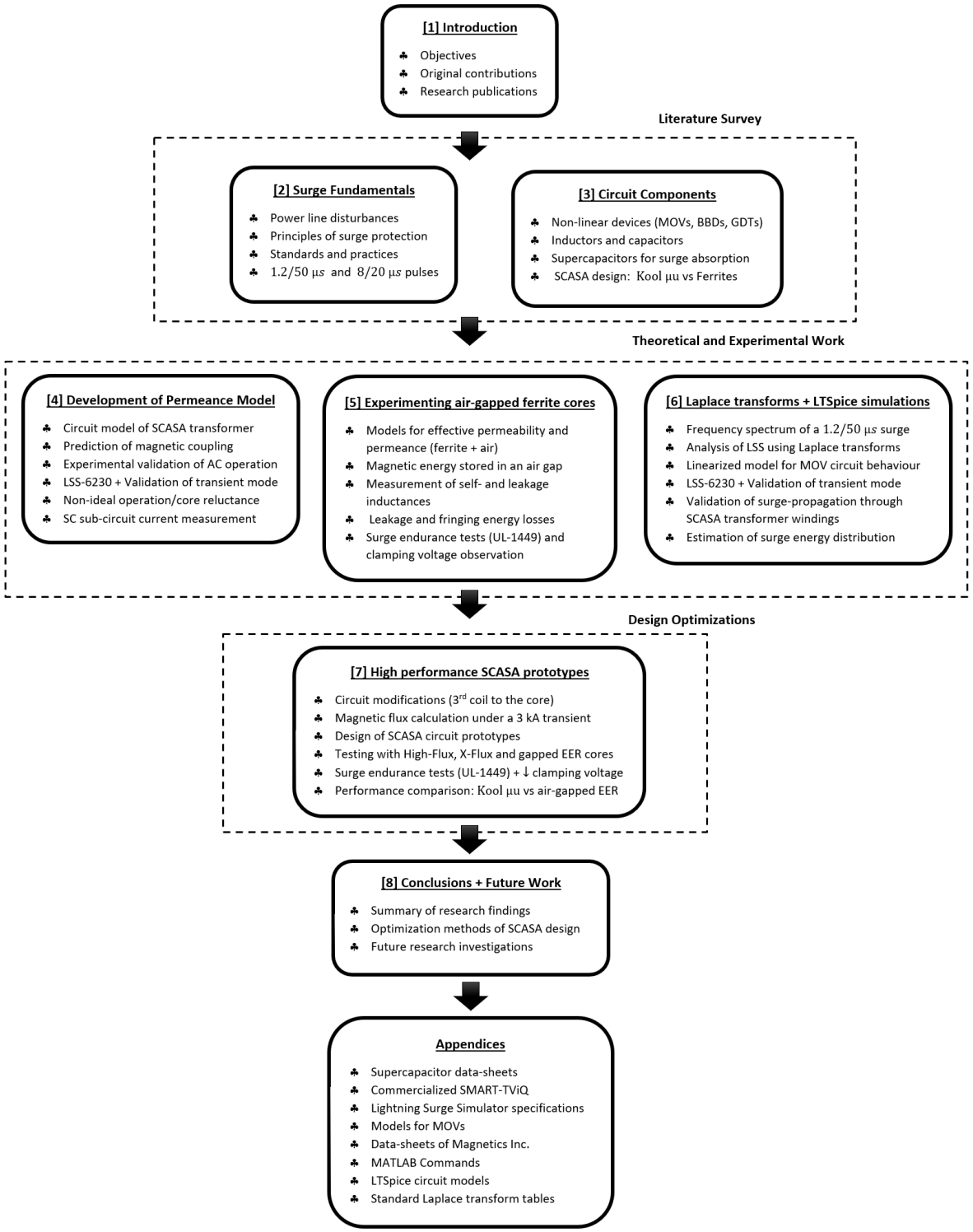

Figure 1.3: Summary of the chapter contents presented in this thesis

Chapter 2 presents a literature survey describing power-line disturbances, power quality issues, surge protection principles and other important standards and practices. Also, we analyse circuit concepts used in surge protection for common-mode and differential-mode applications. In addition, experimental, theoretical and numerical comparison of standard open-circuit and short-circuit test waveforms is carried out with the use of lightning surge simulator LSS-6230. Surge immunity test procedures specified by UL-1449 standards are explained towards the end

of this Chapter.

In **Chapter 3**, we investigate details of traditional circuit components used in surge protector circuits. Operation of non-linear devices such as MOVs, BBDs and gas tubes and their non-linear impedance behaviour is discussed in relation to the typical applications of each type. Notably, we highlight the novel use of supercapacitors (SCs) for surge absorption in this Chapter. Moreover, transient withstanding capability of SCs is explained using the RC charging curve, thus comparisons are made to normal electrolytic capacitors. Development of SCASA technique is also presented here, and the importance of implementing a coupled-inductor topology to allow SCs to be utilized in a surge protector is explained. In advancing SCASA to its next level, we identify limitations of the present design and elucidate ways to overcome them with improvements made to circuit's magnetic components.

Chapter 4 focuses onto the development of a permeance based circuit model for SCASA non-ideal transformer using magnetizing and leakage parameters of the magnetic core. Here, we discuss essential magnetic characteristics such as hysteresis behaviour, magnetic permeability and reluctance associated with the existing core material. The analytical model predicts SCASA operation under contrasting voltage conditions based on the inductive impedance calculations. 50 Hz AC steady state and the transient propagation state of the equivalent circuit model are elucidated here with experimental validations.

In **Chapter 5**, we research the use of air-gapped ferrite cores for the present SCASA design, and elucidate ways to enhance surge endurance and energy storage capability to optimize its overall performance. Starting from the permeance based analytical approach presented in Chapter 4, we expand our theoretical work with new models for effective-permeability and effective-permeance of an air-gapped core. Furthermore, energy losses (leakage and fringing flux effects) associated with gapped toroids are studied as applicable to surge protector development. Experimental outcomes as per UL-1449 surge immunity test methods are discussed towards end of this Chapter.

Given the non-ideal behaviour of SCASA transformer, in **Chapter 6**, we develop Laplace transform based theoretical foundations to predict the surge current propagation through coupled-inductor windings of magnetic core. Compared to 50 Hz RMS operation, the significance of inductive impedance is emphasized with regard to the high-frequency spectrum of a 1.2/50 μs surge pulse. In addition, numerical validation using a LTSpice circuit model of SCASA surge protector is presented to justify the accuracy of our analytical approach.

Considering the applicability of air-gapped cores in SCASA design, in **Chapter 7**, we present experiments conducted using commercial magnetic assortments facilitated by Magnetics Incooperation, USA. In predicting the optimum core material and shape within the commercial price constraints, our selections were based on permeance coefficients (inductance factor-A_{L}) of Kool μu, High Flux, X Flux and air-gapped EER core types. Overall optimizations achieved using these magnetic components are discussed in terms of clamping-voltage improvement, cost-reduction and better surge endurance. In addition, we describe the topological modifications done to SCASA circuit with the aim of improving surge energy absorption.

Chapter 8 highlights research findings and main conclusions arising from theoretical and experimental work of this thesis. Moreover, a discussion about possible future research work and circuit topology enhancement techniques are suggested in this chapter.

In addition, industry specifications of magnetic cores, supercapacitor data-sheets, LTSpice circuit models, MATLAB codes and Laplace tables are included in the appendices.

1.7 List of Publications

Following peer-reviewed journal papers and conference papers were produced and presented during the time of this research:

Journal papers

- S. U. Silva Thotabaddadurage, N. Kularatna, and D. A. Steyn-Ross, "Optimization of Supercapacitor Assisted Surge Absorber (SCASA) Technique: A New Approach to Improve Surge Endurance Using Air-Gapped Ferrite Cores", *Energies 2021*, vol. 14, no. 14, p. 4337, July 2021, doi: 10.3390/en14144337.
- S. U. Silva Thotabaddadurage, N. Kularatna and D. A. Steyn-Ross, "Permeance based Design and Analysis of Supercapacitor Assisted Surge Absorber for Magnetic Component Selection", *IEEE Transactions on Industrial Electronics* (submitted in August, 2021).
- S. U. Silva Thotabaddadurage, N. Kularatna and D. A. Steyn-Ross, "Importance of Leakage Magnetic Field and Fringing Flux in Surge Protector Design: An Investigation based on Supercapacitor Assisted Surge Absorber", *IEEE Transactions on Power Electronics* (submitted in October, 2021).
- S. U. Silva Thotabaddadurage, N. Kularatna and D. A. Steyn-Ross, "Magnetic Design Aspects of the Supercapacitor Assisted Surge Absorber (SCASA) Technique", *IEEE Transactions on Magnetics* (submitted in October, 2021).

Peer-reviewed conference papers

- S. T. Sadeeshvara Udayanga, S. Kokuhennadige, J. Fernando, N. Kularatna and D. A. Steyn-Ross, "Supercapacitor assisted surge absorber (SCASA) technique: selection of magnetic components based on permeance," *36th IEEE Applied Power Electronics Conference and Exposition (APEC)*, Arizona, USA, 2021, pp. 2299-2304, doi: 10.1109/APEC42165.2021.9487254.
- S. T. Sadeeshvara Udayanga, N. Kularatna and D. A. Steyn-Ross, "Permeance based model for the coupled-inductor utilized in the supercapacitor assisted surge absorber (SCASA) and its experimental validation," *2020 2nd IEEE International Conference on Industrial Electronics for Sustainable Energy Systems (IESES)*, Cagliari, Italy, 2020, pp. 267-272, doi: 10.1109/IESES45645.2020.9210663.
- S. T. Sadeeshvara Udayanga, N. Kularatna and D. A. Steyn-Ross, "Investigating the impact of ferrite magnetic cores on the performance of supercapacitor assisted surge absorber (SCASA) technique," *2019 IEEE 28th International Symposium on Industrial Electronics (ISIE)*, Vancouver, BC, Canada, 2019, pp. 130-135, doi: 10.1109/ISIE.2019.8781402.

- S. T. Sadeeshvara Udayanga, N. Kularatna and D. A. Steyn-Ross, "Modelling of a RL circuit subjected to a high voltage transient and investigating the importance of inductors in surge protection," *2018 Waikato Young Research Engineers Symposium (WYRES)*, University of Waikato, Hamilton, Waikato, New Zealand, 2018.
- S. T. Sadeeshvara Udayanga, N. Kularatna and D. A. Steyn-Ross, "Supercapacitor Assisted Dual-mode Surge Protector," *2018 Waikato Young Research Engineers Symposium (WYRES)*, University of Waikato, Hamilton, Waikato, New Zealand, 2018.

Chapter 2

Surge Protection Fundamentals and Standards

This thesis aims at optimizing a patented surge protector technique—supercapacitor assisted surge absorber (SCASA)—based on the improvements made to circuit's magnetic components. In this chapter I present selected elements of power quality issues, surge protection principles, traditional surge protector designs, and a summary of surge protection standards and industry test protocols.

2.1 Power Line Disturbances

Over the last few decades, the electronics industry has shown a remarkable growth; thus, the need for processing and managing electricity has emerged as an essential requirement to get reliable disturbance-free power. Based on the developments of international technology roadmap for semiconductors (ITRS) and its predictions, protection of modern electronic systems from power line disturbances has become mandatory [2]. Today, more than 75% of the power generated across the world is processed by power electronics [3]. In a single- or three-phase utility main supply, it is expected that the commercial power companies deliver AC mains at a nominal RMS voltage with a minimum percentage tolerance of ±5–10% [4]. Apart from the voltage requirement, sensitive load equipment demand continuous RMS power flow at a fixed frequency of 50 Hz. However, due to faulty situations and natural phenomena, most of which are beyond control and are acts of God, it is impossible to acquire disturbance-free power. Most common types of anomalies that downgrade power quality include RMS voltage fluctuations, transients, noise and harmonics. Figure 2.1(a) illustrates different types of RMS fluctuations and Figure 2.1(b) depicts how transients, noise are superimposed on the 230 V utility main. Figure 2.1(c) shows the ideal situation of a 50 Hz, 230 V AC waveform which has only 50 Hz component in its frequency spectrum.

2.1.1 RMS voltage fluctuations

RMS fluctuations are classified into four main categories as indicated in Figure 2.1(a): surges, sags, over-voltages and under-voltages.

- **Voltage surges:** A surge is about 110%-180% voltage increase which typically lasts from about 15 milliseconds to one-half of a second [16]. Common causes of surges are switching of heavy loads and power-network based switching. Surges do not exhibit high magnitudes

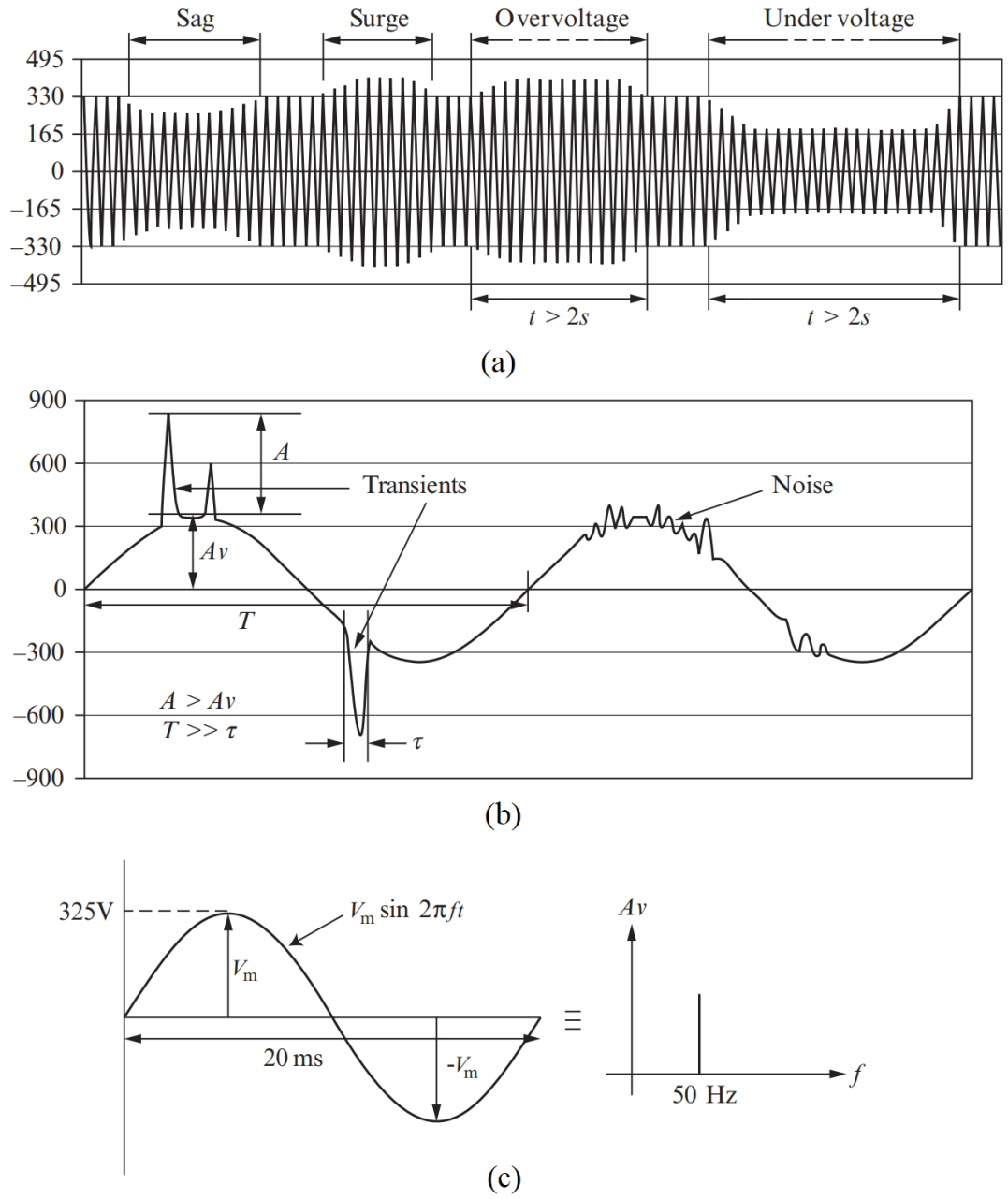

Figure 2.1: Power line disturbances and ideal 230 V RMS, 50 Hz AC waveform: (a) RMS voltage fluctuations; (b) transients and noise superimposed on the waveform; (c) ideal 230 V RMS waveform and its frequency component [18, 19]

as in the case of sharp spikes, but can result in computer data losses, equipment damage, and even causing erroneous readings in monitoring systems. If a surge lasts more than 2 s, it is generally considered as an *over-voltage* [17].

- **Voltage sags:** Under-voltage conditions that result in 10%-90% voltage reductions from the recommended level are named as sags [17]. Similar to a surge event, a sag can also lasts from few milliseconds to half a second, and can have a ripple voltage effect across multiple pieces of equipment under function. Sags mainly arise when high-current loads such as shop tools, elevators and compressors are connected to the power line. Common problems

caused by sags include computer data losses and alteration issues in live data. A sag that can impact for more than 2 s is generally defined as an *under-voltage* [17].

In addition to above RMS fluctuations, if an interruption of power supply prevails for more than two AC cycles it is regarded as a *blackout*. Blackouts can happen due to a utility power generation failure, power distribution failure or tripping of a power line circuit breaker. Having a backup stored energy system is the best way to mitigate the effect of a blackout. In some cases, without a complete interruption of power, voltage reductions of 10%-30% last for a longer period of time. These are known as *brownouts* [20], and commercial electricity providers may an intentionally carry out such procedures to cope up with peak load times as it becomes harder to maintain the required voltage levels. Brownouts are very common in households; these can sometimes be detected by flickering or dimming of light bulbs.

2.1.2 Transients

The term transient is commonly used in the power quality analysis to denote a voltage event that is unpredictable and momentary in nature. As depicted in Figure 2.1(b) transients are sharp spikes that can occur as both positive and negative voltage spikes. These can generate due to on and off switching of heavy inductive loads such as air conditioners, electric power tools, machinery, and elevators. Transients caused by lightning can lead to high-magnitude spikes of several kilovolts with high-frequency components between 3-30 kHz and beyond [21]. In Chapter 6, a simulated *Fourier transform* of a standard 1.2/50 μs transient surge waveform is included with further details. Although they usually last up to 200 μs, typically in the order of few microseconds, transients can be dangerous to unprotected equipment, with amplitudes ranging from about 180% of the peak value to over a several thousands of volts: sometimes as high as 6000 V or even larger [5]. Such high amplitudes of sudden voltage variations can wipe out stored data, alter data in progress, and cause electronic-hardware damage. In general, the peak utility voltage carried into a circuit with the superimposed transient surge can have a greater potential for damage. Out of various power line disturbances, transient phenomena are considered to have the greatest voltage stress in an electronic system if not properly mitigated [5].

2.1.3 Electrical noise

Noise is defined as unwanted electrical signals (Figure 2.1(b)) with a frequency spectrum of 7000 Hz to over 50 MHz [22]. Noise can be transmitted and picked up by a power cord acting as an antenna, or it can be carried through the power line. These disturbances are commonly generated by radio frequency interference, such as radio, TV, cellular, and microwave transmission, radar, arc welding, and distant lightning. Noise can also be due to electromagnetic interference produced by heaters, air conditioners, white goods, and other thermostat-controlled or motor-operated devices.

Although electrical noise is non-destructive, it disturbs electronic devices such as microcomputer and programmable controllers causing erroneous data outputs. Noise related issues can be generally mitigated by filters, isolation transformers, and line conditioners.

2.1.4 Harmonics and inter-harmonics

Harmonics are distortions in sinusoidal voltage or current waveforms comprising frequencies that are integer multiples of the frequency at which the utility supply is designed to function [23]. The fundamental frequency of the utility main in most countries is usually 50 Hz as shown in Figure 2.1(c); however, these periodically distorted waveforms can be decomposed into its fundamental frequency and harmonics-frequencies. Harmonic effects generally originates due to the use of non-linear loads such as computer power supplies, UPS rectifiers and even energy saving LED lamps. Figure 2.2 illustrates a harmonically distorted waveform based on the Fourier spectral representation. Although the dominant frequency component is 50 Hz, as low-amplitude higher order frequencies consisting odd multiples of the fundamental add up, the sinusoidal waveform gets distorted.

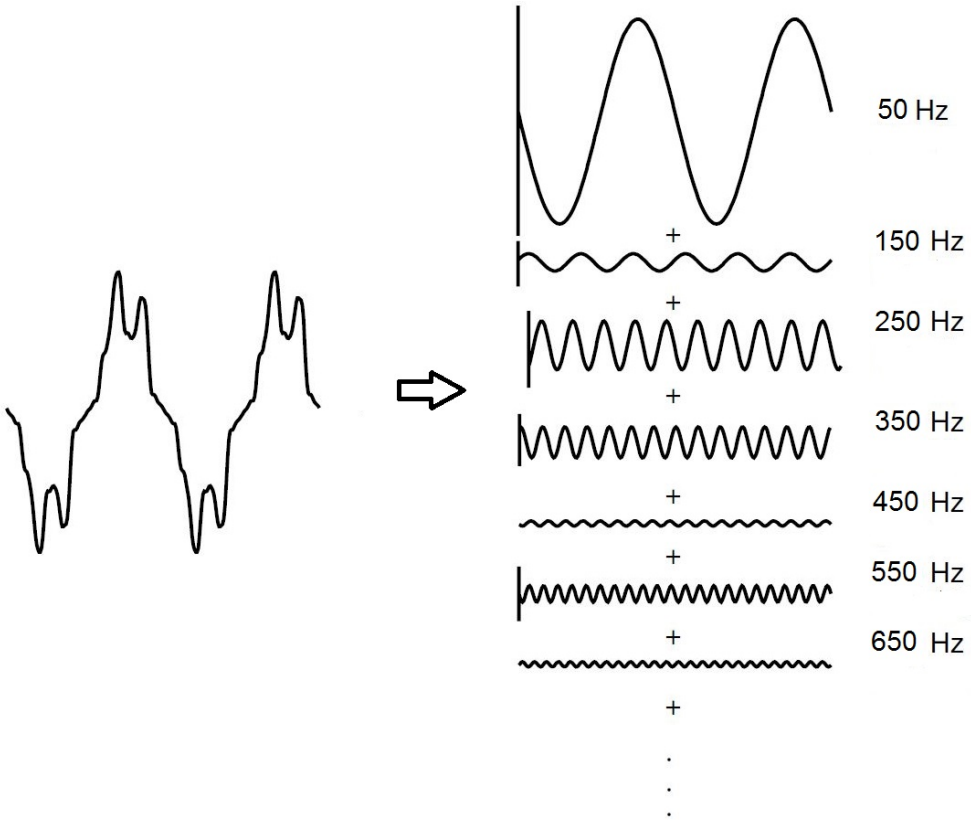

Figure 2.2: Spectral representation of a harmonically distorted waveform based on Fourier series: fundamental frequency of 50 Hz and its odd multiple frequencies (3,5,7,9,11,13) [23].

Inter-harmonics are considered as voltages or currents having frequency components that carry non-integer multiples of the fundamental [24]. Apart from non-integer nature, these can sometimes appear as discrete frequencies or as a wideband spectrum. However, inter-harmonics are common in networks of all voltage classes. Inter-harmonic waveform distortions are mainly caused by static frequency converters, cycloconverters, induction furnaces, and arcing devices [24]. In addition, power line carrier signals can also be considered as inter-harmonics. Since most harmonic effects are mainly due to end-user loads, it is almost inevitable to get harmonics-free sinusoidal electricity, but with the use of shunt/series filters these issues can be minimized.

2.2 Power Quality Issues

The above power line disturbances result in causing various power quality issues such as burned circuits, memory losses and equipment/program failures. Power outages or instrument failures are critical at sites where environment and health/safety are at risk. Institutions such as hospitals, high security areas, sewage treatment plants and mining based operations are among critical examples. As indicated in 2.1.2, transient surges cause the greatest damage to electronic systems.

2.2.1 Levels of damage due to transient surges

An electronic device show optimum performance when powered from 230 V/50 Hz utility main; but, degradation starts to occur as the transient voltage spikes superimposed on AC main pass into the internal circuits. Figure 2.3 shows different levels of degradation due to a transient surge superimposed on AC-input. Voltage amplitudes above 900 V are highly detrimental to electronic circuits [25, 26], whereas 600–900 V is the range where internal circuit degradations start to occur. However, transients below 600 V are usually considered to be safe [25, 26].

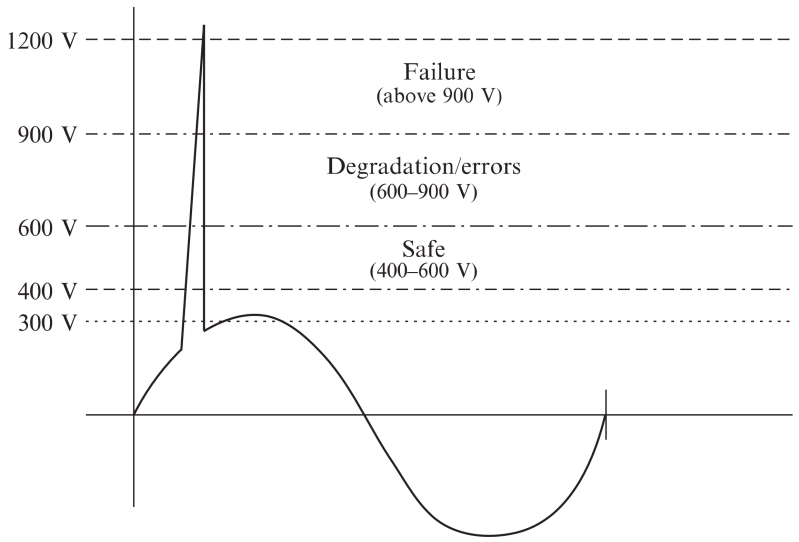

Figure 2.3: A transient superimposed on AC-input with degradation levels [25].

Transients, surges and noise based power issues can be superimposed on the utility main in two different forms: common mode and differential mode disturbances. Differential mode is further known as normal mode or transverse mode. In terms of severity, common mode transients can be more powerful than normal mode. However, in maintaining a safe voltage at the load end, it is necessary to minimized the effects of both modes.

2.2.2 Differential-mode transients

Differential-mode transients/noise appear between the live wire and the accompanying neutral wire of an AC supply input. In the case of a DC power supply, it means the positive or negative rail and its return current path. For a load device functioning under 230 V AC, these two lines represent the normal path of power through the electric circuits, hence the name normal mode

is commonly used. Occurrence of differential-mode (DM) signals are indicated using a block diagram as shown in Figure 2.4.

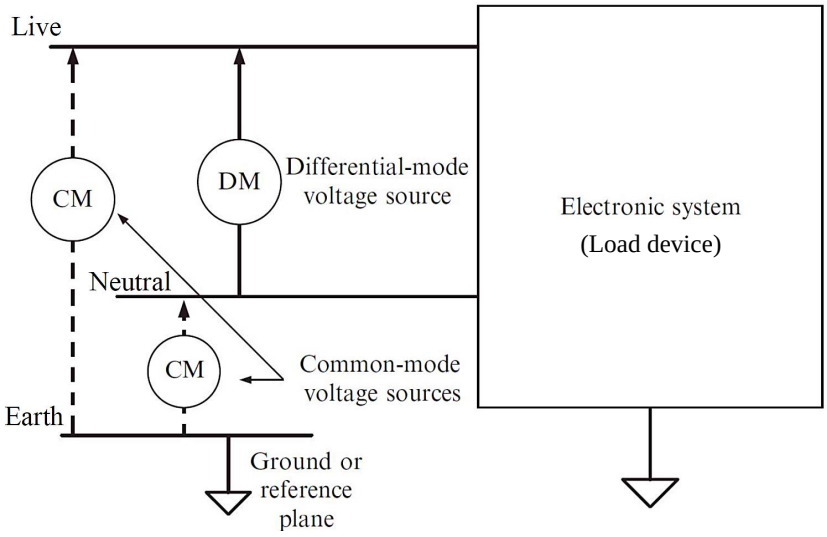

Figure 2.4: Different modes of signal inputs: differential-mode and common-mode [19]

2.2.3 Common-mode transients

Common-mode (CM) power disturbances appear between ground and the two supply lines of live and neutral. Common-mode transients are most disruptive voltage spikes as digital logic or analogue signals are either directly or capacitively tied to the safety ground as a zero-voltage data reference point for semiconductors. In certain cases, even a minute CM voltage difference of 0.5 V can cause data reference point to shift momentarily, thus leading to program failures of semiconductor chips. As illustrated by Figure 2.4, CM signals can sometimes occur between both live-earth and neutral-earth with equal amplitudes. By using an isolation transformer, primary side CM signals can be coupled to the secondary side due to inter-winding capacitances of the transformer. If managed with reduced inter-winding capacitances, then the impact of CM noise/transients passing to load connected secondary can be greatly minimized [27].

2.3 Principles of Surge Protection

Transients and surges are highly unpredictable and statistical in nature. Though 100% elimination is impossible, surge protectors are engineered to minimize transmission of transient surge energy. Electronic circuit components are usually damaged due to an over-current or over-voltage; both these two extreme conditions result in transferring greater amount of surge energy damaging the components. Therefore, an effective SPD must absorb and dissipate the transient related energy within the unit, while continually facilitating the mains electricity flow at line frequency to the electronic load under protection. In designing circuits for surge absorption, a designer must take into account two main factors: (1) the surge absorber circuit should not disturb the normal AC operation of the connected device, and (2) components used to attenuate

the surge must be able to withstand and absorb the surge energy. An ideal SPD must limit the surge energy passing to the load to a minimum level such that the load can operate without a failure. The energy passing to the load is determined using the integral of surge voltage and current product, $\int vi\ dt$ [28, 29]. A practical SPD should develop a lower clamping voltage to reduce the surge current passing to the load and must have a low dynamic resistance and fast response time. Longevity, repeatability, board size, cost, reliability, and a safe failure mechanism are also important factors in SPD design.

2.3.1 Voltage division principle as applied to surge protectors

All SPD circuits function according to voltage division principle [30]. Figure 2.5 depicts the general conceptual design approach to surge absorption, by adopting a simple pair of impedances. As per Figure 2.5(a), the load Z_{L} to be protected comes in series with a small impedance Z_{S}, which represents the Thevenin's impedance of the closed loop, formed by stray line inductance and ohmic resistance, etc. When a surge occurs, voltage dividing effect of the Z_{L} and Z_{S} is such that a larger share of surge is appearing at the load in a destructive form. Figure 2.5(b) shows the case of an externally inserted impedance block Z_{block} which can show a larger value for the high-frequency components associated with a transient. For example, if an inductance is inserted as Z_{block}, at higher frequencies inductive-impedance will dominate. This can help to reduce the impact of transient on the Z_{L} due to voltage divider action.

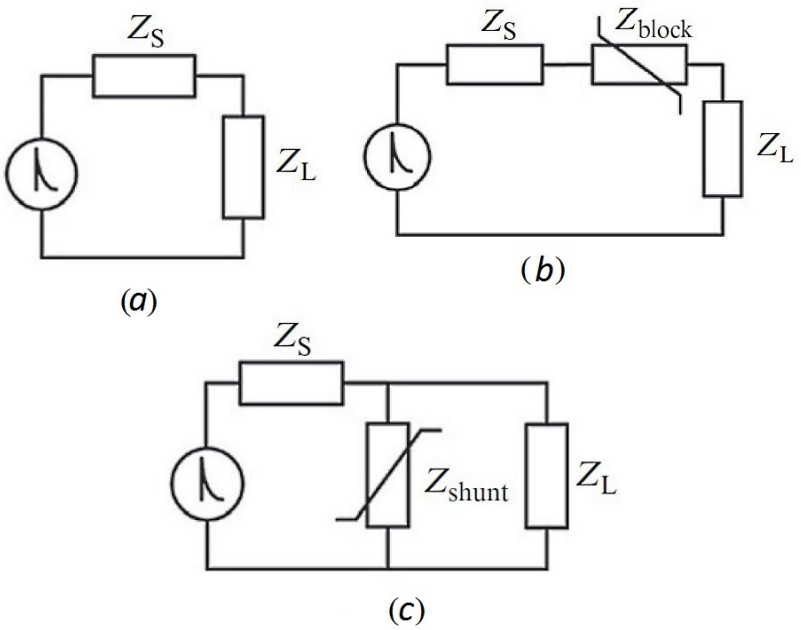

Figure 2.5: Voltage division principle with transient/surge protector circuits: (a) without any protection; (b) with a series blocking device; (c) with a shunting device [8].

Another way to reduce the voltage stress of a transient is to insert a shunt-type impedance block Z_{shunt} as in Figure 2.5(c) which behaves complementary to the Z_{block}, where at high frequency or high amplitude of the incoming surge, impedance value of the Z_{shunt} decreases. This results in diverting the surge away from the sensitive load.

Diversion of a transient can be accomplished with a voltage-clamping device or with a crow-bar device that switch into a very low impedance mode to short circuit the transient. The designs of these two types, as well as their operation and the application methods are different from one another [31]. In designing practical surge arrestor circuits, these non-linear devices are combined with inductors, and capacitors. In Chapter 3, we discuss most commonly used series and shunt devices that are inherent to surge protection circuits.

2.3.2 A differential-mode surge protector with series and shunt devices

A traditional surge protector which operates only for differential mode signals is shown in Figure 2.6(a) based on series blocking inductors (L_1, L_2), and two shunt elements Z_{shunt_1} and Z_{shunt_2}. In the case of Z_{shunt_1}, it is a combination of capacitor C_{1X} (where impedance $1/wC$ reduces at high frequencies) and a metal oxide varistor (MOV) M_1. The MOV M_1 reduces its resistance at higher voltages in a non-linear fashion. Similarly Z_{shunt_2} acts as a secondary shunt element, where C_{2X} acts similar to C_{1X}, with the bidirectional break-over diode (BBD) T_1 which also acts non-linearly at a higher speed compared to MOV. More details about how non-linear devices (NLDs) such as MOVs and BBDs are used in SPDs are available in Chapter 3.

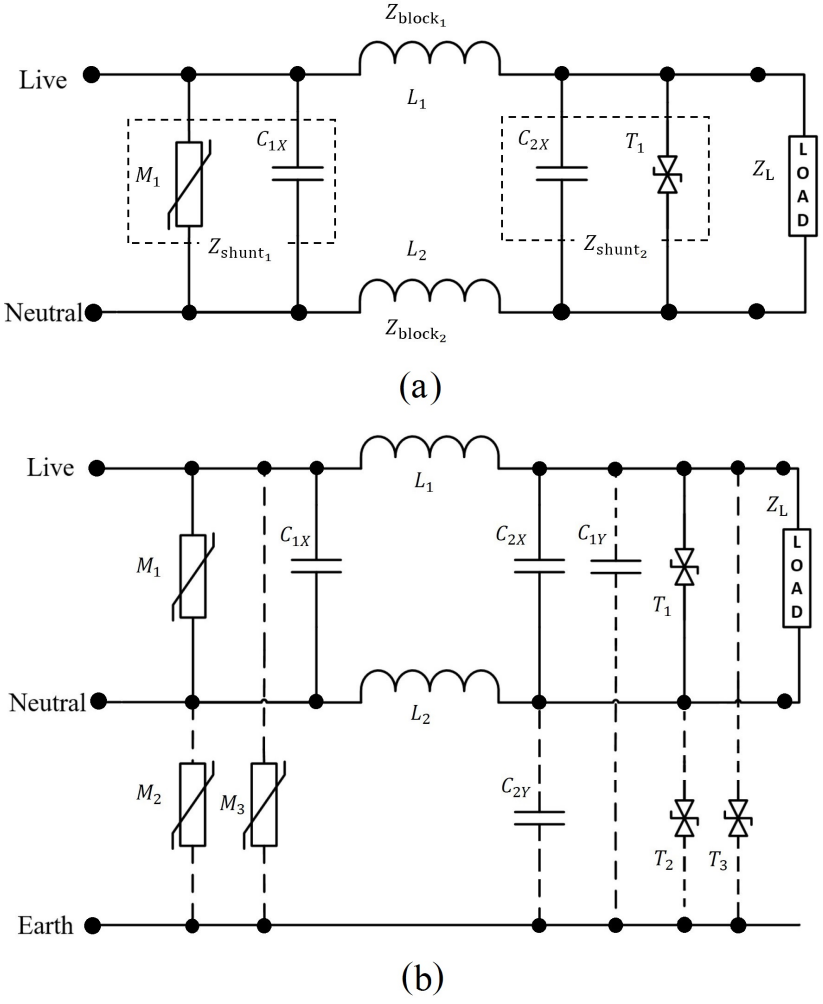

Figure 2.6: Traditional surge protector designs using series and shunt devices: (a) differential-mode surge protector; (b) common-mode surge protector [9]

2.3.3 A typical dual-mode surge protector designed for a three-wire power system

As mentioned in Section 2.2 transients can appear in both differential and common modes (as depicted in Figure 2.4), an advanced SPD must carry much larger combinations of these series and shunt protective elements. Figure 2.6(b) is a typical surge protector designed for a three-wire (live, neutral and earth) power system incorporating both modes of protection, where circuit parts shown in dotted lines are for common mode transient absorption. Here, the MOV M_2 and the BBD T_2 complemented with inductor L_2 and capacitor C_{2Y} eliminate part of the common-mode transients (between neutral to earth). In a similar manner, live-earth transient surges are blocked and diverted by M_3/T_3 pair and L_1/C_{1Y} combination. Under transient conditions, it is important that any MOVs/BBDs used have desired transient energy absorption ratings within a short period of time ($\simeq$ 2-5 ms). This recovery time interval allows absorbed transient energy to be dissipated into heat. However, given the unpredictability of surges, a second possible surge may fire MOV or BBD before the recovery time. Under such conditions, the device may permanently fail due to excess heat, having several blocks of series and shunt absorbing devices can prevent the damage to the sensitive load.

2.3.4 Selection of surge protectors

A SPD comprises of certain important characteristics whether it is designed for common-mode or differential-mode protection. Selection of a surge protector for a particular application is based on these attributes.

Clamping voltage

Clamping occurs mainly due to non-linear devices (NLDs) such as MOVs or BBDs present in the surge protector circuit. As indicated in Figure 2.6, when these NLDs enter into conduction phase due to high voltage transients, a particular clamping level is maintained to safeguard the load. In developing SPDs, a key criterion is to achieve a lower clamping voltage for better protection. Basically, there are three levels of protection according to the Underwriters Laboratory (UL) rating system (Figure 2.7(b)): 330 V, 400 V and 500 V [15]. Generally, a clamping voltage more than 600 V is considered as too high. More information about the operation of NLDs is presented in Chapter 3.

Energy absorption/dissipation

Energy rating, in joules, indicates the maximum surge energy that an SPD can absorb before it fails. Anything below the limit is safely withstood; however, as high voltage transients propagate through the protector, internal degradation of circuit components occur leading to failure. High energy rating indicates better protection. In general, surge protectors are at least rated at 200 to 400 joules. For greater levels of surge absorption, a rating of 600 joules or more is required [32]. In Section 2.4, we present a detailed discussion about various surge protector categories classified according to their energy ratings and location of instalment.

Response time

When a surge protector comes into action either by blocking or diverting a transient, it usually takes few micro-milliseconds to respond. The time required to fully turn on the SPD and conduct surge current through the voltage clamping device when subjected to a transient is defined as the *response time* [33]. In Chapter 3 a component based comparison of response time

is presented for different shunt protection devices. SPDs that are slow to respond with longer response times pass part of the transient voltage to critical load. This effect can lead to failure of certain sensitive circuits as the load becomes highly vulnerable to the surge during longer exposed times. Therefore, response time is a critical factor in selecting SPDs.

Life time/surge endurance

Durability of any surge protector is measured using its surge endurance capability against consecutive surge pulses. As per the IEEE C62.45 (2002) standards [34], the number of consecutive transients of specified voltage, rise time and duration, that the SPD can withstand before the threshold clamping voltage changes by more than a specified amount [35] is defined as the life time of a SPD. In Section 2.4, we discuss a summary of surge endurance test procedures specified by UL test standards.

2.4 Surge Protection Standards and Practices

Given the overview of surge protection fundamentals in above Sections, in this Section we review essential standards defined by the international test agencies as recommended for SPDs connected to the utility mains.

2.4.1 Standard test agencies and their recommended standards

Among most European, Asian, African and Oceanian countries (83 countries in total), the power equipment connected to the utility grid has to be certified by nationally accredited testing laboratories. Most of these national standards are traceable to the international standard of the *International Electrotechnical Commission* (IEC). However, in North America the IEC standards are not valid. Other locally established standards and guide lines of the *Underwriters Laboratory Incorporation* (UL), the *American National Standard Institute* (ANSI)/the *Institute of Electrical and Electronics Engineers* (IEEE) and the *National Electrical Code* (NEC) are followed [36]. These standards define the specifications for domains such as SPD selection for different locations, surge based testing procedures and standard test waveforms. Table 2.1 includes some of the primary institutions and their recommendations in relation to SPDs [37,38].

As indicated in Table 2.1, IEC 61000-4-5 and ANSI/IEEE C62.41 provide the basis for designers of transient protection systems to address the most extreme conditions on both power and data lines caused by lightning strikes and by heavy-load switching. Lightning transients may generate from a direct strike or induced voltages and currents due to an indirect strike. Transients due to switching may be the result of power system switching, load changes in power distribution systems, or even short-circuit fault conditions creating inductive voltage surges.

The IEC 61000-4-5 standard defines an entry point for transients and guides on installation conditions for advanced surge protectors [39]. Based on the measurements conducted by the IEEE over a number of years, on a statistical basis, the organization has established typical surge-waveform characteristics such as amplitudes and wave-shapes to be expected in various locations as a result of artificial and naturally occurring electrical phenomena. Summary of these outcomes are published in IEEE C62.41. The contents outlined in the IEC 61000-4-5 and

Table 2.1: Standard test agencies and their recommended standards for SPDs [31, 35, 38–40]

Standard agency	SPD related standards	Remark
IEC	IEC 61000-4-5	Provide a model to simulate surges and then to be able to check if the equipment is able to survive them.
	IEC 60364	General rules
	IEC 61643-11	Product standard
	IEC 61643-12	Selection and application guide
UL	UL 1449	Primary concern is safety.
	UL 1449 3rd Ed.	Devoted to surge protection manufacturers, defines the parameters as well as the test procedure to qualify an SPD
ANSI/IEEE	IEEE C62.41.1	Risk of transient over voltages to low voltage networks
	IEEE C62.41.2	Surge environment and types of transients
	IEEE C62.45	Method for testing equipment against transients that are connected to the low voltage network
	IEEE C62.62	Tests and ratings for SPDs installed on the load side of the service equipment, used to compare SPD performance
	IEEE C62.72	Installation of SPDs in electrical power distribution equipment
NEC	Article 280	Surge arrestor installed on wiring systems over 1000 V
	Article 285	Selection and installation conditions of SPDs
NEMA	LS1 Low Voltage Surge Protective Devices	Provides specific SPD performance. This results can be used to compare actual test results of SPDs

UL – Underwriters Laboratory Inc., IEC– International Electrotechnical Commission
ANSI/IEEE – American National Standard Institute / Institute of Electrical and Electronics Engineers
NEMA – National Electrical Manufacturers Association

the ANSI/IEEE 62.41 standards create an important framework for the design of AC power-line based SPDs.

2.4.2 Surge protector locations and categories

During the propagation of transient surges through power lines, data lines, or various circuit branches, its energy gets dissipated in numerous ways. Wire resistance, flashovers, and SPDs in the surge path dissipate part of the energy, whereas the branched circuits divide the energy into minor quantities depending on the path impedances (inductive and capacitive). These energies are transferred into individual circuit branches. As the total transient energy is reduced along the circuit branches compared to the entry point, facilities are classified into different location categories and specific protection levels are defined based on the locations. Different standards characterize the requirements of surge protector type depending on the potential impact of the transient surge, and the corresponding location for installation. As per the IEEE C62.41 standard, there are three categories defined: category A,B and C [35], while UL 1449 standard specify location based protectors as types 1,2 and 3 [28]. Figure 2.7 illustrates a comparison of the two classification methods.

2.4.3 ANSI/IEEE C62.41 categories

The voltage stress created by transients and surges generally depends on the location of the equipment connected. If the equipment to be protected is inside a building, the stress vary with

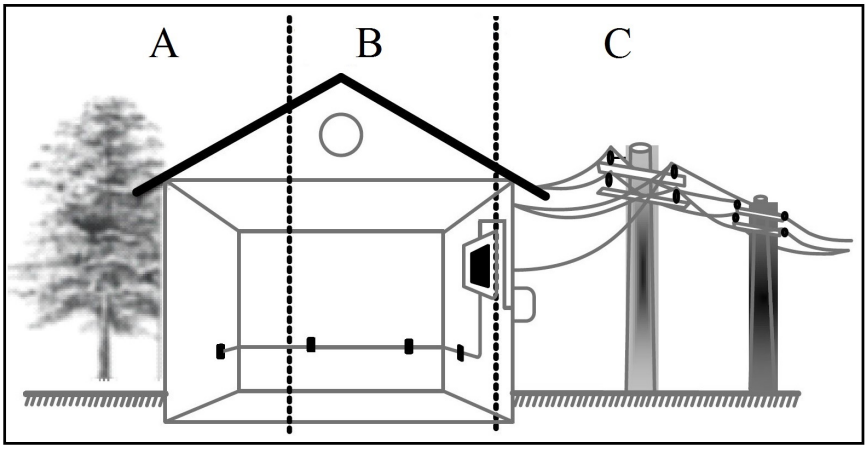

Category A: Branch and receptacle locations
Category B: Load side of the main overcurrent protection device to distribution panels
Category C: Secondary side of the service transformer drop to the line side of the main overcurrent protection device

(a)

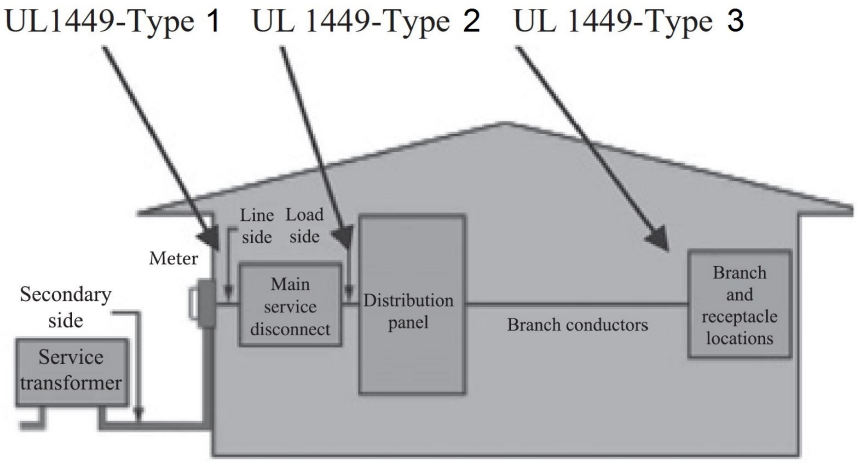

Type 1: Permanently connected device installed before or after the service disconnect overcurrent device and intended to be installed with no external overcurrent protective device
Type 2: Permanently connected device installed after the service disconnect overcurrent device
Type 3: Point of use SPDs that are installed with a minimum of 30 feet of conductor length from the service panel

(b)

Figure 2.7: Surge protector categories based on their locations: (a) ANSI/IEEE C62.41 categories; (b) UL-1449 types [15, 40]

the distance from the electrical service entrance to the location, the size and length of connection wires, and the complexity of the branched circuit network [41]. Basically, due to capacitive and inductive impedance effects which increases with the connection path, the voltage stress drops. Accordingly, the need to use sophisticated high endurance SPDs also reduces.

IEEE C62.41 identifies 2 main location categories within a building: category A and B. The "A" and "B" location prefixes along with suffixes 1,2 and 3 (A1, A2, A3, B1, B2, and B3) represent wiring distances and severity of incoming surges inside a building. In a similar

note, category C refers to SPDs installed at the entry point of electricity outside the building. Following is a summary of three category types.

Category C

As shown in Figure 2.7(a), category C encloses the region outside a building and main service entrances which includes main supply lines, transformers, service connections, and the feeder line to the main entrance panel, any overhead sub-feeder lines or underground wirings. Category C based SPDs are expected to protect against the most vulnerable power disruptions such as lightning strikes entering a building via the power line. According to research, highest-magnitude natural and man made surge currents and voltages originate in this category zone [42].

Category B

Category B corresponds to the zone within a residence or building that extends at least 30 ft (10 m) from the service entrance, and includes all major sub-feeders, bus systems, and short branch circuits such as distribution panels, industrial buses and feeder systems, heavy appliance circuits and lighting systems [42]. Protection provided in this category helps suppressing frequently internally generated transients due to switching of electric motors and motor-driven apparatus. It is a mandatory requirement of most hospitals, private diagnostic facilities, and research laboratories to protect their sensitive equipment installed in this zone to maintain quality and reliability in testing.

Category A

The indoor category A is the farthest zone from the electricity entry point. As per the definition, this region encloses any outlets and long branch circuits within the building that are extending more than 30 ft (10 m) from Category B outlets, and more than 60 ft (20 m) from the service entrance point [42]. Most of the load end devices such as computers, televisions, weighing bridges, measuring equipment, process control equipment and DC power supplies belong to this zone of protection. Individual SPDs with specified characteristics are often used under this category to prevent any damages from surges.

In this research, we are investigating the performance and optimization methods for a category A surge protector based on the patented SCASA technique. More details are described in Chapter 3.

2.4.4 UL-1449 location types

Any commercial SPD is considered to have a UL-1449 surge suppression rating on its label to verify that the device has been tested in accordance with standard ANSI/IEEE C62.41 waveforms. It is generally considered that devices not specified by UL rating are not very reliable SPDs to be purchased or used. In 2014, UL-1449 4th edition was released and it covers enclosed and open-type surge protectors designed to withstand repeated transient surges superimposed on the 50/60 Hz power line. Manufacturers classify their SPD designs into various types based on the surge endurance capability. A summary of UL-1449 types is presented below.

Type 1

Type 1 SPDs are hard wired designs which are permanently connected and used outside the buildings. As indicated in Figure 2.7(b), these are installed between the secondary side of the service transformer and the line terminal of the service equipment over-current device as well as the watt-hour meter busbars [43]. This particular class of surge protectors can be directly used without an external over-current protection device.

Type 2

Type 2 zone is defined between the main service disconnect and distribution panel. SPDs belong to this class are permanently installed on the load side of the service equipment over-current device [43]. Also, type 2 comprises both enclosed (moulded case SPDs) and open-type protector circuits connected to the branch panels.

Type 3

This type of SPDs are located inside the buildings with a minimum of 10 m (30 feet) conductor length from the electrical service panel (category B outlets) [43]. Typically these are cord-connected, receptacle type, or direct plug-in SPDs which can easily be used with consumer electrical items.

Type 4

Assemblies of surge suppressing components including one or more Type 5 electronic components together with a service disconnect (internal or external) belong to this class [43]. Moreover, any methods of complying with the limited current tests in UL 1449 is further considered here.

Above advanced types (Type 1, 2, 3) of surge protectors consist of a Type 4 component assembly with internal or external short circuit protection.

Type 5

Type 5 mainly includes discrete surge suppressing components such as MOVs or BBDs that are mounted on a printed circuit board (PCB) connected by its leads or provided within an enclosed case with mounting means and wiring terminals [43].

If we compare UL-1449 types with above ANSI/IEEE standards, a similarity can be seen with the Type 1 SPDs fall into the category C of IEEE standards, and Type 2 mainly comprises devices in both category B and C. Furthermore, Type 3 in UL classification is identical to category A. The SCASA surge protector we investigate during this research falls to the UL Type 3. More details about surge testing procedures are given in Chapters 4, 5 and 7.

2.5 Standard Surge Test Waveforms

According to the IEEE C62.41.2-2002 standard [40], there are two recommended waveforms for surge testing. One is defined as the 0.5 μs 100 kHz Ring Waveform, whereas the other is 1.2/50 µs - 8/20 μs Combination Wave. As the name suggests, the Combination Wave involves two waveforms: an open circuit voltage waveform named 1.2/50 μs combination voltage and a short circuit current waveform which creates 8/20 μs combination current. Both these voltage and current standards have different shapes due to varying internal impedances of the surge generators that are not purely resistive. Also, the surge simulators must be in two states (open and short circuit modes) to generate the corresponding combinational waves.

2.5.1 The 0.5 μs–100 kHz ring waveform

As most of the surge frequencies lie within the natural frequency of the indoor wiring systems, oscillatory waves (based on resonance effects) of varying amplitudes and frequencies can be observed from place-to-place in the wiring system inside most houses or factory environments. The frequency of these oscillations generally lies in the range 5–500 kHz [40]. According to the IEEE standard, 100 kHz (± 20 kHz) is defined as the realistic frequency to represent the oscillatory Ring Waveform. A plot of the nominal 100 kHz Ring Wave is shown in Figure 2.8. As indicated in Figure 2.8, the frequency (100 kHz) is calculated from the first and third zero-crossing after the initial voltage peak. By definition, the rise time of Ring Wave is considered as the time difference between 10% and 90% amplitude points on the rising edge of the waveform.

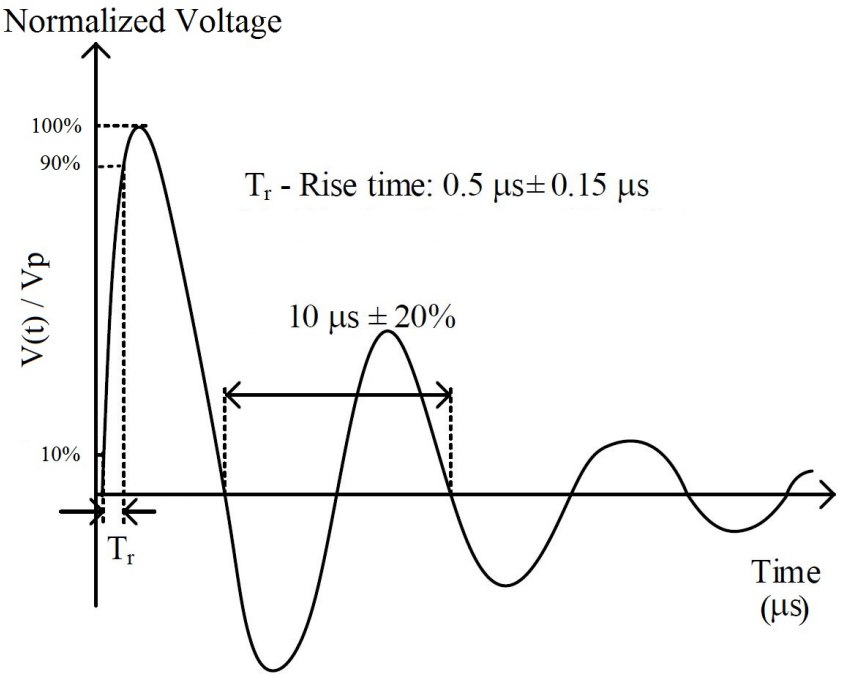

Figure 2.8: Nominal waveform of the 0.5 μs–100 kHz Ring Wave [40]

The Ring Waveform can be mathematically expressed according to Eq. (2.1):

$$V(t) = AV_p\left(1 - e^{-t/\tau_1}\right) e^{-t/\tau_2} \cos(\omega t) \tag{2.1}$$

where, the constants are $A = 1.590$, $\tau_1 = 0.533$ μs, $\tau_2 = 9.7888$ μs and V_p is the peak value of the first voltage peak. The brief 0.5 μs rise time of the rising edge of the wave, together with a large peak current, corresponds to a significant di/dt, which will produce greater induced transients in the path connections of equipment under test (EUT). Furthermore, the negative voltage peaks of the Ring Wave can cause damage to semiconductor based devices which are sensitive to the polarity.

2.5.2 The 1.2/50 μs – 8/20 μs combinational surge waveforms

The combinational surge waveforms are generated by a lighting surge simulator (LSS) under two circumstances. When under open circuit conditions, a 1.2/50 μs voltage wave is produced across LSS terminals, whereas an 8/20 μs current waveform is generated in a short circuit situation [34, 39]. Both these combinational waves provide appropriate models for lighting based transient surges in outdoor environments. High energy unidirectional transients are common in outdoors apart from the oscillatory waveforms as described in Section 2.5.1.

The 1.2/50 μs combinational voltage waveform

As per the definition, open-circuit voltage waveform (Figure 2.9) has following characteristics:

— Front time/Rise time (T_r): 1.2 μs ± 0.36 μs

— Duration (T): 50 μs ± 10 μs

The rise time of voltage wave is determined using $T_r = 1.67 \times t_1$, where t_1 is the difference between 90% and 30% of amplitude points on the rising edge of the waveform ($t_1 = t_{90} - t_{30}$). In addition, duration T of the waveform is defined as the time between virtual origin and the time of 50% voltage point on the falling edge. Virtual origin is considered as the point where a straight line between the 90% and 30% points on the rising edge intersects with voltage zero line. This waveform is defined as 1.2/50 μs combination voltage wave because of its 1.2 μs rise time and the 50 μs duration.

A mathematical representation of 1.2/50 μs open-circuit voltage wave is given by Eq. (2.2):

$$V(t) = A_V V_p (1 - e^{-t/\tau_1}) e^{-t/\tau_2} \tag{2.2}$$

where the constants are $A_V = 1.037$ $(\mu s)^{-3}, \tau_1 = 0.4074$ $\mu s, \tau_2 = 68.22$ μs and V_p is the peak voltage of the waveform.

To fully understand the behaviour of open-circuit combinational voltage wave, we present a detailed comparison of analytical, experimental and numerical wave shapes in Figure 2.10. Analytical plot is based on Matlab, whereas experimental and numerical plots are based on LSS data and LTSpice simulations respectively.

The 8/20 μs combinational current waveform

The combination current wave is generated when the above voltage waveform is short circuited, and the corresponding short-circuit current (Figure 2.11) has the following characteristics:

— Front time/ Rise time (T_r): 8 μs (+1.0, –2.5) μs

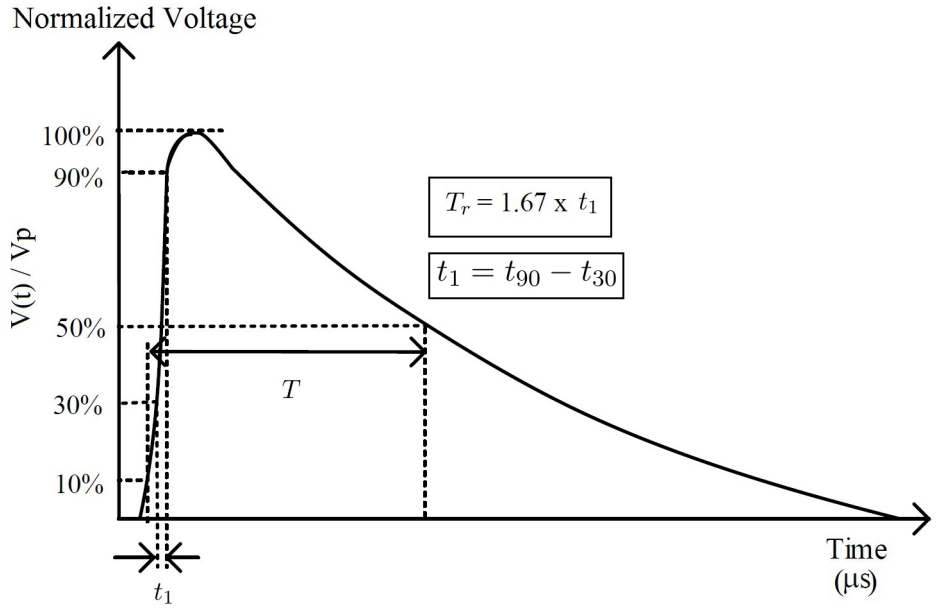

Figure 2.9: Nominal waveform of the 1.2/50 μs combinational voltage waveform [34, 39]

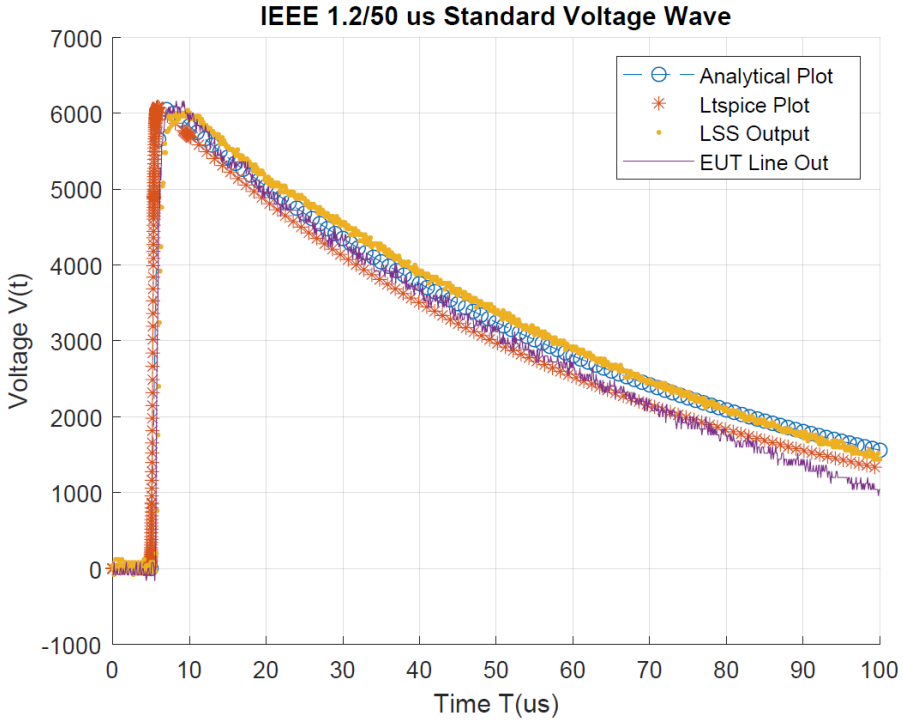

Figure 2.10: Comparison plots for 6 kV 1.2/50 μs combinational voltage waveform: analytical plot, LTSpice plot, LSS output and EUT line out

— Duration (T): 20 μs (+8, –4) μs

The rise time of current wave is determined using $T_r = 1.25 \times t_1$, where t_1 is the difference between 90% and 10% of amplitude points on the rising edge of the waveform ($t_1 = t_{90} - t_{10}$). In addition, duration T of the waveform is defined as the time between virtual origin (t_0) and the time of 50% (t_{50}) voltage point on the falling edge. Virtual origin is considered as the point where a straight line between the 90% and 10% points on the rising edge intersects with current

zero line. The time difference $T = t_{50} - t_0$ of the standard current wave is 20 μs. This waveform is defined as 8/20 μs combination current wave because of its 8 μs rise time and the 20 μs duration.

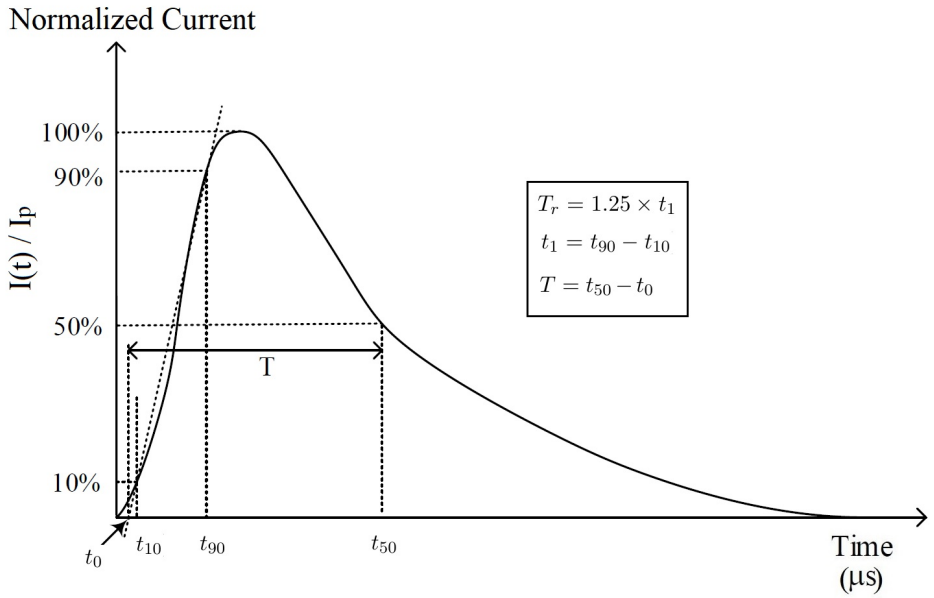

Figure 2.11: Nominal waveform of the 8/20 μs combinational current waveform [34, 39]

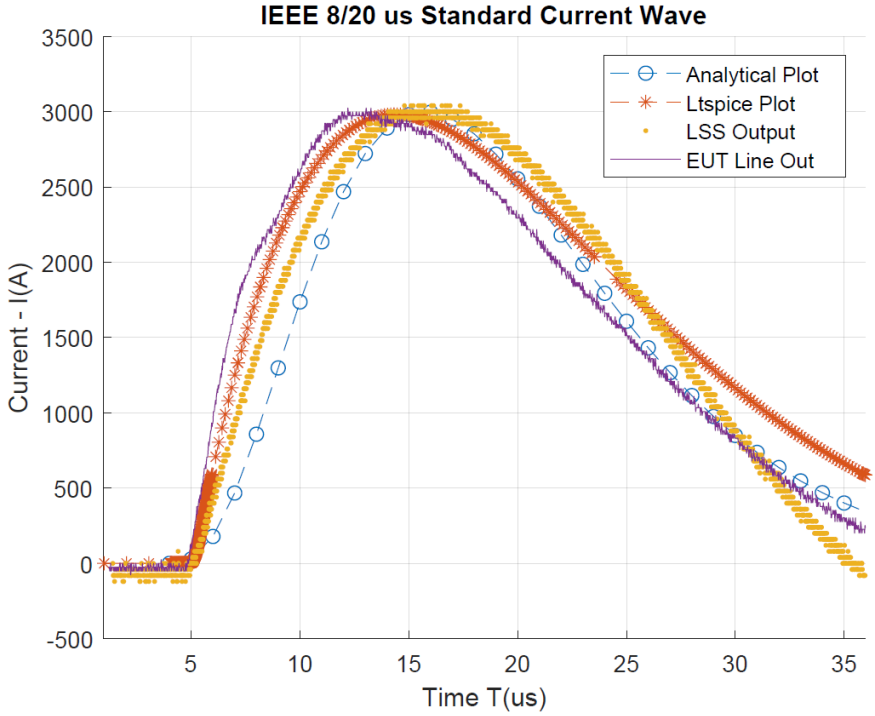

Figure 2.12: Comparison plots for 3 kA 8/20 μs combinational current waveform: analytical plot, Ltspice plot, LSS output and EUT line out

The short-circuit current waveform can be mathematically expressed according to Eq. (2.3):

$$I(t) = A_I I_p t^3 e^{-t/\tau} \tag{2.3}$$

where the constants are $A_I = 0.01243\ \mu s^{-3}$, $\tau = 3.911\ \mu s$ and I_p is the peak current of the waveform.

To comprehend the behaviour of short-circuit combinational current wave, we present a detailed comparison of analytical, experimental and numerical wave shapes in Figure 2.12. Analytical plot is based on Matlab, whereas experimental and numerical plots are based on LSS data and LTSpice simulations respectively.

2.5.3 Lightning surge simulators

A Lightning Surge Simulator (LSS) is an electronic instrument which can simulate voltage and current wave shapes due to lightning discharges and associated induced transient effects in an laboratory environment. All commercial LSS systems have a maximum voltage/energy setting based on the internal generation circuit. For example bench-mode Noiseken LSS 6130/6230 have a maximum capacity of 6.6 kV open-circuit voltage and 3.3 kA short-circuit current [44]. However, much advanced versions like Noiseken LSS-F03 series can generate simulated waveforms up to 15 kV/7.5 kA [45]. All these simulators are compliant with IEC61000-4-5/IEEE C62.41.2-2002 standards. Figure 2.13 depicts two of the most commercially available LSS systems manufactured by Noiseken, Japan.

Figure 2.13: Noiseken lightning surge simulators: (a) LSS 6230; (b) LSS-F03 series [44, 45]

Equivalent circuit of Noiseken LSS 6130/6230

Internal generation circuit of any LSS is the same irrespective of its type and voltage setting. Figure 2.14 illustrates the common equivalent circuit required for the generation of standard surge test waveforms as explained in Section 2.5.2. Details of LSS specifications are given in Appendix B.

The 10 μF capacitor in generation circuit is the main energy storage element, whereas the two inductors 2.7 μH and 6 μH act as rise time shaping components to produce standard waveforms. In addition, resistors 7 Ω and 1MΩ are pulse duration shaping resistors of the output

waveforms. More importantly, impedance matching is of the circuit is achieved by the 1.1 Ω resistor.

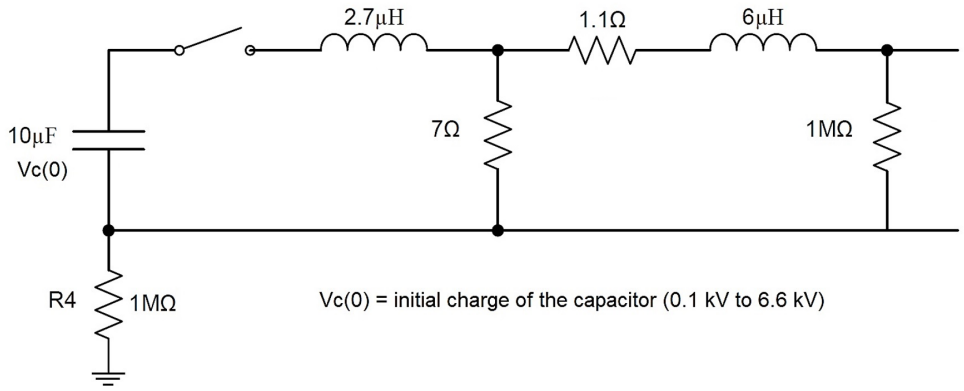

Figure 2.14: Internal generation circuit of Noiseken LSS 6130/6230 [45, 46]

Connection with EUT

For surge immunity testing, an Equipment Under Test (EUT) must be connected to the output terminals of the LSS. It must be noted that the actual voltage injected to EUT is not identical (less than) to the voltage setting of LSS. As indicated in Figure 2.15, various internal impedances which affects the total loop resistance of the path connecting LSS and EUT heavily influence the injected voltage. Mainly, factors such as internal resistance of the high voltage source of the LSS, wave-shaping circuit of the LSS (Z_{source}) and path impedances (Z_{path}) created by the inductive/capacitive and resistive wire connections are of extreme importance in circuit analysis. During our surge testing, we observed the LSS output surge magnitude as ≈ 4 kV for a maximum setting of 6.6 kV. More information about surge current propagation into an EUT is presented in Chapter 6.

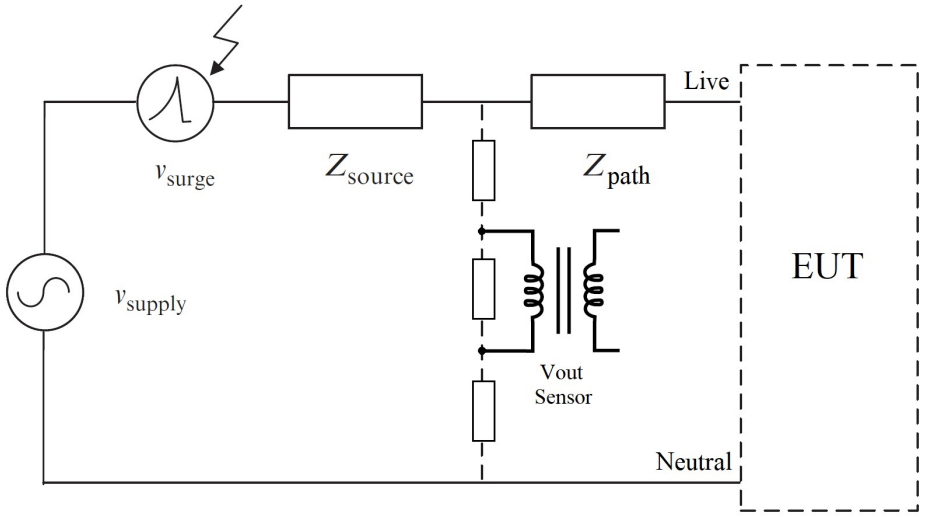

Figure 2.15: Simplified circuit diagram of LSS system connected to an EUT

Table 2.2: IEEE C62.41 location based current/voltage waveforms [47]

Category	Level of exposure	Voltage	0.5 μs 100 kHz Ring Wave		1.2/50 μs (V) 8/20 μs (A) Combination Wave	
			Current	Energy	Current	Energy
		(kV)	(A)	(J)	(kA)	(J)
A1	Low	2	70	0.63	–	–
A2	Medium	3	130	2.34	–	–
A3	High	6	200	5.43	–	–
B1	Low	2	170	1.53	1	9
B2	Medium	4	330	5.94	2	36
B3	High	6	500	13.5	3	81
C1	Low	6	–		3	81
C2	Medium	10	–		5	225
C3	High	20	–		10	900

2.6 Surge Testing for Low-voltage AC Power Circuits

Based on the LSS and EUT connection setup indicated above, IEEE C62.45 (2002) standards provide appropriate surge testing guidelines for equipment survivability, methods, surge coupling/decoupling circuit parameters, testing safety requirements and various other surge suppression techniques. As there are no specific models to represent all possible surge environments; the complexities of real world situations need to be simplified in order to perform a manageable set of standard surge tests. Depending on the ANSI/IEEE C62.41 categories mentioned in Section 2.4.3, waveforms and amplitudes for surge-voltages and surge-currents applied to evaluate the surge withstand capability are selected.

2.6.1 Location-based surge waveforms according to IEEE C62.41

The three standard test waveforms discussed in the previous Section are injected into SPD devices for surge immunity testing, however, as category C protectors lie outside at the service entrance, they are tested against the most severe peak voltages. Conversely, those SPDs inside the building (category A and B) are subjected to minor surge amplitudes with limited energy. Table 2.2 presents a summary of standard test waveforms/peak amplitudes used in different location categories.

As external lightning related transients in location A are negligible due to the protection provided by service disconnect and inductances of the building wires, this particular category is not tested with combinational waveforms. However, location B inside the building (distribution panels) is exposed to both internally and externally created transient effects (switching and lightning based); therefore, both Ring Wave and Combination Wave test conditions are applied. In addition, category C has limited exposure to switching issues, and as a general practice Ring Wave based surge tests are not defined. As shown in Table 2.2, combination waveforms with peak current and voltage amplitudes such as 3–10 kA and 6–20 kV are specified for category C surge protectors under prime safety regulations. Details about safety aspects are found in [34,40].

2.6.2 Requirements for surge decoupling

During surge tests, an essential safety requirement is satisfied by the decoupling circuit network inside the LSS. Without these components, the low line impedance of the AC supply would load the generator and prevent it from delivering the full output voltage. Moreover, all other equipment powered from the same utility line would be subjected to the surge generated by LSS, with attendant equipment damage and personnel hazard resulting. Surge decoupling, generally includes a collection of filter capacitors/inductors placed between the power line and LSS; it is referred to as back filter network as well. It is also necessary to have decoupling filters in all phase lines into and out of the EUT, excluding the equipment grounding which will not be disconnected during surge tests. Figure 2.16 shows how a decoupling network is connected to a three-phase power line inside Noiseken LSS.

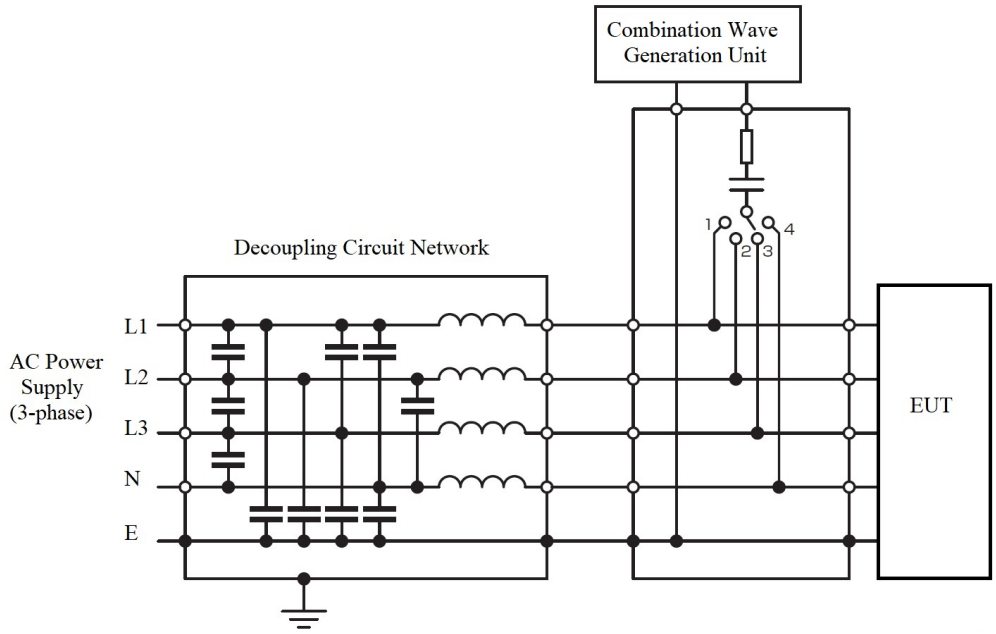

Figure 2.16: Decoupling circuit network connected to a three-phase power line inside Noiseken LSS-F03 [45]

The parallel combination of shunt capacitors shown in Figure 2.16 provide short circuit path between the surge wave generation unit and AC power supply. Any possible effects of transient energy pumping back to the power line is diverted to the earth terminal by these capacitors. In a similar manner, milli-henry order inductors placed in series create a high impedance path to block the leakage surge currents during testing. Overall, the combined action of shunt-capacitors and series-inductors in decoupling network make sure no transient effect is passing to the power line.

2.6.3 Surge immunity tests specified by UL-1449 standards

UL-1449 3rd edition standards specify three essential tests that an SPD connected as the EUT must pass. Following is a brief description to characterise each test method as required in surge-immunity evaluation.

Voltage protection rating (VPR) test

Prior to the UL-1449 3rd edition, surge impulse tests were conducted with a surge waveform of 6 kV/500 A to obtain suppressed voltage rating (SVR) [15], that is the clamping voltage for the SPD. As mentioned previously, clamping helps to reduce the passage of surge energy to the sensitive load.

With the release of revised 3rd edition, impulse test is characterised by combinational voltage/current waveforms of 6 kV/3000 A to obtain the clamping voltage. This new clamping level is defined as the VPR of SPD [15, 43]. There is six times more surge energy present in this revised waveform, and it results in a relatively higher clamping voltage. Therefore, VPR values will be numerically larger than the former SVR. In addition, the surge pulse injected in VPR test will be superimposed at a phase angle of 90±10 degrees on top of AC mains to simulate the worst possible transient effect.

Nominal discharge current (NDC) test – for type 1 and type 2 SPDs

As per the NDC test newly introduced in the 3rd edition, a SPD must remain fully operational after being subjected to a total of 15 surges in three groups of five surges [15]. This method is also considered as the "Stress Test" for SPDs to measure its durability/endurance in practical situations. As per the definition, SPD can be rested for maximum of 1 minute ±15 seconds between the surges. After the 15th surge pulse, SPD is allowed to rest for a minimum 15 minutes. Generally NDC test is conducted in combination with the VPR test mentioned above; hence, combinational voltage/current waveforms are applied. A clamping voltage deviation beyond 10% in VPR during these repetitive surge tests is considered as a failure. The manufacturer of SPD can select the magnitude NDC I_n, and it varies from 10 kA to 20 kA for Type 1 surge protectors, whereas Type 2 devices can have currents of 3 kA, 5 kA, 10 kA or 20 kA. Before commercialization, the manufacturer should mark the actual nominal discharge current level withstood by the device as a label indicating I_n [48].

Surge immunity test procedures used in our experiments for Type 3 SCASA surge protector adhere to UL-1449 3rd edition standards, and they are performed by NoiseKen lightning surge simulators (LSS-6130/6230 and LSS-F03). More information about destructive test procedures carried out to evaluate surge endurance of SCASA is presented in Chapter 5.

2.7 Chapter Summary

In this chapter, I presented findings of the literature survey describing power-line disturbances, power quality issues, surge protection principles and other important standards and practices. Also, circuit concepts used in surge protection for common-mode and differential-mode applications were elucidated.

In the next chapter, traditional circuit components used in surge protectors will be studied with a focus on the novel application of supercapacitors for surge absorption.

Chapter 3

Traditional Circuit Components and Supercapacitors for Surge Protection

In Chapter 2, we elucidated how voltage division principle is applied in surge protection circuits. By inserting series and shunt devices which behave in a non-linear fashion, transient propagation towards the load side can be prevented. In this Chapter, we investigate in detail traditional circuit component types used in surge protection, their non-linear impedance behaviour, and highlight the novel use of supercapacitors (SCs) for surge absorption.

3.1 Traditional Circuit Components Used for Surge Protection

As discussed in Section 2.3, traditional transient suppressors are non-linear devices (NLDs) that exhibit high or low impedance during transient propagation. These devices can be classified into two fundamental types according to their operation [49]:

- components that can attenuate transients and block the propagation towards sensitive load; and
- components that divert the transient away from the critical load while reducing the residual voltage.

Since we discussed the circuit arrangements of series and shunt protection blocks (Figure 2.6) in the previous Chapter, V-I characteristics/construction principles of various NLDs that allow surge blocking and diversion are explained here. First, we focus on to traditional shunt-type circuit components. These diverting elements are basically divided into two sub-categories: voltage-clamping devices or voltage-switching (crowbar) devices [19, 49]. Both types switch to an extremely low impedance mode against transients to short circuit the effect. However, these types have different operating mechanisms, and used for distinct applications.

Component air gaps, gas discharge tubes (GDTs) and semiconductor thyristors are the common crowbar devices that effectively exhibit short circuit conditions when operating in response to voltage surges. As these devices divert a substantial surge current, it leads to voltages significantly lower than the normal operating voltage of the load. When this occurs, the surge energy needs to be dissipated elsewhere in the circuit (mostly within the internal impedance of crowbar device). However, a major drawback of this type is that these components can momentarily interrupt the operation of load devices that require continuous power supply. This is mainly due to the short-circuiting effect of crowbar devices, but in a clamping device, this limitation is circumvented.

A voltage clamping/limiting device produces variable impedance depending on the current flowing through the device or on the voltage across its terminals. These devices exhibit a non-linear impedance characteristics, that can be explained using Ohm's law, but with a variable resistance unlike linear devices. The variation of impedance is monotonic; it shows a continuous behaviour unlike a crowbar device, which exhibits a turn-on -off action. Voltage limiting type SPDs effectively show low impedances under transients, but not short circuit conditions. Therefore, for the same magnitude of surge currents, these devices can dissipate greater power than air gaps or gas tubes [50].

In contrast to air gaps and tubes, the voltage appearing across clamping devices during a surge is greater than the normal voltage. Consequently, continuous power flow is not normally a concern for these devices as it is with crowbar components, and their operation does not normally interfere with the load circuits [51]. The most common semiconductor based voltage clamping devices are metal oxide varistors (MOVs), TVS thyristors, and avalanche-type back-to-back zener diodes (BBDs). Selection of these components for SPD circuits depends on the clamping voltage, response time, durability and maximum current/energy capability. In the following Sections, we provide details of various crowbar/clamping type NLDs used in surge protection circuits.

3.2 Voltage Switching (Crowbar) Devices

3.2.1 Carbon block spark gap

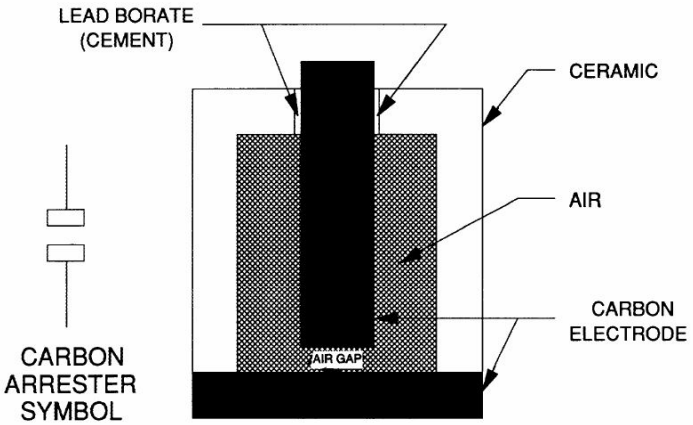

Figure 3.1: Cross-sectional view of a two-electrode carbon block spark gap [31]

Carbon block spark gap is the oldest technology of overvoltage suppressors and is still been used in telephone circuits and power distribution panels. Two carbon rods are held with an insulator at a specific distance apart (typically 80–150μm) to create a protection gap [31]. The gap dimension determines the transient voltage at which a spark is created between the two carbon blocks. Transient energy is dissipated in the arc created safeguarding the circuits under protection. During operation, one of the rods is connected to the system earth and the other one is connected to the main signal cable. Carbon block surge suppressors are similar to a gas arrestor but with the two electrodes exposed to the air. Figure 3.1 shows the interior view of a carbon block spark gap.

3.2.2 Gas discharge tubes (GDTs)

GDTs consist of two metallic electrodes that are separated by an air-gap(s) sealed in an envelope containing an inert gas or a mixture of inert gases (Figure 3.2(a)). Usually the pressure inside a gas tube is kept at less than atmospheric pressure. Common gases used in production are argon, helium, hydrogen, and nitrogen [31]. GDTs exhibit a similar operation to cathode ray tubes where one electrode acts as the anode and the other functions as cathode. During high voltage transients, the inert gas ionizes and starts conducting dissipating the excessive energy. A gas tube can take several microseconds to turn on or 'fire' as an inert gas usually takes time to ionize. In practical situations, the reaction time, and the firing voltage are dependent on the slope of the transient. In fact, the faster the rate of rise of surge wavefront, the higher the firing voltage.

In manufacturing GDTs, several factors such as the spacing between electrodes, type of gas used, gas pressure, electrode configuration, and surface coating are considered important to get optimal performance [31].

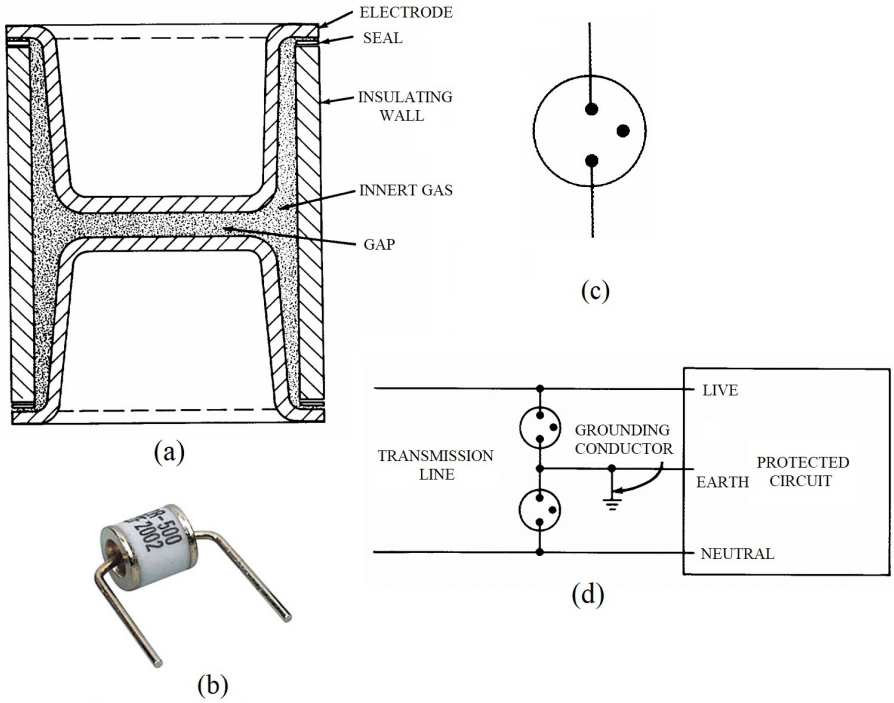

Figure 3.2: A gas discharge tube: (a) cross-sectional view; (b) physical view; (c) circuit symbol; (d) practical gas tube surge arrester [31]

GDTs have a very high firing voltage for their size. They are designed for use over a broad voltage range. Firing voltages typically start at 500 V and can exceed over 1000 V. These high firing voltages make them unsuitable to protect microchips; however, GDTs can be used in conjunction with TVS diodes/MOVs to provide effective protection for low clamping level for 5 V signal lines.

Gas tubes have a range of applications as shunt-type SPDs in telecom equipment such as power lines, communication lines, signal lines and data transmission lines to protect them against transient surge voltages that may occur due to lightning strikes and heavy equipment switching.

Moreover, protection against 230 V/50 Hz overvoltages is normally provided by selecting the maximum DC breakdown voltage equal to the peak value of the tolerable AC waveform.

As mentioned in Section 3.1, GDTs do not influence normal operation of equipment (Figure 3.2(d)) due to high-impedance mode below its firing voltage. However, in its conduction mode, due to high-voltage ionization of the gas, transient surge is diverted away from the load through its extremely low-impedance path. Failure of a gas tube surge protector can be caused by several factors. Most common failures are due to mechanical shock, corrosion, tube-seal failure, and repeatedly or excessively subjected to severe transients. Table 3.1 compares the characteristics of gas tubes with other widely used TVS devices.

3.2.3 Transient voltage suppressor (TVS) thyristors

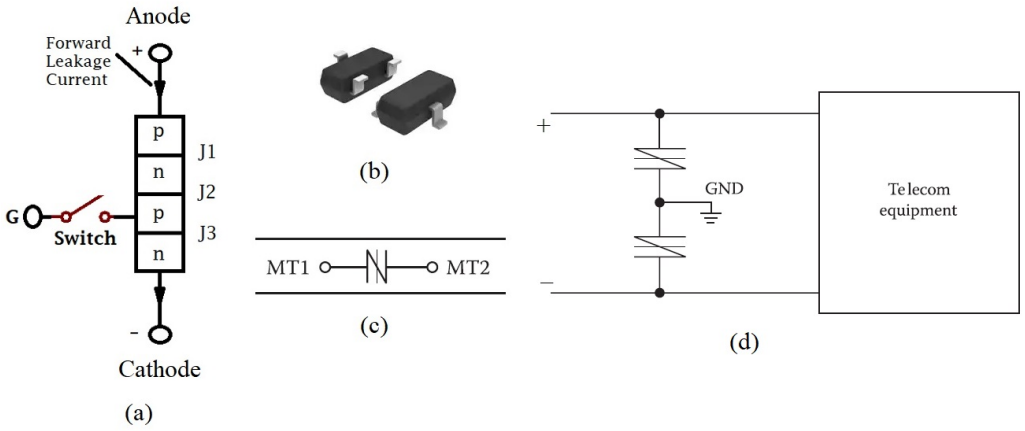

Figure 3.3: TVS thyristor: (a) cross-sectional view; (b) physical view; (c) circuit symbol; (d) typical application circuit in telecommunication plant [18]

TVS thyristors are semi-conductor based devices constructed with four alternating layers of p-type and n-type materials as indicated in Figure 3.3(a). When the avalanche triggering occurs under high-voltage transients, thyristors protect sensitive loads by switching to a low on-state of a few volts, thus provide a 'crowbar' effect with high-current capability [18]. Switching to on-state initiate at the break-over voltage of the device. These are usually not used for protection against DC power sources as they may not restore to non-conduction after breakdown. TVS diode would be a better solution for such applications; more information regarding TVS diodes is described in Section 3.3.2. The surge current capability of a TVS thyristor is normally determined by p-n layer structure as well as size. Operating voltage levels begin at 12 V and are available in several increments up through several hundred volts. They do not wear out, but when electrically overstressed fail as a short-circuit. Noticeably, TVS thyristors are used extensively in surge protection of communication equipment due to their low operating voltages and extremely fast nanoseconds order response times. Table 3.1 compares the characteristics of TVS thyristors with other commonly used TVS devices.

3.3 Voltage Clamping Devices

3.3.1 Metal oxide varistors (MOVs)

MOVs are the most common SPD components used in surge protection circuits; these are typically in the shape of a round disc-like body or rectangular and tubular shapes. Varistors have two metal electrodes that embody a matrix of conductive zinc-oxide (ZnO) or other metal-oxide grains (Figure 3.4(a)) separated by grain boundaries providing p–n junction semiconductor characteristics with highly non-linear voltage-current behaviour. Each inter-granular boundary displays a rectifying action and possesses a specific voltage barrier (break-down voltage) [52]. As transients appear across MOV terminals exceeding this barrier voltage, metal-oxide grains conduct by forming a low ohmic path to absorb and dissipate transient energy. Many layers of metal-oxide grains act in series-parallel combination between varistor electrodes to allow surge diversion at high-voltages; hence, these are considered as multi-junction semiconductor devices. In developing SCASA technique, two MOVs are used both of which rated to 275 RMS conditions with an energy rating of ≈ 30 J. More details about SCASA circuit development will be discussed in Section 3.8. A schematic cross-sectional view of a varistor is depicted in Figure 3.4(a).

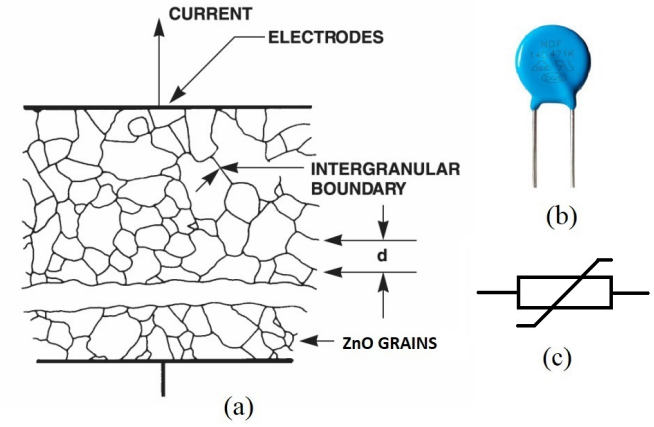

Figure 3.4: Metal oxide varistor: (a) cross-sectional view; (b) physical view; (c) circuit symbol [31]

As the name "varistor" suggests, an MOV act as a variable resistor that shows non-linear V–I characteristics as illustrated by Figure 3.5(a). In order to demonstrate the three distinct modes of MOV operation over a range of currents, a log–log plot is used. The generalized circuit model shown in Figure 3.5(c) can relate to all three different regions: leakage region (OFF-state), Normal varistor operation (ON-state) and upturn region (fully conductive state) [18]. At extremely low currents (microampere order) the V-I relationship shows a linear ohmic behaviour with very high resistance (≈ 1 GΩ or higher). This state is considered as a near open-circuit condition, hence denoted as an OFF-state with only minor possibility for leakage currents. Usually, the magnitude of OFF-state resistance R_{OFF} (shown in parallel in Figure 3.5(c)) depends on the MOV body temperature, but lies in the range of 10–1000 MΩ. It also changes with the frequency of voltage signals in an inversely proportional manner. When the voltage across MOV terminals exceeds its break-down barrier, metal-oxide grains start conducting by changing the non-linear resistance R_{X} to much smaller values significantly less than R_{OFF}. During this normal varistor operation region, R_{X} facilitates the absorption and release of surge energy through power

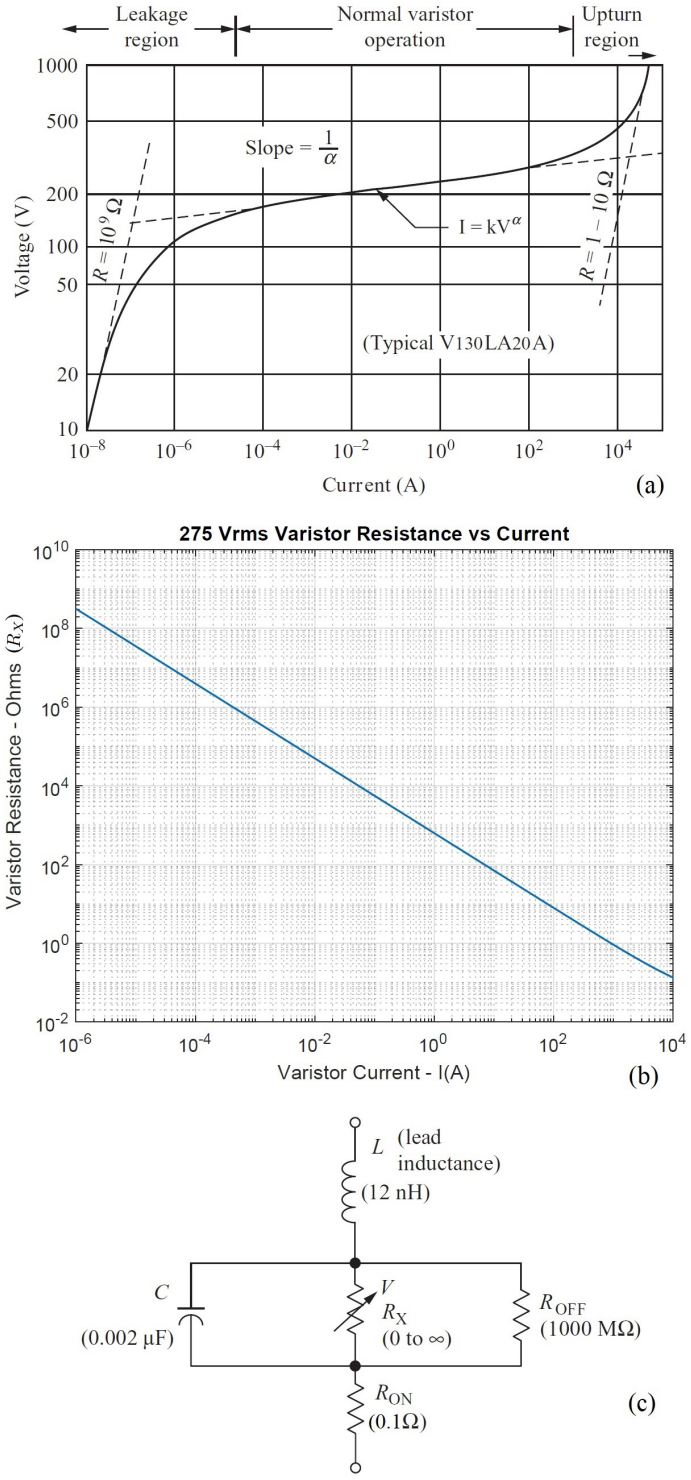

Figure 3.5: Metal oxide varistor characteristic curves and equivalent circuit: (a) V–I characteristic [45]; (b) R_X–I characteristic; (c) generalized equivalent circuit [53, 54]

dissipation. The equivalent circuit shown in Figure 3.5(c) is still applicable to normal varistor operation, but with OFF-state properties (R_{OFF} and C) being ignored. At extremely high transient currents, the non-linear resistance is in a low-resistance mode that approximates a short circuit condition which results in fully diverting the transient away from the load. This upturn region can be represented by an ON-resistance (R_{ON}) which is the resistance of fired metal oxide grains, and would be in the range 0.1–10 Ω depending on the chemistry of grains [54, 55]. The

series inductance L indicated in equivalent circuit, resulting from the varistor leads can increase the voltage appearing across the device terminals when surge currents with steep wave fronts pass through. This inductive voltage effect may appear as an overshoot on the voltage waveform and may cause a minor delay in varistor response.

In order to model the non-linearity of MOVs, various mathematical models are used in literature. Understanding the complex nature of R_{X} is important as surge dissipation primarily transpire through its dynamic resistance. As per the industry specifications, the most appropriate mathematical model in predicting MOV non-linearity is given by power-law [55, 56]. Two useful relationships of power-law that govern the operation of R_{X} are given by Eqs (3.1) and (3.2), where I is the current through and V is the voltage across the varistor.

$$I = KV^{\alpha} \tag{3.1}$$

$$\log(V) = A_1 + A_2 \log_{10}(I) + A_3 \exp^{-\log_{10}(I)} + A_4 \exp^{\log_{10}(I)} \tag{3.2}$$

In Eq. (3.1), the constants k and α are varistor dependent unique parameters; where k is dependent on the device geometry and the exponent α defines the degree of non-linearity in the resistance characteristic. Both these parameters are controlled by the selection of materials and the manufacturing process. As indicated in Figure 3.5(a), α can be found experimentally by curve-fitting, where slope of V–I characteristic determines $1/\alpha$ and k can be obtained using the intercept of a log-log plot. A high α implies a stronger clamping action for an MOV, and zinc-oxide based varistors have typical α values lie in the range of 15 to 30 [55]. The parameters A_1, A_2, A_3 and A_4 in Eq. (3.2) are also dependent on the varistor type; these coefficients are linked to the highly non-linear log representation between V and I which signifies the MOV's dynamic resistance from a few microampere (leakage region) order to several kilo-amperes in the conducting mode [53,57]. Due to mathematical complexity, above coefficients are difficult to be found using curve-fitting method, however, industry manufacturers such as *Littlefuse* have provided appropriate models comparable to Eq. (3.2) with some modifications.

Another remarkable straight-line relationship is shown in Figure 3.5(b), where non-linear resistance R_{X} can be expressed as a linear function of current I in its logarithmic form $\log(I)$ as per the Eq. (3.3) [54]:

$$R_X = A + 10^{B+C\,\log(I)} \tag{3.3}$$

where the constants A=0.035 Ω and B, C are unit less quantities with 2.8 and -0.95 respectively (see Appendix D). Eq. (3.3) provides a useful relationship for our analytical work based on the Laplace Transform method. In Chapter 6, we discuss theoretical validation of surge current propagation through the SCASA magnetic core supported by the predictions of Eq. (3.3) for MOV behaviour. As substantiated by empirical testing, this equation is formulated without the consideration of physical units (see Chapter 6), and is valid for a wide range of currents from 10 μA–10 kA [54]. The parameters A, B and C are dependent on the varistor type and its materials used for construction.

Transient energy absorption capability of MOVs are achieved by increasing the size of the disc-shaped body. Typical diameters range from 3 to 20 mm, where 20 mm varistors show high energy ratings (100 J or more) with greater power dissipation. MOVs can turn on in a few nanoseconds and have high clamping voltages, ranging from approximately 30 V to 1.5 kV. Due to their fast response times and high clamping voltages, MOVs are superior to GDTs. In Table 3.1, a comparison of MOV characteristics with other common TVS devices is presented.

If an MOV is exposed to continuous high voltage conditions instead of short-duration transients, thermal runaway state may occur in the MOV, resulting in excessive heat, disc-cracking, smoke, and possible fire. To limit the impacts of such severe conditions, modern varistors include special thermally protected MOVs are known as TPMOV and possess much improved durability with less degradation levels than traditional MOVs. TPMOVs are highly applicable in situations where there are continuous AC line over-voltages, but due to high cost these are not often used in class-A surge protectors. In developing the SCASA technique, two *Littlefuse* varistors have been utilized based on their clamping properties and high-current handling capability. More details about varistor usage in SCASA circuit is revealed in Section 3.8.

3.3.2 Transient voltage suppressor (TVS) diodes

TVS diodes are avalanche p-n junction based solid-state devices that show two operating modes: OFF (high impedance) state and ON (low impedance) state [29]. When operating under OFF condition, the device has a low current possibility known as leakage current which will vary with p-n junction temperature. The transition from an OFF state to the ON state occurs with the breaking down of avalanche region. When two p-n junctions merged back-back, TVS diodes function as bidirectional break-over devices (BBDs) [31, 58]. BBDs are suitable for protection against positive or negative surges appearing at power/signal entry inputs. Unlike unidirectional devices, BBDs have symmetrical response in both positive and negative regions; thus provide protection clamping in both sides. Similar to MOVs, the TVS diode is also a clamping device, which suppresses all voltages above its breakdown voltage.

V–I characteristic curves of unidirectional and bidirectional diodes are shown in Figure 3.6(a) and Figure 3.6(b) respectively. The symmetry of two p-n junctions placed in opposite directions is reflected on the V–I curve as avalanche breakdown in BBDs occurs in both sides. As in the case of varistors, TVS diodes shift into heavy conduction mode beyond the breakdown allowing surge currents divert through the device. This results in providing a safer clamping level to protect the load. A simple shunt circuit of an unidirectional diode is shown in Figure 3.6(e). Complex circuit topologies can be constructed to enhance surge suppression as discussed in Section 2.3.2.

The major advantage of these diodes is their very effective clamping, which comes closest to an ideal constant voltage clamp that is lower compared to varistor clamping [60]. But, in terms of cost TVS diodes are more expensive than varistors; hence limit the use in practical surge protection circuits. Another benefit of TVS diodes is that avalanche breakdown of these occur in picoseconds, hence they are specified as instant responding devices. The fast response time of the suppressor diodes means that inductive voltage overshoots may occur due to lead inductances and capacitances. Moreover, the transient power and current capabilities of a TVS

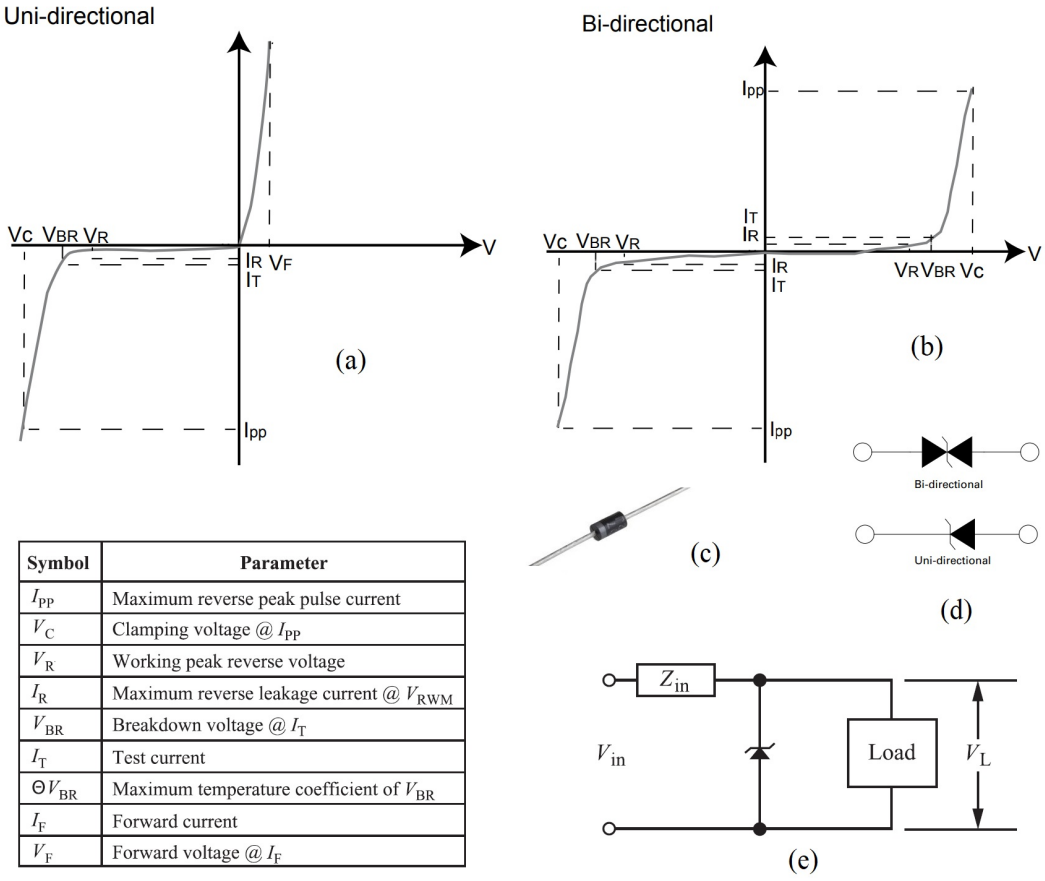

Symbol	Parameter
I_{PP}	Maximum reverse peak pulse current
V_C	Clamping voltage @ I_{PP}
V_R	Working peak reverse voltage
I_R	Maximum reverse leakage current @ V_{RWM}
V_{BR}	Breakdown voltage @ I_T
I_T	Test current
ΘV_{BR}	Maximum temperature coefficient of V_{BR}
I_F	Forward current
V_F	Forward voltage @ I_F

Figure 3.6: Transient voltage suppressor diode: (a) unidirectional V–I characteristic; (b) bidirectional V–I characteristic; (c) physical view; (d) circuit symbols; (e) application circuit [59]

is proportional to the cross-sectional area of the p-n junction. A higher cross section allows high-transient currents, but with the excessive power dissipation in the active p-n junction, thermal degradation occurs. A comparison of TVS diode characteristics with other SPD components is presented in the next Section.

3.4 Comparison of Traditional Transient Suppression Components

In above Sections, we described the operational behaviour of various voltage-clamping and crow-bar devices. In this section we discuss their advantages and limitations in relation to surge absorption. As previously mentioned, there is no ideal component that can fulfil all the technical requirements of surge protection equally effectively; therefore, in designing protector circuits a combination of components is selected to complement each other. In most cases GDTs, MOVs, and/or BBDs are coupled with series inductors. The following distinctive characteristics are considered as a key criterion in individual component selection:

- superfast reaction time
- high instantaneous current carrying capacity
- lower clamping/residual voltage; and
- long service life

Table 3.1: Comparison of characteristics of component surge protection devices as per IEEE C62.42 [38, 60]

Suppression Element	Advantages	Disadvantages	Expected Life
Gas Tube	Very high current handling capability Low capacitance High insulation resistance	Very high firing voltage Finite life cycle Slow response times Non-restoring under DC	Limited
MOV	High current handling capability Better voltage clamping Broad current spectrum Broad voltage spectrum	Gradual degradation Relatively high clamping voltage High capacitance	Medium-Long
TVS Diode	Low clamping voltage Extremely fast response time Broad voltage spectrum Easy power dissipation	Limited surge current rating High capacitance for low-voltage types High cost	Long
TVS Thyristor	Fast response time High current handling capability Less degradation Small size	Non-restoring under DC Narrow voltage range Turn-off delay time High cost	Long

Table 3.1 provides a detalied comparison of characteristics of different clamping-type and crowbar devices, based on these attributes we select components for SCASA technique. More information about SCASA circuit components is revealed in Section 3.8.

3.5 Inductors and Capacitors

Practically all surge protectors have inductor/capacitor (LC) filters combined with non-linear devices (NLDs) such as MOVs and BBDs to more effectively absorb and divert the surge energy. In Section 2.3, we demonstrated how inductors and capacitors can be utilized in practical surge protector circuits. Based on series and shunt arrangements, transient energy was either blocked or diverted at high-frequencies by these components. In the following sections, we examine simple empirical calculations to show the usefulness of L and C in SPD circuits.

3.5.1 Inductors as series blocking elements

A typical transient pulse lies between 5–100 μs having waveforms as discussed in Section 2.5, thus we can model the transient as a spectrum of frequencies in the range of 10–200 kHz, and their higher-order harmonics (Fourier Transform of a standard 1.2/50 μs surge waveform is presented in Chapter 6). Since an inductor possesses a series impedance of $2\pi fL$, it will impede transient surges at higher order frequencies. Compared to the impedance at 50/60 Hz line frequency, the inductor will show 400–20,000 higher impedance against the surge components. For example, a 10-μH inductor will show an impedance of 3.14 mΩ at 50 Hz, compared to 6.28 Ω at 100 kHz which is 20,000 times larger.

Given this property, inductors are often coupled with NLDs such as MOVs and BBDs to achieve useful surge blocking circuits. In most cases, inductive coils are placed in series; hence they are expected to carry the line frequency current fed into load, without creating a significant voltage drop at 50 or 60 Hz. In developing SCASA technique, series inductors are inserted in the form of a coupled-inductor wound to a powdered-iron toroidal core. Details about coupled inductor implementation is revealed in Section 3.8.

3.5.2 Capacitors as shunt filter elements

As in the case of inductors, a similar argument based on the impedance can be put forward with a capacitor placed in a parallel path between the live and neutral wires. Opposite to inductor action, the impedance of a capacitor given by $1/2\pi fC$ decreases at high frequencies of transient surges. For example, a 100 kHz surge component superimposed on the power line will generate 20,000 times lesser impedance compared to 50 Hz power frequency. Therefore, transient currents will divert through this low impedance path maintaining a safer voltage between live and neutral.

Special types of ceramic capacitors are used for electromagnetic interference (EMI) filter stage in surge protectors, hence these are referred as X and Y. As shown in Section 2.3 parallel blocks of these capacitors are placed between live-neutral (X) and live-earth (Y) to achieve EMI filtering [61]. Like normal capacitors, the capacitive reactance of these is inversely proportional to the frequency. The combination of inductors and capacitors determines the pass band of the EMI filter in SPD circuits. As a safety requirement, the voltage rating of X and Y capacitors are usually considered to be more than double the expected RMS voltage in the application [62]. In developing SCASA surge protector, class X type is used to eliminate electromagnetic oscillation; more information about circuit design is given in Section 3.8.

Apart from using normal capacitors in surge protector design, the use of supercapacitors (SCs) in SPDs is a relatively new concept developed and tested by the power electronics research group at University of Waikato. Prior to an investigation of surge withstanding capability of SCs, we introduce various types and highlight their essential characteristics in the next section.

3.6 Essentials of Supercapacitor Technology

Here, we discuss SCs' energy storage mechanisms, electrode arrangement and applicability in surge protection circuits based on the design fabrications.

3.6.1 Types of supercapacitors

With the modern-day developments in electric-energy storage applications that require high power capability and longer cycle-life, SCs have shown a promising establishment over the years. Specially with their high-power density compared to batteries and greater energy density than electrolytic capacitors (ECs) [63], supercapacitors can bridge the gap between battery technology and conventional capacitor domain. Based on the mechanism of energy storage, SCs can be categorized into three major types [63, 64]: (1) electrical double layer capacitors (EDLCs), (2) pseudo-capacitors (PCs) and (3) hybrid capacitors (HCs). Out of all, EDLCs were the first SCs to emerge followed by PCs and HCs [65]. This major classification further extends into sub-types according to the chemistry of electrodes; Figure 3.7 demonstrates the complete categorization of SC types.

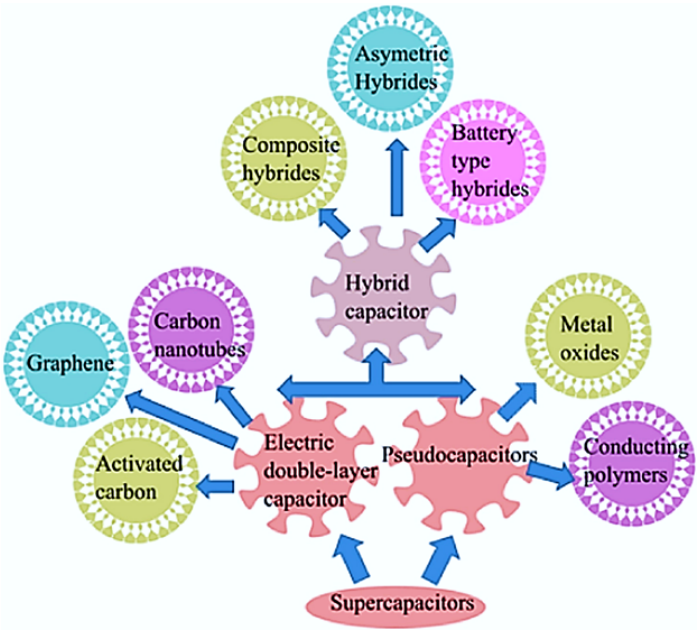

Figure 3.7: Classification of supercapacitor types [63, 64]

3.6.2 Charging mechanisms and usability in surge protectors

EDLCs posses similar capacitive behaviour as parallel plate capacitors, but due to high surface area and extremely small charge separation distances, exhibit much larger farad-order capacitances. Electrodes in this type are constructed using activated carbon based porous structures, where charge accumulation due to porosity is highly significant with better energy storage. Figure 3.8 illustrates interior arrangement of electrodes and compare charged and discharged states in relation to the confinement of charge particles (More information about EDLC charging mechanisms can be found in [67, 68]). Notably, with the remarkable capacitance/time-constant (compared to ECs) and symmetrical arrangement of electrodes (Figure 3.8), EDLCs are applicable to surge protection circuits. In Section 3.7 we prove this concept with a SC-surge model derived from the *RC* circuit behaviour as depicted by Figure 3.9.

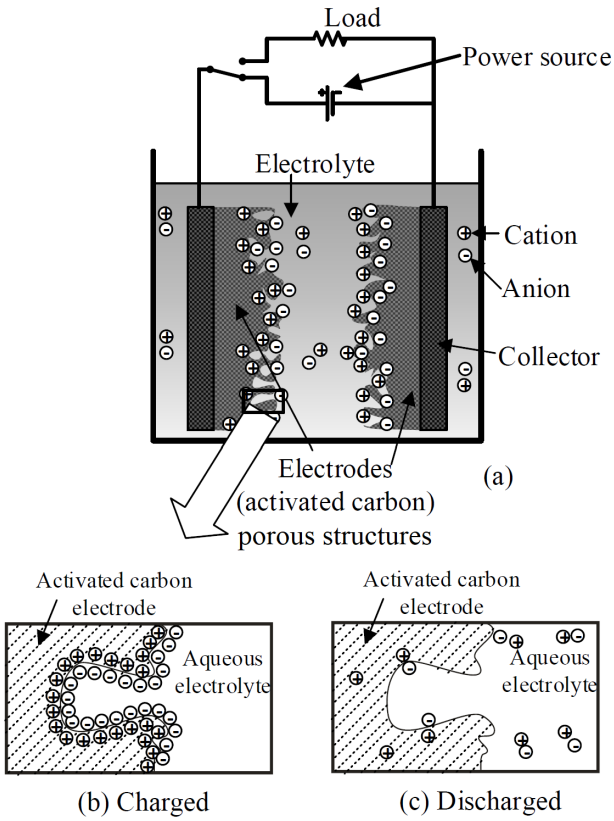

Figure 3.8: Activated carbon based porous structures of EDLCs: (a) electrode arrangement; (b) charge accumulation inside a pore; (c) a discharged state [66]

The pseudo-capacitor charging mechanism is governed by faradaic process; in such reactions, electron transfer across the two electrode interface occurs by the chemical oxidation and reduction [69]. These redox reactions can be reversible or irreversible depending on the chemical agent. Although the energy density of PCs is larger than EDLCs, the power density is much lower. Moreover, due to chemical degradation of PC electrodes (under repeated oxidation and reduction), the life-time/cycling stability is comparably lower than EDLCs and HCs. Also, when

Table 3.2: Characteristic comparison of supercapacitor types

Supercapacitor characteristics	Electrical double layer capacitors (EDLCs)	Pseudo-capacitors (PCs)	Hybrid capacitors (HCs)
Power density	High	Low	Medium
Energy density	Relatively low	High	Medium
Life time/Cycling stability	Long	Low	Medium
Electrode symmetry/asymmetry	Symmetrical	Symmetrical or Asymmetrical	Asymmetrical
Usability in surge protectors	Usable	Highly limited	Highly limited

subjected to transient pulses, structure deterioration can occur in chemical electrodes of PCs; thus their suitability in surge protection is highly limited. More details about pseudo-capacitor properties are given in [70, 71].

Hybrid capacitors (HCs) create a combination of EDLC and PC characteristics: these can have a greater energy density than EDLCs and a high power density than PCs [63, 72]. The general mechanism for construction is the hybridization of a capacitor-type electrode (activated carbon) and a battery-type chemical electrode [64]. Due to the dissimilarity of two electrodes, HCs are considered as highly asymmetric. Notably, as transients can appear in both polarity (positive or negative transients), the usability of HCs in transient suppression circuits is extremely modest. A detailed comparison of SC characteristics of EDLCs, PCs and HCs is given in Table 3.2.

The overview of supercapacitor technologies provided above clearly justify that out of three main types, EDLC SCs are the most applicable type in SPD circuits; a detailed discussion about EDLCs' surge withstanding capability is presented next.

3.7 EDLCs for Surge Absorption

With million times larger capacitance compared to electrolytic capacitors (ECs) of the same canister volume, electrical double layer capacitors (EDLCs) have emerged as prominent energy storage devices. EDLCs have a very low equivalent series resistance (ESR) and a low DC voltage (about 2–4 V) rating [73]. Specifications of Maxwell EDLCs found in Appendix C. Surprisingly, EDLCs are capable of surviving transient surge pulses of several thousand volts [66, 74]. In this Section, we describe a surge-based model to justify how EDLCs can withstand transient energies.

3.7.1 Maximum current capability of a supercapacitor

As SCs (EDLCs) have low ESR and high power density, SCs can be charged and discharged at relatively larger currents than most conventional energy storage devices. Table 3.3 indicates manufacturer recommended maximum continuous current ratings for each capacitor type based on their thermal limits of internal materials. The theoretical maximum output current as predicted by V_{rated}/ESR flows when a fully charged SC is short circuited by an ideal zero resistance [18, 75]. However, under practical limitations, a distinction between theoretical and empirical maximum currents is seen; Table 3.3 summarizes this discrepancy.

Apart from sustaining continuous maximum currents, SCs can defend the passage of high-magnitude transients without subjecting to thermal degradation. To understand the thermal stability of SCs, we must look into the temperature rise due to 8/20 μs combination surge current-waveform when heat dissipates across ESR [54]. According Eq. (3.4), temperature rise is calculated as:

$$\Delta T = \frac{R_C\ A_I^2\ I_p^2}{C_{th}} \int_0^\infty t^6 e^{-2t/\tau} dt = \frac{45}{8} \frac{1}{C_{th}} R_C\ A_I^2\ I_p^2\ \tau^7. \tag{3.4}$$

Table 3.3: Comparison of energy storage and maximum current capabilities of 2.7 V supercapacitors by Maxwell Technologies, Inc. [75]

Capacitance (F)	DC ESR (mΩ)	V_{rated}/ESR (A)	Maximum rated current (A)	Energy storage capacity ($\frac{1}{2}CV^2$) (J)
1	700	3.9	0.8	3.6
3.3	290	9.3	1.9	12.0
5	170	15.9	3.2	18.2
10	75	36	7.2	36.4
25	42	64.3	20	91.1
50	20	135	27	182.2
100	15	180	36	364.4
150	14	192	40	546.8

where the constants are $A_I = 0.01243\ \mu s^{-3}$, $\tau = 3.911\ \mu s$, I_p is the peak surge current and R_C is the ESR of SC and C_{th} (with units J/°C) is the thermal capacitance of the SC [19, 75]. Following is a comparison of temperature rise in various Maxwell SCs.

Table 3.4: Comparison of temperature rise, ΔT, HC series supercapacitors by Maxwell Technologies for a 2000 A peak current of 8/20 μs combination waveform [19, 75]

Capacitance (F)	C_{th} (J/°C)	ESR (mΩ)	ΔT (°C)
1	1	700	76.6
3.3	1.4	290	22.7
5	2	170	9.3
10	3.6	75	2.3
25	6.3	42	0.7
50	13	20	0.2
100	23	15	0.07
150	32	14	0.05

As per the Table 3.4, larger SCs possess smaller ESR values, and the corresponding temperature rise for a single transient (I_p=2000 A) reduces significantly. These temperature changes are calculated assuming perfect insulation. But, in practical circuits thermal impact is further minimized as the heat dissipation occur to the surroundings. Based on the these calculations, it is apparent that a SC will not be thermally damaged by a transient pulse. We extend this concept further in the next section with a SC-surge model.

3.7.2 An RC circuit subjected to a high-voltage transient

The simple model we discuss here shows how surge energy is distributed among the resistive and capacitive components of an RC circuit during a rectangular surge pulse of time interval T (10 μs). Figure 3.9(a) illustrates the capacitance (C) of the SC, the ESR (R) of the SC, and the path resistance (R_P) of the connecting wires. As indicated in Figure 3.9(b), the SC has an extended charging curve (larger time-constant) compared to an electrolytic capacitor

(EC); hence, during a surge pulse, the voltage build up across a SC (v_{sc}) is comparably small. Significantly, v_{sc} is typically much smaller than the rated voltage of a SC, giving it a better chance of survival under a high-voltage pulse. But in the case of a standard capacitor (EC), the developed voltage (v_c) can be higher than its rated voltage, leading to failure of the device as shown in Figure 3.9(c). The following equations quantify the energies distributed between capacitive and resistive circuit elements during a transient pulse.

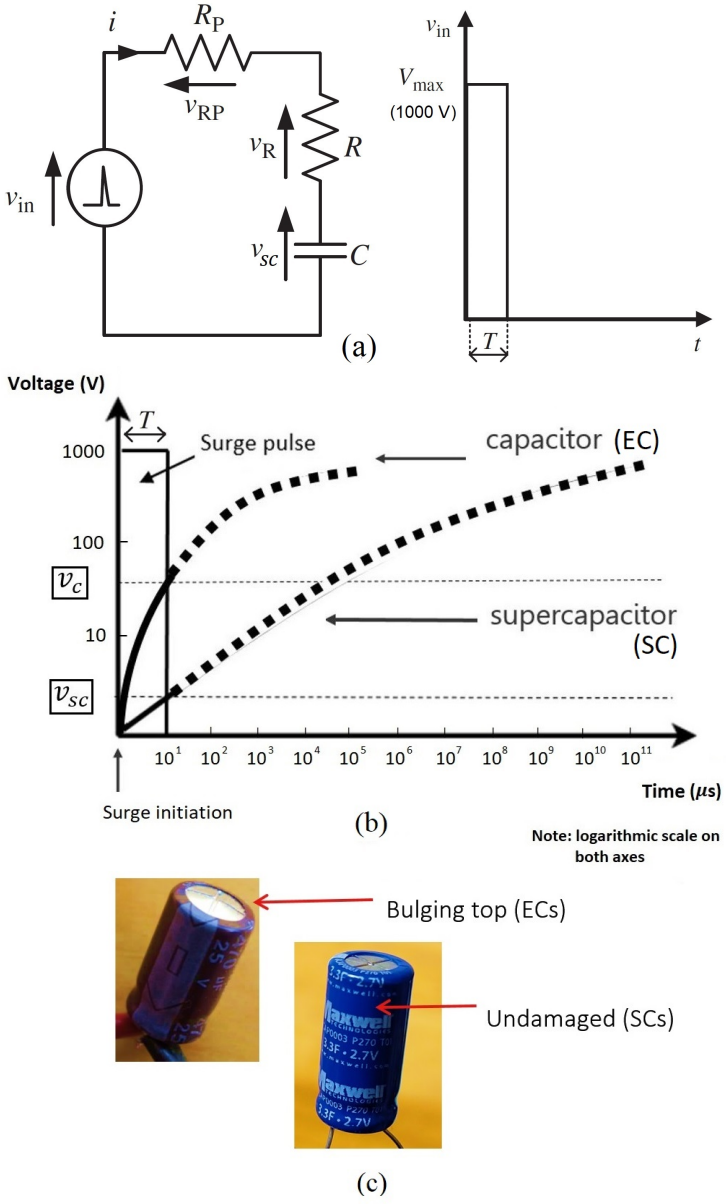

Figure 3.9: RC circuit subjected to a rectangular high-voltage pulse: (a) equivalent circuit of a SC with path resistance and step voltage transient; (b) supercapacitor vs capacitor (comparison of voltage accumulation); (c) supercapacitor vs capacitor (comparison of physical degradation)

$$E_{sc} = \frac{1}{2} C {v_{sc}}^2 \tag{3.5}$$

$$v_{sc} = V_{max}(1 - e^{-t/CR_T}) \tag{3.6}$$

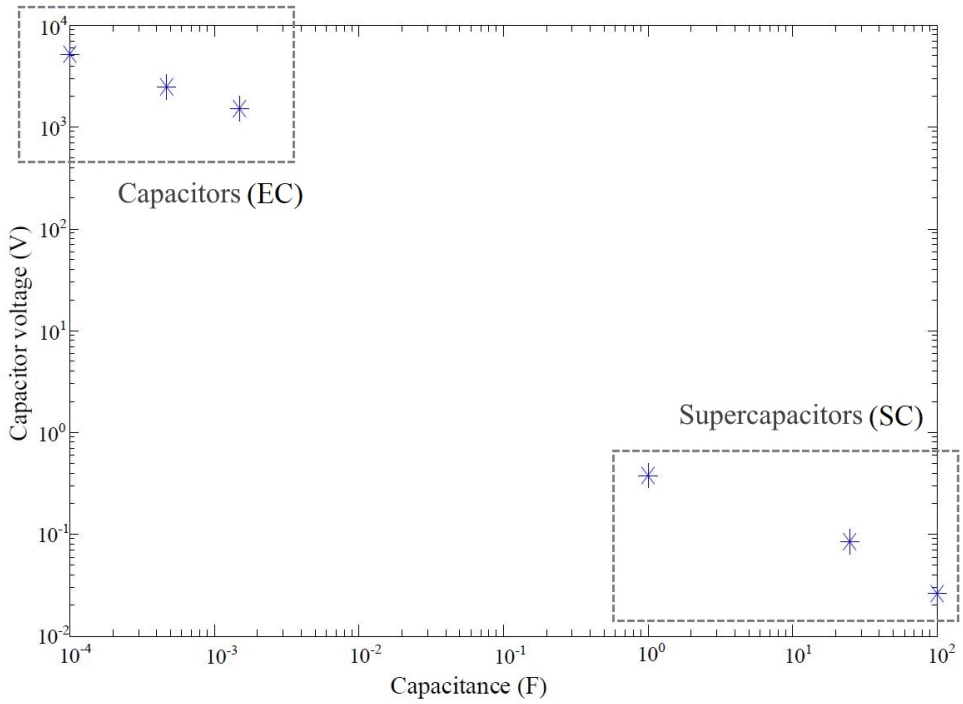

Figure 3.10: Voltage accumulation of capacitors and supercapacitors for a 6 kV, 1.2/50 µs surge pulse [10]

Eq. (3.5) shows the energy accumulation of the SC as the voltage (v_{sc}) across its terminals varies according to Eq. (3.6). The surge pulse in this example has a maximum voltage (V_{max}) of 1000 V.

Energy dissipated in the ESR (R) of SC due to surge current i ($i = {}^{V_{max}(e^{-t/CR_T})}/_{R_T}$) is given by the integral in Eq. (3.7), where R_T refers to the total series resistance ($R + R_P$).

$$E_R = \int_0^T i^2 R\, dt = \frac{CR}{2R_T} V_{max}^2 (1 - e^{-2T/CR_T}) \tag{3.7}$$

Using Eq. (3.5), Eq. (3.6) and Eq. (3.7), consider the ratio E_R/E_{sc} after time T:

$$\frac{E_R}{E_{sc}} = \frac{R}{R_T} \frac{(1 + e^{-T/CR_T})}{(1 - e^{-T/CR_T})} \tag{3.8}$$

When $R = 170$ mΩ, $R_T = 2.17$ Ω, $C = 5$ F and $T = 10$ μs,

$$\frac{E_R}{E_{sc}} \approx 10^5 \tag{3.9}$$

A key result comes from Eq. (3.8) and Eq. (3.9) which suggest greater amount of surge energy is dissipated in ESR while only a minor amount is sinking into the SC. This result further confirms how SCs can withstand transient activities facilitating excessive energy dissipation in its internal resistance. Similarly, if the path resistance is significant, then substantial amount of transient energy will be dissipated as heat across the resistive path wires.

Our transient voltage tests confirm that SCs develop fairly insignificant voltages compared to ECs. A comparison of this phenomenon is shown in Figure 3.10 with two distinct regions for

the two types of capacitors. From micro-farad level ECs to farad level SCs, there is a substantial difference in accumulated capacitor voltages. Normal capacitors (ECs) develop several thousands of volts when subjected to a 6 kV surge, whereas SCs develop only few volts, in most cases several millivolts.

The remarkable surge endurance of SCs is clearly relevant to surge protection applications; but the main drawback is their low DC voltage rating. The low DC rating makes SCs unfit for direct application against AC utility mains. To address this limitation, the Waikato power electronics team designed a coupled-inductor topology to allow SCs to be incorporated into a practical surge protector. A detailed discussion about the development of this new design is presented next.

3.8 SCASA Technique

In the previous section, we explored how SCs are able to withstand transient surges without physical destruction. Despite the low ESR of SCs, their million times larger capacitance yields a greater time-constant (RC) which creates an extended charging curve. As indicated in Figure 3.9, this extended RC curve of a SC is an essential property for handling transient events due to its millivolt order voltage development. However, the low continuous DC voltage rating ($\approx$ 2.7 V) of SCs is a major concern which limits SCs being used in 230 V mains power applications as a direct replacement to typical surge protector devices (MOVs/BBDs). Generally, the SPDs are placed in parallel to the live-neutral terminals as shunt elements, but if a 2.7 V rated SC is positioned across live-neutral, immediate failure occurs. Given this limitation, it is important to develop a circuit that allows SCs to be placed across low-voltage terminals during AC operation. In the following sections, we present how supercapacitor assisted surge absorber (SCASA) technique was designed using a coupled-inductor topology.

3.8.1 Implementation of the coupled-inductor

The use of inductors in surge protector development is an essential requirement. An inductor placed in series (Figure 2.6) possess the following distinctive characteristics against transient surges:

- for a power-line tranisent where surge-current (i) instantaneously rises, the inductor induces a voltage proportional to di/dt that will appear as an opposing voltage barrier to the incoming surge.
- an inductor generates a high series impedance of $2\pi fL$ against transient surges. Compared to 50/60 Hz power line frequency, the inductive impedance at higher order frequencies is 400–20,000 times greater.
- given a suitable magnetic core, an inductor can store transient energy as per $\frac{1}{2}Li^2$, where surge based magnetic-flux stores inside the core safeguarding the load side.

Based on above inductive properties, a coupled-inductor approach is adopted in SCASA technique by utilizing a toroidal core with two windings as illustrated by Figure 3.11(b). Following is a description of the development. As shown in Figure 3.11(a), the two windings are configured in such way that the primary arm with 6 turns (N_1) provides a lower impedance path than

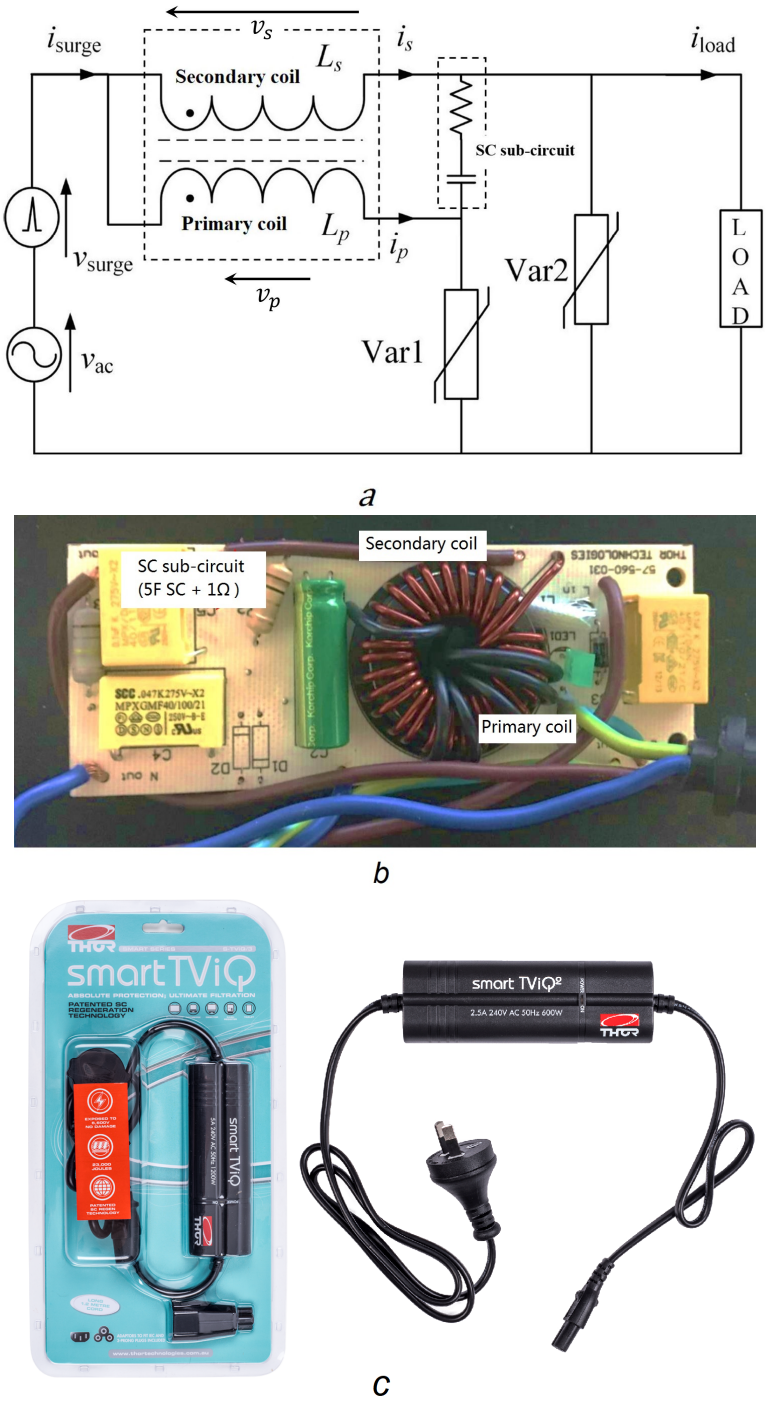

Figure 3.11:
SCASA circuit design and the real view of components: (a) circuit diagram of SCASA design; (b) transformer core with coupled-inductor windings, SC sub-circuit and associated components; (c) commercial implementation of SCASA as SMART TViQ [14]

the secondary with 28 turns (N_2) during the propagation of a surge. This results in passing a major share of transient current towards the primary coil, while the inductive voltage barrier v_s developed in secondary is significant enough to restrict currents through it. We have modelled the surge current propagation using Laplace transform method; more information about the sharing of currents is discussed in Chapter 6. The significant feature in SCASA circuit topology is the inclusion of a supercapacitor based sub-circuit. A 1 Ω high power resistor and a 5 F SC

connected serially are placed between the ends of two inductive coils (Figure 3.11(a)) to ensure that the RMS voltage across the sub-circuit never exceeds the DC rating of a SC. Therefore, any possibility of damaging the SC is prevented. Specifications of Vinatech 5 F SC used in SCASA design is given in Appendix C. In Chapter 4, we provide a circuit analysis of SCASA topology for its two distinctive modes of operation based on a permeance model.

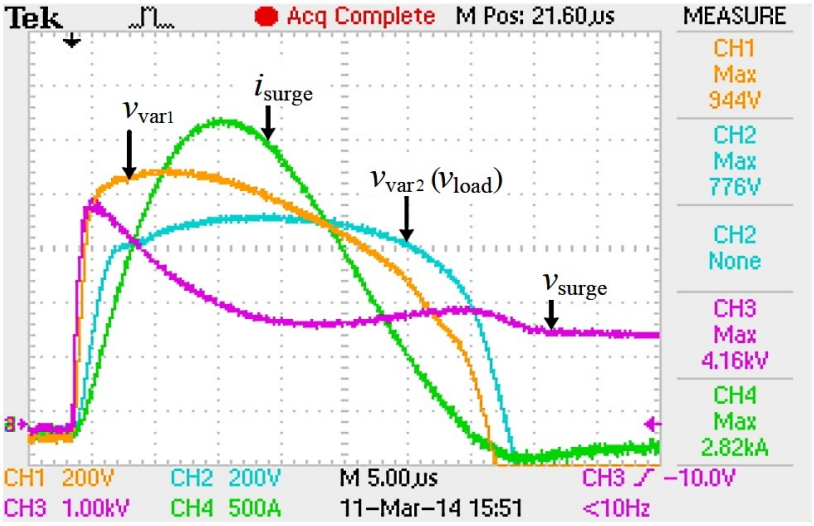

Figure 3.12: Experimental results of SCASA surge protector for a 6 kV/3kA, 1.2/50 µs surge pulse [66]

Moreover, as shown in Figure 3.11(a), the SCASA circuit holds two MOVs (Var1 and Var2) to dissipate the excess surge energy while clamping the transient voltage to a safe level. The two varistors are configured in a way that Var2 (load-side) has a lower clamping than the Var1. This is due to the placing of SC sub-circuit which develops a voltage against Var1 during transient-mode operation. Experimental results are shown in Figure 3.12. Overall, the combined action of the coupled-inductor and two varistors protect the critical load by storing (magnetically within the toroidal core) and dissipating (as heat) most of the surge energy.

The patented SCASA technique has led to a commercial product named SMART TViQ (see Appendix A), developed and manufactured by Thor technologies, Australia in 2016 [14]. A real view of the circuit components and the commercial implementation are illustrated by Figure 3.11(b) and Figure 3.11(c) respectively. In the following section, we investigate the design details of SCASA magnetic core.

3.8.2 SCASA magnetic core

During early developments of first SCASA version, one major concern was the magnetic core selection problem: commercially available ferrite cores did not perform well, while a powdered-iron core was able to satisfactorily perform. As of now, the commercialized SMART-TViQ design utilizes a powdered-iron toroidal core as depicted by Figure 3.13(a) (Kool µu: 0077071A7-Magnetics Inc.) which has an initial relative permeability μ_r= 60 (see Appendix E) [76]. In contrast to high permeability (μ_r=1000-10,000) ferrites (Figure 3.13(b)) [78], powdered cores are manufactured by distributing micro-sized air-gaps inside which results in providing an enhanced energy storage capability [79]. To study this phenomenon, we conducted experiments to reveal

Figure 3.13: Magnetic properties comparison: (a) Kool μu 0077071A7 powdered-iron toroid; (b) W-Ferrite ZW43615TC toroid [76, 77]

the magnetic action of SCASA coupled-inductor windings. As shown in Figure 3.11(a), the primary and secondary windings induce voltage barriers v_p and v_s to oppose the incoming surge currents. According to the design configuration where secondary is wound at a much larger number of turns, induced voltages $v_s > v_p$. Therefore, the inductive energy stored in both powdered-iron and ferrite toroids can be estimated by the difference between v_s and v_p which releases as a reversed voltage peak towards Var2 in SCASA circuit (more information about this effect is described in Section 3.8.3). To compare this inductive energy release, oscilloscope waveforms were captured across Var2 for both core types as illustrated by Figure 3.14. According to Figure 3.14(a), the reversed voltage peak extends up to -860V for the powdered-iron toroid, whereas a low voltage magnitude of ~ -40V is observed for ferrite core (Figure 3.14(b)). This depletion effect of inductive voltage release indicated by the SCASA coupled-inductor suggests that the energy stored in ferrite core is very limited. Therefore, it was experimentally proven

Table 3.5: Usability comparison of Kool μu powdered-iron and W-Ferrite toroids

Magnetic Core	Relative Permeability (μ_r)	Saturation Flux Density (gauss)	Energy storage capability	Usability in SCASA
Kool μu Powdered-iron toroid (0077071A7)	60	10,500	High	Usable
W-Ferrite toroid (ZW43615TC)	10,000	3,900	Low	Highly Limited

that the surge absorption capacity of powdered-iron is far superior to ferrite based materials (Table 3.5).

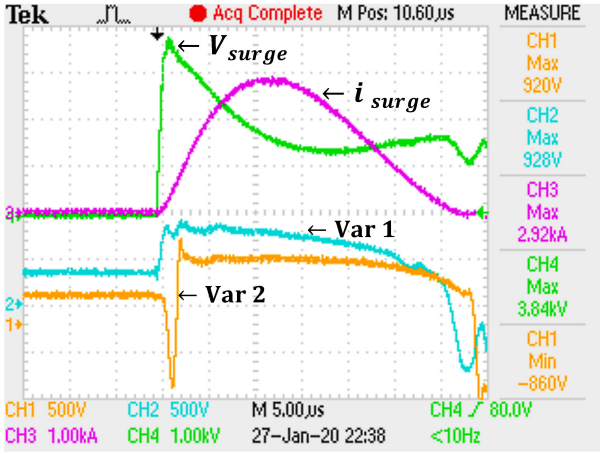

(a)

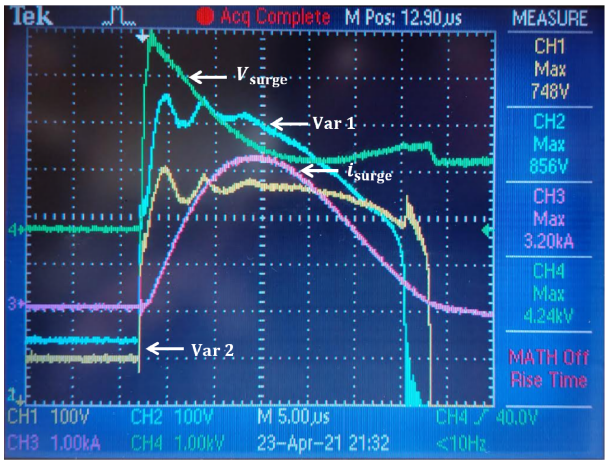

(b)

Figure 3.14: Comparison of inductive voltage release: (a) Kool µu 0077071A7 powdered-iron toroid; (b) W-Ferrite ZW43615TC toroid

Our initial investigations carried out in understanding the surge storing capability of Kool µu and W-ferrite toroids led the foundation to optimize SCASA technique by improving its magnetic components; more details about design optimizations are given in Chapter 5 and Chapter 7.

Apart from having high energy storage, Kool µu powdered-iron core is characterised by its relatively high magnetic saturation (10,500 gauss) compared to 3,900 gauss of W-ferrite core. Theoretical calculation relating to the maximum flux density corresponding to a 3kA transient pulse is provided at the beginning of Chapter 7. The reduced saturation level of ferrite core is another drawback that limits its application to surge protection. However, when an air gap is introduced to the ferrite body, saturation problem can be minimized: Chapter 5 presents advantages of air-gapped toroids. Furthermore, the low core losses (550 mW/cm^3) make Kool µu core excellent for operation under transient and 230 V AC modes without significant heat build up [79].

However, the distributed air-gap effect of powdered-iron results in a high magnetic reluctance causing the SCASA core to deviate from its ideal transformer action. If the coupled-inductor operates ideally, then leakage inductances are considered as near zero and magnetizing inductances are extremely dominant; but, due to powdered-iron based core, there are significant operational changes that push SCASA into the non-ideal domain. For example, despite the simplicity of circuit, the transformer core of SCASA possess several non-ideal characteristics including non-infinite magnetizing inductances L_1 & L_2 as well as leakage inductances l_1 & l_2 of both primary and secondary windings (Figure 3.11(b)). In Chapter 4, we develop a descriptive permeance based model to investigate these characteristics in depth.

3.8.3 Limitations of the present design

We can identify the limitations of existing SCASA design in two basic forms: the inductive energy release associated with the coupled-inductor and the relatively high output clamping level under transients. To address the first, magnetic action of the two inductive coils must be considered. During the event of an incoming surge, both primary and secondary coils of the coupled-inductor induce opposing voltages to limit surge propagation as depicted by Figure 3.11(a). According to the design configuration, the secondary with higher turns induce a voltage v_s that is greater than that of the primary v_p. Moreover, both v_s and v_p are generated in the same direction against the incoming transient surge [66]. Accordingly, it can be predicted that the difference between v_s and v_p ($v_s - v_p$) passes to the load/Var2 causing a reversed negative voltage peak [80]. The inductive release occurs only in transient operation as voltage induction is significant under rapidly changing currents and since this passes via Var1 which is in its conduction-mode. A clear understanding about the release of these two induced voltages can be obtained by disconnecting the supercapacitor sub-circuit of SCASA main circuit. Oscilloscope waveforms corresponding to this effect are shown in Figure 3.14(a). To eliminate this limitation and to elevate surge protector's performance, we decided to incorporate thin air-gaps to the toroidal body of ferrite cores. Apart from achieving similar characteristics to existing powdered-iron core, this new modification of using air-gapped ferrite toroids leads to several positive outcomes by optimizing the overall performance of SCASA technique. A complete analysis about this advancement is presented in Chapter 5.

According to experimental results (Figure 3.12) obtained for SCASA surge protector for a 6 kV/3kA surge pulse, it is observed that output clamping voltage lies between 780–800 V. However, as discussed in Chapter 2, internal degradations may occur in load circuits when clamping voltage resides above 700 V for a long operating period. Therefore, to overcome this limitation, we built new circuit prototypes using R-ferrite based EER type air-gapped cores (R43521A125-Magnetics Inc.) [81]. The new approach helped us to achieve better load-side characteristics with greater surge endurance levels; more information about the implementation and test results will be discussed in Chapter 7.

As a commercially manufactured surge protector by Thor technologies (Figure 3.11), it is a key criterion to consider the manufacturing cost of SMART-TViQ devices. Due to the production complexity of powdered-iron toroids with distributed air-gaps, these core are expensive than ferrite based cores. With the use of commercially available EER type air-gapped cores, we

were able to find a solution to this price constraint by reducing the cost approximately by 40%, a detailed comparison about the magnetic properties of two core types and their costs are examined in Chapter 7.

3.9 Chapter Summary

In this chapter, we presented traditional circuit components used in surge protection, and investigated how supercapacitors (SCs) can withstand transient pulses based on a simple RC circuit model. Moreover, we discussed the potential of utilizing SCs in a practical surge protector (SCASA) by adopting a coupled-inductor topology which assists SCs to safely operate without exceeding their DC voltage rating.

In the next chapter, we introduce a detailed circuit model for the transformer core of SCASA technique based on magnetic permeance and predict its operation under RMS and transient conditions.

Chapter 4

Permeance Model for the Coupled Inductor of SCASA Technique

In this chapter, we investigate the transformer core of SCASA surge protector using a non-ideal circuit model based on magnetic permeance, and predict its operation under contrasting voltage conditions. 50 Hz AC steady state and the transient propagation state of the equivalent circuit model are elucidated with experimental validations.

4.1 Essential Concepts of Magnetic Theory

4.1.1 Hysteresis behaviour

When a coil (with N turns) wound on a magnetic core carries a current i, a magnetic flux Φ is generated due to electromagnetic induction. The resulting flux gets distributed along the core path length l_c as indicated by Figure 4.1(a). Increasing the current in the coil results in a magnetic field intensity H as derived by the Ampere's law according to Eq. (4.1). At first, the slowly rising section of the hysteresis curve shown in Figure 4.1(b) corresponds to the initial magnetization of the core where flux density B (Φ/A_c) does not increase significantly. During the second section, the induced B increases linearly with the increase of H and the curve is steep. However, B-H loop comes to a stage where further increase in H does not yield significant

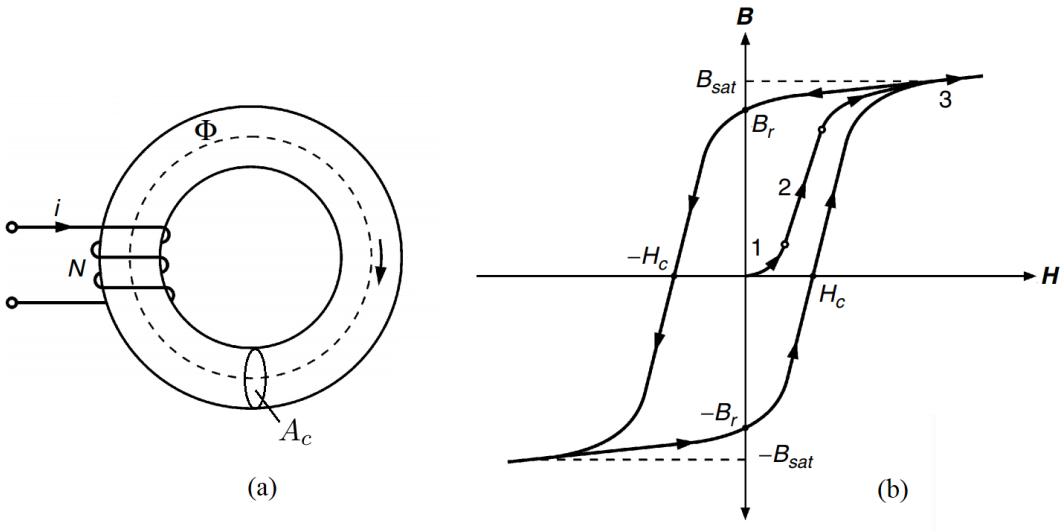

Figure 4.1: Magnetization of a ferromagnetic based toroid: (a) toroidal core during magnetization; (b) hysteresis loop (B-H loop) [82]

increments in B, and this third section of the magnetization curve is mostly flat. This is due to the magnetic saturation of the material which sustains its maximum flux density B_{sat} leading to a plateau in B-H curve.

$$H = \frac{Ni}{l_c} \tag{4.1}$$

The reverse process of decreasing H with the reduction of excitation current varies form the initial phase of magnetization; more details about complete hysteresis behaviour is described in [82, 83]. Also, when H reduces to zero, the magnetic core retains part of the flux knows as residual flux density or remanence B_r. To remove the residual flux to zero, a reversed (negative) H field called coercive force or coercivity H_c is necessary to be applied. Both B_r and H_c depend on the magnetic material of the core, more information is included in [84, 85]. The magnetic core utilized in the standard SCASA surge protector is made of powdered-iron material (Kool μu: 0077071A7) as mentioned in Section 3.8. Hysteresis behaviour characteristics of Kool μu powdered-iron and various other magnetic materials used in prototype design is presented next (Figure 4.2 and Table 4.1).

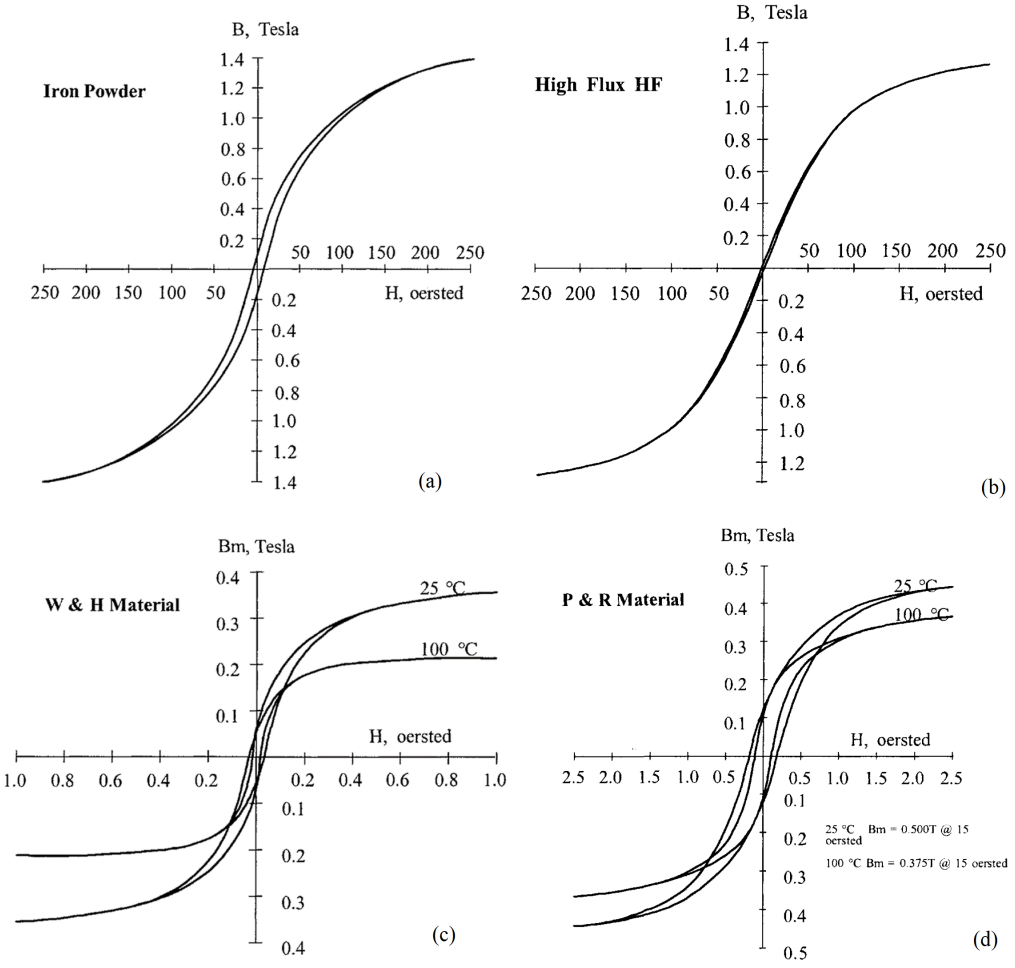

Figure 4.2: Hysteresis behaviour comparison of different powdered-iron and ferrite materials used in SCASA prototype design: (a) hysteresis loop of Kool μu powdered-iron; (b) hysteresis loop of High-Flux material; (c) hysteresis loop of W and H ferrites; (d) hysteresis loop of P and R ferrites [83]

4.1.2 Magnetic permeability

Magnetic permeability μ_r (relative to free space) is an important magnetic characteristic of a material which indicates how easily a material is magnetized [86]. Generally, it is derived from the gradient of flux density vs magnetizing force (B-H) curve (Eq. (4.2)), but this definition relates to the linear second region of Figure 4.1(b). Other interpretations applicable for different regions are described in [82].

$$\mu_r = \frac{dB}{dH} \tag{4.2}$$

Steeper magnetizing curves corresponds to greater μ_r leading to quick magnetic saturation; these are typically considered as soft magnetic materials with low H_c [87]. Conversely, hard magnetic materials have a modest gradient (low μ_r) in respective (B-H) curves, and have high H_c [87, 88]. In Chapter 5, we discuss how SCASA circuit performance varies when prototypes are built using W/J soft ferrites and hard-magnetic Kool μu powdered-iron. Furthermore, we investigate the impact of several other powdered materials (High-Flux and X-Flux-Magnetics Inc.) and R/P ferrites based air-gapped cores on the SCASA coupled-inductor action in Chapter 7. Table 4.1 and Figure 4.2 illustrate properties of these various magnetic materials and respective B-H loops used in this research. More information about experimental techniques are presented in Chapters 5 and 7.

Table 4.1: Comparison of magnetic properties of different powdered-iron and ferrite based materials used in SCASA prototype design [78, 79]

Magnetics material	Material composition	Initial relative permeability (μ_r)	Saturation flux density (gauss)	Coercive force H_c (oersteds) 50% μ_r	Core loss @100 kHz (mW/cm^3)
Kool mu	Al, Si, Fe	14-125	10,500	100	550
High Flux	Fe, Ni	14-160	15,000	185	625
X Flux	Fe, Si	19-125	15,000	170	1280
W Ferrite	Fe, Mn, Zn	10,000	3900	0.15	–
J Ferrite	Fe, Mn, Zn	5,000	4300	0.2	–
R Ferrite	Fe, Mn, Zn	2,300	4700	0.18	∼100
P Ferrite	Fe, Mn, Zn	2,500	4700	0.18	∼100

Next, we aim at linking this fundamental magnetic property of permeability with the self-inductance of a coil wound to a toroid as indicated in Figure 4.1(a).

4.1.3 Self-inductance and magnetic permeance

As discussed above, when a coil with N turns wound on a toroid is excited by an electrical current i, the magnetic flux generated Φ circulates around the core body (Figure 4.1). A similar geometry is observed in SCASA topology with two inductive coils wound on a toroidal core

body as illustrated by Figure 3.11. The self-inductance L of a coil relates to the flux linkage produced by the coil, and by definition [89], L is the total flux due to a unit current as described by Eq. (4.3). Since each turn of the coil generates field lines, total magnetic flux is given by $N \cdot \Phi$;

$$L = \frac{N\Phi}{i} = \frac{N^2 \mu_c A_c}{l_c} \tag{4.3}$$

where core permeability $\mu_c = \mu_r \mu_\circ$ ($\mu_\circ$=permeability of free space) and A_c, l_c depend on the toroid geometry (Figure 4.1). A more generalized way of expressing self-inductance can be found using the fundamental magnetic property known as *permeance*. Permeance Λ is defined as the inductance per unit turn squares as described by Eq. (4.4) [82]:

$$\Lambda = \frac{L}{N^2} \tag{4.4}$$

The magnetic permeance is analogous to the conductance in an electrical circuit, and emphasizes the ease with which flux can be set up in a magnetic material [90]. In most industrial data sheets [82], the permeance is considered as the inductance factor A_L with the unit [H/turn^2], where H is henry. Using Eq. (4.3) and Eq. (4.4), we can obtain a fundamental expression for permeance as,

$$\Lambda = \frac{\mu_c A_c}{l_c} \tag{4.5}$$

Eq. (4.5) shows the fundamental nature of permeance as it depends only on magnetic material (μ_c) and core geometry (A_c, l_c). This uniqueness facilitates the prediction of self-inductance for a coil (with a given number of turns) wound to core whose permeance coefficient Λ (A_L) is known ($L = A_L N^2$). Table 4.2 presents a comparison of A_L values of different powdered-iron and ferrite based materials used for SCASA prototype designs (see Appendix E). More

Table 4.2: Comparison of magnetizing permeance coefficients Λ_m (also known as inductance factor A_L) of different powdered-iron and ferrite based materials used in SCASA prototype design [78, 79]

Magnetics Part No.	Material	Magnetizing permeance (Λ_m) Inductance factor (A_L) (nH/turns^2)
0077071A7	Kool μu	61
058071A2-4	High Flux	61
078550A7	X Flux	28
ZW43615TC	W Ferrite	13,400
VJ42206TC	J Ferrite	3,020
R43521A125	R Ferrite (EER gapped)	125
P42213A125	P Ferrite (PQ gapped)	125

details about inductance measurements for coupled-inductor windings using these core types are included in Chapters 5 and 7.

Since the physical magnetic flux relating to a toroid can appear in two forms (magnetizing and leakage flux) as depicted by Figure 4.3, the definition for permeance is basically two types: magnetizing permeance (Λ_m) and leakage permeance (Λ_σ). Λ_m is useful in determining the magnetizing inductance of the coil wound to toroid, whereas Λ_σ can be used to express leakage inductance of the coil. More importantly, both Λ_m and Λ_σ can be put together to represent the self-inductance corresponding to the core windings. We develop a descriptive permeance based model for the transformer windings of SCASA design in the next section; more information relating to equivalent circuit model is presented using Λ_m and Λ_σ.

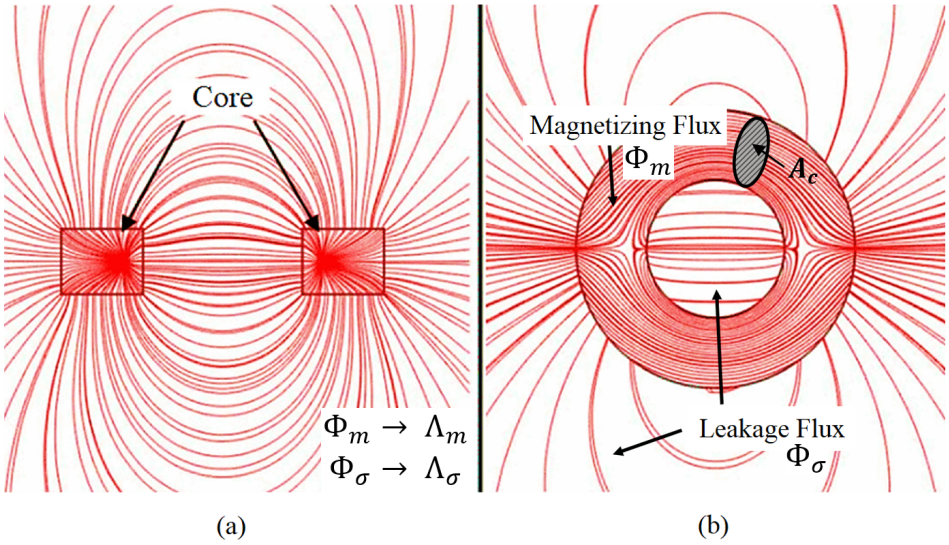

Figure 4.3: Magnetic flux distribution in and around a toroidal core: (a) side view; (b) top view [68]

Another significant aspect of permeance is that it relates to the magnetic reluctance of core; it is an important property in predicting the transformer action during the core magnetization. Theoretical considerations of magnetic reluctance applied to practical (non-ideal) transformer behaviour are described next.

4.1.4 Magnetic reluctance

The magnetic flux generated inside a material due to EM induction depends on the material's resistance to flux, which is known as magnetic reluctance $\mathfrak{R}$. Similar to permeance, the reluctance of a core depends on the composition of the material (μ_c), and its physical dimensions (A_c and l_c) as described by Eq. (4.6). It is analogical to the concept of electrical resistance, but differs from resistance as the reluctance stores magnetic energy and releases it afterwards instead of dissipation [91]. This effect is highly relevant to SCASA operation, and we discuss this in detail in Chapter 5. Importantly, the reluctance for a transformer core is given by the reciprocal of permeance as per Eq. (4.6) [91].

$$\mathfrak{R} = \frac{1}{\Lambda} = \frac{l_c}{\mu_c A_c} \tag{4.6}$$

where core permeability $\mu_c = \mu_r\mu_\circ$ ($\mu_\circ$=permeability of free space) and A_c, l_c depend on the toroid geometry (Figure 4.1).

For a practical two-winding transformer with N_1 and N_2 turns (as in the case of SCASA coupled-inductor), applying the Ampere's law yields a relationship between core reluctance [92], number of turns and coil currents as given by Eq. (4.7);

$$\Phi\Re = N_1 i_1 + N_2 i_2 \tag{4.7}$$

In the case of an ideal transformer, the core reluctance is zero and when the resistances of the windings are neglected, Eq. (4.7) becomes;

$$0 = N_1 i_1 + N_2 i_2 \tag{4.8}$$

Since SCASA utilizes a powdered-iron toroid, the air-bubbles distributed inside the core material make the medium more reluctive to the formation of magnetic flux; thus, this extra reluctance of the Kool μu toroid alters the circuit function to deviate from ideal transformer as satisfied by Eq. (4.7). We provide calculations relating to SCASA coupled-inductor operation in Section 4.3.3. Furthermore, we investigate reluctance based equivalent magnetic circuits for air-gapped toroids in Chapter 5 with an emphasis on energy storage inside the more reluctive air-gap. In the next section, we apply the theoretical base of magnetic permeance/reluctance discussed above to model the non-ideal transformer core of SCASA surge protector.

4.2 Permeance based Model for SCASA Non-ideal Transformer

4.2.1 Model development for magnetizing and leakage inductances

In the case of an ideal transformer core, leakage inductances are considered as near zero and magnetizing inductances are almost infinite (due to zero core reluctance); but, the core of SCASA circuit possesses several leakage effects (Figure 4.3) as well as non-infinite magnetizing inductances. Due to these non-ideal characteristics, operation of the circuit deviate from the ideal transformer behaviour. Moreover, reluctance of the core is also dominant due to air-bubbles

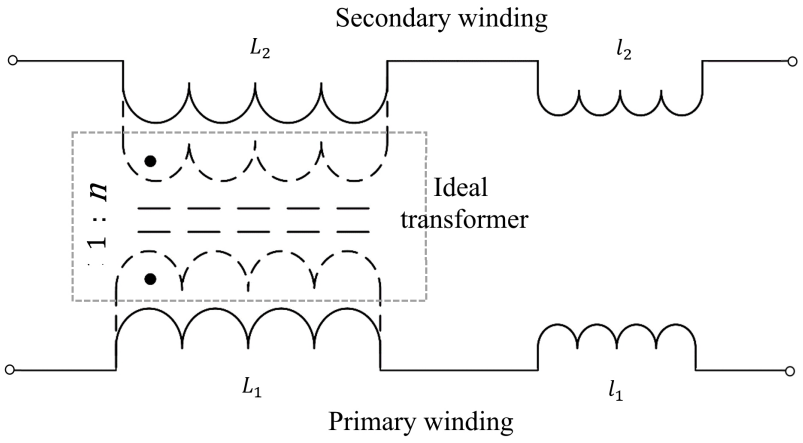

Figure 4.4: Equivalent circuit model of the non-ideal transformer core of SCASA
Note: copper losses associated with primary and secondary windings are assumed to be negligible

distributed inside powdered-iron. Similar non-ideal effects are shown by an air-gapped ferrite core, though an un-gapped ferrite yields near ideal behaviour. More information regarding air-gapped/un-gapped SCASA prototypes are described in Chapter 5. First, we develop an equivalent circuit model for the non-ideal core of SCASA design in this Section. Figure 4.4 illustrates magnetizing inductances (L_1,L_2) and leakage inductances (l_1,l_2) associated with primary and secondary coils of SCASA transformer core.

In the transformer circuit shown in Figure 4.4, both L_2 and l_2 can be referred to the primary side by dividing them by n^2, where n (N_2/N_1) is the secondary:primary turns ratio. We have omitted the winding resistances as their impact on this analysis is negligible. Moreover, the core losses associated with Kool μu powdered-iron core is highly minimized during the manufacturing process (as described in Section 3.8.2), therefore, we can neglect the core loss effect as well. As per the definition of self-inductance [93], the total self inductances of primary (L_p) and secondary (L_s) windings can be expressed as a sum of magnetizing and leakage components:

$$L_p = L_1 + l_1 \tag{4.9}$$

$$L_s = L_2 + l_2 \tag{4.10}$$

By referring all inductive components to the primary, effective primary referred inductance $L_p{}'$ takes the form:

$$L_p{}' = L_1 + l_1 + L_2/n^2 + l_2/n^2 \tag{4.11}$$

For the convenience of derivations, we now rearrange our equations using a "permeance" based approach; permeance is defined as the inductance per unit turn squares ($\Lambda = L/n^2$) [82,93].

If we consider both magnetizing permeance (Λ_m) and leakage permeance (Λ_σ) separately [82], then Eq. (4.9) and Eq. (4.10) can be expressed as:

$$L_p = \Lambda_m {N_1}^2 + \Lambda_\sigma {N_1}^2 \tag{4.12}$$

$$L_s = \Lambda_m {N_2}^2 + \Lambda_\sigma {N_2}^2 \tag{4.13}$$

This standard model based on permeance is applied to ferrite core transformers in evaluating self inductances. However, in transformer designs where leakage inductance is significant (as in Kool μu powdered-iron toroid), and considering the geometrical symmetry of the core, we found 50% of leakage permeance ($\Lambda_\sigma/2$) best models the self inductance of each winding [82,94]. Also, for gapped toroids where leakage flux is dominant around the air-gap, this modification made to Eq. (4.12) and Eq. (4.13) is consistent with the test measurements. SCASA self-inductance properties presented in Figure 4.6 and coupling coefficient prediction described in Section 4.2.3 are based on this adjustment made to leakage permeance.

Moreover, magnetic interaction between the two windings depends on mutual inductance (M) of the core; it can be indicated using Λ_m as per Eq. (4.14).

$$M = \Lambda_m N_1 N_2 \tag{4.14}$$

In the next section, we investigate how each of these inductive components varies for Kool μu powdered-iron toroidal core (0077071A7-Magnetics Inc.), and compare the measurements with permeance based theoretical predictions. Furthermore, test results associated with other core types (ferrite-iron and air-gapped ferrites) are presented in Chapter 5.

4.2.2 Measurements of non-ideal characteristics of SCASA transformer core

Open-circuit/short-circuit (Figure 4.5(a)-(d)) measurements of the transformer core were carried out to obtain self inductances (L_p,L_s), leakage inductances (l_1,l_2) and series/inverse-series test methods (Figure 4.5(e) and (f)) were used to determine mutual inductance M. All these tests were carried out using an LCR meter (Fluke PM6304) over a range of higher order frequencies. First, we indicate the connection arrangements of primary and secondary coils of SCASA core adopted in above test methods; Figure 4.5 illustrates a summary of these six different configurations.

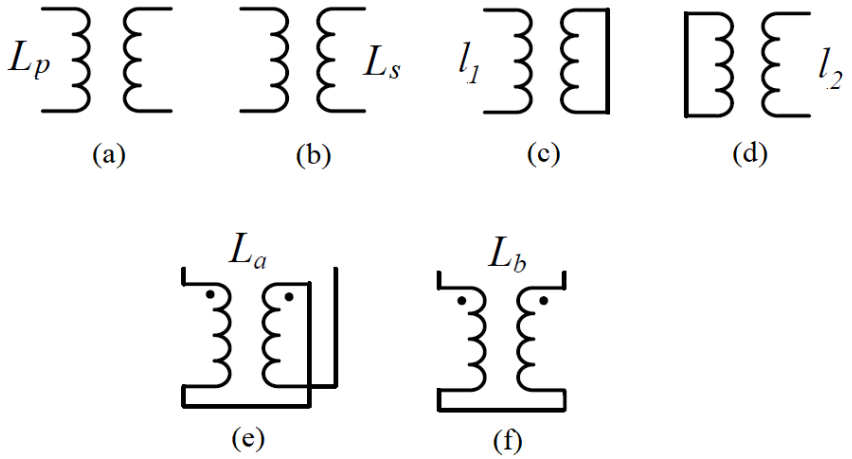

Figure 4.5: Measurement of transformer inductances: (a) primary self inductance - L_p; (b) secondary self inductance - L_s; (c) primary leakage inductance - l_1; (d) secondary leakage inductance - l_2; (e) inverse-series connection inductance - L_a; (f) series connection inductance - L_b

Based on series/inverse-series arrangements the following expressions can be written for L_a and L_b [82, 83]:

$$L_a = L_1 + L_2 + 2M \tag{4.15}$$

$$L_b = L_1 + L_2 - 2M \tag{4.16}$$

where M is the mutual inductance in both Eq. (4.15) and Eq. (4.16). Subtracting L_b and L_a yields M as:

$$M = \frac{L_a - L_b}{4} \tag{4.17}$$

However, both magnetizing inductances L_1 and L_2 of the primary and secondary windings are found by subtracting leakage inductances from self inductances ($L_1 = L_p - l_1$, $L_2 = L_s - l_2$). As indicated in Chapter 3, the original core of SCASA design comprises a powder-iron material with two coils (primary and secondary) wound at unequal number of turns. Primary winding has 6 turns, whereas secondary composed of 28 turns. All inductance measurements as per Figure 4.5 of both windings were carried out using a LCR meter (Fluke PM6304) over a range of frequencies from 1 to 15 kHz. Such procedures confirm the accuracy of test results as frequency components of a 1.2/50 μs surge waveform are significant in the kilohertz range [95]. Table 4.3 summarizes selected measurements taken for powdered-iron core at 3 kHz; other test results up to 15 kHz are presented in Figure 4.6. Theoretical predictions in Table 4.3 were determined as per Eq. (4.12),Eq. (4.13) and Eq. (4.14). We obtained magnetizing and leakage permeance coefficients from the manufacturer (Magnetics Inc.) specifications of Kool μu powdered-iron core (0077071A7): $\Lambda_m = 61 \pm 8\%$ nH/turn^2 and $\Lambda_\sigma = 42 \pm 8\%$ nH/turn^2 respectively (see Appendix E for industry specification sheets) [76].

According to Eq. (4.12) and Eq. (4.13), we can express magnetizing inductances as:

$$L_1 = \Lambda_m {N_1}^2 \tag{4.18}$$

$$L_1 = 61\,\text{nH/turn}^2 \times 6^2 \; = 2.2\,\mu\text{H}$$

and

$$L_2 = \Lambda_m {N_2}^2 \tag{4.19}$$

$$L_2 = 61\,\text{nH/turn}^2 \times 28^2 \; = 47.8\,\mu\text{H}$$

Furthermore, leakage inductances of the primary and secondary windings are:

$$l_1 = \Lambda_\sigma {N_1}^2 \tag{4.20}$$

$$l_1 = 42\,\text{nH/turn}^2 \times 6^2 \; = 1.52\,\mu\text{H}$$

and

$$l_2 = \Lambda_\sigma {N_2}^2 \tag{4.21}$$

$$l_2 = 42\,\text{nH/turn}^2 \times 28^2 \; = 32.92\,\mu\text{H}$$

Moreover, mutual inductance M between the coupled primary and secondary windings of SCASA core is found using Λ_m as per Eq. (4.14);

$$M = \Lambda_m N_1 N_2 = 61\,\text{nH/turn}^2 \times 6 \times 28 = 9.9\,\mu\text{H}$$

Table 4.3 presents a summary of above calculations with the corresponding inductance measurements and respective percentage variations.

Table 4.3: Magnetizing and leakage inductances of powdered-iron core (0077071A7) based on open-circuit and short-circuit test measurements at 3 kHz

Inductance	Measurement (μH)	Model prediction (μH)	Percentage variation
L_1	2.12	2.2	~4%
l_1	1.56	1.52	~3%
L_2	46.1	47.8	~4%
l_2	31.6	32.92	~5%
M	9.88	9.9	~0.2%

LCR-meter based measurements (from 1 to 15 kHz) for SCASA primary (N_1=6) and secondary (N_2=28) transformer windings are shown in Figure 4.6, deviation between predicted and measured values is also indicated.

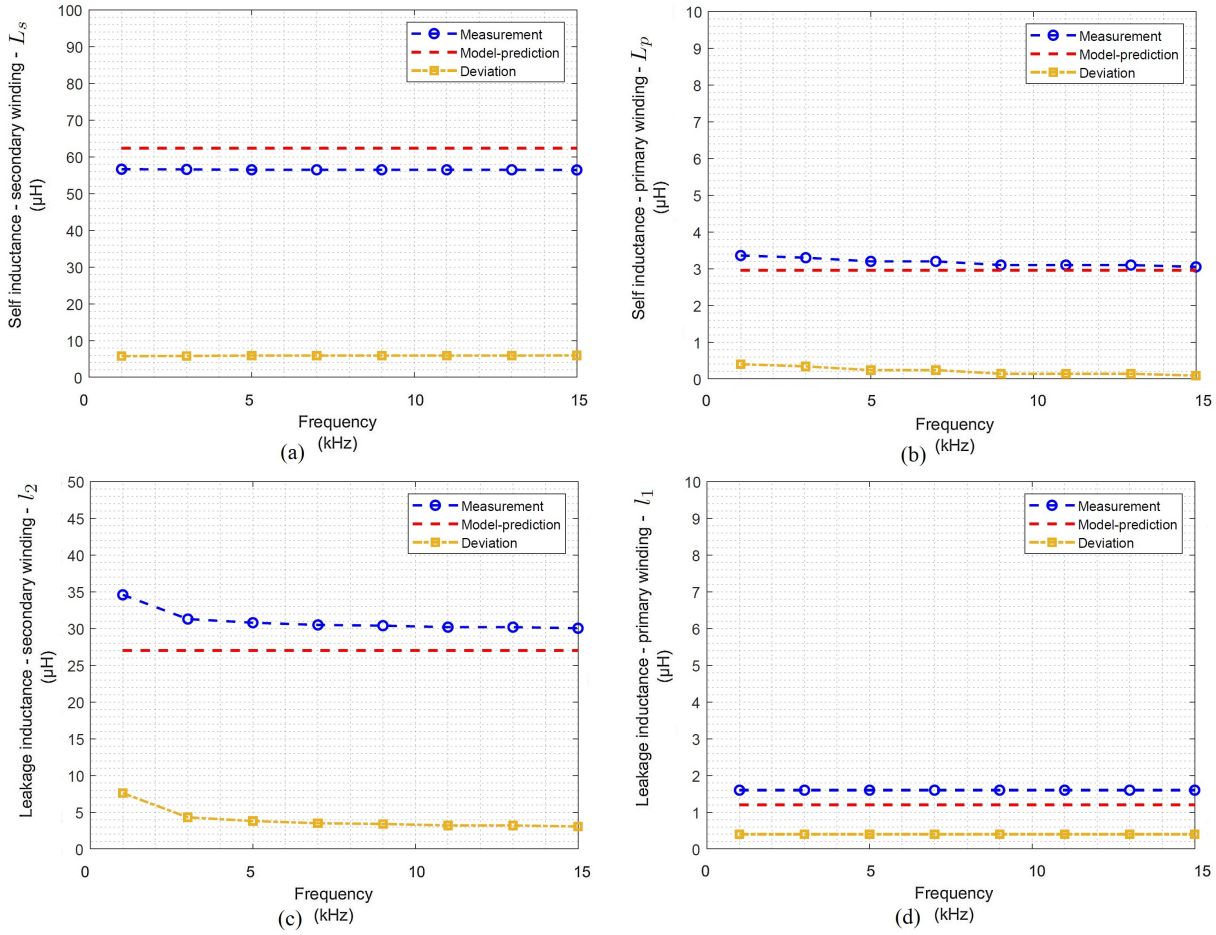

Figure 4.6: Measurement of SCASA transformer inductances: (a) Variation of self-inductance of secondary - L_s; (b) Variation of self-inductance of primary - L_p; (c) Variation of leakage-inductance of secondary - l_2; (d) Variation of leakage-inductance of primary - l_1

With the permeance based analytical approach described above, we can evaluate the magnetic coupling between the SCASA coupled-inductor coils to understand more about its transformer action. More details about theory development and experimental measurements are

presented next.

4.2.3 Magnetic coupling between the SCASA transformer windings

During SCASA operation, as surge currents propagate through the coupled-inductor windings the physical magnetic flux Φ linking the two coils circulates through the toroidal core (Figure 4.1). This mutual flux common for the two coils is quantified by the mutual inductance M of the coupled-inductor. According to the definition of inductance (Section 4.1.3) based on magnetic flux, we can express mutual inductance between primary and secondary windings as [82]:

$$M = \frac{N_1\Phi_{12}}{i_2} = \frac{N_2\Phi_{21}}{i_1} = \Lambda_m N_1 N_2 \tag{4.22}$$

where N_1 is the turn number of the primary winding, i_1 is the primary current, Φ_{12} is the magnetic flux linking the primary due to current in the secondary, N_2 is the turn number of the secondary winding, i_2 is the secondary current and Φ_{21} is the magnetic flux linking the secondary due to current in the primary.

The magnetic coupling between the two coils wound to SCASA core is related to the mutual inductance as per the definition of coupling coefficient k [82]:

$$k = \frac{M}{\sqrt{L_p L_s}} \tag{4.23}$$

where L_p and L_s are the self-inductances of primary and secondary coils respectively. The coupling coefficient is in the range 0 to 1 [83], and it represents the degree of magnetic coupling between the primary and the secondary windings. If a transformer is perfectly coupled, then the leakage inductances l_1 and l_2 are zero, hence the resulting k is 1. But, due to the non-ideal characteristics (Fig. 4.4) of SCASA core with significant leakage effects, the k value for drops below 1. Calculations associated with k determination are included in the following explanation.

Our next aim is to express coupling coefficient using the permeance values specified to Kool μu powdered-iron core. Starting from Eq. (4.12), Eq. (4.13) and Eq. (4.14), we can incorporate both magnetizing permeance (Λ_m) and leakage permeance (Λ_σ) into Eq. (4.24) as below:

$$k = \frac{\Lambda_m N_1 N_2}{\sqrt{[\Lambda_m {N_1}^2 + \frac{\Lambda_\sigma}{2} {N_1}^2][\Lambda_m {N_2}^2 + \frac{\Lambda_\sigma}{2} {N_2}^2]}} \tag{4.24}$$

By rearranging Eq. (4.24);

$$k = \frac{\Lambda_m N_1 N_2}{\sqrt{[\Lambda_m + \frac{\Lambda_\sigma}{2}]^2 {N_1}^2 {N_2}^2}} \tag{4.25}$$

Eq. (4.25) simplifies into;

$$k = \frac{\Lambda_m}{\Lambda_m + \frac{\Lambda_\sigma}{2}} \tag{4.26}$$

Substituting Λ_m and Λ_σ from the manufacturer (Magnetics Inc.) specifications of Kool μu powdered-iron core (0077071A7):

$$k = \frac{61\ \text{nH/turn}^2}{61\ \text{nH/turn}^2 + \frac{42}{2}\ \text{nH/turn}^2}$$

$$k = 0.7439$$

Based on experimental measurements for series/inverse-series tests (Eq. (4.17)) and open-circuit tests, we can evaluate coupling coefficient for SCASA non-ideal transformer core as:

$$k = 0.7484$$

From above k values, it is clearly seen that the permeance-model prediction and the experimental measurement are almost identical with a minimum percentage deviation (∼1%). Furthermore, we can identify how SCASA magnetic core deviates from the ideal transformer behaviour with significant leakage effects ($k < 1$).

4.3 Operational Modes of the SCASA Transformer Core

The SCASA equivalent circuit model (Figure 4.4) has two distinct operational modes: 50 Hz AC steady state, and transient propagation state. With the permeance-model presented above, we now aim at investigating the surge protector operation under these contrasting voltage conditions. Here, we must consider the fact that two transformer coils which act as a coupled-inductor, share currents under all voltage circumstances. However, the two operational modes are governed by the impedance level of both primary and secondary windings at different voltage conditions. Figure 4.7 summarizes the experimental methodology used for validating modes of SCASA operation.

In the following sections, we emphasize each of these experimental phases in detail. First, we explain 230 V/120 V steady state operation of SCASA circuit.

4.3.1 50 Hz AC operation

Here, we consider the full equivalent circuit model of SACASA design with a high-power load device connected to the output. Under 230 V AC, neither of the varistors Var1 and Var2 are fired; hence, they do not conduct currents as MOVs have mega ohms level resistances during non-conduction phase. In Figure 4.8, we indicate these open-circuit conditions using dotted lines, and under such conditions RMS currents only pass through the two inductor arms.

Considering both resistive and reactive elements, it is possible to determine the total impedance in the primary path as,

$$|Z_1| = |R + j\omega L_1 + j\omega l_1 + \frac{1}{j\omega C}| \tag{4.27}$$

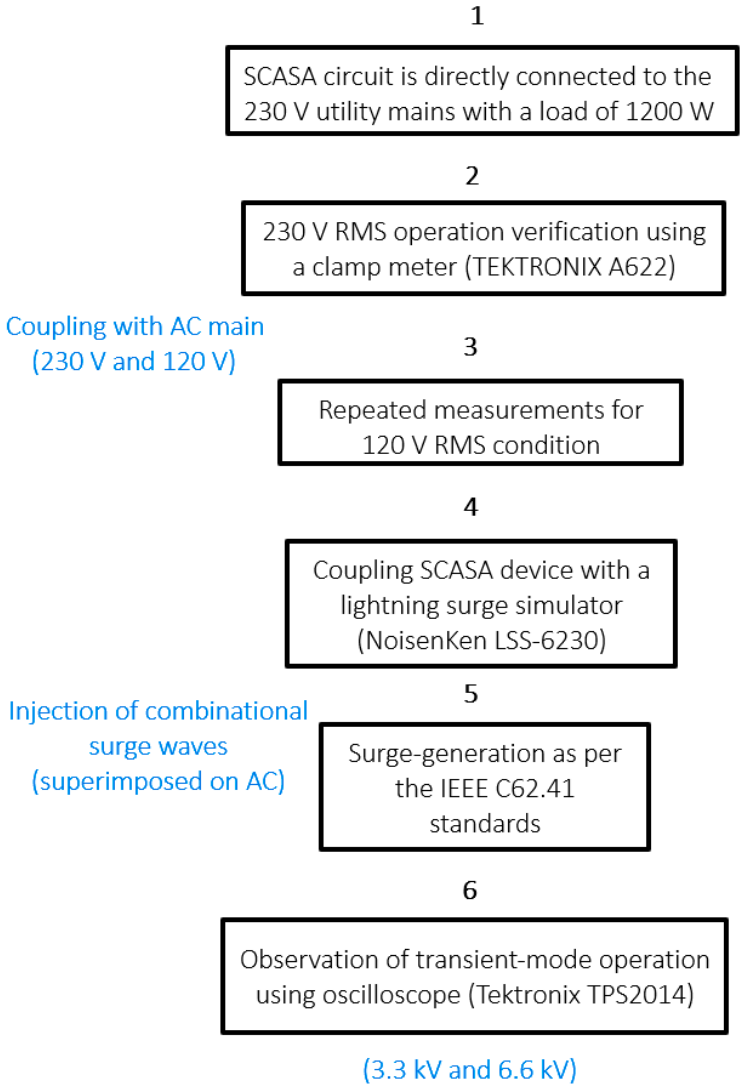

Figure 4.7: Summary of experimental steps used in validating AC and transient operations of SCASA surge protector

where L_1,l_1 are primary magnetizing and leakage inductances and C is the capacitance of 5 F supercapacitor (SC) utilized in SC sub-circuit. Moreover, R is the 1 Ω high-power resistor in the SC sub-circuit.

Similarly, the total impedance in the secondary can be expressed as a sum of two inductive reactances:

$$|Z_2| = |j\omega L_2 + j\omega l_2| \tag{4.28}$$

Now that, by putting a high current device (electric iron) across the load terminals, it is possible to measure how RMS currents are shared between the two coils. It is recognizable that the total RMS current through the load is the sum of individual currents in both primary and secondary (as varistors are in non-conduction mode). Compared to the high frequency components of a surge (Figure 6.1), 50 Hz is a less significant value. Therefore, with the μH

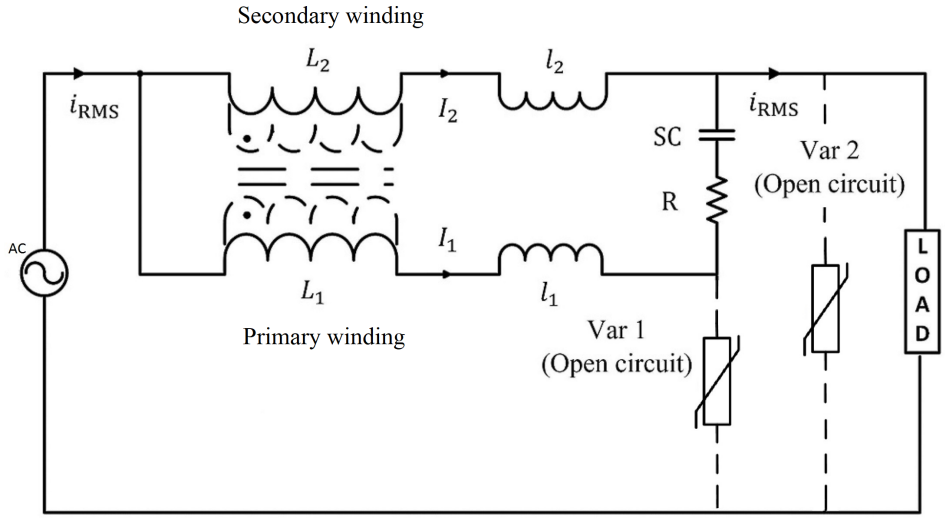

Figure 4.8: 50 Hz AC operation of the non-ideal transformer core of SCASA

level inductive coils wound to the SCASA core, we can predict that 50 Hz based inductive-impedances are fairly insignificant.

$$|Z_1| \approx 1.002\ \Omega \text{ and } |Z_2| \approx 0.04\ \Omega$$

As a result, it is expected to have a major RMS current flow in the less resistive secondary side of the core; whereas, resistive primary gets the least RMS current. Here, SCASA circuit is directly connected to the 230 V/120 V utility mains while a load of 1200 W (electric iron) is plugged to the output side. To justify our prediction, we include clamp-meter based test results in the following explanation.

Table 4.4: Comparison of primary and secondary RMS currents of SCASA coupled-inductor during 50 Hz AC operation (under 230 V/120 V utility mains) when powering a 1200 W resistive load

Test Condition	Voltage V_{RMS} (V)	Primary coil current I_1(A) (RMS)	Secondary coil current I_2(A) (RMS)	Measured total current I_{RMS}(A)
SCASA + IRON	230	0.15	4.81	5.04
SCASA + IRON	120	0.12	2.61	2.64
IRON	230	-	-	5.08
IRON	120	-	-	2.64

Two coupled-inductor coils inside the SCASA transformer were separately clamped using a clamp meter (Tektronix A622) to observe the sharing of currents (Figure 4.9). Table 4.4

summarizes the RMS current measurements and different test conditions considered.

Test results obtained for AC operation mode showed good compatibility with our modelling approach. As predicted above, we measured nearly 95% (CH1) of the RMS current flow in secondary; whereas only 5% (CH2) passed through the primary coil (Figure 4.9/Table 4.4). All currents were measured as RMS values; the total RMS current drawn from the wall socket was expected to be ∼5 A for the 1200 W load under 230 V. For a better accuracy, measurements were repeated for 120 V RMS condition as well.

We considered four main test conditions under 50 Hz AC operation; total RMS currents were measured with and without SCASA device for two voltage conditions: 120 V and 230 V. The main reason behind such an attempt was to understand the impact of SCASA circuit on AC main propagation. As highlighted in Table 4.4, the reduction of I_{RMS} in the presence of SCASA device is almost negligible (5.08 A → 5.04 A); noticeably, this observation is true for both voltage conditions. This further confirms the continuous facilitation of AC power flow by the SCASA design.

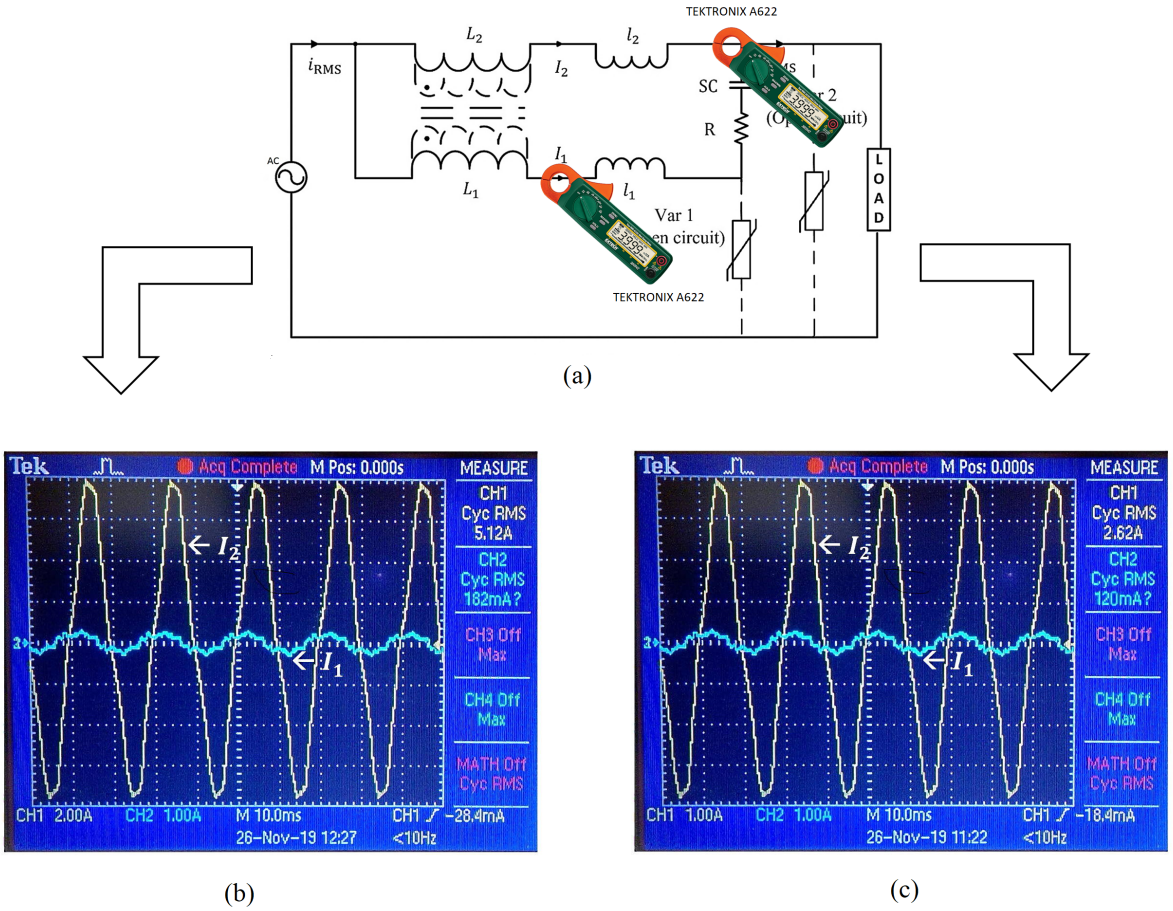

Figure 4.9: 50 Hz AC operation of SCASA: (a) measurement system using current transformers (Tektronix A622); (b) primary and secondary currents for 230 V AC; (c) primary and secondary currents for 120 V AC

4.3.2 Transient-mode operation

Here, we emphasize how the coupled-inductor of the SCASA transformer switches operation from 50 Hz AC to transient conditions. Under high voltage conditions, both Var 1 and Var 2 exceed their breakdown points; hence, enter into their conduction phases. Then, the open circuit conditions must be replaced with appropriate "ON resistances" (R_{ON}) as illustrated in Figure 4.10. According to the varistor model [96] of V20E275 (UltraMOV Series-Littlefuse) utilized in SCASA circuit, ON resistances of both Var1 and Var2 under transient currents is between 0.2-1 Ω [54, 96].

Modelling the transient propagation becomes a complex task specially with the continuous spectrum of frequencies (Figure 6.1); unlike the case of 50 Hz AC, under transients, we expect to see a distribution of impedances associated with each frequency component. Laplace Transform based analysis will yield analytical solutions to accurately predict the propagation of surge currents through SCASA coupled-inductor; a detailed mathematical analysis is presented in Chapter 6. Equivalent circuit model of the SCASA design during transient propagation is demonstrated below.

To verify the transient operation, a lightning surge simulator (NoisenKen LSS-6230) and a digital oscilloscope (Tektronix TPS2014) were used as the main instruments (Figure 4.11). Decoupling network inside the LSS ensures that none of the injected surge pulses are flowing back to the utility mains. Moreover, an isolation transformer was placed between LSS and wall socket as a safety precaution. Surge currents propagation through the core was indirectly measured by

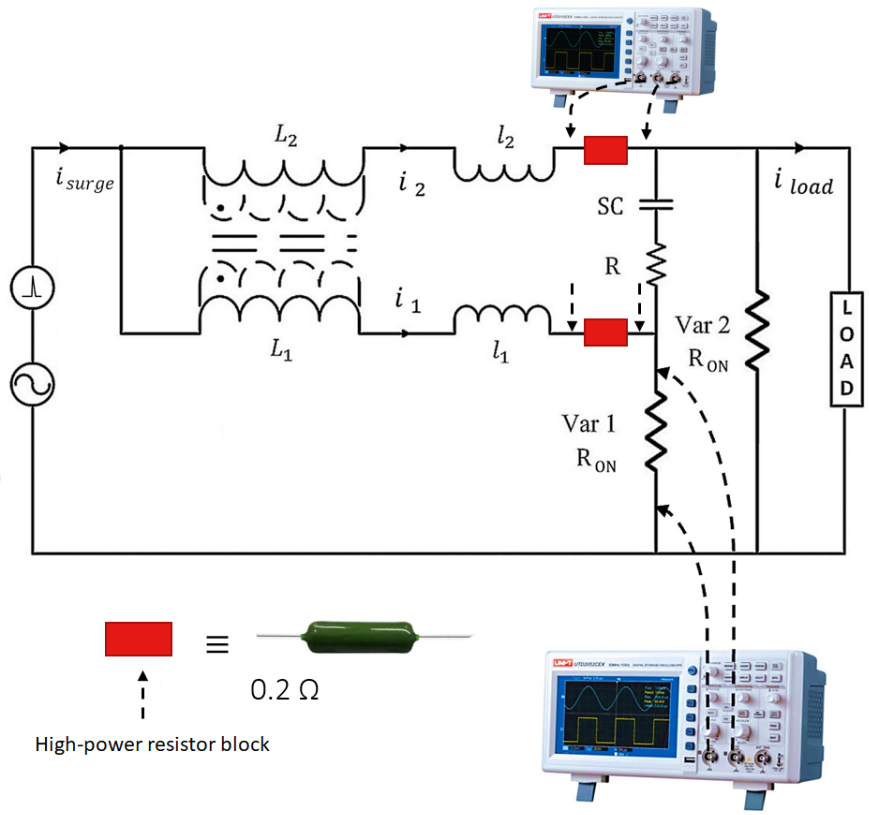

Figure 4.10: Transient operation of the non-ideal transformer core of SCASA (measurement system for transient currents using high-power resistors)

capturing the variations of voltages across externally inserted high-power resistors (Figure 4.10). Here, we placed a parallel combination of five 1 Ω, 10 W high-power resistors (0.21 Ω) across the primary and secondary sides of SCASA transformer core, and captured the voltage variations across them. Then, these peak voltage values were divided by 0.21 Ω to find the corresponding peak surge currents. In observing transient operation, different magnitudes of 1.2/50 µs surge pulses were generated using the LSS-6230 and injected into SCASA prototypes. Therefore, oscilloscope waveforms were recorded for 3.3 kV and 6.6 kV peak voltages as illustrated by Figure 4.11. Table 4.5 presents a summary of test results captured for peak surge currents under 3.3 kV and 6.6 kV.

Even though our method yields slightly diminished current values (due to the insertion of additional 0.21 Ω resistors), the ratio between transient currents (i_1/i_2) stays the same. Thereby, we can identify the percentages of i_{surge} shared among both coils. According to Figure 4.11, it is clear that $\sim$ 62% (CH1) total surge current propagates through the primary, whereas only $\sim$ 38% (CH2) flows through the secondary. This distinctly is a contrasting transition from the 50 Hz RMS operation.

4.3.3 Non-ideal behaviour of transient propagation

The most noticeable aspect in transient operation is the reversing effect of current flows compared to 50 Hz steady state. Under high frequencies, inductive impedances dominate; therefore, as indicated by Figure 4.11 the more inductive secondary side gets the least amount of transient currents. Conversely, a substantial portion of surge current passes to Var1 through the primary side. Here, we do not provide detailed analytical solutions (Chapter 6 presents a Laplace Transform based analysis), but we now delve into magnetic reluctance of the non-ideal SCASA core to see why the ratio of transient currents (i_1/i_2) does not satisfy the inverse ratio (N_2/N_1) of number of turns.

Table 4.5: Comparison of primary and secondary surge currents of SCASA coupled-inductor during transient operation (under 3.3 kV and 6.6 kV standard surge pulses)

Test Condition	Peak Surge Voltage V_{surge} (V) (CH4)	Peak Surge Current i_{surge} (A) (CH3)	Primary peak current i_1(A) (CH1/0.21)	Secondary peak current i_2(A) (CH2/0.21)
1.2/50 µs surge pulse	3.3 kV	1380	914.3	476.2
1.2/50 µs surge pulse	6.6 kV	2940	1790.5	1142.8

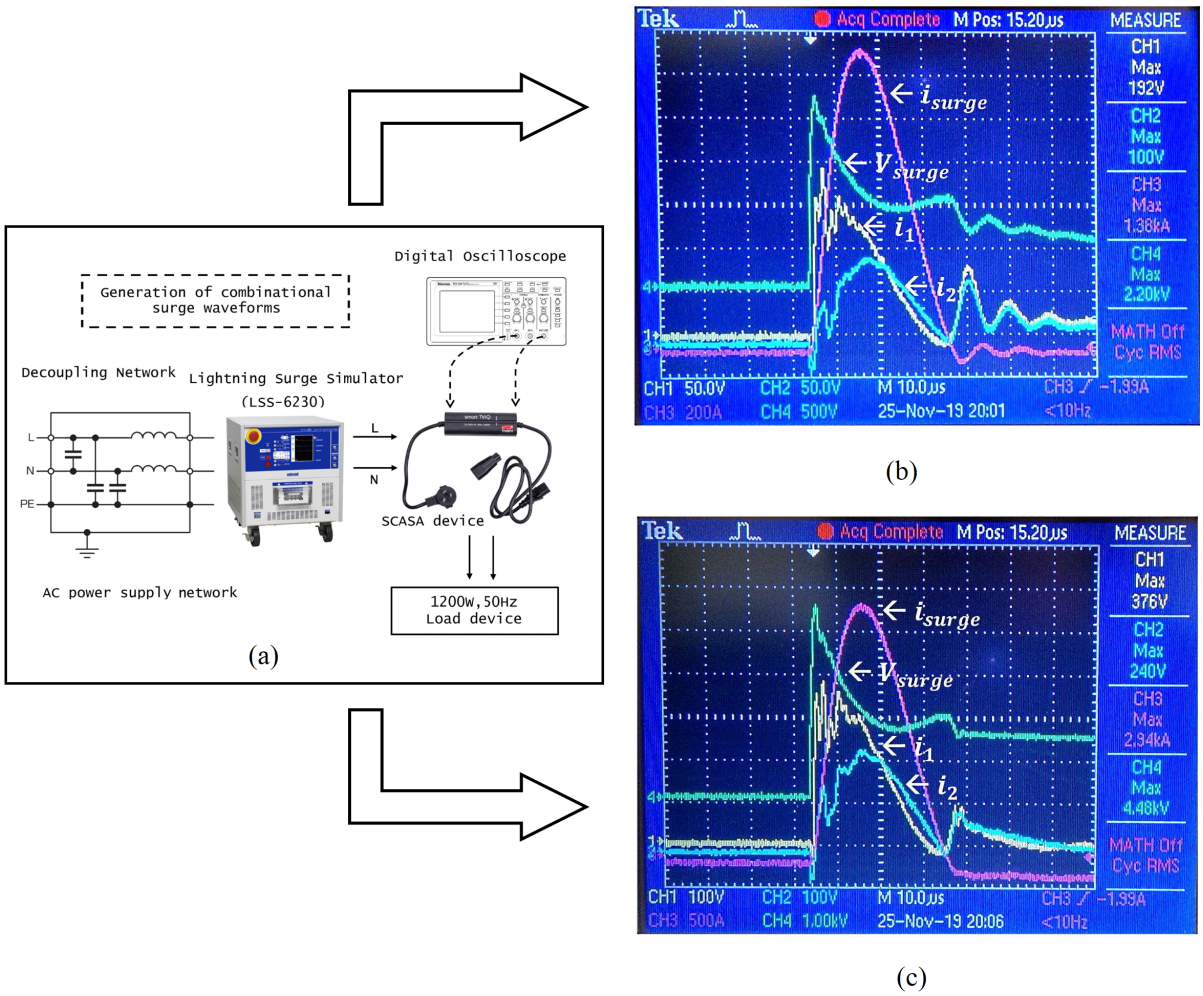

Figure 4.11: Transient operation of SCASA: (a) experimental setup using the lightning surge simulator (LSS-6230); (b) sharing of transient currents between primary and secondary windings (3.3 kV); (c) sharing of transient currents between primary and secondary windings (6.6 kV)

In Section 4.3.2, it became clear to us that the coupled-inductor core does not behave ideally as expected; basically a transformer must operate according to its turns ratio unless affected by magnetic reluctance of the core material. In an ideal case, when core reluctance is zero, the Ampere's law yields the following relationship as shown by Eq. (4.29) between primary and secondary currents.

$$N_1 i_1 + N_2 i_2 = 0 \tag{4.29}$$

Since SCASA utilizes a powdered-iron toroid, the air-bubbles distributed inside the core material make the medium more reluctive to the formation of magnetic flux. This extra reluctance modifies Eq. (4.29) into Eq. (4.30) as below [82]:

$$N_1 i_1 + N_2 i_2 = \Phi \mathfrak{R} \tag{4.30}$$

where Φ is the net magnetic flux through the toroidal core of SCASA during transient operation. Equation Eq. (4.30) can be rearranged into:

$$i_1 = \frac{\Phi\Re}{N_1} - \frac{N_2}{N_1}\, i_2 \tag{4.31}$$

This result clearly indicates why SCASA's coupled-inductor arms do not share currents as an ideal transformer. This study further revealed us that non-ideal behaviour of the core is highly significant specially during the propagation of transient currents. We look forward to bring this discussion further into Chapter 6 to compare the compatibility of our theoretical approach with experimental findings. As an initial verification, we calculate reluctance of the Kool μu powdered-iron core (0077071A7) to compare with the non-ideal behaviour as described by Eq. (4.30).

As per the Table 4.5 , it is understandable that the surge current percentages are not in reciprocal agreement with the turns ratio ($\frac{N_2}{N_1} = 28/6$). As predicted above in Eq. (4.30)

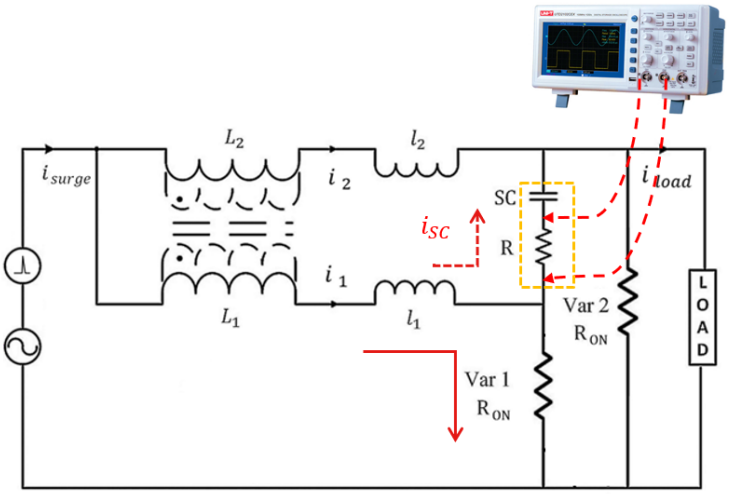

(a)

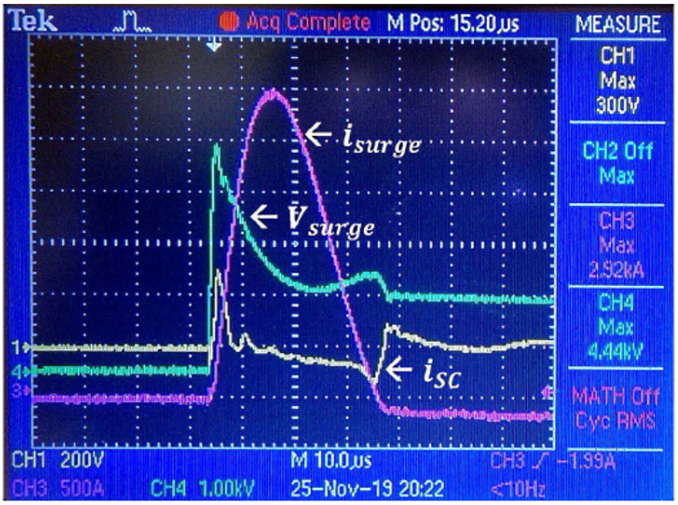

(b)

Figure 4.12: SC sub-circuit operation under transients: (a) measurement system; (b) SC sub-circuit current for a 6.6 kV transient pulse

this discrepancy is due to the magnetic reluctance caused by the powdered-iron toroid. Using manufacturer's specifications for magnetizing permeance Λ_m (61×10^{-9} H) [76], it is possible to quantify the core reluctance as previously discussed by Eq. (4.6):

$$\mathfrak{R} = \frac{1}{\Lambda_m} = 1.64 \times 10^7 \text{ A.turns/Wb}$$

By knowing the magnitudes of i_1 and i_2 (Table 4.5), we can empirically confirm the accuracy of Eq. (4.31). Note that for the calculation of maximum possible flux Φ_{max} through the core, we assume a no load condition in which ∼90% of surge current i_{surge} passes completely through the primary [97]. This gives us a good approximation for the possible peak flux ($\Phi_{max} = 1.098 \times 10^{-3}$ Wb) inside the SCASA transformer core. More information is given in Chapter 6.

4.3.4 SC sub-circuit operation in transient mode

The SC sub-circuit in SCASA circuit topology play a major role in eliminating transient based oscillations. Therefore, it is an essential electromagnetic interference (EMI) filter inside the surge protector [66]. Our next aim is to determine currents through the sub-circuit in transient mode.

Figure 4.12(b) illustrates the flow of transient currents into the SC sub-circuit (i_{SC}). This reveals approximately ∼10% (CH1:300 A) of i_{surge} (CH3:2920 A) is passing on to SC; it's fairly insignificant under these circumstances. For this measurement system, insertion of external resistors were not required as the SCASA circuit itself has a 1 Ω high-power resistor; thus, voltage variation across that is as same as the current variation through the sub-circuit (Figure 4.12(a)). However, depending on this observation, we can argue that entire secondary current i_2 and nearly ∼16% of i_1 is flowing into Var2 which is very likely with the breaking down of Var2. Under such sharing of currents, it is clear that Var1 gets most of i_{surge} as i_1 is significantly greater than i_2. This is mainly due to the fairly small ON-resistance (R_{ON}∼0.3 Ω) of Var1. More information about varistor behaviour under transient currents is explained in Chapter 6. Moreover, as major portion of surge current flows through the Var1, it is most likely to destroy under repetitive surge pulses. In the next Chapter, we explore a new method to enhance surge endurance of SCASA technique based on air-gapped ferrite cores.

4.4 Chapter Summary

In this chapter, we developed a permeance based circuit model for the magnetic core utilized by the coupled-inductor of SCASA surge protector technique. Various non-ideal characteristics of the core were also investigated with a special emphasis on the magnetic reluctance of Kool μu powdered-iron material. In addition, experimental validation of RMS and transient operations of the SCASA transformer was discussed with comparisons made by theoretical predictions.

In the next chapter, we explore a new approach to improve the surge endurance of SCASA design using air-gapped ferrite cores, and suggest methods to overcome limitations of the existing circuit topology.

Chapter 5

Optimization of SCASA using Air-gapped Ferrite Cores

In this chapter, we investigate the use of air-gapped ferrite cores for the present SCASA design, and elucidate ways to enhance surge endurance and energy storage capability to optimize its overall performance. Starting from the permeance based analytical approach presented in last Chapter, we expand our theoretical work with new models for effective-permeability and effective-permeance of an air-gapped core. Experimental outcomes as per UL-1449 3rd edition test methods are discussed towards end of this Chapter.

5.1 Importance of an Air-gap in Ferrite-iron

5.1.1 Alteration of magnetic properties

A high permeability material such as ferrite-iron (Table 4.1) is one that has a low reluctance for a given magnetic path length (MPL) and core cross-section [83]. Specially soft ferrites (W and H ferrites) have relative permeabilities in the range 5000-15,000; thus, they can be magnetized and demagnetized easily, and their flux-based core losses are small [83]. Moreover, soft ferrite materials are resistant to sustain magnetism; thus, have a very low magnetic energy storage capability with a minor remanence [83, 98]. This is due to their low magnetic reluctance which leads to poor energy (magnetic flux) storage.

As previously discussed in Chapter 4, coupled-inductor coils that embodies powdered-iron as the core shows greater capability of absorbing surge energy. Air-bubbles distributed in powdered-iron make the core more reluctive (due to high magnetic reluctance and low permeability) and suitable for surge applications. Therefore, in adapting this new approach of a ferrite core for the coupled-inductor, we must first ensure that it has sufficient energy storage capability. That led us to insert an air-gap to the ferrite core body by means of external cuts. This modification elevates the magnetic hardness of the soft ferrite material leading to a better energy storage. When an air-gap is inserted (Figure 5.4) to a low reluctivity material like ferrite-iron, almost all of the reluctance in the equivalent magnetic circuit will be at the gap [99]. This is due to the fact that reluctivity of air is much greater than that of a magnetic material. Therefore, in practical purposes, controlling the size of the air-gap controls the reluctance of the core.

First, we studied possible air-gap configurations that can be adopted to ferrite based cores. Figure 5.1 depicts possible gap placement methods for different core configurations. Similar to the geometry of original powdered-iron core, we decided to incorporate thin air-gaps to the

toroidal body of ferrite cores. Apart from achieving similar characteristics to powdered-iron, this new modification of ferrite toroids leads to several positive outcomes by optimizing the overall performance of SCASA technique. A complete analysis about this advancement is presented in Section 5.6.2.

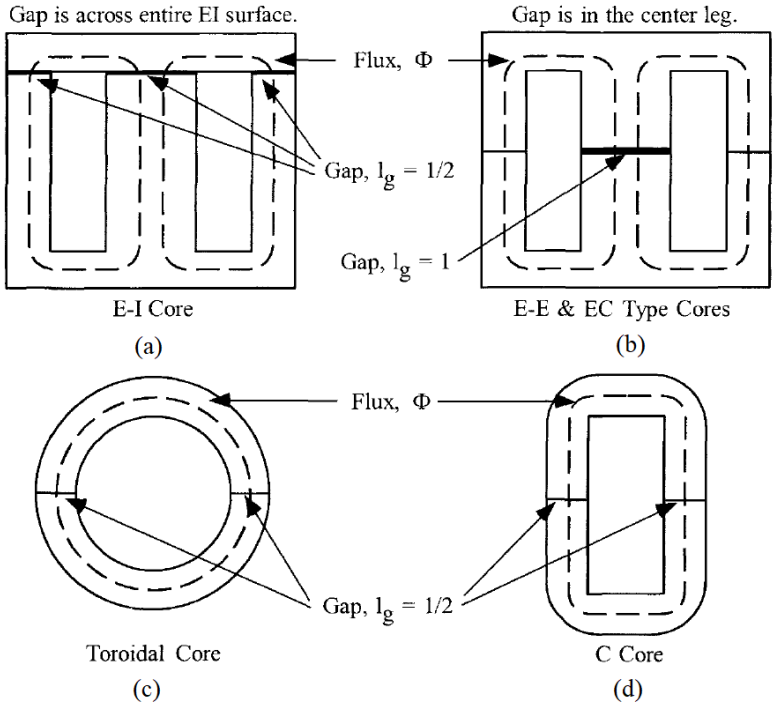

Figure 5.1: Air gap placement using different core configurations: (a) EI core; (b) EE and EC core; (c) toroidal core; (d) C core [83]

As our selection is biased towards gap placement in toroidal cores, it is important to analyse the changes to hysteresis behaviour (B-H loop) of a toroid in the presence of an air-gap.

5.1.2 Changes to hysteresis behaviour

The typical B-H loops of toroidal cores are normally seen in the manufacturers' specifications, and depends on the sample magnetic material. As described in Chapter 4, the gradient ($\frac{d\vec{B}}{d\vec{H}}$) of the B-H curve associated with the linear region defines permeability of the material [100]. The toroidal core, without a gap, is the ideal shape to view the B-H loop of a given material. The relative permeability μ_r will be seen at its highest in the ungapped toroidal shape, as shown in Figure 5.2. When an air-gap (highly reluctive) is inserted to the magnetic path, the resulting B-H loop is sheared leading to a significant reduction in core's permeability. Under such conditions, an effective permeability is defined for the toroid considering the effect of two materials (core-iron and air) present in the magnetic path [82, 84]. Noticeably, the magnetizing force H required to reach saturation flux density (B_{sat}) is much larger for an air-gapped core that would otherwise reach saturation at a fairly low level under ungapped conditions (Figure 5.2). Therefore, an essential attribute of the air gap in surge applications is to prevent saturation of the core under high-magnitude transient currents. Moreover, as emphasized above, this modification improves the overall energy absorption of the toroidal core.

In the next section, we model the equivalent magnetic circuit of an air-gapped toroidal core in order to examine how the relative permeability of an ungapped core is altered due to an air gap inside. Furthermore, we extend our model to show how surge-related magnetic flux can be stored as remanent flux in air-like media.

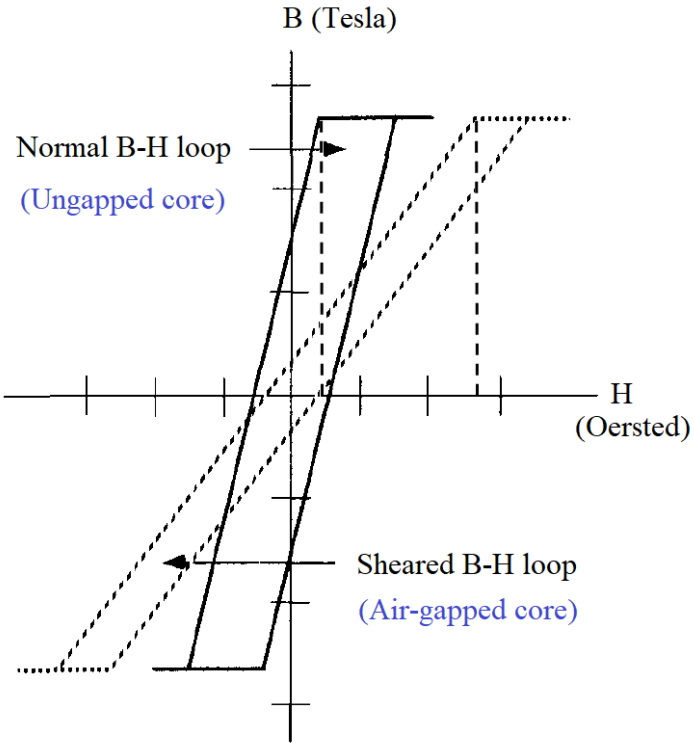

Figure 5.2: The shearing of an idealized B-H loop due to an air gap: comparison between ungapped and air-gapped toroidal cores [83]

5.2 Development of Models for an Air-gapped Toroid

5.2.1 Effective relative permeability of an air-gapped core

To predict the variations of permeability of a toroidal core in the presence of an inserted air gap (Figure 5.3), we construct a reluctance-based equivalent magnetic circuit in which total magnetic flux $\Phi(t)$ equally passes through both core reluctance $\Re_c$ and air-gap reluctance $\Re_g$. As shown in Figure 5.4, when the flux passes through, magnetic energy is stored in each of these reluctive components. This modification in total reluctance due to the air-gap is essential for our application of surge absorption; the following equations mathematically describe the effects in detail.

Total reluctance $\Re_T$ of the core with air-gap is the sum of individual reluctances [82],

$$\Re_T = \Re_c + \Re_g \tag{5.1}$$

$$\Re_T = \frac{l_c}{\mu_c A_c} + \frac{l_g}{\mu_\circ A_c} \tag{5.2}$$

where l_c is circular length of core, l_g is length of air-gap, A_c is core cross-sectional area, μ_c is permeability of the core and $\mu_\circ$ is permeability of free space.

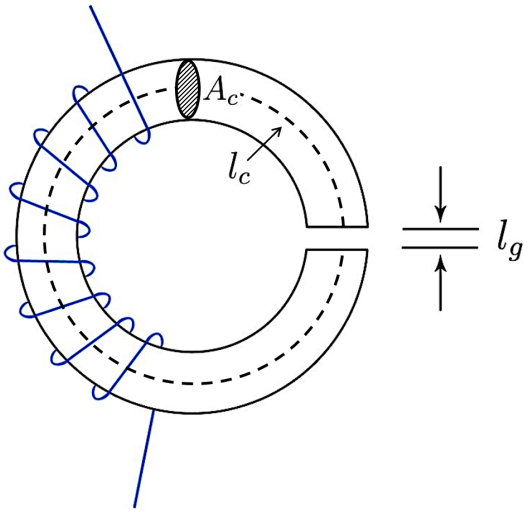

(a)

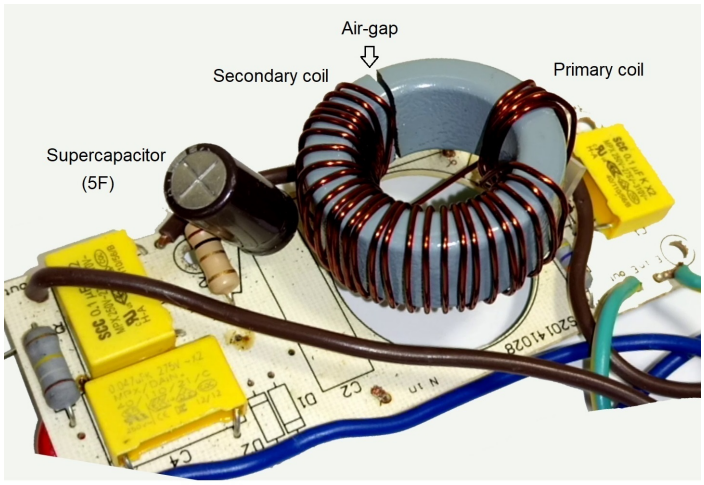

(b)

Figure 5.3: Air-gapped core (modelled view vs physical view): (a) geometrical configuration of a toroidal core with an air gap [80]; (b) air-gapped ferrite core installed in the SCASA circuit

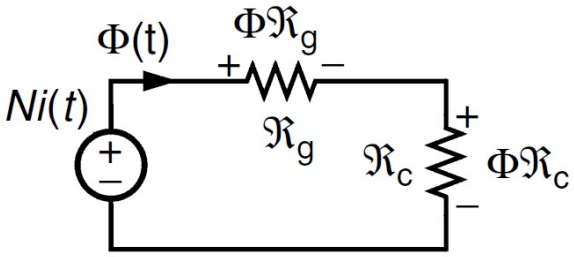

Figure 5.4: Equivalent magnetic circuit of an air-gapped core [82]

As per the definition of relative permeability $\mu_r = \mu_c/\mu_\circ$, we can rearrange Eq. (5.2) as:

$$\Re_T = \frac{1}{\mu_\circ A_c}\left[\frac{l_c}{\mu_r} + l_g\right] \tag{5.3}$$

By introducing an effective permeability (μ_l) to the core as a whole, total reluctance can alternatively be written as Eq. (5.4):

$$\Re_T = \frac{l_c + l_g}{\mu_l A_c} \tag{5.4}$$

From Eq. (5.3) and Eq. (5.4), it is possible to deduce the effective relative permeability ($\mu_l{}'$) of the core considering both materials in the magnetic path, and this result shows how permeability of the air-gapped core varies with the gap length.

$$\mu_l{}' = \frac{\mu_l}{\mu_\circ} = (l_c + l_g)\left[\frac{\mu_r}{\mu_r l_g + l_c}\right] \tag{5.5}$$

Eq. (5.5) is further simplified by approximating $l_c + l_g \approx l_c$ (since $l_g << l_c$); therefore, it reduces into:

$$\mu_l{}' = l_c\left[\frac{\mu_r}{\mu_r l_g + l_c}\right] \tag{5.6}$$

This result confirms the reduction of permeability in the presence of a reluctive medium such as air [82, 101]. When:

$$l_g = 0 \rightarrow \mu_l{}' = \mu_r$$

$$l_g > 0 \rightarrow \mu_l{}' < \mu_r$$

For a single air-gapped ferrite shown in Figure 5.3 with a gap length $l_g = 2$ mm, $l_c = 100$ mm and $\mu_r = 10,000$, using Eq. (5.6):

$$\mu_l{}' = 100\,\text{mm}\left[\frac{10,000}{10,000 \times\ 2\,\text{mm} + 100\,\text{mm}}\right]$$

$$\mu_l{}' \approx 50$$

This calculation clearly justifies that insertion of an air column to the toroid provides a significant reduction in relative permeability (10,000 $\rightarrow$ 50), while enhancing the magnetic energy storage capability [100, 101]. More importantly, this new effective relative permeability $\mu_l{}'$ is comparable with the permeability of Koolμu powdered-iron core ($\mu_r = 60$) used in present SCASA design. We derive an expression for magnetic energy stored in an air-gap in Section 5.2.3 with a detailed discussion.

5.2.2 Effective permeance of an air-gapped core

With the modification made to ferrite toroid by inserting an air-gap, it became evident that the equivalent magnetic circuit is altered (Figure 5.4) along with the reduction of relative permeability. Specially, due to the presence of two materials (ferrite metal and air) inside the toroid, we can derive a new relationship for the core's effective permeance starting for the definitions described in Chapter 4. As per Eq. (4.5), magnetizing permeance Λ_m of the pure ferrite core:

$$\Lambda_m = \frac{\mu_r \mu_o A_c}{l_c} \tag{5.7}$$

Also, according to Eq. (5.6), effective relative permeability $\mu_l{}'$ in the presence of an air-gap:

$$\mu_l{}' = l_c \left[\frac{\mu_r}{\mu_r l_g + l_c} \right]$$

Since μ_r of an ungapped core changes to $\mu_l{}'$ in an air-gapped toroid, we can combine the two equations to introduce an effective permeance Λ'_m for the overall core:

$$\Lambda'_m = \frac{l_c \left[\frac{\mu_r}{\mu_r l_g + l_c} \right] \mu_o A_c}{l_c} \tag{5.8}$$

Eq. (5.8) simplifies into:

$$\Lambda'_m = \frac{\mu_r \mu_o A_c}{[\mu_r l_g + l_c]} \tag{5.9}$$

Rearranging Eq. (5.9):

$$\Lambda'_m = \frac{\mu_o A_c}{\left[l_g + \frac{l_c}{\mu_r} \right]} \tag{5.10}$$

As μ_r for a pure ferrite is significantly larger ($\mu_r >> 1$, $\mu_r \sim 10,000$), it is clear that even the effective permeance (Λ'_m) for an air-gapped toroid is substantially lower than the magnetizing permeance (Λ_m) of an ungapped toroid. Dividing Eq. (5.9) by Eq. (5.7) yields:

$$\frac{\Lambda'_m}{\Lambda_m} = \frac{1}{\left[1 + \frac{\mu_r l_g}{l_c} \right]} \tag{5.11}$$

For a single-gapped ferrite core as shown in Fig. 5.3, when $l_g = 2$ mm, $l_c = 100$ mm and $\mu_r = 10,000$:

$$\Lambda'_m \approx 0.005\, \Lambda_m \tag{5.12}$$

$$\Lambda_m >> \Lambda'_m$$

This result further confirms the reduction of magnetizing permeance in the presence of an air-gap.

According to the manufacturer specifications [77] of W-ferrite toroid (ZW43615TC), Λ_m = 13,400 nH/turn^2 (see Appendix E); thus, Λ'_m for the single-gapped core can be calculated as:

$$\Lambda'_m \approx 0.005 \times 13,400\, \text{nH/turn}^2$$

$$\Lambda'_m \approx 67\, \text{nH/turn}^2$$

This effective permeance of the gapped-core matches well with the existing Kool μu (0077071A7) powdered-iron core (present SCASA design) that has a permeance-coefficient of 61 nH/turn^2.

Based on the inverse relationship (Eq. (4.6)) between magnetizing permeance and total reluctance ($\Lambda'_m = 1/\mathfrak{R}_T$), it is clear that,

$$\mathfrak{R}_T >> \mathfrak{R}_c$$

where $\mathfrak{R}_c$ is the core reluctance of ungapped core, and $\mathfrak{R}_T$ is the total reluctance ($\mathfrak{R}_T = \mathfrak{R}_c + \mathfrak{R}_g$) of an air-gapped core. As described above, this extra component of reluctance $\mathfrak{R}_g$ added to the equivalent magnetic circuit (Figure 5.4) by the air-gap retains more of surge-related flux leading to a better level of surge absorption [102]. Theoretical prediction of magnetic energy stored in the air-gap is presented next.

5.2.3 Magnetic energy stored in an air-gap

The main purpose of inserting an air-body into the ferrite core is to enhance its energy storage capacity; as previously mentioned, magnetic energy $E_\circ$ stored in the air-gap helps to reduce surge energy from being transferred to the load side. Using Ampere's law and flux-based definition of inductance [82], we can derive an expression for $E_\circ$ in as described below.

By applying Ampere's law to a toroidal core with N number of turns,

$$\oint_L \vec{B} \cdot \vec{dl} = \sum \mu_\circ I_{en} \tag{5.13}$$

where $\sum I_{en} = NI$ and $\vec{B}$ is the magnetic flux density across the core when a current I passes through the windings. Since $\vec{B}$ is uniform across any cross-section,

$$B \oint_L dl = \mu_\circ NI \tag{5.14}$$

Instead of considering the total circular length L, if we integrate only for the limit of air-gap l_g,

$$B = \frac{\mu_\circ NI}{l_g} \tag{5.15}$$

Self-inductance of a coil is defined as the magnetic flux (ϕ) per unit current $L = N\phi/I$ (Section 4.1.3), where $\phi = BA_c$. Using Eq. (5.15), we can show that the inductance $L_\circ$ of the coil across the air-gap length l_g is given by,

$$L_\circ = \frac{N^2 \mu_\circ A_c}{l_g} \tag{5.16}$$

The magnetic energy stored in the air-gap ($E_\circ$) helps to reduce surge energy from being transferred to the load side. Therefore, we can quantify $E_\circ$ according to $\frac{1}{2}L_\circ I^2$. Using Eq. (5.15) and Eq. (5.16),

$$E_\circ = \frac{1}{2}\frac{B^2 v_g}{\mu_\circ} \tag{5.17}$$

Here, v_g is the volume of air-body that is inserted to the toroid as indicated by Figure 5.5. This air volume can be easily found using $A_c l_g$.

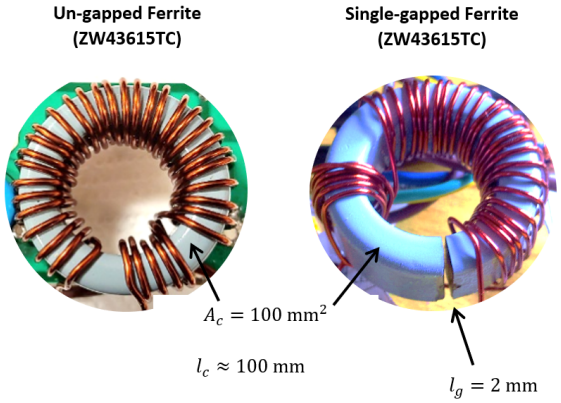

Figure 5.5: Geometrical configurations of ungapped and single-gapped ferrite toroids

Using Eq. (5.17), it is possible to compare the energy storage capability of ungapped and single-gapped ferrite toroids shown in Figure 5.5. As surge related magnetic flux due to transient currents flows uniformly through the core and air-gap, we can express energy E_c stored in the pure ferrite as proportional to,

$$E_c \propto \frac{A_c l_c}{\mu_\circ \mu_r}$$

Similarly, energy stored in the air-column of single-gapped core is proportional to,

$$E_\circ \propto \frac{A_c l_g}{\mu_\circ}$$

Based on above relationships, we can express $E_\circ / E_c$ as:

$$\frac{E_\circ}{E_c} = \frac{\mu_r l_g}{l_c}$$

For a single-gapped toroid with a gap length $l_g = 2$ mm, $l_c = 100$ mm and when $\mu_r = 10,000$ for the pure ferrite core, using above relationship:

$$\frac{E_\circ}{E_c} = \frac{10,000 \times 2\ \text{mm}}{100\ \text{mm}}$$

$$E_\circ = 200 \times E_c$$

Noticeably, this proves that the magnetic energy stored in the air-gap itself is 200 times greater than the energy stored in entire core body of the ungapped toroid.

With the goal of verifying above discussed theoretical base, we first establish a mathematical relationship for the alteration of self-inductance in the presence of an air-gap inside a toroid.

5.2.4 Reduction of self-inductance in the presence of an air-gap

In the previous Section 5.2.1, we developed an equation to quantify the drop in magnetic permeability for a core with an air-gap. Here, we extend that analysis to predict the reduction of self-inductance for a coil wound to a similar core. By rearranging Eq. (5.6):

$$\mu_l{}' = \frac{\mu_r}{\left[\mu_r \frac{l_g}{l_c} + 1\right]} \tag{5.18}$$

A coefficient α can be introduced to the ratio l_g / l_c;

$$\mu_l{}' = \frac{\mu_r}{\left[\mu_r \alpha + 1\right]} \tag{5.19}$$

By definition [82], self-inductance L_c of a coil wound on an ungapped toroidal core is:

$$L_c = \frac{N^2 \mu_c A_c}{l_g} \tag{5.20}$$

where $\mu_c = \mu_r \mu_\circ$.

Using Eq. (5.19) and Eq. (5.20), the resulting self-inductance $L_c{}'$ of a coil wound on an air-gapped core can be written as:

$$L_c{}' = \frac{L_c}{\left[\mu_r \alpha + 1\right]} \tag{5.21}$$

This clearly indicates $L_c{}'$ always yields a reduced value compared to L_c regardless the value of α. Though larger α results in significant reduction of $L_c{}'$, we found optimum energy storage is obtained for $\alpha = 0.025$ (single-gapped core) and 0.05 (double-gapped core). The theoretical approach used here can be verified with experimental findings taken from SCASA coupled-inductor windings; supporting test results are presented next.

5.3 Measurement of Self- and Leakage Inductances of Gapped Toroids

As described in Chapter 4, we measured self-inductances and leakage components of the air-gapped core samples and compared these values with ungapped cores. All the toroids we tested for SCASA design comprised a coupled-inductor (primary and secondary) wound at unequal number of turns. As in the original topology, primary winding has 6 turns, whereas secondary composed of 28 turns. Inductance measurements of both windings were carried out using a LCR meter (Fluke PM6304) over a range of frequencies from 1 to 15 kHz (Figure 5.6). Such procedures confirm the accuracy of test results with relation to frequency components of a 1.2/50 μs surge waveform that is highly dominant in the kilohertz range [21, 103].

Table 5.1: Comparison of mutual, leakage and self inductances of primary and secondary windings of air-gapped cores used in SCASA prototype design

Measurement	Un-gapped Ferrite (ZW43615TC)	Single-gapped ferrite	Double-gapped ferrite
			
L_p (μH)	**312**	**13**	**6**
L_s (μH)	**11,200**	**170**	**65**
N_1	**6**	**6**	**6**
N_2	**28**	**28**	**28**
l_1 (μH)	**2**	**4**	**4**
l_2 (μH)	**78**	**58**	**45**
M (μH)	**1870**	**42**	**12**
k	**0.995**	**0.82**	**0.585**

L_p: primary self-inductance, L_s: secondary self-inductance, l_1: primary leakage-inductance, l_2: secondary leakage-inductance, M: mutual inductance, k: coupling coefficient, N_1: primary turns, N_2: secondary turns

In order to determine leakage inductance of both primary and secondary, short-circuit test method was used, whereas open circuit test procedure was implemented in finding self-inductances of both windings. By applying series and inverse-series test methods, mutual inductance of the transformer cores wound to air-gapped toroids were obtained [104]. Using

the mutual inductance, magnetizing inductances L_1 and L_2 are easily found (MN_1/N_2 and MN_2/N_1 respectively) [82,104]. Table 5.1 presents essential inductance measurements taken for single-gapped and double-gapped core at 5 kHz; other test results up to 15 kHz are illustrated in Figure 5.6. Fluctuation of these LCR meter based measurements for gapped ferrites were compared with pure ferrite core (ungapped) as well. More information about energy storage capability of gapped toroids is discussed in the following description.

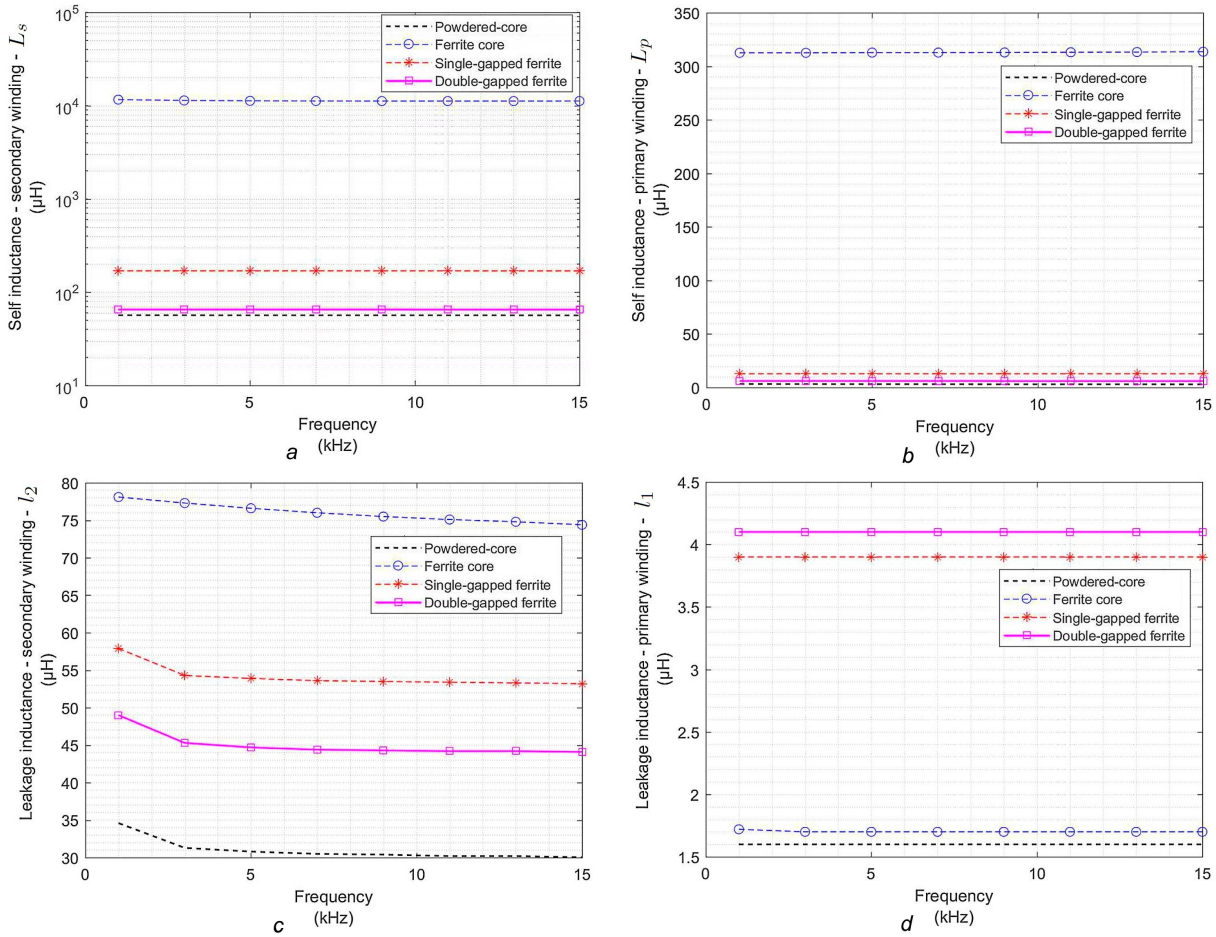

Figure 5.6: Comparison of self and leakage inductances of primary and secondary windings for the four core types under test: (a) variation of self-inductance of secondary; (b) variation of self-inductance of primary; (c) variation of leakage-inductance of secondary and (d) variation of leakage-inductance of primary

Next, we investigated how SCASA technique performs when the powdered-iron core is replaced with different gapped and ungapped ferrite cores as mentioned in Table 5.1. We selected ZW43615TC, a pure W-ferrite based toroid that has similar geometry as the original powdered-iron core with cross sectional areas and internal diameters of both cores being approximately equal. However, ZW43615TC core possesses an extremely high relative permeability (μ_r = 10,000) [77], far greater than the permeability of 0077071A7 (μ_r = 60). See Appendix E for manufacturer specifications of these core samples. In addition, the pure ferrite inductor has a very large self-inductances (L_s, L_p) due to its high permeability. This is a drawback to surge protection since it results in a significant impedance that can hinder 50 Hz AC transfer. Another

drawback is that ferrite materials have very limited energy storage as described in Section 5.1. By reducing permeability and improving energy storage, we aim to devise a modified ferrite core that has superior characteristics to powered-iron. Hence, as a satisfactory modification, as predicted in Section 5.2.1, we decided to incorporate air-gaps into the ferrite core (Figure 5.3). Two main gapped approaches were considered here (Table 5.1). One was to insert a single air-gap of length l_g (2 mm), and the other was to double the effect by inserting two air-gaps on opposite sides. It was experimentally challenging to cut pure ferrite due to its brittleness; therefore, grinding tools with diamond coated blades were used to insert fine cuts in both cases.

As indicated earlier, different parameters of our circuit model (Figure 4.4) vary in the presence of different core types. Therefore, to visualize these variations, we plotted self-inductances and leakage inductances of both core windings over a range of frequencies. Figure 5.6 compares the inductances for the four toroidal cores under test. Measurements from open-circuit tests (self-inductance) are presented in Figure 5.6(a) and Figure 5.6(b); whereas, measurements from short-circuit tests (leakage inductance) are illustrated in Figure 5.6(c) and Figure 5.6(d). According to Figure 5.6(a), the secondary winding yielded a significantly larger self-inductance when a pure ferrite material (ZW43615TC) is used as the inductor-base; but, the opposite characteristics observed when wound on the powdered-iron core. This observation remained steady throughout the full frequency range. Consistent with their contrasting permeabilities, ferrite and powder-iron are expected to have a substantial difference in their measured inductance. Moreover, ferrite cores with air-gaps exhibited significant drops in primary and secondary self-inductances. This is expected due to the considerable reduction in relative permeability in the presence of an air-gap. According to Figure 5.6(a), the double-gapped core showed an inductance reduced to the same level as powdered core while single-gapped ferrite core recorded a moderate inductance. This pattern continued for the primary winding self-inductance as revealed by Figure 5.6(b). It is notable that three out of four main core types (powdered-iron, single-gapped and double-gapped ferrite) exhibited similar inductance characteristics with a minimum disparity; this phenomenon was observed throughout the frequency range. More importantly, Figure 5.6(a) and Figure 5.6(b) further justified how close the self-inductances were for the doubled-gap core in comparison with powdered-iron core.

Another important observation is the reduction of mutual inductance in air-gapped toroids. As per Table 5.1, both single-gapped and double-gapped cores indicated remarkable drops in M. Since M depends on magnetizing permeance Λ_m, it is expected to have such alterations with the reduced effective permeance as mentioned above ($M = \Lambda'_m N_1 N_2$). This signifies how magnetic coupling between SCASA coupled-inductor coils reduces leading more flux leakage. In surge protection applications, leakage effects (energy losses) are considered crucial in minimizing the surge energy passing to the load-side. Our argument is further reflected by the depletion of coupling coefficient k in air-gapped toroids as per 5.1.

In the context of leakage inductance analysis, it is hard to identify a clear pattern between primary and secondary windings. Since leakage depends on core dimensions and availability of air gaps, we see that, as expected, the doubled-gap core displays elevated leakage inductances in Figure 5.6(d). As per Eq. (4.12) and Eq. (4.13), leakage is a component of self-inductance; hence, the core that yields largest secondary self-inductance shows the greatest leakage level

(Figure 5.6(c)). However, to get a better picture of leakage levels, we extended our study by considering a percentage analysis in the next section.

5.4 Energy Losses associated with Air-gapped Toroids

In Chapter 4, we explained how SCASA magnetic core operates as a non-ideal transformer which comes into action only when transients currents propagate. Under 50 Hz AC, RMS currents pass dominantly through the secondary coil of the coupled-inductor based on its low impedance. We further validated the non-ideality of the core with regard to magnetic reluctance of Kool μu powdered-iron toroid (Section 4.3.3). Though the reluctance of pure ferrites are very much limited, an air-gapped ferrite yields similar characteristics to powdered-iron in terms of its reluctance and leakage effects. In this section, we explore various such energy losses associated with air-gapped toroids that are essential to our surge protection application. In particular, leakage flux and fringing flux based losses (Fig. 5.7) are investigated in detail.

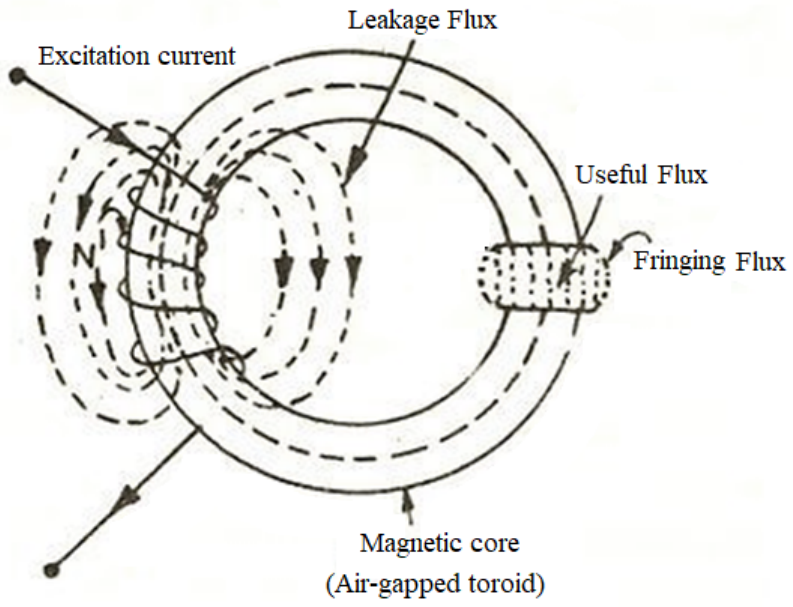

Figure 5.7: Leakage and fringing flux associated with an air-gapped toroid [90, 105]

5.4.1 Leakage flux

Leakage flux is generally considered as the part of magnetic flux which does not follow the particularly intended path in a magnetic circuit, thus it is not used for magnetization of the core [106]. As shown in Fig. 5.7, leakage flux field in a toroid can appear across the core diameter as well as outside. Moreover, in cases where magnetic reluctance dominates, part of the flux that gets stored inside the reluctive components such as air-gaps also leads to significant leakage. From our initial investigation of leakage inductance measurements of gapped cores as per Figure 5.6(c)-(d) and Table 5.1, it was hard to obtain a clear pattern to explain the changes of leakage flux in SCASA prototypes. Therefore, a percentage analysis based on the leakage percentages of primary and secondary windings wound to gapped-toroids was carried out with

comparisons to powdered-iron toroids. Figure 5.8 illustrates the fluctuation of leakage percentage of different core types under test. Eq. (5.22) indicates the calculation method used to determine leakage percentages for both windings.

$$\text{Leakage percentage} = \frac{\text{Leakage inductance}}{\text{Self inductance}} \times 100\% \tag{5.22}$$

Figure 5.8 reveals consistent leakage percentages for the two windings. In both cases, similarities are seen. According to Figure 5.8(a) and Figure 5.8(b), it is clear that the unmodified ferrite core has almost zero leakage percentage, supporting a strong magnetic coupling between the two coils. Despite that, as pure ferrite core shows poor energy storage capability, primary and secondary coils fail to capture much of the surge energy passing to the load. With the insertion of air-gaps, we aimed at increasing leakage levels, and this is validated by the test measurement with both primary and secondary windings exhibiting significant increments. Accordingly, the double-gapped core was the most dominant with about 65% –70% leakage (Figure 5.8) compared to $\sim$ 30% for the single-gapped core. These observations remained steady for the full frequency range considered. Powdered-iron core showed leakage values around 55% and 60% for the primary and secondary respectively.

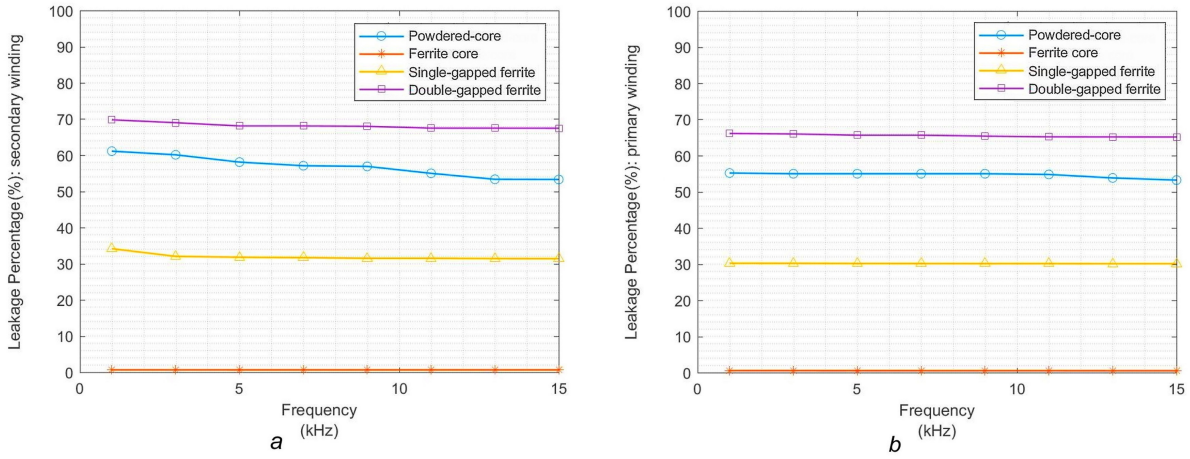

Figure 5.8: Comparison of leakage percentages of primary and secondary windings for the four core types under test: (a) leakage percentage analysis of secondary winding; (b) leakage percentage analysis of primary winding

Increased leakage is a positive aspect in surge protection circuits. The key idea is to leak the surge-related magnetic flux during immediate propagation of a transient surge to protect the critical load. Therefore, measurements in Figure 5.8 justify our motivation in designing SCASA prototypes using air-gapped ferrite cores. We discuss further benefits of this design change in the next section.

5.4.2 Fringing flux

The useful magnetic flux inside the core when passes through the the air gap, tends to bulge outward at as shown in Fig. 5.7. Due to this bulging effect, the effective cross-section of the

air gap increases, and the flux density of the air gap decreases. This phenomenon is known as Fringing, and it is proportional to the length of the air gap. Thus, a significant fringing loss is created with relatively larger air-gaps as depicted by Figure 5.9 [83].

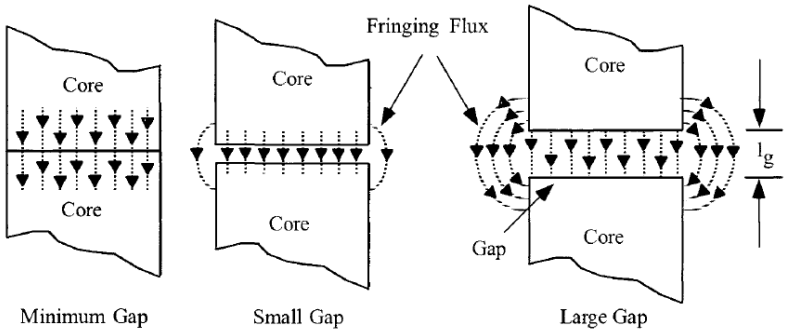

Figure 5.9: Effect of air-gap length on fringing flux [83]

In testing with SCASA prototypes, the two gapped core configurations we experimented had gap lengths $l_g = 2$ mm (single-gapped) and $l_g = 4$ mm (double-gapped) with significant flux based losses compared to pure ferrite toroids. However, determination of the air gap size requires consideration of the fringing flux which depends on gap dimension l_g, the shape of the pole faces, and the shape, cross-section A_c, and location of the winding. The winding length G of the core has a big influence on the fringing as well. Though accurate prediction of gap losses is very difficult to calculate, a fringing flux factor F can be introduced using l_g, A_c and G as below [107]:

$$F = 1 + \frac{l_g}{\sqrt{A_c}} \ln\left[\frac{2G}{l_g}\right] \tag{5.23}$$

For the single-gapped toroid used in SCASA prototype shown by Figure 5.3, F is evaluated as per following calculation:

$$F = 1 + \frac{2 \text{ mm}}{\sqrt{100 \text{ mm}^2}} \ln\left[\frac{2 \times 50 \text{ mm}}{2 \text{ mm}}\right]$$

$$F \approx 1.78$$

Fringing flux factor F is a useful result to predict about the alterations to self-inductance and magnetic saturation in the presence of fringing losses [108]. However, we do not plan to investigate further into this matter as it is beyond the scope of this thesis; but, an indication about heat losses is provided here. The fringing flux lines when intersects the copper windings, can create excessive eddy current losses in the windings and inside the core. Though we could not evaluate eddy-current losses associated with fringing effect due to experimental limitations, Figure 5.10 in [109] depicts how significant the corresponding heat dissipation can be for a gapped-core.

According to the above discussion regarding leakage and fringing effects, it is evident that air-gapped magnetic cores do possess significant energy losses which can facilitate the elimination of surge-based flux under transient operation. To justify our aim, the SCASA prototypes built

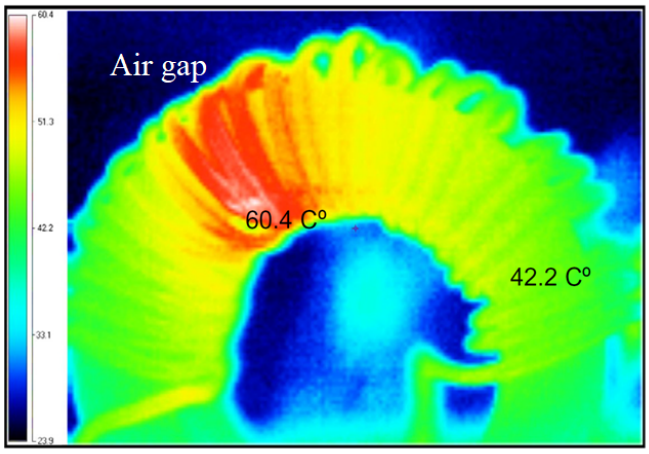

Figure 5.10: Thermal image of a toroidal inductor with an air gap [109]

using gapped ferrites were subjected to consecutive surge pulses as per UL-1449 3rd edition test procedure specified in Chapter 2.

5.5 Testing of SCASA Prototypes designed using Air-gapped Toroids

In order to facilitate surge testing of SCASA prototypes, a lightning surge simulator (NoisenKen LSS-6230) and a digital oscilloscope (Tektronix TPS2014) were used as the main instruments.

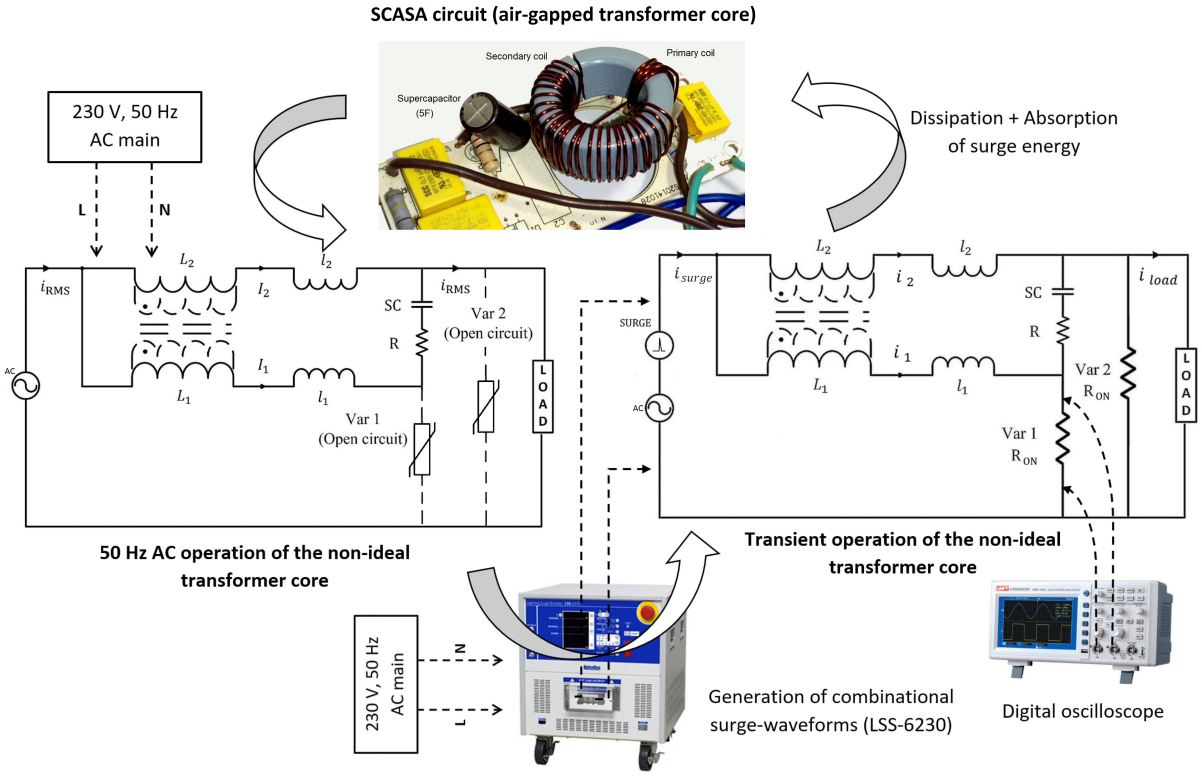

Figure 5.11: Experimental setup used for testing air-gapped SCASA prototypes

Figure 5.11 depicts the experimental setup implemented for combinational surge-waveform generation according to IEEE C62.41 standard. Here, 1.2/50 μs surge pulses were generated using the LSS-6230; hence, oscilloscope waveforms were recorded under a transient of 6 kV/3 kA. Figure 5.12 illustrates the experimental procedure used for testing air-gapped SCASA prototypes.

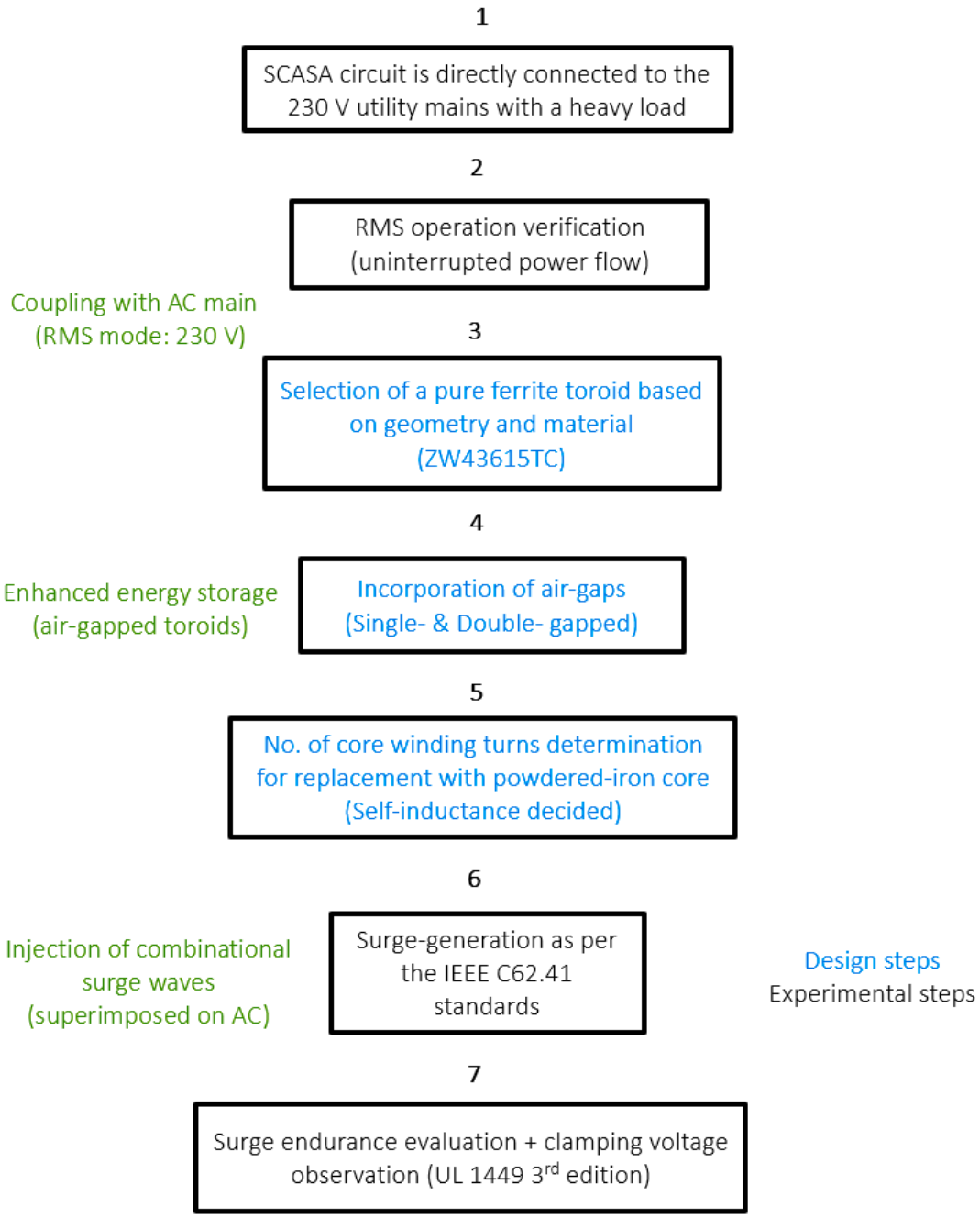

Figure 5.12: Experimental and design steps used for testing air-gapped SCASA prototypes

As described in Chapter 4, the equivalent SCASA circuit has two distinct operational modes: 50 Hz AC steady state, and transient propagation state. As shown in Figure 5.11, under 230 V AC, neither of the MOVs Var 1 and Var 2 are fired; therefore both MOVs exhibit open-circuit conditions. But, under transient conditions both MOVs become highly conducting [110]; this state can be indicated by replacing dashed lines (open-circuit stage) in Figure 5.11 with relevant

"ON resistances" (R_{ON}) of both varistors. A detailed analysis about sharing of currents under both operational modes was presented in Chapter 4.

Based on the test procedure specified above (Figure 5.11 and Figure 5.12), we evaluate the performance of SCASA surge protector designed using air-gapped ferrites in the next section.

5.6 Comparison of Performance: Powdered-iron vs Air-gapped Ferrites

The study of gapped cores was carried out to optimize the overall performance of SCASA design. Improving load-side voltage, and advancing its surge endurance capacity were the two main gaols. In this section, we explore how each magnetic-core type discussed above meets those goals by comparing their performance under transient operation.

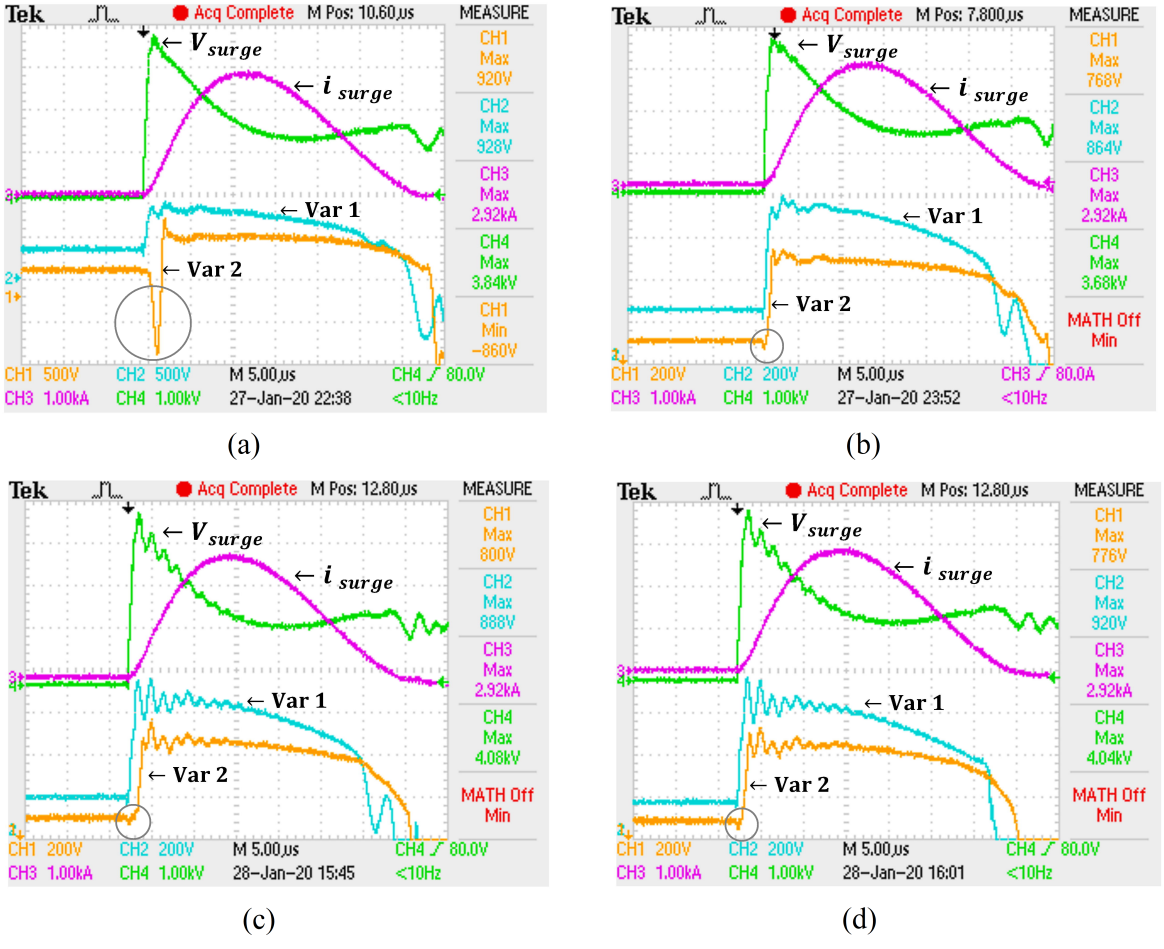

Figure 5.13: Oscilloscope waveforms for different gapped and ungapped cores under a transient of 6 kV/3 kA: (a) powdered-iron core (0077071A7), (b) ferrite-iron core (ZW43615TC), (c) single-gapped ferrite core, (d) double-gapped ferrite core

5.6.1 Improvements to the load voltage

In Chapter 3, we examined a drawback of the existing SCASA topology: during transient events, a reverse-sided voltage peak (a negative surge) is observed at the load end. This effect is a direct result of the energy stored inside the core being released immediately after the propagation of a surge pulse. Energies stored in primary and secondary windings of SCASA core develop voltages v_p and v_s respectively; hence, during the instantaneous release, the voltage difference (v_s–v_p) is what we see as the negative peak at the load. More information is found in Section 3.8.3. According to Figures 3.11 and 5.11, it can be noted that varistor 2 (Var2) and the load share similar patterns for voltage fluctuations; therefore, by capturing the voltage variation across Var2 it is possible to get a picture of this inductive energy release. However, due to parasitic inductances and capacitances, load and Var2 may not see identical voltages; more details regarding this implication are discussed at the end of Section 5.6.2.

As shown in Figure 5.14, when SCASA is coupled with 230 V AC via LSS-6230, and when a combinational surge of 6 kV/3 kA is injected, both MOVs (Var1 and Var2) provide clamping to protect the load. In order to capture clamped voltages, we used a digital oscilloscope with 100 MHz bandwidth and 1 GS/s sample rate (Tektronix-TPS2014) which has four isolated channels suitable for high-voltage floating measurements. These oscilloscope channels are isolated from each other as well as from earth ground, thus provide accurate differential measurements of MOV clamping with the Tektronix P6015A high voltage probes connected to varistor terminals (Figure 5.14). Moreover, two of the isolated channels were separately connected to LSS-6230

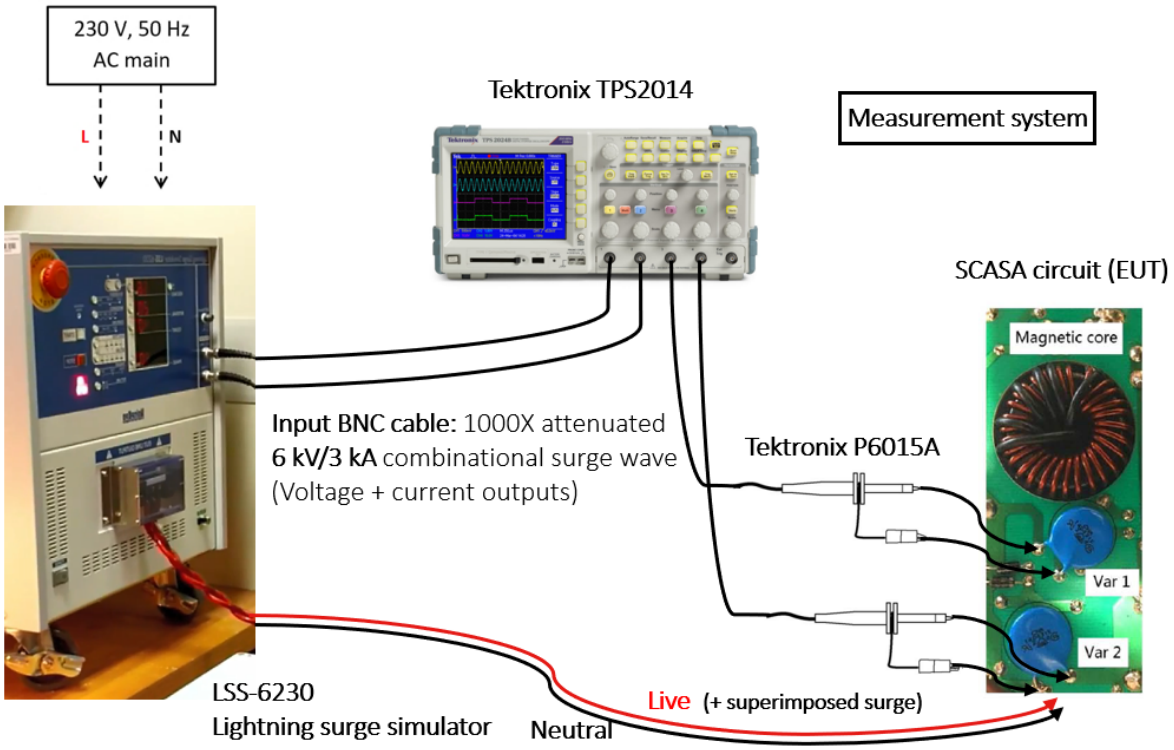

Figure 5.14: Measurement setup used to capture SCASA varistor clamping and LSS output under a combinational transient of 6 kV/3 kA

reference outputs (1000X attenuated) to obtain the actual surge waveforms (V_{surge} and i_{surge}) injected into EUT line.

Figure 5.13 illustrates several oscilloscope waveforms obtained for different core types tested. According to Figure 5.13(a) (captured for powdered-iron), when surge current (i_{surge}) and surge voltage (V_{surge}) rise, both MOVs enter into clamping phase exceeding their breakdown voltages. But, as powdered-iron retains and releases more surge energy than any other core, a negative surge of significant magnitude (–860 V) is observed in Figure 5.13(a). Table 5.2 summarizes essential details corresponding to all waveforms presented in Figure 5.13. In the case of ferrite core, approximately 95% reduction was recorded (Figure 5.13(b)). However, our measures to reduce the impact of negative peak has to be very selective that it must not limit the overall energy storage capability of SCASA. Since pure ferrite possesses a poor flux storage, though it showed a reduced peak, we can eliminate the possibility of using ZW43615TC ungapped core for further improvements. More information about its disadvantages is presented in the destructive test summary (Table 5.4).

Table 5.2: Comparison of negative surge reduction by different gapped and ungapped core types used in SCASA prototypes

Magnetic core type	Magnitude of negative surge passing to the load (V)	Negative surge reduction (V)	Reduction percentage
Powdered-iron (0077071A7)	−860	0	0%
Ferrite (ZW43615TC)	−40	820	∼ 95%
Single-gapped Ferrite	−20	840	∼ 98%
Double-gapped Ferrite	−20	840	∼ 98%

Next, similar oscilloscope waveforms were captured for the air-gapped ferrite cores. As previously discussed, by incorporating air-gaps, we aimed at enhancing flux absorbing capacity; air-columns potentially store surge-related magnetic flux, and then leak (and fringe) stored energy to the environment without passing to the load-side. Alternatively, magnetic reluctance of the core-material increases due to air-gaps (Figure 5.4); hence, the core itself is turning to a lossy medium with greater residual capacity. Figure 5.13(c) and Figure 5.13(d) reflect these advancements as negative surge-peak reduces by approximately 98% in the case of single-gapped and double-gapped ferrite cores (5.2). This is a substantial reduction of about 820 V as the initial –860 V peak drops to –20 V.

SPDs are primarily characterized by their clamping-voltage level. Lower clamping indicates better surge absorption, hence more protection. Therefore, we analysed how clamping levels

vary for the different core types; a comparison is presented in Table 5.3. Here, voltages across both MOVs of SCASA circuit (Var1 and Var2) are considered (Figure 5.13). But, Var2 is of greater concern as load-end is directly connected to it.

Table 5.3: Comparison of clamping level reduction by different gapped and ungapped core types used in SCASA prototypes

Magnetic core type	Clamping voltage of Var2 (V)	Reduction of clamping voltage (V)	Reduction percentage
Powdered-iron (0077071A7)	920	0	0%
Ferrite (ZW43615TC)	768	152	$\sim$ 17%
Single-gapped Ferrite	800	120	$\sim$ 13%
Double-gapped Ferrite	776	144	$\sim$ 16%

In the present SCASA design built using powdered-iron core, a clamping level of about 920 V was noticed, and in comparison all ferrite-based cores yielded much lower clamping voltages. However, as we eliminated the use of ungapped ferrite toroid (ZW43615TC) in our application, it is important to compare the reduction levels of two air-gapped approaches. Single-gapped core showed an encouraging 120 V reduction in clamping voltage which noticeably is a 13% reduction compared to powdered-iron. Moreover, the double-gapped core recorded a promising drop of 144 V and clamped around 776 V. This is a significant improvement to the Var2 voltage, and is a 16% reduction (Table 5.3) from the initial 920 V.

The test results so far validate our attempts to optimize the overall surge absorption capability of SCASA technique. Substantial improvements in load/Var2 voltage were recorded with the elimination of a negative surge-peak and with a lower level voltage-clamping. Next, we extend our investigation with a destructive testing method as per UL 1449 3rd edition standard.

5.6.2 Evaluation of surge endurance

An essential attribute of any SPD is its durability, depending on the level of endurance a SPD shows under consecutive transient surges, we can assess how resilient it is against surges. Thus, final performance evaluation tests of SCASA air-gapped prototypes were conducted according to the international standards of Underwriters Laboratories (UL-1449 3rd edition) [111]. A simplified version of this procedure is demonstrated in Figure 5.15.

Under this test method, combinational surge-waveforms (6 kV/3 kA) are consecutively injected to the AC mains using a lightning surge simulator; in the meantime, SPD kept coupled with the AC mains (Figure 5.11). Sufficient rest periods of 60 s and 30 minutes were provided

throughout the procedure to allow the dissipation of heat. Consecutive surge generation was achieved by means of repeating several steps. The pass criteria for this test is that the sample SPD must still function at the nominal system, and that the clamping voltage is still achieved at the end. UL-1449 test method is a form of destructive testing as at times protection circuits fail to withstand continuous application of surges. According to the summary given in Table 5.4, we can further verify why ungapped ferrite toroid is not applicable for SCASA technique. In Section 5.6.1, we described that due to poor energy storage capability of ZW43615TC, its usability in surge protection circuits is highly limited. Hence, during the transient propagation, more surge energy passes to the Var1 via less inductive primary winding. This results in blowing up the Var1 prior to the 200-surge mark; accordingly, we can notice a failure in clamping and negative surge reduction.

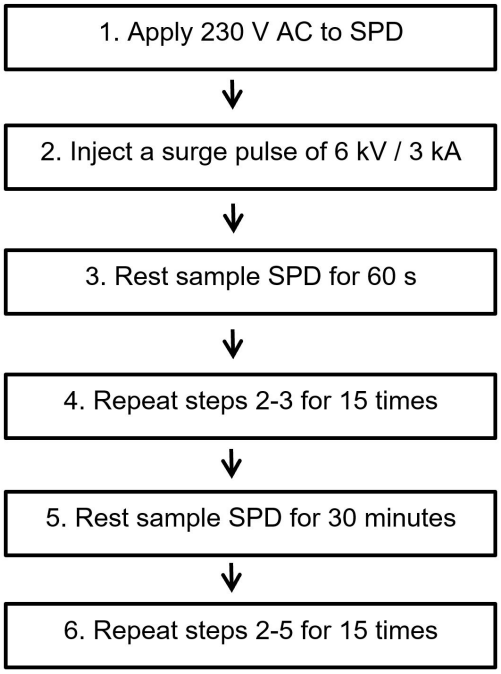

Figure 5.15: UL-1449 3rd edition test procedure

Despite that, other three core types (powdered-iron and two air-gapped cores) indicated success by passing the test criterion of UL-1449. In all three cases, Var1 and Var2 of SCASA circuit withstood surge energy without failing prior to the 200-surge mark. However, by comparing powdered-iron based SCASA prototype with two air-gapped approaches, we can clearly identify two major improvements. Optimized clamping levels were recorded in both single-gapped and double-gapped cores with approximately 800 V and 770 V; whereas, powdered-iron core still showed a high clamping of 950 V. All above clamping voltages were monitored across Var2, but the load voltage is 50–70 V lower than that in each case due to parasitic inductances/capacitances of the circuit path. We have experimentally verified this phenomenon for 6 kV, and found it as a useful voltage reduction mainly due to SCASA's 1.2 m length power outlet cable. Overall, the improved SCASA circuit can prevent sensitive load equipments from being damaged as most household appliances have a surge-immunity level up to 700 V [25]. Another encouraging

Table 5.4: Destructive testing summary: surge endurance assessment according to UL-1449 test standards

Magnetic core type	Observations when subjected to 200 consecutive surges	Clamping voltage after 200 surges	Impact of negative surge (load-end)
Powdered-iron (0077071A7)	MOVs withstood surge energy (Clamping achieved)	$\sim$ 950 V	Observed (-900 V)
Ferrite (ZW43615TC)	Failed (Failure of Var1)	Failed	Failed
Single-gapped Ferrite	MOVs survived (Improved clamping)	$\sim$ 800 V	$\sim$95% reduction (-20 V to -40 V)
Double-gapped Ferrite	MOVs survived (Improved clamping)	$\sim$ 770 V	$\sim$95% reduction (-20 V to -40 V)

advancement of the two air-gapped cores was the elimination negative surge-peak. Apart from withstanding 200 test surges, both single-gapped and double-gapped toroids revealed a promising $\sim$95% reduction of the negative-surge effect at load-end. As explained in Section 5.4, by leaking and fringing the stored surge-energy instead of passing it to the load side, ferrite cores with air-gaps yielded better performance than powdered-iron core.

5.7 Chapter Summary

In this chapter, we elucidated the possibility of using air-gapped ferrite toroids for performance enhancement of SCASA technique. Specially, new theoretical models were developed for effective permeability with an emphasis on alterations to reluctance and permeance of the equivalent magnetic circuit. Optimization of the present technique was highlighted as per surge endurance testing and clamping voltage improvements.

In the next chapter, transient current propagation through SCASA coupled-inductor windings will be analysed in detail using the Laplace Transform method. In addition, LTSpice circuit simulator based numerical simulations will be presented to validate our theoretical approach.

Chapter 6

Validation of Surge-propagation in SCASA using Laplace Transforms and Numerical Techniques

Given the non-ideal behaviour of SCASA transformer, in this Chapter, I develop Laplace transform based theoretical foundations to predict the surge current propagation through coupled-inductor windings of magnetic core. Compared to 50 Hz RMS operation, the significance of inductive impedance is emphasized with regard to the high-frequency spectrum of a 1.2/50 μs surge pulse. In addition, numerical validation using a LTSpice circuit model of SCASA surge protector is presented to justify the accuracy of our analytical approach.

6.1 Importance of Laplace Transform in Frequency Domain

6.1.1 Introduction to S-domain

Laplace Transform (LT) is a useful mathematical technique that transforms $f(t)$, a signal in time domain into $F(s)$, a signal in the complex frequency domain known as 'S' domain. By definition [112], this complex frequency domain is denoted by S and the frequency variable is represented by 's'. For mathematical convenience, the transformation of a signal from time domain to frequency domain is indicated by the Laplace operator '$\mathscr{L}$' as shown below.

$$\mathscr{L}\{f(t)\} = F(s) \tag{6.1}$$

According to the integral representation [113], Laplace Transformation of a time-domain signal $f(t)$ into complex frequency-domain is defined as:

$$F(s) = \int_0^\infty f(t)e^{-st}dt \tag{6.2}$$

where complex frequency variable $s = \sigma + j\omega$; σ in this case is the real part of s and $j\omega$ is the imaginary part of s [113]. In this definition, ω stands for the real frequency of the signal. The complex frequency plane used in LT is a mathematical abstraction applicable to simplifications of differential equations. Though Laplace method does not have a physical significance, it is useful in solving mathematical computations, and specially for the easy analysis of complex time varying signals such as transients.

Among various mathematical techniques available for the analysis of transient waveforms in linear circuits, Laplace transforms can be regarded as a very convenient method. Investigations discussed in this Chapter uses Laplace method to study surge propagation through the linearised SCASA circuit. Our initial goal is to study the output responses of Lightning Surge Simulator (described in Chapter 2) using LT; but first we explain the relevance of Laplace domain (S-domain) in the analysis of rapidly varying transient signals.

6.1.2 Frequency spectrum of a 1.2/50 μs surge pulse

The 1.2/50 μs open-circuit voltage waveform [40] is the standard surge pulse delivered to SPD circuitries during surge testing. As described in Chapter 2, the standard voltage wave is expressed using a double-exponential model which determines the rise-time and fall-time of the shape.

A mathematical representation of 1.2/50 μs open-circuit voltage wave is given by Eq. (6.3):

$$V(t) = A_V V_p (1 - e^{-t/\tau_1}) e^{-t/\tau_2} \tag{6.3}$$

where the constants are $A_V = 1.037\ (\mu s)^{-3}, \tau_1 = 0.4074\ \mu s, \tau_2 = 68.22\ \mu s$ and V_p is the peak voltage of the waveform.

Noticeably, the overall shape of this open-circuit voltage waveform is governed by a set of high frequencies compared to the single-frequency 230 V, 50 Hz utility mains flow. To understand the frequency distribution, as shown in Figure 6.1, we used LTSpice software tools to obtain the Fourier transform of a 6 kV surge waveform considering a time window of 500 μs; it includes a range of high frequencies starting from below 1 kHz to almost 1 MHz. Here, DC component of the surge has been removed to enhance the spectral representation. Unlike the

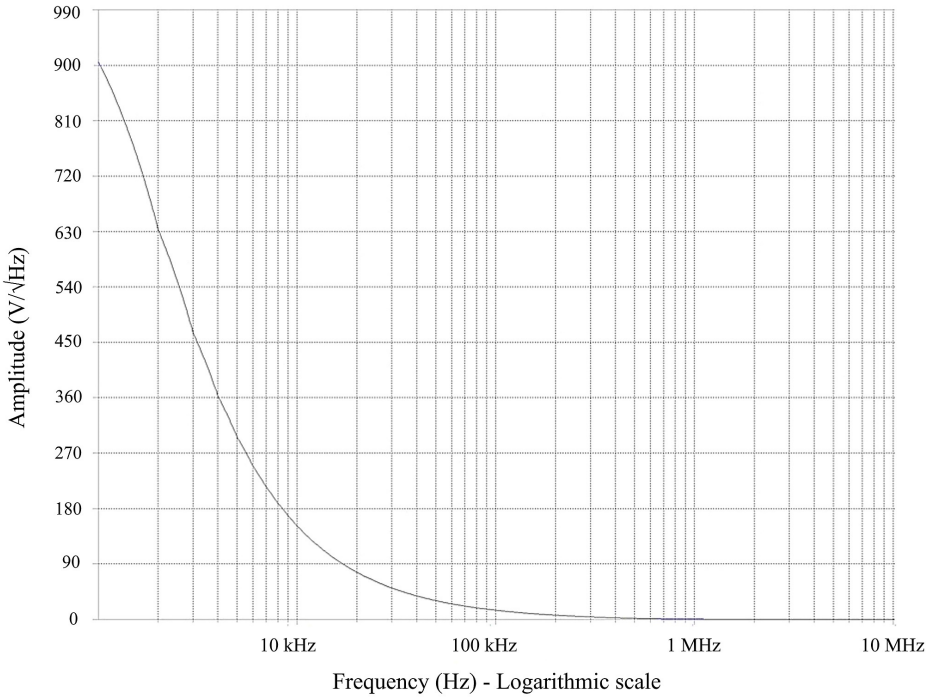

Figure 6.1: Simulated Fourier transform of a 1.2/50 μs standard surge pulse

steady RMS condition (50 Hz), inductive impedances dominate at high frequencies; this effect completely changes the operation of SCASA design [97] as explained in Chapter 4. Also, it can be conceptualized that SCASA coupled-inductor coils generate a spectrum of impedances that correspond to the spectrum of high frequencies depicted by Figure 6.1.

In Chapter 4, we briefly explained using oscilloscope waveforms how the coupled-inductor arms generate different impedances during transient events. However, to further understand the actual propagation of these high frequency surge components, we need to consider the permeance model of SCASA non-ideal transformer with the Laplace transform method. First, the internal generation circuit of LSS-6230 is analysed in the frequency domain.

6.2 Analysis of LSS using Laplace Transform Method

The Noiseken Lightning Surge Simulator (LSS-6230) is the key instrument used for standard 1.2/50 μs surge pulse generation during our experiments. As described previously in Chapter 2, LSS-6230 is compliant with IEC61000-4-5/IEEE C62.41.2-2002 surge standards. Therefore, in modelling the internal circuit of LSS-6230 using Laplace method, we first transformed all circuit parameters shown in Figure 6.2(a) into S-domain parameters as illustrated by Figure 6.2(b).

As indicated by Figure 6.2, the capacitor C_1 is the main energy storage element which can charge between 100 V to 6.6 kV. When the high-voltage energy is released into the wave shaping circuit (described in Chapter 2) consists of inductors L_1, L_2 and resistors R_1, R_2 and R_3, the standard wave-shape defined by IEC61000-4-5/IEEE C62.41.2-2002 is generated between the open ends of LSS [89]. In order to obtain analytical solution for this open-circuit voltage wave, the transformed circuit network (S-domain) shown in Figure 6.2(b) was analysed using Kirchhoff's laws.

Applying Kirchhoff's voltage law for the first loop in transformed LSS circuit:

$$\frac{V_c}{s} = \tilde{I}_1(s)\big[sL_1 + \frac{1}{sC_1}\big] + \big[\tilde{I}_1(s) - \tilde{I}_2(s)\big]R_1 \tag{6.4}$$

Similarly, Kirchhoff's voltage law for the second loop yields:

$$0 = \tilde{I}_2(s)\big[R_2 + R_3 + sL_2\big] + \big[\tilde{I}_2(s) - \tilde{I}_1(s)\big]R_1 \tag{6.5}$$

By rearranging Eq. (6.4):

$$\tilde{I}_1(s) = \frac{\dfrac{V_c}{s} + \tilde{I}_2(s)R_1}{\left[sL_1 + \dfrac{1}{sC_1} + R_1\right]} \tag{6.6}$$

Moreover, by rearranging Eq. (6.5):

$$\tilde{I}_1(s) = \frac{\tilde{I}_2(s)\big[R_1 + R_2 + R_3 + sL_2\big]}{R_1} \tag{6.7}$$

Introducing a new parameter $R_T = R_1 + R_2 + R_3$, Eq. (6.7) simplifies into:

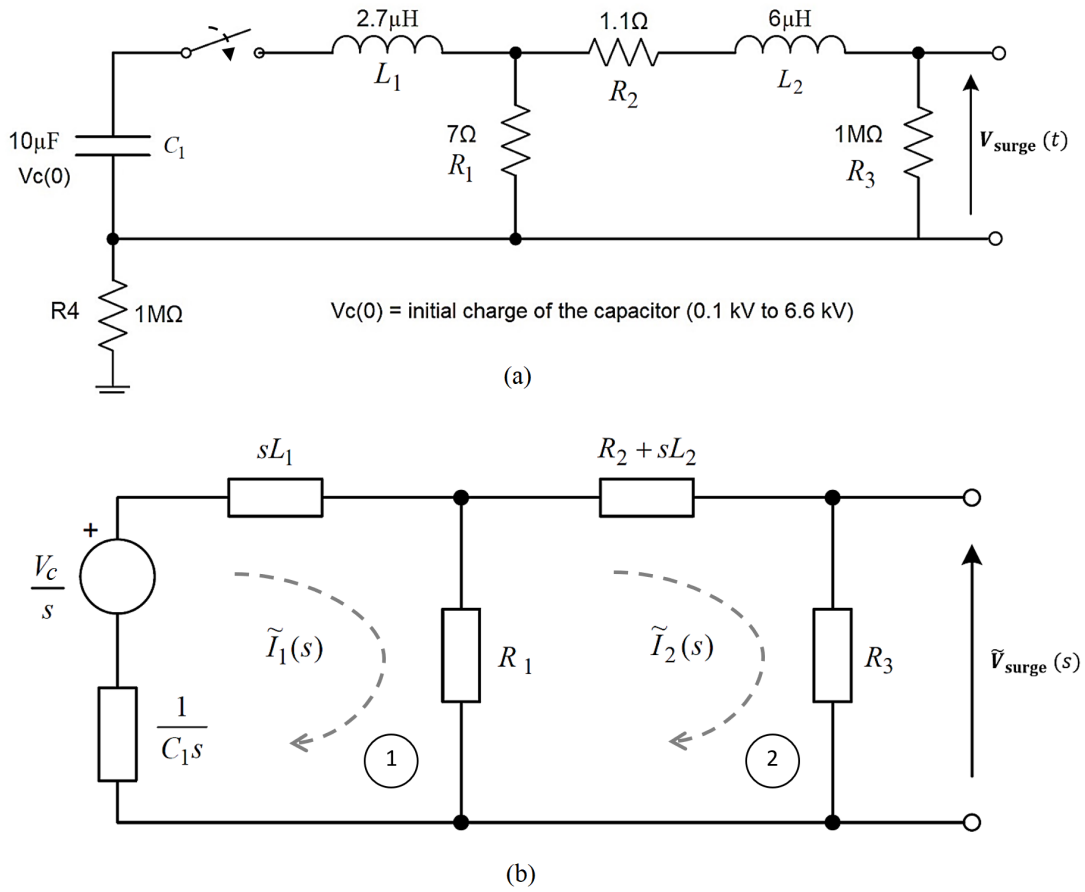

Figure 6.2: Internal generation circuit of lightning surge simulator (LSS-6230) in time and frequency domains: (a) equivalent circuit in time domain; (b) transformed circuit network in Laplace domain (S-domain)

$$\tilde{I}_1(s) = \frac{\tilde{I}_2(s)\left[R_T + sL_2\right]}{R_1} \tag{6.8}$$

Using Eq. (6.6) and Eq. (6.8), we can isolate $\tilde{I}_2(s)$ as below:

$$\tilde{I}_2(s) = \frac{C_1 R_1 V_c}{(sC_1R_1 + s^2L_1C_1 + 1)(R_T + sL_2) - sC_1{R_1}^2} \tag{6.9}$$

By simplifying and rearranging Eq. (6.9), it is possible to obtain a standard S-domain representation for $\tilde{I}_2(s)$ as:

$$\tilde{I}_2(s) = \frac{C_1 R_1 V_c}{s^3 L_1 L_2 C_1 + s^2(C_1L_2 + C_1L_1R_T) + s(C_1R_1R_T + L_2 - C_1{R_1}^2) + R_T} \tag{6.10}$$

Since LSS parameters are unique for the standard surge generation circuit, we can introduce new constant terms as K_0, K_1, K_2, K_3 and K_4:

$$K_4 = C_1 R_1 V_c$$
$$K_3 = L_1 L_2 C_1$$
$$K_2 = C_1 L_2 + C_1 L_1 R_T$$
$$K_1 = C_1 R_1 R_T + L_2 - C_1 {R_1}^2$$
$$K_0 = R_T$$

Using these constants, Eq. (6.10) can be further simplified into:

$$\tilde{I}_2(s) = \frac{K_4}{K_3 s^2 + K_2 s^2 + K_1 s + K_0} \tag{6.11}$$

When $L_1 = 2.7\mu\text{H}, L_2 = 6\mu\text{H}, C_1 = 10\mu\text{F}, R_1 = 7\Omega, R_2 = 1.1\Omega$ and $R_3 = 1\text{M}\Omega$, using MATLAB Symbolic Toolbox, we can obtain the inverse transform (`ilaplace`) of Eq. (6.11) to find the time-domain representation $I_2(t)$.

$$I_2(t) = K_4 \times \sum_{\beta} \frac{e^{\beta t}}{3K_3\beta^2 + 2K_2\beta + K_1} \tag{6.12}$$

where β = roots of the S-domain cubic function $K_3 s^2 + K_2 s^2 + K_1 s + K_0$ found in Eq. (6.11).

More information regarding MATLAB Symbolic Toolbox commands found in [114] is given in Appendix F. Knowing $I_2(t)$, we can determine the open-circuit surge voltage $V_{\text{surge}}(t)$ delivered by the LSS-6230 as per Figure 6.2 using $I_2(t) \times R_3$. For a 6 kV initial voltage ($V_c = 6$ kV) loaded to the LSS capacitor C_1, the standard output waveform $V_{\text{surge}}(t)$ delivered by the LSS is depicted by the Figure 6.3 with comparisons from Laplace method and experimental data.

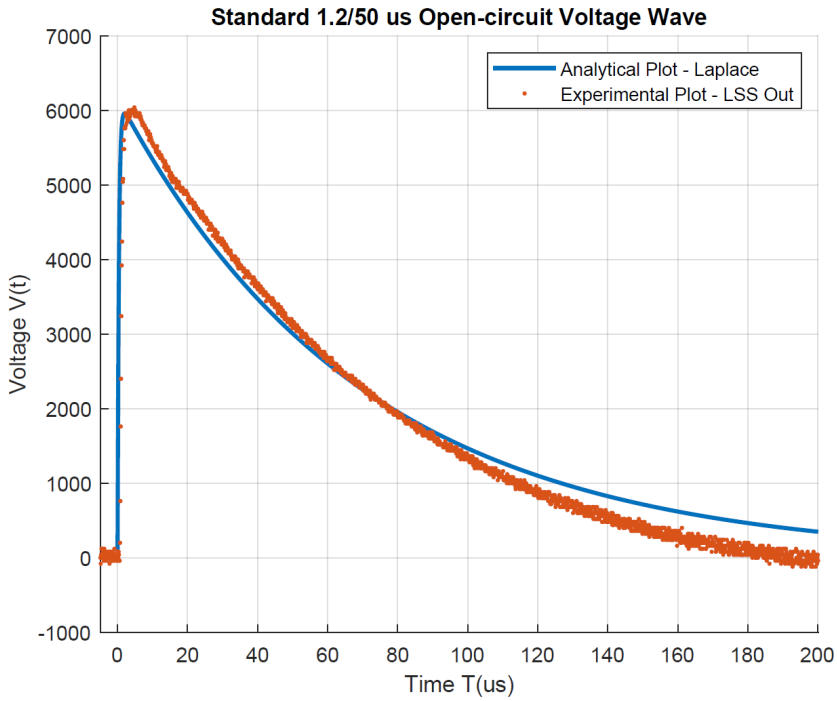

Figure 6.3: Comparison of 1.2/50 μs surge wave-shape using Laplace transform and LSS experimental data

In Chapter 2, we presented more comparisons for the standard wave-shape using LTSpice simulation plots and EUT (equipment under test) line plots to demonstrate the rapid variation of this 1.2/50 μs surge pulse. The analytical waveform given by the IEEE C62.41.2 standard and the Laplace solution we obtained in Eq. (6.12) can also be compared as shown by Figure 6.4. The LTSpice simulation plot for a 6 kV open-circuit wave is also drawn on the same graph of Figure 6.4.

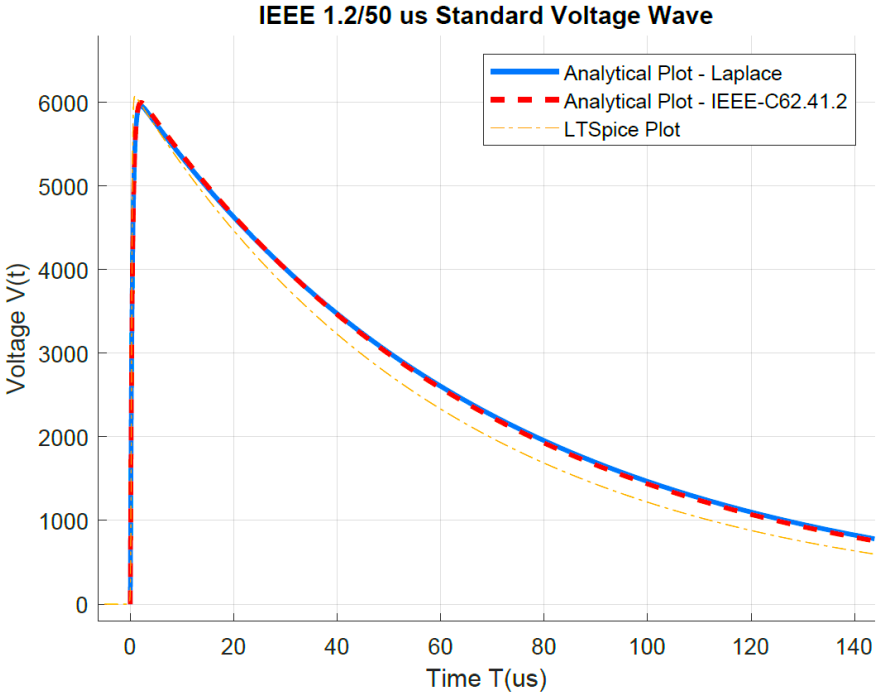

Figure 6.4: Comparison of 1.2/50 μs surge wave-shape using Laplace transforms, LTSpice simulation and IEEE C62.41.2 standard definition

According to Figure 6.4, it is observed that our Laplace solution and the IEEE definition are identical with extremely minor deviations. Also, LTSpice simulation shows a minimum discrepancy with respect to the two analytical plots. However, at higher voltage settings of LSS (beyond 3 kV), the simulation tends to deviate a bit specially for the falling half of the open-circuit waveform. But, for rising half of the wave, all three plots display a remarkable agreement without any deviation. The MATLAB commands used to import LTSpice data and plotting related codes are found in Appendix F. LTSpice circuit model used to generate the above simulation using Lightning Surge Simulator (LSS-6230) is illustrated by Figure 6.5. It must be noted that due to the μs order simulation of standard surge-wave created by LTSpice model, we selected a step size of 1 ns to obtain accurate data for our numerical analysis.

The combinational surge-generator circuit of LSS-6230 produces 1.2/50 μs voltage waveform only under open-circuit conditions. However, when SCASA device is connected to LSS as the EUT, the resulting equivalent circuit deviates from the open condition based on the impedance of SCASA device and LSS internal resistance. This transforms the combinational generator to inject a modified surge voltage (less than 6 kV) into SCASA system. In the next Section, we examine this phenomenon in detail and predict the actual output surge wave of the LSS in the presence of EUT coupled.

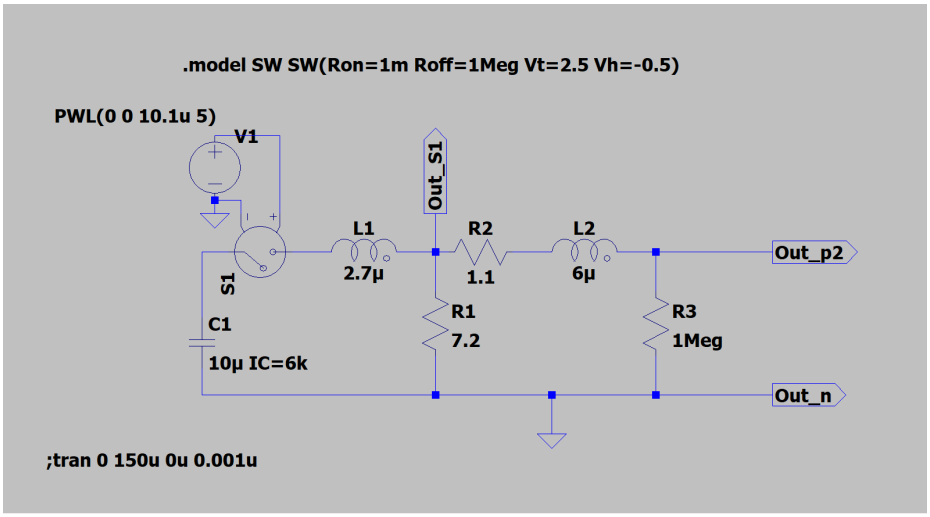

Figure 6.5: LTSpice circuit model for lightning surge simulator (LSS-6230)

6.3 Laplace Validation of SCASA Surge Propagation

6.3.1 Fitting a model for the LSS-6230 output surge waveform

The standard open-circuit surge waveform deviates from its actual peak voltage (6 kV) and original wave-shape due to impedance effects of the LSS (Z_{LSS}) and connection path (Z_{path}). As described in Chapter 2, $Z_{\text{LSS}} \approx 2\Omega$ and path resistance lies in milli-ohm order. Therefore, Z_{LSS} is a significant factor for consideration when modelling the LSS output surge waveform $V'_{surge}(t)$ in the presence of SCASA device as the EUT. According to the voltage division effect shown in Figure 6.6, it is clear that $V'_{surge}(t)$ injected to SCASA circuit is less than the actual open-circuit voltage $V_{surge}(t)$. Hence, we fitted a model to predict this alteration of surge waveform prior to the Laplace transform analysis. Based on the experimental output-wave of LSS illustrated by Figure 6.7, we can identify that the 6 kV peak voltage has dropped to ~4 kV while there is

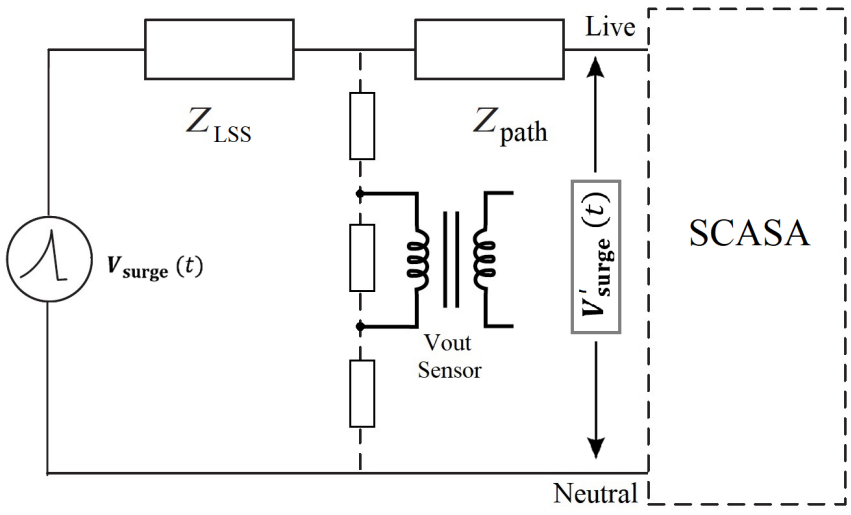

Figure 6.6: Effect of internal impedance of LSS-6230 on transient delivery to SCASA

rapid decaying in the falling edge of the waveform. Our fitted model depicted on the same plot is in good agreement with modified mathematical constants for the double-exponential equation as explained below.

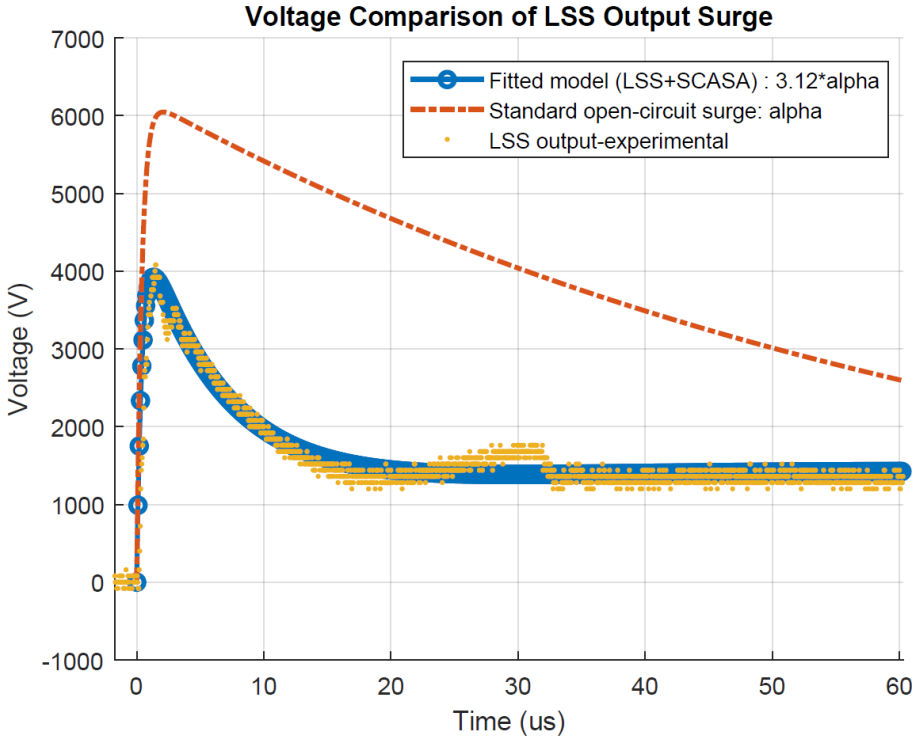

Figure 6.7: Comparison of standard open-circuit surge and LSS-6230 transient output to SCASA

According to the IEEE C62.41.2 standard definition of 1.2/50 μs open-circuit voltage wave,

$$V_{surge}(t) = A_V V_p (1 - e^{-t/\tau_1}) e^{-t/\tau_2} \tag{6.13}$$

where the constants are $A_V = 1.037\ (\mu s)^{-3}, \tau_1 = 0.4074\ \mu s, \tau_2 = 68.22\ \mu s$ and V_p is the peak voltage of the waveform. Introducing a new constant $N = A_V V_p$, and by rearranging Eq. (6.13),

$$V_{surge}(t) = N[e^{-t/\tau_2} - e^{-t(1/\tau_1 + 1/\tau_2)}] \tag{6.14}$$

By considering $1/\tau_2 = \alpha$ and $1/\tau_1 + 1/\tau_2 = \beta$, it is possible to express a simplified model for $V_{surge}(t)$ as:

$$V_{surge}(t) = N(e^{-\alpha t} - e^{-\beta t}) \tag{6.15}$$

In order to match for the experimental output of LSS, the fitted equation shown in Figure 6.7 must be in the form,

$$V'_{surge}(t) = N'(e^{-3.12\alpha t} - e^{-\beta t}) \tag{6.16}$$

where $N' = A_V V'_p$ which agrees well with the reduced voltage $V'_p = 4$ kV when SCASA is connected as the EUT to LSS output terminals. Moreover, in order to compensate for the rapid

decaying of output surge, we considered a high-α that 3.12 times greater than α in the original wave-shape. Standard and fitted surge models are compared with the experimental waveform in Figure 6.7.

To proceed further into the frequency domain analysis of SCASA circuit, let us consider the Laplace transform of this modified surge-wave $\tilde{V}'_{surge}(s)$ as,

$$\tilde{V}'_{surge}(s) = N' \left(\frac{1}{s-\alpha'} - \frac{1}{s-\beta} \right) \tag{6.17}$$

where $\alpha' = 3.12 \times \alpha$, and $N' = A_V V'_p$ with $\alpha = {}^{1}\!/_{68.22}\ \mu s^{-1}$, $\beta = {}^{1}\!/_{0.4074}\ \mu s^{-1} + {}^{1}\!/_{68.22}\ \mu s^{-1}$, $A_V = 1.037(\mu s)^{-3}$ and $V'_p = 4$ kV. Eq. (6.17) will be used in Section 6.3.3 for our analysis of SCASA circuit in $S-$domain. Next, we present a linearised varistor model for Var1 and Var2 (Figure 6.9) to simplify the highly non-linear behaviour of MOVs.

6.3.2 Linearised varistor model for SCASA Var1 and Var2

As Metal Oxide Varistors (MOVs) are highly non-linear devices with a dynamic resistance (R_{X}), we introduce a logarithmic relationship (Eq. (6.19)) to predict linearised states of Var1 and Var2 under transient propagation. According to the power-law discussed in Chapter 3, the voltage–current relationship is given by,

$$I = kV^{\gamma} \tag{6.18}$$

where the constants k and α are varistor dependent unique parameters: k is dependent on the device geometry and the exponent α defines the degree of non-linearity [96]. For a 275 V (V20E275-Littlefuse) varistor, $k = 4.6 \times 10^{-74}$ and $\gamma = 25.8 \pm 5\%$ [55, 96]. Even though the $V-I$ characteristic takes above form, there is a remarkable straight-line relationship specified by industry manufacturers in which non-linear resistance R_{X} can be expressed as a linear function of current in its logarithmic form $\log(I)$ as [54]:

$$R_X = A + 10^{B+C\ \log(I)} \tag{6.19}$$

where the constant A=0.035 Ω and B, C are unitless quantities with 2.8 and -0.95 respectively [54]. This is an empirical formula based on the magnitudes of current/non-linear resistance (without the consideration of physical units); more information extracted form industry data-sheets is found in Appendix D. However, considering dimensional consistency, we divide I by 1 A and multiply the second term of Eq. (6.19) by 1 Ω. Eq. (6.19) predicts linearised states of the varistor essential for our analytical work using Laplace Transform method. Figure 6.8 illustrates different ON and OFF states of the 275 V Littlefuse varistor used in SCASA circuit. According to Figure 6.8, when:

$$I = 1\ \ \mathrm{mA} \rightarrow R_{\mathrm{X}} = 0.4\,\mathrm{M}\Omega$$

$$I = 30\ \ \mathrm{A} \rightarrow R_{\mathrm{X}} = 20\,\Omega$$

$$I = 300\ \ \mathrm{A} \rightarrow R_{\mathrm{X}} = 3\,\Omega$$

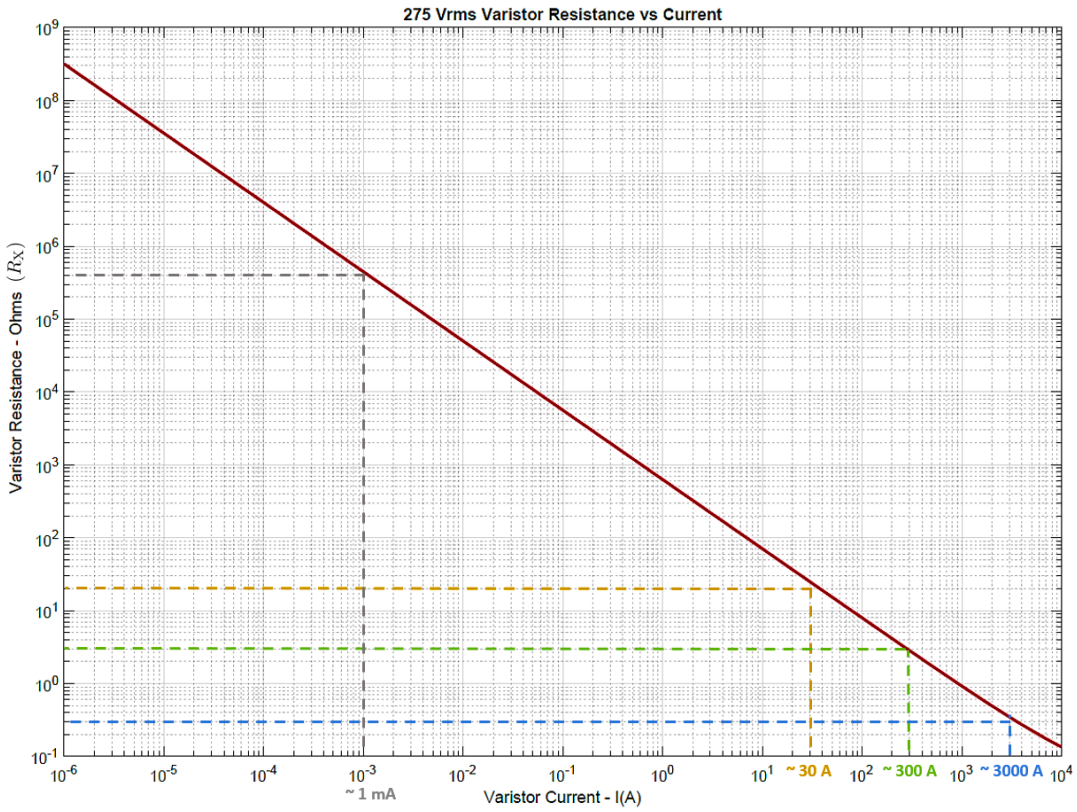

Figure 6.8: Variation of 275 V (V20E275-Littlefuse) varistor resistance with current (logarithmic scale)

$$I = 3000 \text{ A} \rightarrow R_{\text{X}} = 0.3\,\Omega$$

The calculated values for R_{X} based on Eq. (6.19) verifies how the MOV shifts from MΩ order open-circuit condition to a highly conduction mode (Figure 6.8) with few milli-ohms order ON resistance (R_{ON}). Notably, we can identify $R_{\text{X}} = R_{\text{ON}} \sim 0.3\ \Omega$ for a standard 3 kA transient current generated by the Lightning Surge Simulator. These linearised states of R_{X} are essential for the frequency domain analysis of SCASA surge protector, detailed analytical solutions are presented next.

6.3.3 Frequency domain analysis of Laplace transformed SCASA circuit

In Chapter 4, we presented a permeance based equivalent circuit model for the SCASA transformer core. The significance of leakage flux associated with primary and secondary windings was indicated by means of leakage inductances l_1 and l_2. The magnetizing inductances L_1 and L_2 depicted in Figure 6.9 corresponds to the magnetic coupling between the two coils (More information given in Chapter 4). Furthermore, in Section 4.3.4, we proved that the SC sub-circuit current is $\sim$ 300 A for a 6 kV/3 kA combinational transient wave. Under these circumstances, the current through SC loop is fairly insignificant ($\sim$ 10 %) compared to the 3 kA transient; thus, we ignored the SC sub-circuit for the convenience of Laplace Transform based analysis. Figure 6.9 illustrates the time-domain and frequency-domain (S-domain) equivalent circuit models of SCASA topology without the sub-circuit. The transformed network represented by Figure 6.9(b) is subjected to the normalized output surge waveform $\tilde{V}'_{surge}(s)$ in Laplace-domain

as discussed above. Accordingly, the fitted model (Eq. (6.17)) for LSS output in the presence of SCASA unit is considered for our analysis.

By Applying Kirchhoff's voltage law (KVL) for the first loop of transformed SCASA circuit shown by Figure 6.9(b):

$$\tilde{V}'_{surge}(s) = \tilde{i_1}(s)\big[sL_1 + sl_1\big] + \tilde{i_1}(s).R_{\text{ON}} \tag{6.20}$$

Similarly, we can apply KVL for the second loop in Figure 6.9(b);

$$\tilde{V}'_{surge}(s) = \tilde{i_2}(s)\big[sL_2 + sl_2\big] + \tilde{i_2}(s).R_{\text{ON}} \tag{6.21}$$

Here, we have assumed the load transient current $i_{load}(t)$ (thus $\tilde{i}_{load}(s)$) is negligible due to the fact that it has a relatively high internal resistance (R_{LOAD}) compared to the on-resistance (R_{ON}) of Var2. In Chapter 7, we calculate $R_{\text{LOAD}} \sim 26\,\Omega$ for a 2 kW load powdered from AC

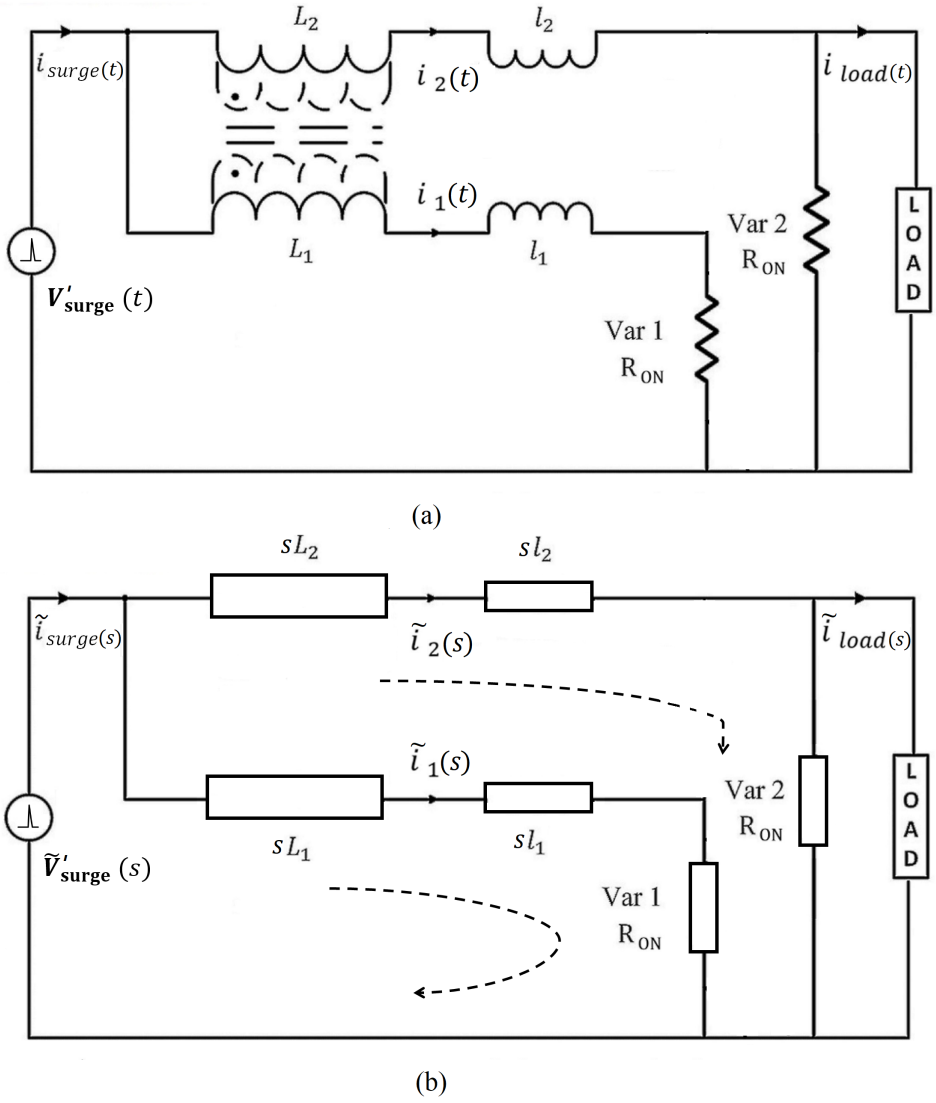

Figure 6.9: Equivalent circuits of SCASA topology without the sub-circuit: (a) time-domain circuit; (b) frequency-domain (S-domain) circuit

mains. Since $R_{\mathrm{ON}} \sim 0.3\,\Omega$ as per the linearised varistor model (V20E275-Littlefuse) discussed in the previous Section, we can assume all secondary coil current $i_2(t)$ (thus $\tilde{i}_2(s)$) flows into Var2.

Isolating $\tilde{i}_1(s)$ from Eq. (6.20),

$$\tilde{i_1}(s) = \frac{\tilde{V}'_{surge}(s)}{\left[sL_p + R_{\mathrm{ON}}\right]} \tag{6.22}$$

where self-inductance of primary coil $L_p = L_1 + l_1$ according to the permeance based circuit model described in Chapter 4. By substituting the fitted analytical model (Eq. (6.17)) $\tilde{V}'_{surge}(s)$ for LSS output waveform when SCASA functions as the EUT,

$$\tilde{i_1}(s) = N' \left[\frac{1}{(s-\alpha')(sL_p + R_{\mathrm{ON}})} - \frac{1}{(s-\beta)(sL_p + R_{\mathrm{ON}})}\right] \tag{6.23}$$

Rearranging Eq. (6.23):

$$\tilde{i_1}(s) = \frac{N'}{L_p}\left[\frac{1}{(s-\alpha')(s + \frac{R_{\mathrm{ON}}}{L_p})} - \frac{1}{(s-\beta)(s + \frac{R_{\mathrm{ON}}}{L_p})}\right] \tag{6.24}$$

To proceed further to find the inverse Laplace transform, we introduce a new constant term $B = {}^{R_{\mathrm{ON}}}/_{L_p}$. Then, Eq. (6.24) simplifies into:

$$\tilde{i_1}(s) = \frac{N'}{L_p}\left[\frac{1}{(s-\alpha')(s+B)} - \frac{1}{(s-\beta)(s+B)}\right] \tag{6.25}$$

Using standard Laplace transform table (found in Appendix H), taking the inverse transform of Eq. (6.25), the time-domain representation of primary current $i_1(t)$ can be obtained as,

$$i_1(t) = \frac{N'}{L_p}\left[\frac{1}{K_1}\left(e^{\alpha' t} - e^{-Bt}\right) - \frac{1}{K_2}\left(e^{-\beta t} - e^{-Bt}\right)\right] \tag{6.26}$$

where $K_1 = B + \alpha'$ and $K_2 = B + \beta$. Eq. (6.26) gives an important prediction about the transient current propagation through the primary winding of SCASA transformer. When $N' = 4,148\,V$, $\alpha' = 3.12 \times \alpha = {}^{3.12}/_{68.22}\,\mu s^{-1}$, $\beta = {}^{1}/_{0.4074}\,\mu s^{-1} + {}^{1}/_{68.22}\,\mu s^{-1}$, $L_p = 3.6\,\mu$H, $B = 0.126\,\mu s^{-1}$, $K_1 = 0.172\,\mu s^{-1}$ and $K_2 = 2.6\,\mu s^{-1}$, the variation of $i_1(t)$ can be plotted using MATLAB as shown in Figure 6.10.

Furthermore, we can isolate $\tilde{i}_2(s)$ from Eq. (6.21),

$$\tilde{i_2}(s) = \frac{\tilde{V}'_{surge}(s)}{\left[sL_s + R_{\mathrm{ON}}\right]} \tag{6.27}$$

where self-inductance of primary coil $L_s = L_2 + l_2$ according to the permeance based circuit model described in Chapter 4. By substituting the fitted analytical model (Eq. (6.17)) $\tilde{V}'_{surge}(s)$ for LSS output waveform when SCASA functions as the EUT,

$$\tilde{i_2}(s) = N' \left[\frac{1}{(s-\alpha')(sL_s + R_{\mathrm{ON}})} - \frac{1}{(s-\beta)(sL_s + R_{\mathrm{ON}})}\right] \tag{6.28}$$

Rearranging Eq. (6.28):

$$\tilde{i_2}(s) = \frac{N'}{L_s}\left[\frac{1}{(s-\alpha')(s+\frac{R_{\text{ON}}}{L_s})} - \frac{1}{(s-\beta)(s+\frac{R_{\text{ON}}}{L_s})}\right] \tag{6.29}$$

To proceed further to find the inverse Laplace transform, we introduce a new constant term $D = {}^{R_{\text{ON}}}/_{L_s}$. Then, Eq. (6.29) simplifies into:

$$\tilde{i_2}(s) = \frac{N'}{L_s}\left[\frac{1}{(s-\alpha')(s+D)} - \frac{1}{(s-\beta)(s+D)}\right] \tag{6.30}$$

Using standard Laplace transform table (found in Appendix H), taking the inverse transform of Eq. (6.30), the time-domain representation of secondary current $i_2(t)$ can be obtained as,

$$i_2(t) = \frac{N'}{L_s}\left[\frac{1}{K_3}\left(e^{\alpha' t} - e^{-Dt}\right) - \frac{1}{K_4}\left(e^{-\beta t} - e^{-Dt}\right)\right] \tag{6.31}$$

where $K_3 = D + \alpha'$ and $K_4 = D + \beta$. Eq. (6.31) gives an important prediction about the transient current propagation through the secondary winding of SCASA transformer. When $N' = 4,148\ V$, $\alpha' = 3.12 \times \alpha = {}^{3.12}/_{68.22}\ \mu s^{-1}$, $\beta = {}^{1}/_{0.4074}\ \mu s^{-1} + {}^{1}/_{68.22}\ \mu s^{-1}, L_s = 60\ \mu$H, $D = 0.05\ \mu s^{-1}$, $K_3 = 0.0672\ \mu s^{-1}$ and $K_4 = 2.5\ \mu s^{-1}$, the variation of $i_2(t)$ can be plotted using MATLAB as shown in Figure 6.10.

In addition to the analytical solutions derived above, transient currents in both primary and secondary coils $i_1(t)$ and $i_2(t)$ were numerically validated using LTSpice circuit simulation. These simulated waveforms are also plotted on the same graph (Figure 6.10) to compare with Laplace solutions. A discussion about surge current division among SCASA coupled coils is presented next.

6.3.4 Validation of surge current propagation through SCASA coupled-inductor

Notably, the transient current distribution between the two coupled windings of SCASA transformer show a considerable deviation from the AC steady state. Compared to 95%:5% (secondary:primary) RMS current division in AC mode, the transient propagation indicates a remarkable distinction with approximately 10%:90% ratio between secondary and primary peak currents. Contrasting to 50 Hz RMS condition, high frequency transients (Figure 6.1) generate greater impedances in transformer windings. Thus, the more inductive secondary coil ($L_s = 60\ \mu$H), having more turns, produces significantly greater impedance than the less inductive primary ($L_p = 3.4\ \mu$H). This effect results in ∼92% (∼2.86 kA) of total surge current passing through the primary, whereas only ∼8% (∼240 A) through the secondary. Figure 6.10 depicts how transient currents are shared among the two coupled-inductor coils using Laplace solutions and LTSpice simulated waveforms.

In Chapter 4, we presented an experimental validation by placing high-power resistor blocks (0.21 Ω) in series with primary and secondary (Figure 4.10). However, with the insertion of such resistor blocks (though small-sized), our measurement system yielded deviated results compared to analytical and simulated waveforms shown in Figure 6.10. This discrepancy in test results is

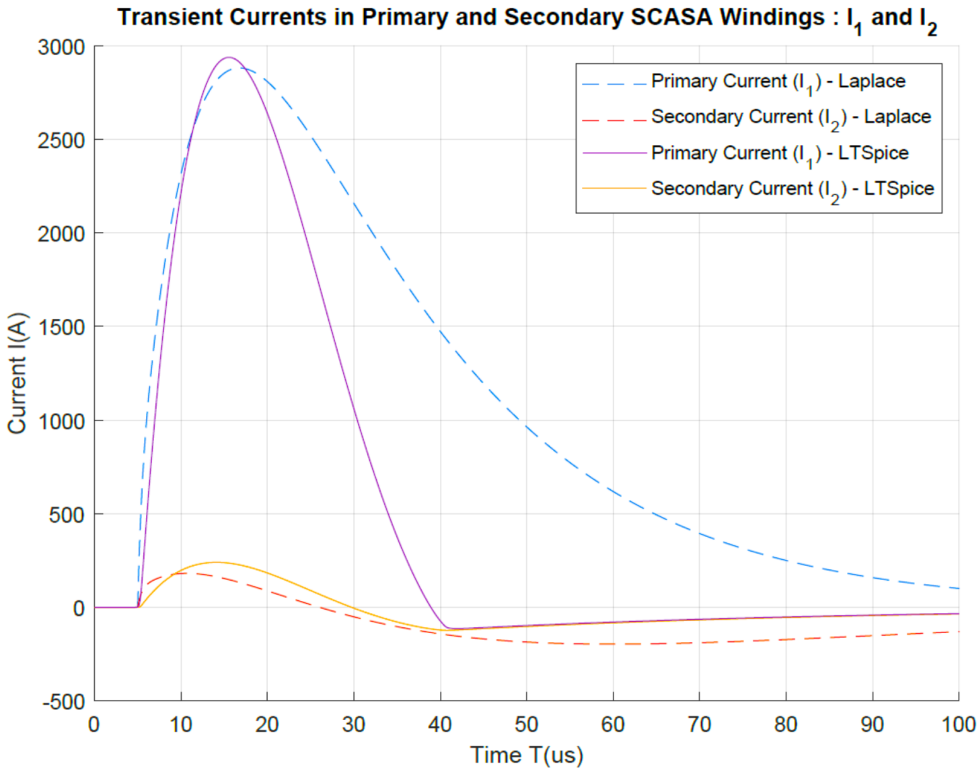

Figure 6.10: Variation of primary and secondary transient currents in SCASA transformer for a 6 kV/3 kA combinational surge

due to the impedance effects of two resistor blocks placed in-line with SCASA transformer windings. It was experimentally challenging (due to high magnitudes and kHz order frequencies) to capture rapidly varying transient currents due to the availability of test-gear facilities. But, we verified Laplace transform based predictions using numerical simulations, and these were in agreement as per the peak current values though a mismatch in wave-shape is seen for primary coil current during the falling edge. This mismatch is due to the non-linearity of Var1 (connected to the primary coil) which was assumed to be at a linear ON-state of $0.3\ \Omega$. Since at the falling edge of primary current Var1 is undergoing a highly non-linear transition from conductive ON-state to OFF-state with its resistance increasing according to a logarithmic fashion, the analytical solution deviates during the falling half primary current. However, considering the mathematical complexity of varistor behaviour, our main aim from the Laplace analysis was to validate peak current division in SCASA coupled inductor. LTSpice circuit model used for numerical validation is found in Appendix G. In the next section, clamping voltage level of two SCASA varistors is explained.

6.3.5 Clamping voltage comparison: Var1 and Var2

With the introduction of SCASA technique in Chapter 3, we explained that the two metal oxide varistors (MOVs) Var1 and Var2 exhibit different clamping levels. Notably, Var1 connected to the primary coil of SCASA transformer (Figure 6.9) demonstrated a comparatively high-clamping voltage (904 V) during 6 kV/3 kA combinational surge tests. But, Var2 connected to the secondary winding showed a relatively lower clamping with 696 V. Figure 6.11(b) illustrates

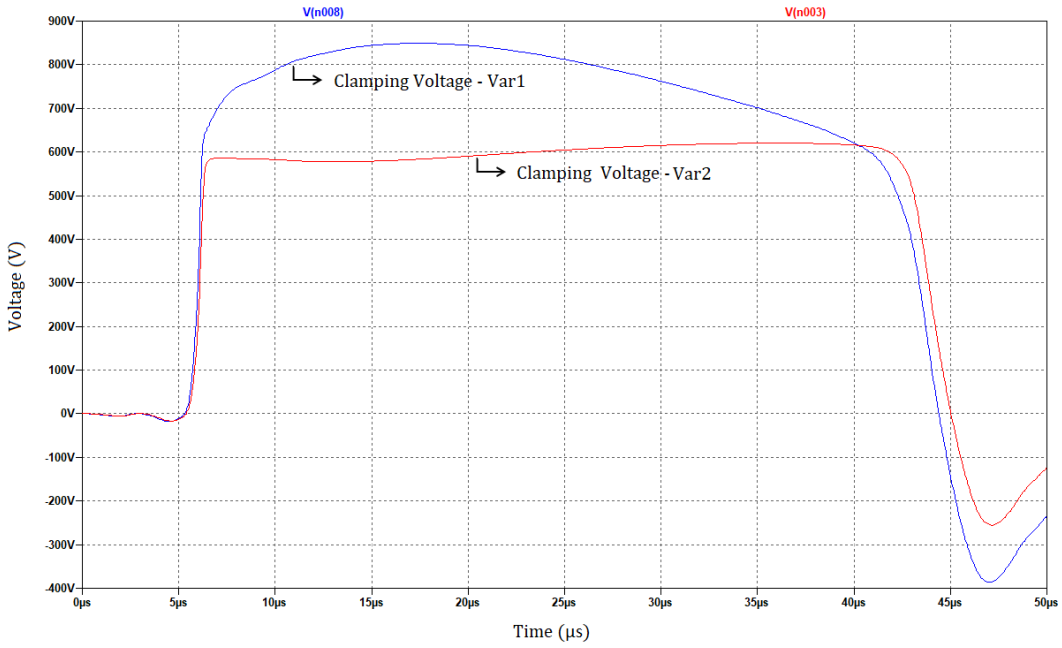

(a)

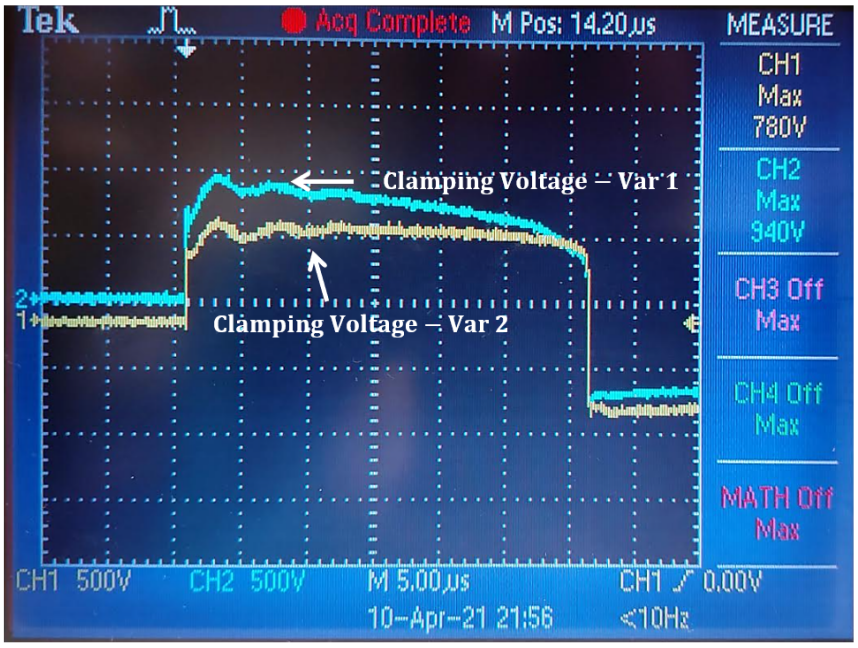

(b)

Figure 6.11: Comparison of clamping voltage of Var1 and Var2 of SCASA for a 6 kV/3 kA combinational surge: (a) LTSpice simulation; (b) experimental waveforms

oscilloscope waveforms for Var1 and Var2 that are captured without superimposing the surge on AC mains. This voltage discrepancy is expected with the high-magnitude transient current flowing (∼2.86 kA) towards the primary coil than the more inductive secondary which carries ∼240 A (Figure 6.10). To justify the experimental observation, we present LTSpice simulation waveforms for both MOVs in Figure 6.11(a). LTSpice netlist-codes used in our simulation for Littlefuse Ultra-MOV series is given in Appendix D. Moreover, permeance based LTSpice circuit

model used for the verification is found in Appendix G. Test and simulated wave-shapes were in good agreement with a minimum discrepancy; however, the peak voltages of Var1 and 2 slightly varied within the 10 % tolerance limit. As the following comparison shown by Figure 6.11 is carried out without the superimposition of 230 V RMS, under normal power conditions, both SCASA varistors indicate much higher clamping voltages. To address this limitation, we conducted new design improvements using high-performance magnetic core assortments to optimize the clamping level. More information is given in Chapter 7. In the next section, surge energy distribution in inductive, capacitive and resistive elements of SCASA circuit is investigated in detail.

6.4 Estimation of Surge Energy Distribution in SCASA Circuit Components

6.4.1 Energy absorbed by the magnetic core

As described previously in Chapter 4, SCASA magnetic core comprises of two coupled-windings wound to a powdered-iron toroid. Therefore, the core absorbs and stores surge in the form of inductive energy. Primary and secondary coils posses self-inductances in micro-henry order ; however, as both coils share high-magnitude surge currents, energy absorption becomes significant. In the following description, we quantify the peak energies stored in the two coils.

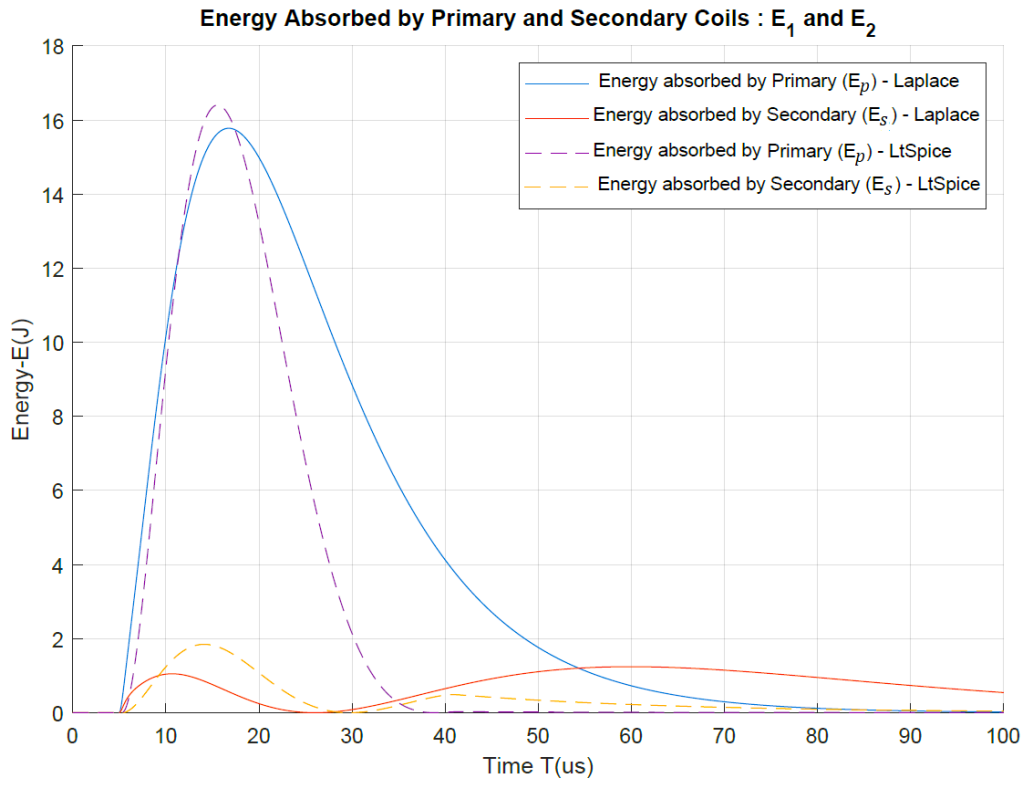

Figure 6.12: Variation of transient energy absorbed by primary and secondary windings of SCASA transformer (under a 6 kV/3 kA combinational surge)

The peak energy stored in the primary coil of self-inductance $L_p = 3.4$ μH carrying a surge current of $i_1 \sim 2.86$ kA,

$$E_p = \frac{1}{2} L_p i_1^2 \tag{6.32}$$

$$E_p = \frac{3.4 \times 10^{-6} \times 2860^2}{2} \approx 16 \text{ J}$$

Similarly, the peak energy stored in the secondary coil of self-inductance $L_s = 60$ μH carrying a surge current of $i_2 \sim 240$ A,

$$E_s = \frac{1}{2} L_s i_2^2 \tag{6.33}$$

$$E_s = \frac{60 \times 10^{-6} \times 240^2}{2} \approx 2 \text{ J}$$

Given the above calculation for the peak energies, it is clear that the total surge energy absorbed by the SCASA magnetic core is ∼18 J ($E_p + E_s$). For a standard 6 kV/3 kA surge which delivers a total energy E_T ∼81 J [19, 40], the percentage of inductive absorption is ∼22 %. It is highly important that during the transient propagation, the Kool μu powdered-iron core does not reach magnetic saturation. We evaluate surge related flux for the Kool μu toroid in Chapter 7, and compares with other core types with better magnetic saturation. Apart from the core absorption, the SCASA circuit dissipates most of the surge energy in two varistors Var1 and Var2. In the next Section, varistor energy dissipation is discussed.

6.4.2 Energy dissipation in SCASA varistors

In Section 6.3.3, it was theoretically proven that the transient currents get divided between primary and secondary windings of SCASA core (Figure 6.9) based on the inductive impedance of two coils. As per Eqs 6.26 and 6.31, the less inductive primary shared ∼92% of total surge current, whereas secondary shared ∼8% (Figure 6.10). Corresponding to this current division, even the heat dissipation by Var1 and Var2 (connected to primary and secondary respectively) show a contrasting difference as most of the surge getting dissipated via Var1. Figure 6.13 depicts the power and energy dissipations across Var1 and Var2 over a 100 µs period under a 6 kV/3 kA transient. According to Figure 6.13(a), Var1 indicates a peak power of ∼2.3 MW, whereas Var2 shows ∼0.1 MW of peak dissipation. However, to get a better understanding, we plotted energy dissipation in Figure 6.13(b). Both power and energy variations shown below were obtained using LTSpice simulation waveforms; details about the simulated circuit models is given in Appendix G. Notably, ∼40 J of peak surge energy is getting lost via Var1 as heat; this is in comparison 20 times greater than the ∼2 J peak dissipation of Var2. Compared to a standard 6 kV/3 kA surge which delivers a total energy E_T ∼81 J, Var1 alone eliminates ∼49% of E_T by sharing the greatest transient stress than all other SCASA circuit components. Conversely, the ∼2 J surge dissipation of Var2 is only ∼2.5% of E_T, meaning that it is not likely to fail under repeated surge pulses and provides reliable protection to the load device.

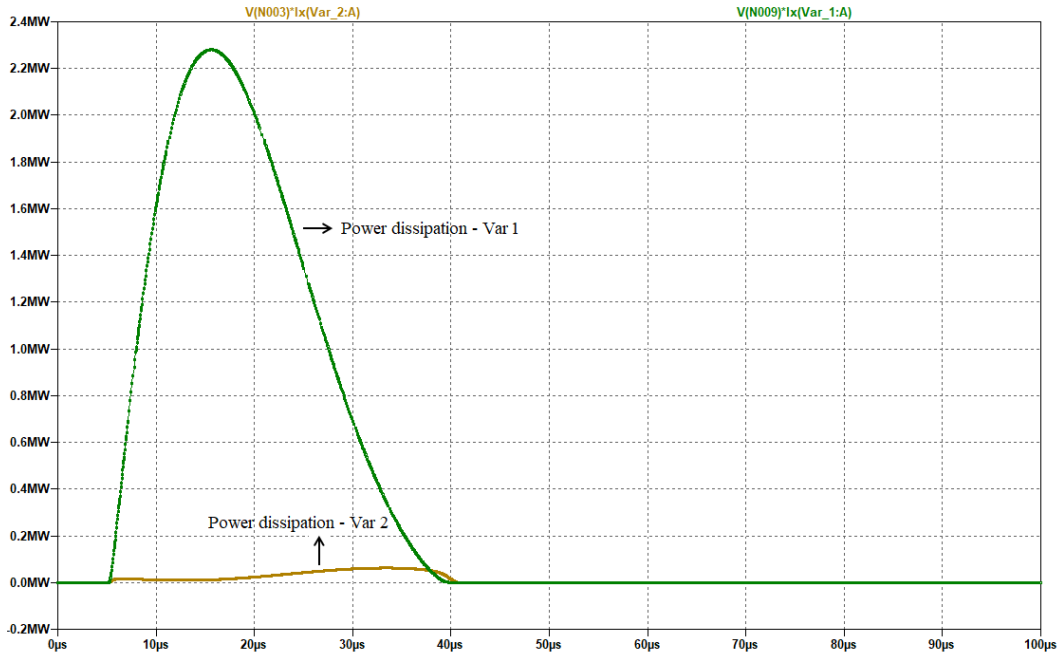

(a)

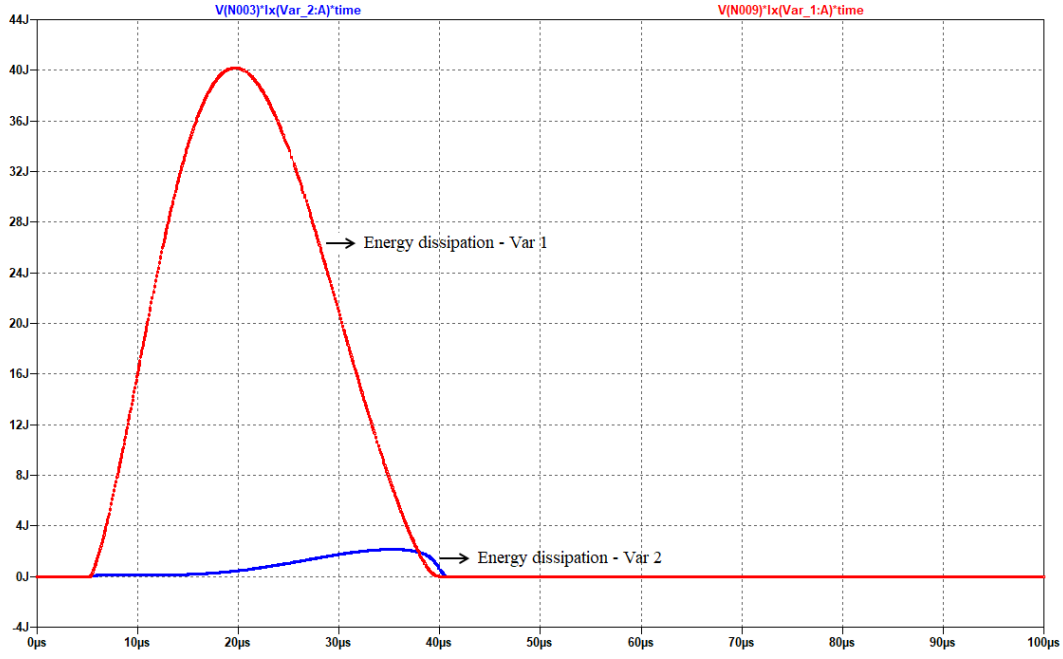

(b)

Figure 6.13: Comparison of heat dissipation by Var1 and Var2 of SCASA for a 6 kV/3 kA combinational surge: (a) power variation; (b) energy dissipation

Both resistive elements (R_{ON}) of two varistors facilitate the surge energy dissipation as explained above, and cool down immediately to recover back to its mega-ohm level open-condition prior to the propagation of next surge. In UL-1449 3rd edition testing, we specified these time intervals between repetitive surges as either 1 minute or 30 minutes (More information is found in Chapter 5). However, with the heat dissipation after each surge pulse internal degradation of zinc oxide granular layers (inside MOV) occur resulting a reduction in MOV life-time. Apart from finding the peak energy dissipation as described above, to understand the average heat

stress of two varistors, we evaluated the following integrals.

The average surge energy dissipation E_1 across Var1 is given by,

$$E_1 = \frac{1}{T}\int_0^T i_1(t)^2 R_{\text{ON}}\, dt \tag{6.34}$$

where $T = 40\ \mu$s, $R_{\text{ON}} \sim 0.3\ \Omega$, and $i_1(t)$ is the primary coil surge current as found using Laplace transforms in Eq. (6.26). Using MATLAB based calculations, we can evaluate the above integral as,

$$E_1 \approx 18\ \text{J}$$

Similary, the average surge energy dissipation E_2 across Var2 is given by,

$$E_2 = \frac{1}{T}\int_0^T i_2(t)^2 R_{\text{ON}}\, dt \tag{6.35}$$

where $i_2(t)$ is the secondary coil surge current as found using Laplace transforms in Eq. (6.31). Using MATLAB based calculations, we can evaluate the above integral as,

$$E_2 \approx 0.8\ \text{J}$$

According to above calculations, it is clear that even for a ∼40 J peak dissipation, Var1 showed a ∼18 J average energy. Conversely, Var2 resulted an average of ∼0.8 J for its maximum ∼2 J dissipation. This proves how both varistors have a reduced heat stress as the transient currents propagate rapidly within few microseconds. However, it must be noted that thermal degradation occurs in MOVs due to repetitive surge pulses can lead to failure in the longer run. More information about MOV degradation can be found in [52,115]. Next, we aim at estimating the energy distribution in supercapacitor (SC) sub-circuit of SCASA circuit.

6.4.3 Energy dissipated by the SC sub-circuit

The SC sub-circuit in the original SCASA design is placed between the primary and secondary coils of coupled-inductor. As described previously in Chapter 3 (Figure 3.11), the sub-circuit consists of a 1 Ω high-power resistor and a 5 F supercapacitor. Due to the milli-ohm order ESR [75] of SC, most surge dissipation within the sub-circuit happen through the 1 Ω resistor. Figure 6.14 illustrates how heat dissipation varies across 1 Ω during the transient propagation. As per this LTSpice simulation, we can identify the maximum energy loss as ∼1.3 J which is then followed by a secondary peak of ∼0.6 J. Compared to the peak transient energy E_T ∼81 J, the loss in 1 Ω high-power resistor is relatively insignificant with ∼1.6%. This is further justified by our experimental results described in Section 4.3.4; due to the 300 A reduced surge current through sub-circuit loop, even the heat loss is considerably lower. However, the importance of SC sub-circuit as an electromagnetic interference (EMI) filter is described in [66]. Furthermore, in Chapters 3 and 4, we explained how useful the sub-circuit was in placing a supercapacitor between coupled-inductor coils without exceeding its rated voltage under AC mode. Next, we present a summary of energy distribution for main circuit components in SCASA design.

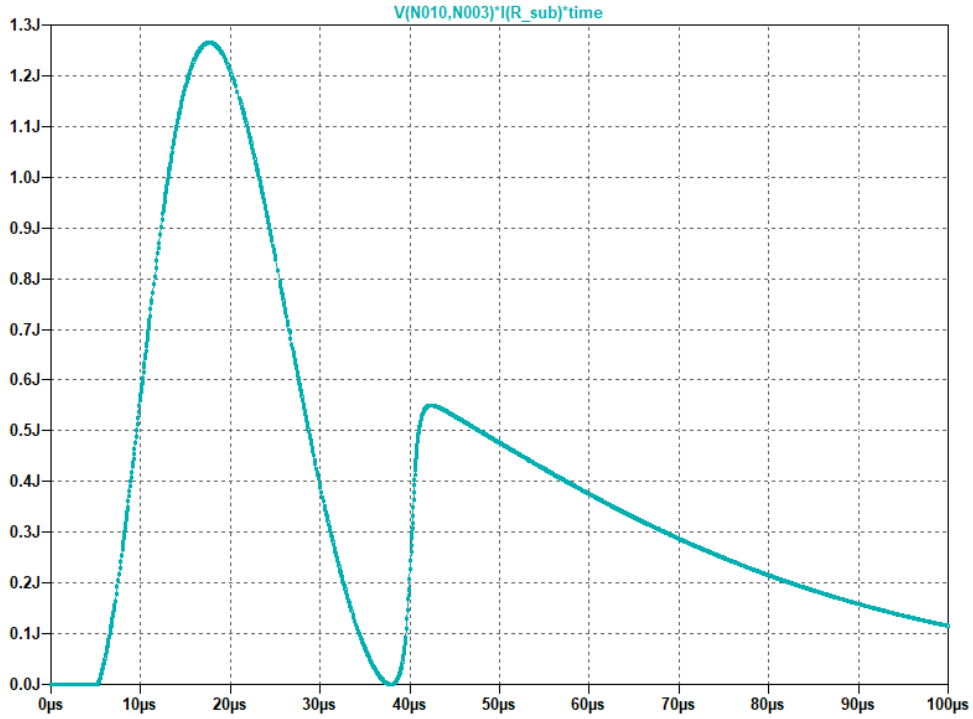

Figure 6.14: Heat dissipation across high-power resistor in SCASA sub-circuit for a 6 kV/3 kA combinational surge

6.4.4 Comparison of surge energy distribution in SCASA

Given the detailed energy estimation for various inductive and resistive elements in SCASA circuit, in this Section, we present a comparison of surge energy distribution using a percentage analysis. Here, it is considered that the peak energy of the standard 1.2/50 µs, 6 kV/3 kA combinational surge is ∼81 J [40]. Table 6.1 demonstrates transient absorption/dissipation associated with the magnetic core, metal oxide varistors and the high-power resistor of SCASA topology. The coupled-inductor core comprises of primary and secondary windings store ∼16 J and ∼2 J in the respective inductive coils, and this can be approximated as 20% and 2.5% respectively with regard to the total surge energy input. Notably, Var1 connected to the primary shows the highest power dissipation with ∼40 J which is ∼49% of the total transient energy. Conversely, Var2 which carries a lower current than Var1 dissipates only 2 J, meaning that Var2 gets lowest voltage stress protecting the load device without failure. Furthermore, as described in the previous section, 1 Ω high-power resistor in the SC sub-circuit yields ∼1.6% of the surge loss assisting supercapacitor to function as an EMI filter (more details about EMI filtering is given in [13, 66]). Interestingly, rest of the transient energy is wasted in path resistance of connecting wires and leads. We measured the total path resistance (R_{path}) as ∼0.2 Ω, and when the 3 kA peak surge current flow through the connecting wires, it dissipates nearly 18 J as heat (Table 6.1). A simplified calculation is shown below.

When the transient current (i_{surge}) peak of 3 kA occurs at t ∼10 µs,

$$E_{path} = i_{surge}^2 \times R_{path} \times t \tag{6.36}$$

$$E_{path} = 3000^2 \times 0.2 \times 10 \times 10^{-6} \approx 18 \text{ J}$$

This ∼18 J is an effective surge loss that reduces the voltage stress on surge protector under operation. As a percentage wise, the path dissipation accounts for ∼22% of the total surge energy, and proves to be significant factor even for the small ∼0.2 Ω resistance. Overall, it is clear that our total energy estimation for various inductive and resistive circuit elements in SCASA is highly comparable with the ∼81 J of 6 kV/3 kA combinational surge.

Table 6.1: Comparison of peak surge energy distribution in SCASA components for a 6 kV/3 kA combinational surge

Estimated energy component	Transient energy absorption/dissipation	Percentage of estimated energy
Primary coil: E_p	∼16 J	20%
Secondary coil: E_s	∼2 J	2.5%
Varistor 1: E_1	∼40 J	49%
Varistor 2: E_2	∼2 J	2.5%
1 Ω High-power resistor: E_R	∼1.3 J	1.6%
Path resistance: E_{path}	∼18 J	∼22%

6.5 Chapter Summary

In this chapter, we validated the surge current propagation through SCASA transformer windings using the Laplace transform method and LTSpice simulations. Based on the non-ideal circuit model of SCASA discussed in Chapter 4, theoretical predictions were formulated in the frequency domain considering the complex nature of transients. In addition, an estimation of surge energy distributed among various inductive and resistive elements of SCASA circuit was carried out using a percentage analysis.

In the next chapter, we present circuit modifications made to the original SCASA topology to enhance its surge absorption capacity. Furthermore, new design optimizations based on commercially available powdered-iron and low-cost gapped core configurations will be discussed.

Chapter 7

Circuit Modifications and Design Optimizations of SCASA Technique

Given the permeance based theoretical model and the applicability of air-gapped cores in SCASA design, in this Chapter, we present experiments conducted using commercial magnetic assortments provided by Magnetics Inc., USA. In predicting the optimum core material and shape within the commercial price constraints, our selections were based on permeance coefficients Λ_m (also known as inductance factor-A_{L}) of Kool μu, High Flux, X Flux and air-gapped EC core types. First, we present the topological modifications made to SCASA circuit with the existing Kool μu powdered-iron core.

7.1 Topological Changes to SCASA Design

7.1.1 Addition of a third coil to the magnetic core

In Chapter 5, we described the importance of storing and leaking transient related magnetic flux to improve surge endurance of the SCASA surge protector. Thus, to enhance flux storage, we first experimented with adding a third coil to the toroidal core of SCASA design. Figure 7.1

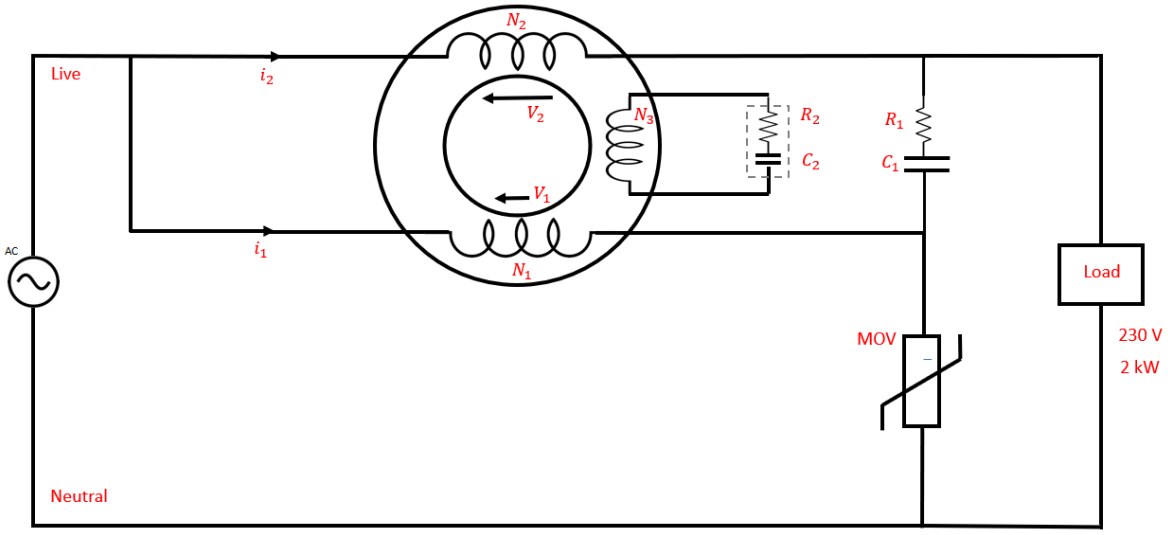

Figure 7.1: Topological change made to SCASA circuit with the addition of a third winding

depicts the topological change made to the base circuit with another supercapacitor (SC) sub-circuit (C_2 and R_2) connected to the third coil wound at N_3 turns. The key idea here is to absorb part of the surge flux flowing through the toroidal core (Figure 4.1) as the SCASA non-ideal transformer becomes active under transient mode. The second SC sub-circuit (R_2 and C_2) coupled to the third winding facilitates the dissipation of that absorbed flux in terms of heat. Under 230 V AC operation, when the varistor (MOV) is not fired, the primary coil (N_1 turns) current i_1 is negligible. Therefore, AC power flow to the load side primarily happens through the secondary coil which has N_2 turns. More details about AC operation is found in Chapter 4. Prior to transient based experiments with this new topology, we first investigated the impact of third winding towards AC power flow due to reflected impedance of the coil. The theoretical description presented below quantifies the extra impedance effect due to R_2 and C_2.

By defining coefficients α, β and γ for the respective turn ratios of primary, secondary and tertiary windings:

$$\alpha = \frac{N_2}{N_1} \quad \beta = \frac{N_3}{N_1} \quad \text{and} \quad \gamma = \frac{N_3}{N_2} \tag{7.1}$$

Since current through the primary winding i_1 is negligible, and secondary current i_2 corresponds to the major power flow, we consider the impact of tertiary:secondary turns ratio (γ) in our analysis.

The total impedance Z_3 due to R_2 and C_2 placed at the tertiary winding can be written as:

$$Z_3 = R_2 + \frac{1}{j\omega C_2} \tag{7.2}$$

where ω is 2π times the line frequency of 50 Hz under 230 V AC. Using Eq. (7.1) and Eq. (7.2), the reflected impedance Z_3' onto secondary winding can be expressed by dividing Z_3 by turns ratio squared,

$$Z_3' = \frac{Z_3}{\gamma^2} = \frac{Z_3}{[N_3/N_2]^2} \tag{7.3}$$

where γ is the tertiary:secondary turns ratio defined. In addition, the 2000 W load device shown in Figure 7.1 has an equivalent ohmic resistance R_L,

$$R_L = \frac{(230\ \text{V})^2}{2000\ \text{W}} = 26.5\ \Omega$$

Considering R_L and reflected impedance Z_3', we can evaluate the new RMS current i_2' flowing through the loop between live and neutral as:

$$i_2' = \frac{230\ \text{V}}{26.5\ \Omega + \dfrac{Z_3}{\gamma^2}\ \Omega} \tag{7.4}$$

Since the SC impedance ($\frac{1}{j \times 2\pi \times 50 \times 5}$) for a 5 F supercapacitor at 50 Hz is fairly small, and when a 10 Ω high power resistor is used for R_2, i_2' can be simplified as:

$$i_2' = \frac{230\ \text{V}}{26.5\ \Omega + \dfrac{10}{\gamma^2}\ \Omega}$$

Under these circuit conditions, the new electrical power P' delivered to the load device is determined using i_2',

$$P' = \left[\frac{230\ \text{V}}{26.5\ \Omega + \dfrac{10}{\gamma^2}\ \Omega}\right]^2 \times 26.5\ \Omega \tag{7.5}$$

Using Eq. (7.5), it is possible to evaluate P' under different turn ratios ($\gamma = \frac{N_3}{N_2}$). This gives a satisfactory indication about the appropriate turns ratio to be implemented. When:

$$\gamma = 2 \rightarrow P' = 1667\ \text{W}$$

$$\gamma = 4 \rightarrow P' = 1906\ \text{W}$$

$$\gamma = 6 \rightarrow P' = 1955\ \text{W}$$

Considering the experimental feasibility and the practicality of number of turns that can be wound to the Kool μu (0077071A7) powdered-iron toroid, we selected $\gamma = 4$ condition where the third coil had 112 turns ($N_3 = 112$) compared to 28 turns ($N_2 = 28$) of the secondary. Furthermore, the active power flow for this condition is 1906 W, and it is not a considerable reduction from the desired 2000 W rated power. As we change the 10 Ω high-power resistor (R_2) connected to the tertiary winding to much smaller values (1 Ω, 2 Ω, 0.5 Ω and etc.) during experiments, the impedance impact towards AC mains flow becomes insignificant.

Motivated by the initial investigation of this third coil modification made to SCASA topology, our next aim is to study its impact under transient operation. Figure 7.2 demonstrates the experimental setup used for recording test results. When estimating the energy dissipation

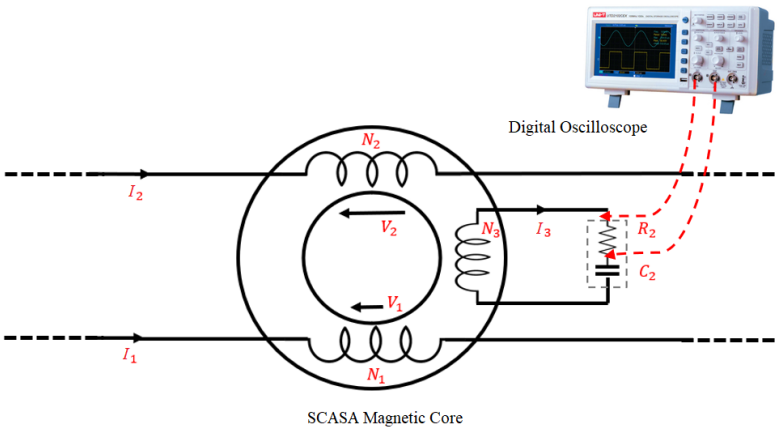

Figure 7.2: Measurement system for third coil based modification made to SCASA (transient mode)

across third coil resistor R_2, we connected a digital oscilloscope (Tektronix TPS2014) to measure the voltage variation across R_2. As the SCASA magnetic core comes into transformer action due

to transient currents I_1 and I_2, the induced magnetic flux circulates around the toroidal core resulting a voltage induction across the third winding. Since 5 F supercapacitor (C_2) develops millivolts order voltage due to its extremely small ESR, the full voltage drop occurs across R_2. Therefore, our measurement system shown in Figure 7.2 yields accurate information about the induced voltage and current I_3 through the third coil. This leads us to evaluate the heat energy dissipation across R_2 under transient operation (we assume the third coil induced current I_3 takes the standard 8/20 μs wave-shape, and peak energy dissipation occurs at 10 μs). Table 7.1 summarizes the peak voltages, currents and corresponding peak energy dissipations for different high-power resistors (varying R_2) placed at the third winding.

Table 7.1: Comparison of peak voltages, currents and peak energy dissipations for different high-power resistors placed at the third winding of SCASA

Applied Surge (kV)	LSS Surge Current (kA)	Resistance in the third coil: R_2 (Ω)	V-peak across single-R (V)	I-peak in the third coil (A)	Energy dissipation $I_3^2 R_2 . t$ (J) ($t \sim 10$ μs)
6.0	3.0	1	440 V	440	1.936 J
6.0	3.0	2 (1×2)	320 V	320	2.048 J
6.0	3.0	10	1200 V	120	1.44 J
6.0	3.0	100	2000 V	20	0.4 J
6.0	3.0	3 (1×3)	220 V	220	1.45 J
6.0	3.0	0.5 (1÷2)	212 V	424	~ 0.9 J

Peak energy estimation presented in Table 7.1 was carried out when SCASA circuit was subjected to standard 6 kV/3 kA combinational surge waveforms. Notably, this topological alteration made to the original SCASA core did not improve the surge energy dissipation significantly. However, according to Table 7.1, it is possible to identify that a maximum energy dissipation ∼2 J can be achieved when two 1 Ω resistors are placed in series (2 Ω) across the third winding. In all other trials with various high-power resistor combinations, serious surge reduction was not achieved. Compared to ∼81 J energy of an incoming surge, the heat dissipations shown in Table 7.1 are fairly insignificant. Therefore, we explore alternative optimization methods in the next Section.

7.2 Magnetic Flux Density associated with a 6 kV/3 kA Transient

Since the introduction of a third inductor winding to the SCASA design did not result in a useful performance enhancement, our next aim was to replace the magnetic core utilized by the coupled-inductor. In selecting an optimum material for the core, the surge based magnetic flux induced during transient propagation must be evaluated to avoid saturation effects. The following calculations provide a detailed theoretical base regarding the magnetic flux distribution inside the SCASA toroidal core.

7.2.1 Toroidal flux in SCASA non-ideal transformer

In Chapter 4, magnetization of a toroidal core was examined in relation to the hysteresis behaviour. We extend that theory here using Ampere's law to derive an expression for the magnetic flux density $\vec{B}$ due to a transient current. By applying Ampere's law to a toroidal core with N number of turns,

$$\oint_L \vec{B} \cdot \vec{dl} = \sum \mu_c I_{en} \tag{7.6}$$

where $\sum I_{en} = NI$ and $\vec{B}$ is the magnetic flux density across the core when a transient current I passes through the windings. Since $\vec{B}$ is uniform across any cross-section of the toroid and when core permeability $\mu_c = \mu_r \mu_\circ$,

$$B \oint_L dl = \mu_r \mu_\circ NI \tag{7.7}$$

where μ_r is the relative permeability and L is the total circular length (magnetic path length) of the toroid with a radius r. As the integral $\oint_L dl = 2\pi r$,

$$B = \frac{\mu_r \mu_\circ NI}{2\pi r} \tag{7.8}$$

In the previous Chapter, We proved that approximately 90% of total surge current I_{surge} is propagating through the primary winding of SCASA transformer that has 5 turns. Moreover, $\mu_r = 60$ for the Kool μu (0077071A7) powdered-iron core which has a circular length of 81.4 mm ($2\pi r$) [116]. Then, the maximum flux density $B_{\max}$ inside the SCASA toroidal core for a 3 kA transient can be evaluated as:

$$B_{\max} = \frac{60 \times 4\pi \times 10^{-7} \times 5 \times 0.9 \times 3000}{81.4 \times 10^{-3}}$$

$$B_{\max} \approx 12.5 \text{ T}$$

When transient current rapidly changes according to the IEEE 8/20 μs standard current wave ($I(t) = A_I I_p t^3 e^{-t/\tau}$) described in Chapter 2, then the magnetic flux density inside the SCASA toroid also varies as illustrated by Figure 7.3. Here, we considered only 90% of the standard short-circuit current flows the primary winding. Figure 7.3 was drawn using MATLAB based on the theoretical prediction of Eq. (7.9) obtained from Eq. (7.8).

$$B(t) = \frac{\mu_r \mu_\circ N \left[A_I I_p t^3 e^{-t/\tau} \right]}{2\pi r} \tag{7.9}$$

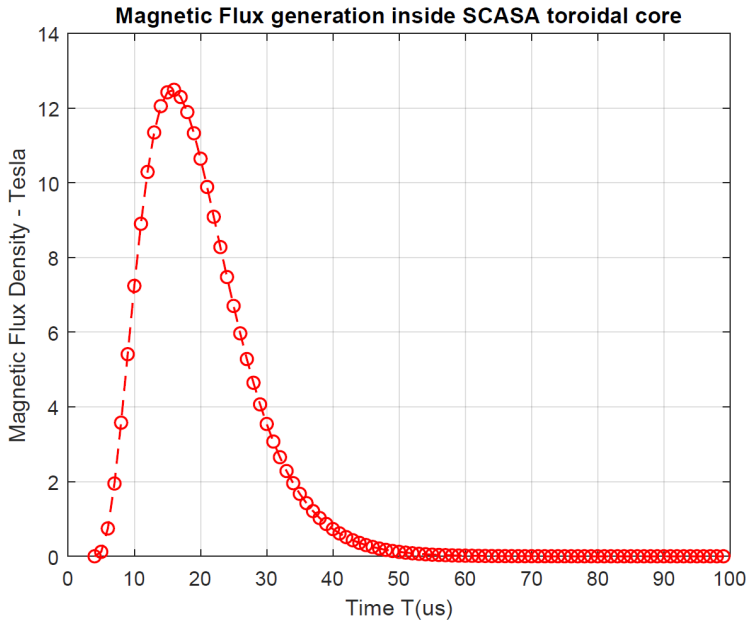

Figure 7.3: Variation of magnetic flux density inside SCASA toroid during a 3 kA transient

Since standard transient current varies instantaneously under 100 µs, a better estimation for the magnetic flux can be obtained by considering the average transient current. Using integration, we obtain an expression for average transient current I_{avg} as:

$$I_{\text{avg}} = \frac{1}{T} \int_0^T A_I I_p t^3 e^{-t/\tau} \, dt \tag{7.10}$$

When the IEEE-Std-C62.45-2002 defined constants $A_I = 0.01243\ \mu s^{-3}$, $\tau = 3.911\ \mu s$ and $I_p = 90\%\ I_{\text{surge}} = 2700$ A, above integral can be evaluated using MATLAB as:

$$I_{\text{avg}} \approx 470 \text{ A}$$

Importantly, we can determine the average magnetic flux density corresponding to this current as:

$$B_{\text{avg}} = \frac{\mu_r \mu_\circ N I_{\text{avg}}}{2\pi r} = \frac{60 \times 4\pi \times 10^{-7} \times 5 \times 470}{81.4 \times 10^{-3}} \tag{7.11}$$

$$B_{\text{avg}} = 2.18 \text{ T}$$

$$B_{\text{avg}} = 21,800 \text{ gauss}$$

This is a useful result on which we base the selection of commercial magnetic toroids for SCASA prototypes with a comparable saturation level. More information about maximum flux density of various powdered-iron and ferrite materials used in our experiments is presented next.

7.3 Testing with High-Flux and X-Flux Powder-iron Cores

Out of the various commercial magnetic assortments mentioned at the beginning of this Chapter, we first experimented with two high performance powdered-iron materials (High Flux and X Flux), and compared SCASA performance with presently used Kool μu. Apart from the permeance coefficients of these toroids, the saturation magnetic flux is also of importance to our selection as explained above. Therefore, a descriptive comparison of magnetic properties of various powdered-iron and ferrite materials used in prototype design is presented below.

7.3.1 Comparison of magnetic properties

Given the summary of first successful implementation of the SCASA protector in Chapter 3, one major problem faced was the selection of the magnetic core, within the cost restrictions of a commercial product. As described in Chapter 5, commercially available pure ferrite cores did not perform well, while a powdered alloy such as 0077071A7 from Magnetics Inc. [76] was able to perform satisfactorily. Given the need to estimate the required coupled-inductor turns ratio, self-inductance and the mutual inductance parameters based on core specifications, varying the number of primary and secondary turns helped in only a limited way; thus, a new analytical approach based on magnetic permeance was used (more details given in Chapter 4). This provided the theoretical foundation to accurately estimate the total self-inductances of the primary (L_p) and secondary (L_s) based on data-sheet specifications, "Λ_m" (magnetizing permeance) and "Λ_σ" (leakage permeance). More importantly, Λ_m is derived from the fundamental magnetic property of permeability (μ_r), and is dependent on both permeability and geometrical configuration (magnetic path length l_c and cross-sectional area A_c) of the core [93]. A comparison of relative permeability and magnetizing permeance of the toroidal core types used in this research is presented in Tables 7.2 and 7.3 respectively. The following equation shows the relationship between Λ_m, μ_r, A_c and l_c:

$$\Lambda_m = \frac{\mu_r \mu_o A_c}{l_c} \tag{7.12}$$

where μ_r is the relative permeability and μ_o is the permeability of free space. This further justifies how magnetizing permeance has a dependency on magnetic material and core geometry, whereas permeability only depends on material properties.

As validated using Laplace transforms (Chapter 6), the theoretical approach based on permeance allowed us to accurately estimate the transient currents flowing in the primary and secondary windings, matching well with the experimental values. In this research we worked with Magnetics Inc. (USA) to model the potential core samples based on materials such as "Kool μu, High Flux, X Flux and W-Ferrite" (Figure 7.4), with the expectation of selecting the optimum core material and the shape, within the commercial price constraints applicable to the product family known as Smart TVIQ2/3 based on SCASA surge protection technique. Tables 7.2 and 7.3 present a summary of magnetic properties and magnetizing permeances Λ_m (known as the inductance factor - A_L according to manufacturer specifications) of above materials (see Appendix E). Our experiments were primarily focused on investigating the surge absorption levels of toroid samples shown in Figure 7.4 as per their performance in SCASA prototypes.

Table 7.2: Comparison of relative permeability and saturation level of different powdered-iron and ferrite based alloys used in SCASA prototype design [78, 79]

Magnetics Part No.	Material	Relative permeability (μ_r)	Saturation flux density $\vec{B}_{\max}$ (gauss)
0077071A7	Kool μu	60	10,500
058071A2-4	High Flux	60	15,000
078550A7	X Flux	26	16,000
ZW43615TC	W Ferrite	10,000	3,900
VJ42206TC	J Ferrite	5,000	4,300

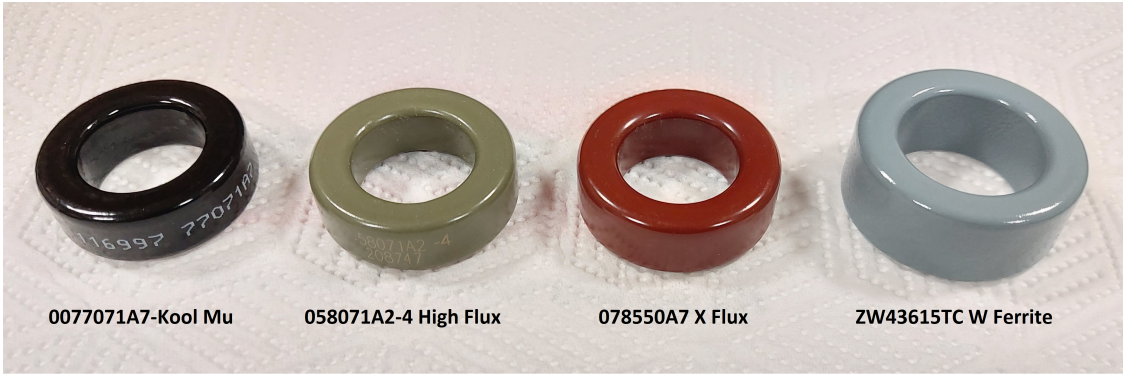

(a) (b) (c) (d)

Figure 7.4: Unwound powdered-iron and ferrite core samples used in SCASA prototype design: (a) **Kool μu toroid (0077071A7): present design**; (b) High Flux toroid (058071A2-4); (c) X Flux toroid (078550A7) and (d) W Ferrite toroid (ZW43615TC)

Table 7.3: Comparison of permeance coefficients Λ_m (also known as inductance factor A_{L}) of different powdered-iron and ferrite based alloys used in SCASA prototype design [78, 79]

Magnetics Part No.	Material	Permeance Coefficient (Λ_m) Inductance factor (A_{L}) (nH/turns^2)
0077071A7	Kool μu	61
058071A2-4	High Flux	61
078550A7	X Flux	28
ZW43615TC	W Ferrite	13,400
VJ42206TC	J Ferrite	3,020

All powdered-iron and ferrite core samples mentioned in Table 7.2 possess low saturation flux capacities compared to the maximum toroidal flux of 21,800 gauss. Therefore, core saturation can occur under the peak primary surge current, hence the SCASA transformer tends to deviate

from its ideal action. In Chapter 4, we measured that primary:secondary current ratio did not match with inverse turns ratio $N_2 : N_1$ of respective coils. Apart from the core reluctance of Kool μu toroid, this non-ideal behaviour in current division is due to core saturation effects. However, as X Flux toroid shows almost 60% better maximum flux capacity (16,000 gauss) compared Kool μu (10,500 gauss), our aim of optimizing surge absorption with ne prototypes can be justified. Test results relating surge energy storage capability of different SCASA prototypes are discussed in the following sections.

7.3.2 Measurement of self- and leakage inductances

In the previous Section, it became evident that the two powdered-iron (High Flux and X Flux) materials in our interest have contrasting magnetic properties. Noticeably, their relative permeabilities and permeance coefficients are different. Therefore, with the aim of constructing SCASA prototypes using High Flux and X Flux toroids, we first evaluated their inductance properties. As described in Chapter 4, using open- and short-circuit tests, we measured self- and leakage-inductances of the core samples and compared these values with original Kool μu core. All the toroids we tested for SCASA design comprised a coupled-inductor (primary and secondary) wound at unequal number of turns. As in the original topology, primary winding has 6 turns, whereas secondary composed of 28 turns. But, for the case of X Flux (078550A7) toroid, the primary and secondary had 8 and 44 turns respectively. Inductance measurements of both windings were carried out using an LCR meter (Fluke PM6304) at 10 kHz. Table 7.4 presents essential inductance measurements taken for High Flux (058071A2) and X Flux (078550A7) toroids with comparisons to Kool μu (0077071A7) core. More information about the energy storage capability of these core samples is discussed in the following description.

According to Table 7.4, it is clear that all three core samples have similar self-inductances for primary and secondary windings. As all toroids have identical geometry (cross-sectional area and circular path length), it is understandable that Kool μu and High Flux cores should possess similar inductance properties due to their equivalent relative permeabilities ($\mu_r = 60$). However, as X Flux core has a reduced permeability ($\mu_r = 26$), to get the desired self-inductances, we increased primary and secondary turns to 8 and 44 respectively. This approach was used to make sure that all core samples generate similar inductive-impedance under transient currents. The most noticeable comparison in Table 7.4 is the variation magnetic coupling coefficient (k) between the cores. High Flux core has a relatively weaker coupling with $k = 0.61$ and slightly larger leakage inductance ($l_2 = 39.8$ μH) compared to Kool μu toroid ($k = 0.74$ and $l_2 = 34.6$ μH). Interestingly, the X Flux core having the lowest relative permeability shows the greatest secondary leakage ($l_2 = 43$ μH). This is further reflected by the reduced magnetic coupling of X Flux toroid which is the lowest of all with $k = 0.56$. Based on this observation we can infer that the high concentration of air-bubbles distributed inside X Flux toroid (leading to permeability reduction) has a significant impact on the leakage flux as well as magnetic-coupling, which alternatively is a useful characteristic for surge protection applications. With the goal of verifying the surge absorption capability of these core samples, we constructed SCASA prototypes for surge testing.

Table 7.4: Comparison of mutual, leakage and self inductances of primary and secondary windings for Kool μu, High Flux, X Flux cores used in SCASA prototypes

Measurement	Kool μu Toroid (0077071A7) $\mu_r = 60$	High Flux Toroid (058071A2) $\mu_r = 60$	X Flux Toroid (078550A7) $\mu_r = 26$
			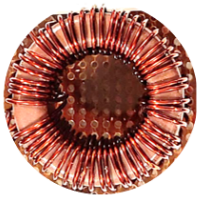
L_p (μH)	**3.4**	**3.3**	**3**
L_s (μH)	**57**	**58**	**59.8**
N_1	**6**	**6**	**8**
N_2	**28**	**28**	**44**
l_1 (μH)	**1.6**	**2.1**	**2**
l_2 (μH)	**34.6**	**39.8**	**43**
M (μH)	**9.8**	**8.6**	**7.5**
k	**0.74**	**0.61**	**0.56**

L_p: primary self-inductance, L_s: secondary self-inductance, l_1: primary leakage-inductance, l_2: secondary leakage-inductance, M: mutual inductance, k: coupling coefficient, N_1: primary turns, N_2: secondary turns

7.3.3 Design of SCASA prototypes

Using High Flux and X Flux toroidal cores discussed in Table 7.4, SCASA prototypes were constructed as shown in Figure 7.5. All circuit designs comprised similar configurations with a coupled-inductor (primary: 6 turns and secondary: 28 turns), two MOVs and a supercapacitor sub-circuit. However, due to the reduced permeability in X Flux core, the primary and secondary

turns were increased 8 and 44 turns respectively to get the desired self-inductance comparable to other designs (Table 7.4). More details discussed in Section 7.3.2. In addition, the three toroids had identical geometrical properties with a similar cross-sectional area $A_c = 65.6$ mm^2 and a magnetic path length $l_c = 81.4$ mm. All three circuit prototypes demonstrated in Figure 7.5 were subjected to standard 6 kV/3 kA combinational surge pulses using a lightning surge simulator.

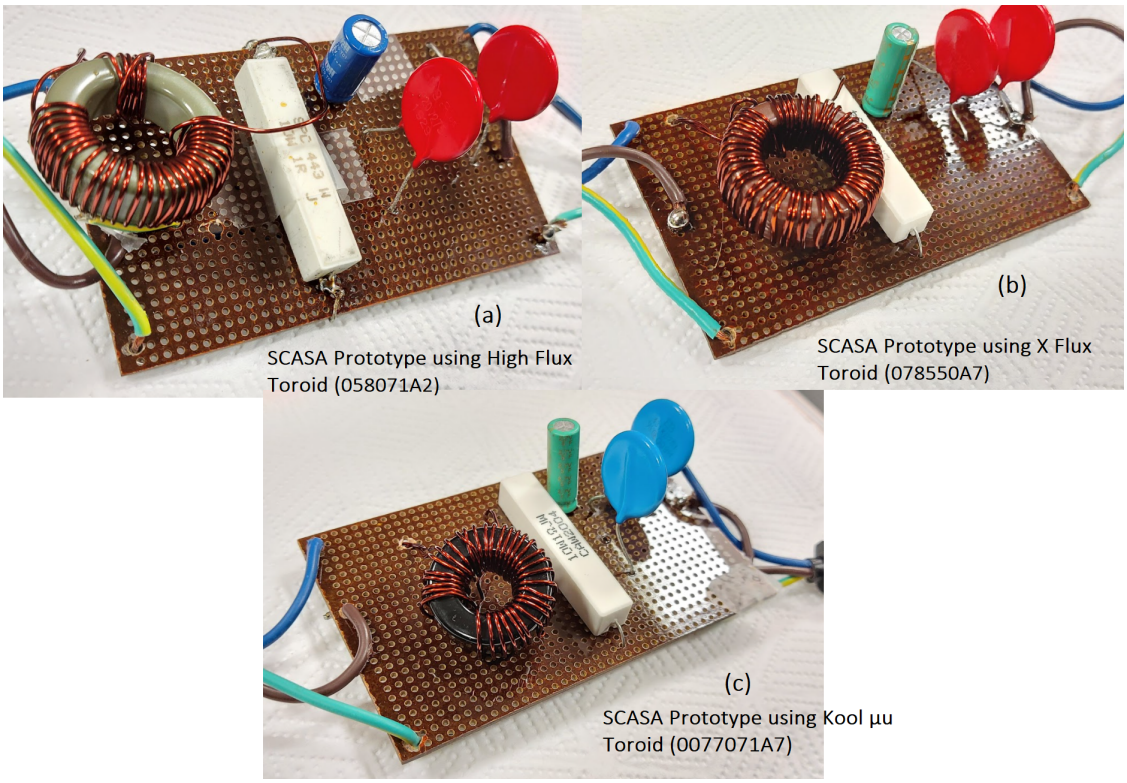

Figure 7.5: SCASA prototypes using powdered-iron core samples: (a) High Flux toroid (058071A2-4); (b) X Flux toroid (078550A7); (c) Kool μu toroid (0077071A7).
Note: circuit prototypes designed using Ferrite toroids are presented in Chapter 5.

7.3.4 Experimental setup and test results

In order to facilitate surge testing of SCASA prototypes, a lightning surge simulator (NoisenKen LSS-6230) and a digital oscilloscope (Tektronix TPS2014) were used as the main instruments. Figure 7.6 depicts the experimental setup implemented for combinational surge-waveform generation. Here, standard 1.2/50 μs surge pulses were generated using the LSS-6230; hence, oscilloscope waveforms were recorded for 6 kV/3 kA peak settings across Var1 and Var2 as shown in Figure 7.7.

To understand the surge absorption of magnetic core, we looked into the fine operation of the coupled-inductor design under transient conditions. As described previously in Chapter 4, the coupled primary and secondary coils of SCASA transformer are wound to a toroidal core which stores transient-related magnetic flux during current propagation. In a separate research mentioned in Chapter 3 and Chapter 5, we proved that a clear indication about the energy storage capability is given by the difference $(v_s - v_p)$ between secondary induced voltage v_s and primary induced voltage v_p. This effect is due to the design configuration of SCASA topology

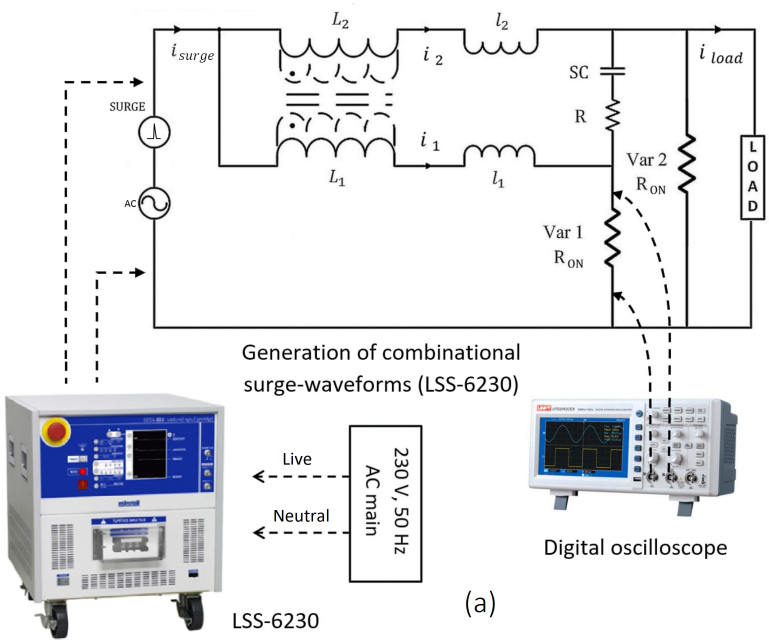

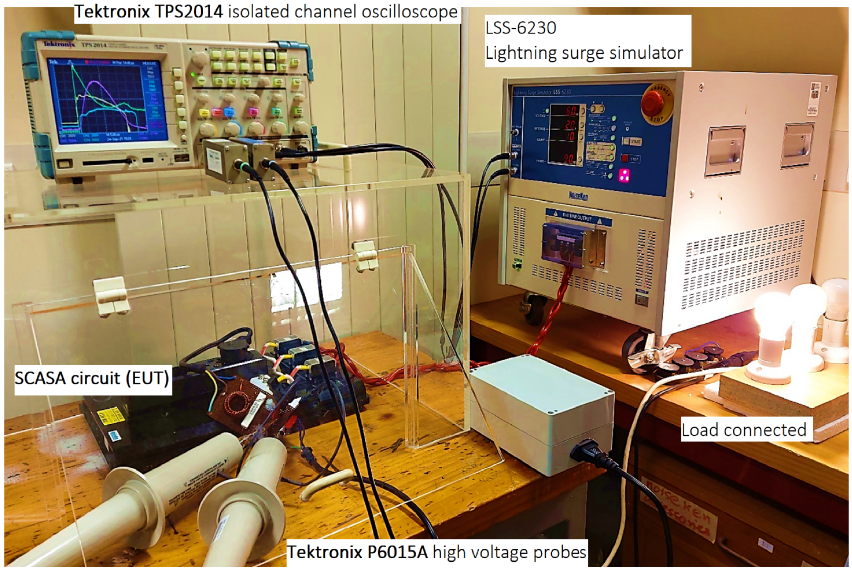

Figure 7.6: Experimental setup and the transient operation of non-ideal transformer core of SCASA: (a) schematic view and (b) real view of the test setup

where secondary coil possesses a much larger self-inductance L_s (∼60 μH) than the primary self-inductance L_p (∼3.8μH). Therefore, as transient currents propagate through the core windings $v_s > v_p$ resulting an inductive energy release given by $v_s - v_p$. In identifying this fine operation, we captured oscilloscope waveforms across Var1 and Var2 by disconnecting the SC-subcircuit (SC and R shown in Figure 7.6(a)), and compared with SCASA prototypes designed using different powdered-iron and ferrite based toroids. Test results are presented next.

Figure 7.7 illustrates experimental and simulated waveforms captured for different toroidal cores under a transient of 6 kV/3 kA. As described above, the inductive energy release (from the magnetic core) given by $v_s - v_p$ is indicated by the voltage variation across Var2, specially the reverse sided (negative) voltage peak shown by all waveforms in Figure 7.7 reveals the extent

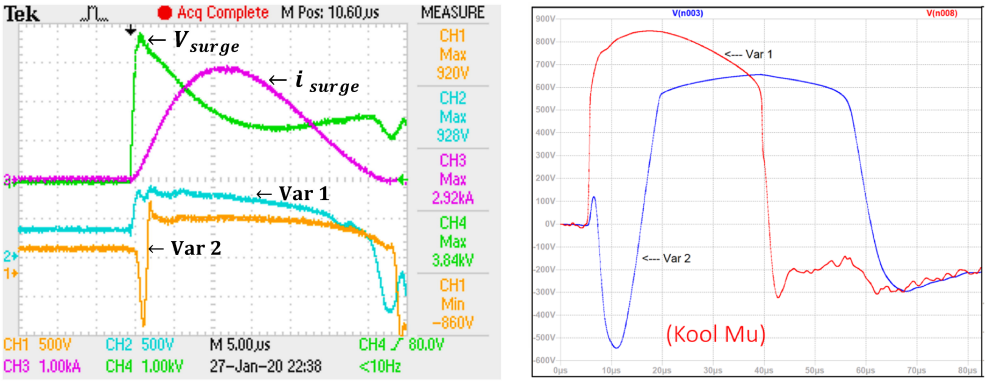

(a)

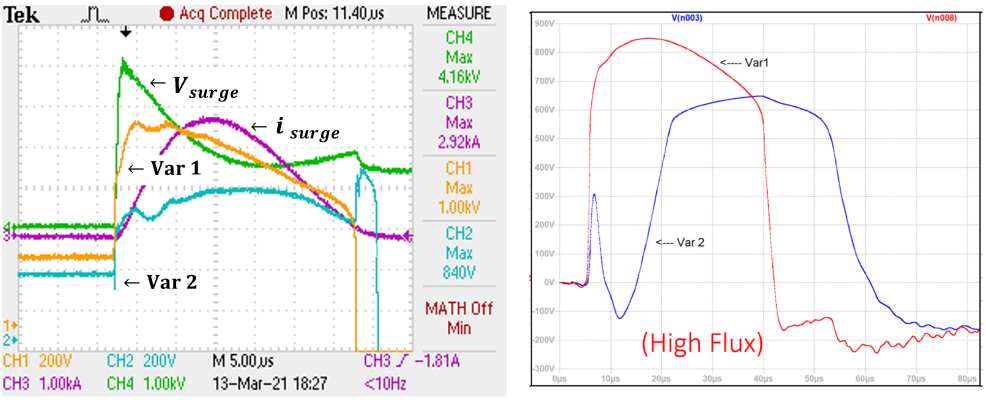

(b)

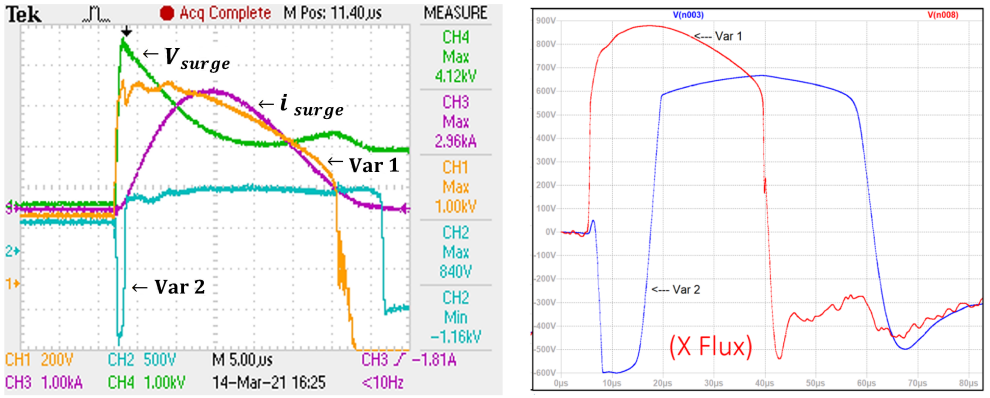

(c)

Figure 7.7: Experimental and simulated waveforms for different powdered-iron cores under a transient of 6 kV/3 kA: (a) Kool µu toroid (0077071A7); (b) High Flux toroid (058071A2-4) and (c) X Flux toroid (078550A7)

of energy storage shown by corresponding toroids. By comparing the magnitudes of negative voltage peak ($v_s - v_p$) relating to different cores under test, it is possible to identify that the most substantial voltage spike (–1160 V) is demonstrated by the X flux toroid (078550A7) as per Figure 7.7(c). Thus, we can argue X Flux core shows relatively better capacity in storing surge energy. Conversely, as shown in Figure 7.7(b), High Flux toroid (058071A2-4) with a minor reversed voltage (~ -100 V) indicates the least flux storage capability. Noticeably, Kool µu toroid (0077071A7) which is presently utilized in the original SCASA design exhibits a substantial, yet

a moderate energy absorption level with –860 V according to Figure 7.7(a). This is relatively a lower voltage magnitude in comparison with X Flux core, and based on this observation we can infer X Flux toroid is superior to Kool μu toroid in terms of its energy absorption. Usability of these powdered-iron cores in SCASA surge protector design is summarized in Table 7.5.

Table 7.5: Performance comparison (surge absorption level) of different powdered-iron and ferrite based alloys used in SCASA prototype design

Magnetics Part No.	Material	Usability in SCASA surge protector based on surge absorption
0077071A7	Kool μu	Usable (present design)
058071A2-4	High Flux	Limited
078550A7	X Flux	Highly Usable
ZW43615TC	W Ferrite	Very Limited
VJ42206TC	J Ferrite	Very Limited

With regard to pure ferrite based toroids (W and J ferrites), we conducted experiments as specified in Chapter 5 to prove that these cores have very limited capability of storing surge related flux. Moreover, pure ferrites are magnetically soft materials with extremely narrow hysteresis behaviour [117] having lower saturation levels compared powdered-iron materials. This is further reflected by the high magnetizing permeance (Λ_m) shown by W and J ferrites (Table 7.3). However, when an air gap is inserted into ferrite cores, these perform much better with improved surge endurance. We described the advantage of gapping a toroid in Chapter 5; a detailed investigation about implementing commercially available air-gapped ferrites is presented next.

7.4 Testing with Commercial Gapped Ferrites

7.4.1 Selection of core geometry and material

In Chapter 5, we explained the importance of air-gapped ferrites in optimizing the performance of SCASA technique. But, the gapping approach we used by introducing external cuts to the toroidal body was a difficult task. Specially due to the brittleness of ferrite like material, there is a high possibility of fracture within the toroid during cutting process. Moreover, the feasibility of mass production using this gapping method is highly limited. Therefore, an initial investigation was carried out in selecting the best commercially available gapped-ferrites suitable for SCASA surge protector design. Figure 7.8 illustrates various ferrite core geometries manufactured by Magnetics Inc., USA.

According to the manufacturer's specifications, any geometrical configuration shown in Figure 7.8 can be incorporated with an air-gap provided that the gap-code or the permeance coefficient Λ_m (A_L) is accurately specified. Given the suitability for SCASA circuit configuration and the overall cost in gapping (varies depending on the shape), we selected EER type core for our

surge protector application. Compared to the A_L of original Kool μu powdered-iron toroid and W-ferrite based air-gapped toroid described in Chapters 4 and 5 respectively, we determined the A_L of this new commercial EER core to be $\sim$ 125 nH/turn^2. Noticeably, this new EER core trimmed according to the specified permeance coefficient resulted in a considerably less cost compared to original Kool μu powdered-iron core. More details about the cost comparison is presented at the end of this Section.

Another significant factor that is highly relevant to our selection is the material composition. Since ferrite based materials used core manufacturing has a wide range including W, J, T, F, P and R ferrites, a detailed comparison about magnetic properties of each type was carried out. Table 7.6 presents a summary of essential magnetic parameters of different ferrite materials.

The above information presented in Table 7.6 is applicable to all pure ferrite materials without air-gaps. When a selected core geometry is manufactured using these materials, the magnetic properties get altered accordingly. Our material choice was biased towards R-ferrite due to its relatively lower initial permeability ($\mu_r = 2,300$) compared to extremely high permeability of W-ferrite ($\mu_r = 10,000$). Hence, the air-gap insertion was not as wider as what was required for W-ferrite toroid discussed in Chapter 5. The effective permeability required for our application can be achieved conveniently using R-ferrite with a thin-gap resulting a reduced manufacturing cost. Also, due to the high availability and greater saturation flux density of R-ferrite compared to W, J and L ferrites, our selection was further confirmed. Materials like T-ferrites, though indicates comparatively better saturation, are rare and expensive with a limited availability for

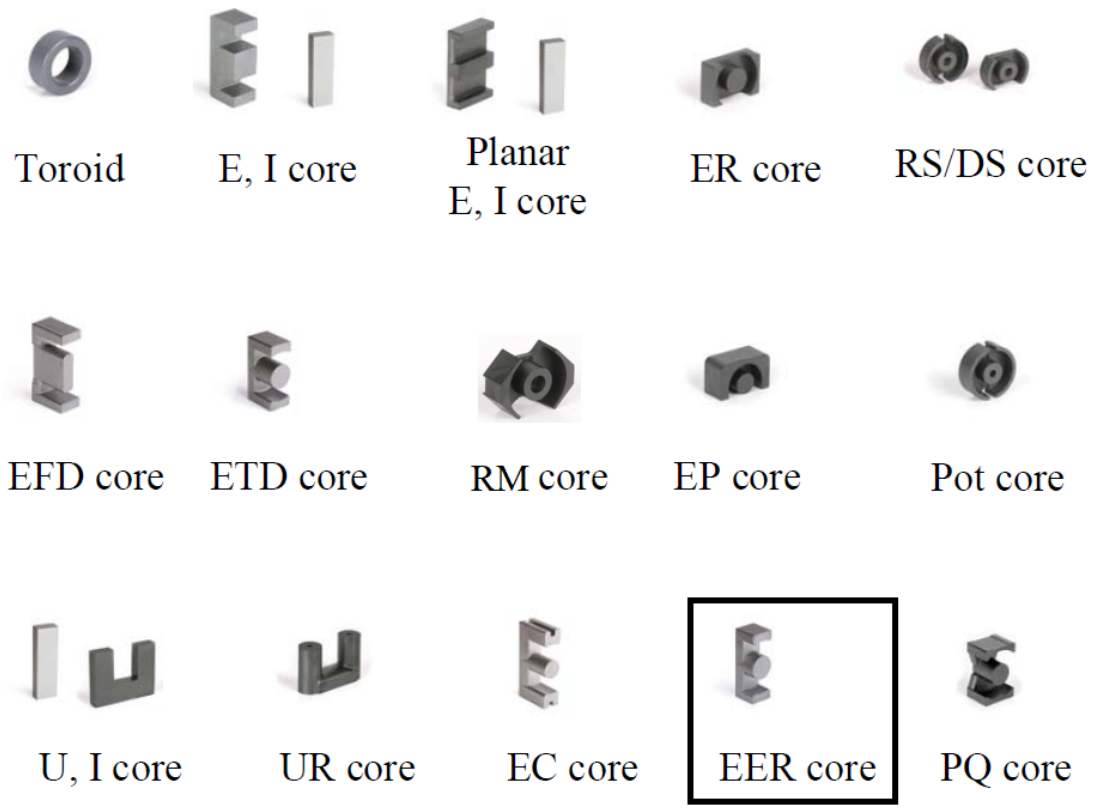

Figure 7.8: Various ferrite core shapes from 2017 Magnetics Inc. ferrite-core catalogue [78]

Table 7.6: Comparison of magnetic properties of ungapped ferrite materials manufactured by Magnetics Inc., USA [78]

			INDUCTORS & POWER TRANSFORMERS					EMI/RFI FILTERS & BROADBAND TRANSFORMERS	
MATERIAL			L	R	P	F	T	J	W
Initial Permeability	μ_i		900 ±25%	2,300 ±25%	2,500 ±25%	3,000 ±20%	3,000 ±25%	5,000 ±20%	10,000 ±30%
Maximum Usable Frequency (50% roll-off)	f	MHz	≤6	≤1.8	≤1.8	≤1.5	≤1.5	≤0.7	≤0.5
Relative Loss Factor X 10^{-6} 25°C		tan δ/μ_{ioc}						≤15 100 kHz	≤7 10 kHz
Curie Temperature	T_c	°C	>300	>210	>210	>210	>220	>145	>135
Flux Density @ 1,194 A/m (15 Oe) 25°C	B_m 10 kHz	G mT	4,200 420	4,700 470	4,700 470	4,700 470	5,300 530	4,300 430	3,900 390

the selected core geometry (EER shape). Considering aforementioned factors, we decided to construct SCASA prototypes using a R-ferrite based gapped EER magnetic core (R43521A125). The gap code for the selection was A-125 meaning that the permeance coefficient $A_L = 125$ nH/turn^2 which is comparable to the original Kool μu powdered-iron core design. Figure 7.9 illustrates the R43521A125 core before and after the winding. More details about the effective permeance and effective permeability of gapped EER core is presented next.

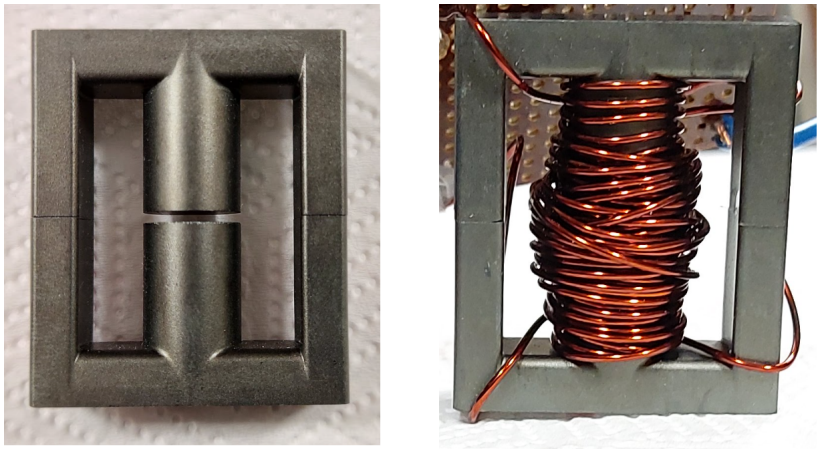

Figure 7.9: R43521A125 air-gapped EER core: (a) unwound core; (b) wound core installed in SCASA surge protector

7.4.2 Effective permeability and permeance of air-gapped EER core

Based on the gap code (A-125) of selected R43521A125 EER core, the permeance coefficient (A_L) is determined as 125 nH/turn^2 (see Appendix E). According to the industry specifications [78, 118], this A_L value is considered as the effective permeance (Λ'_m =125 nH/turn^2) of the air-gapped EER core (see Chapter 4). However, to examine the reduction of Λ'_m in the presence of

an air-gap, we looked into the initial permeance Λ_m of the original ungapped EER core. Given $\mu_r = 2,300$ for R-ferrite material, the Λ_m of original EER core was found as 2725 nH/turn^2 (see Appendix E for manufacturer data-sheets) [81]. This is significantly larger compared to Λ'_m. The following calculations quantify the reduction of Λ'_m.

Permeance of the original ungapped EER core:

$$\Lambda_m = 2725\,\text{nH/turn}^2$$

Effective permeance of the air-gapped EER core:

$$\Lambda'_m = 125\,\text{nH/turn}^2$$

Thus, the ratio between Λ_m:Λ'_m can be approximated as:

$$\frac{\Lambda_m}{\Lambda'_m} = \frac{2725\,\text{nH/turn}^2}{125\,\text{nH/turn}^2} \approx 22 \tag{7.13}$$

$$\Lambda'_m = 0.046 \times \Lambda_m \tag{7.14}$$

This quantification proves the reduction of permeance into effective permeance due to air-gap insertion inside EER core. A theoretical model relating to this phenomenon was developed in Chapter 5 with regard to an air-gapped toroid. Another useful result obtained from Eq. (7.13) is the prediction about effective relative permeability μ'_r of gapped EER core. As per the definition of magnetizing permeance described in Section 7.3.1:

$$\Lambda_m = \frac{\mu_r \mu_o A_c}{l_c}$$

For a given core geometry, Λ_m is proportional to μ_r/l_c:

$$\Lambda_m \propto \frac{\mu_r}{l_c} \tag{7.15}$$

By analogy, for the air-gapped EER core:

$$\Lambda'_m \propto \frac{\mu'_r}{l_c + l_g} \tag{7.16}$$

Dividing Eq. (7.15) by Eq. (7.16), and by using Eq. (7.13) mentioned above:

$$\frac{\Lambda_m}{\Lambda'_m} = \frac{\mu_r \times [\, l_c + l_g \,]}{\mu'_r \times l_c} = \frac{2725\,\text{nH/turn}^2}{125\,\text{nH/turn}^2} \tag{7.17}$$

Since air-gap length l_g is much smaller compared to path length l_c of the core ($l_g << l_c$), by approximating $l_c + l_g \approx l_c$, Eq. (7.17) simplifies into:

$$\frac{\Lambda_m}{\Lambda'_m} = \frac{\mu_r}{\mu'_r} = 22 \tag{7.18}$$

By rearranging Eq. (7.18), effective relative permeability μ'_r of the gapped EER core shown in Figure 7.9 can be obtained as:

$$\mu_r' = \frac{\mu_r}{22} = \frac{2,300}{22} \approx 105 \tag{7.19}$$

The mathematical relationship obtained above clear indicates the significance of air-gap inside EER core which results in a substantial drop in magnetic permeability. Compared to pure R-ferrite material ($\mu_r = 2,300$) described in Table 7.6, this commercially available air-gapped EER core (R43521A125) indicated a remarkable reduction with an effective permeability $\mu_r' = 105$. Noticeably, μ_r' lies in the comparable range with Kool μu powdered-iron core (0077071A7) which had $\mu_r = 60$. A summarised comparison of relative permeability and permeance coefficients of the core types is presented in Table 7.7. In addition, this alteration makes the core more reluctive enhancing its overall energy storage capability. More information regarding energy storage enhancement was discussed in Chapter 5.

Table 7.7: Comparison of relative permeability and permeance coefficients of Kool μu powdered-iron core (0077071A7), gapped and ungapped EER core (R43521A125/R43521) types [78, 79]

	Kool μu Toroid (0077071A7)	Un-gapped EER core (R43521)	Air-gapped EER core (R43521A125)
Relative Permeability/ Effective Relative Permeability (μ_r/μ_r')	$\mu_r = 60$	$\mu_r = 2300$	$\mu_r' = 105$
Permeance/Effective Permeance - Λ_m/Λ_m' (nH/Turn^2)	$\Lambda_m = 61$	$\Lambda_m = 2725$	$\Lambda_m' = 125$

Next, we present self- and leakage inductance measurements of a SCASA surge protector prototype constructed using air-gapped ferrite EER core (R43521A125).

7.4.3 Measurement of self- and leakage inductances of EER core

From the above discussion, it is evident that the commercial EER type gapped ferrite core possesses comparable magnetic properties to Kool μu powdered-iron core utilized in the original design. Therefore, prior to the surge testing of SCASA prototypes using R43521A125 core, we first evaluated their inductance properties. As described in Chapter 4, using open- and short-circuit tests, we measured self- and leakage-inductances of the core samples and compared these values with original Kool μu core. The prototypes designed for SCASA topology comprised a coupled-inductor (primary and secondary) wound at unequal number of turns. Compared to the original design, primary coil wound to the EER core has 5 turns, whereas the secondary composed of 34 turns. Inductance measurements of both coupled-inductor coils were carried out using a LCR meter (Fluke PM6304) at 10 kHz. Table 7.8 presents essential inductance measurements taken for air-gapped EER core (R43521A125) with comparisons to Kool μu powdered-iron core (0077071A7). More information about the energy storage capability of these core samples is provided in the following explanation.

According to Table 7.8, it is identifiable that both primary and secondary self-inductances (L_p and L_s) are relatively higher in EER core compared to that of Kool μu powdered-iron toroid. This is due to the comparatively high magnetizing permeance (inductance per turns squared) of

Table 7.8: Comparison of mutual, leakage and self inductances of primary and secondary windings for Kool μu powdered-iron toroid (0077071A7) and air-gapped ferrite EER core (R43521A125) used in SCASA prototype design

Measurement	Kool μu Toroid (0077071A7) $\mu_r = 60$	Air-gapped EER core (R43521A125) $\mu_r' = 105$
		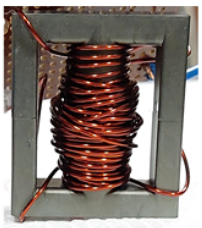
L_p (μH)	**3.4**	**7.7**
L_s (μH)	**57**	**236.8**
N_1	**6**	**5**
N_2	**28**	**34**
l_1 (μH)	**1.6**	**3.6**
l_2 (μH)	**34.6**	**115.6**
M (μH)	**9.8**	**31.5**
k	**0.74**	**0.74**

L_p: primary self-inductance, L_s: secondary self-inductance, l_1: primary leakage-inductance, l_2: secondary leakage-inductance, M: mutual inductance, k: coupling coefficient, N_1: primary turns, N_2: secondary turns

EER core ($\Lambda'_m = 125$ nH/turn^2) in contrast to $\Lambda_m = 61$ nH/turn^2 of Kool μu core. Since both coils posses μH level self-inductances, they do not impede 230 V mains flow under 50 Hz for this new EER configuration. As primary and secondary turns do not vary considerably for the two designs, our principal concern is the alteration of leakage inductances. The gapped EER based coupled-inductor showed significant increments in leakage components with $l_1 = 3.6$ μH and $l_2 = 115.6$ μH for the respective coils compared to $l_1 = 1.6$ μH and $l_2 = 34.6$ μH of powdered-iron core. As per the percentage analysis of leakage effect described in Section 5.4.1 (Leakage percentage $= \frac{\text{Leakage inductance}}{\text{Self inductance}} \times 100\%$), we can evaluate 47 % and 46.7 % associated with the primary coil of Kool μu and EER cores. Interestingly, both core types possessed similar leakage percentages for the primary. But, the secondary winding yielded slightly different leakage effects for the two designs with $\sim 60\%$ and $\sim 50\%$ respectively. However, the most noticeable comparison in Table 7.8 is the variation magnetic coupling (k) between the cores. Both powdered-iron and air-gapped EER cores showed a remarkable similarity in magnetic coupling with $k = 0.74$ for the two prototypes. Based on the above observations, we can infer that the relatively low-priced commercially available gapped EER core is ideally suited for SCASA surge suppression. With the aim of verifying the surge absorption capability, we constructed a SCASA prototype (Figure 7.10) using R43521A125.

7.4.4 Performance comparison: powdered-iron core vs air-gapped EER core

Improving load-side voltage, and advancing the surge endurance capacity of SCASA surge protector were the two main gaols of using this new core configuration. In this section, we explore how EER type magnetic-core meets these goals by comparing its performance under transient operation. The SCASA prototype designed using gapped EER core (Figure 7.10) was subjected

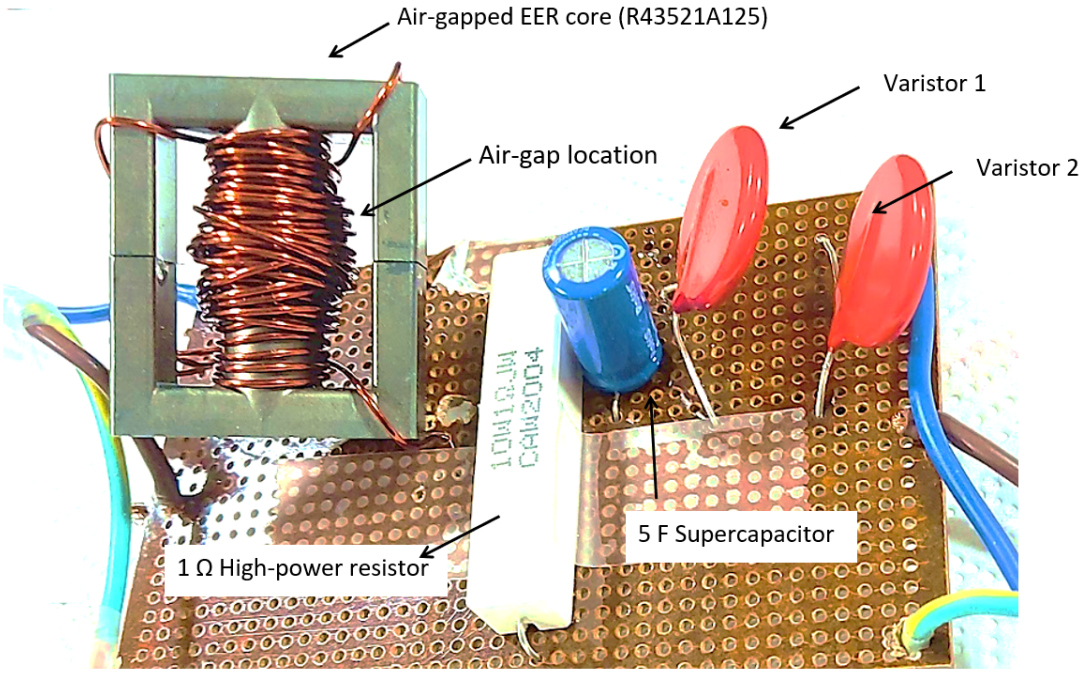

Figure 7.10: SCASA prototype design using R43521A125 air-gapped ferrite EER core

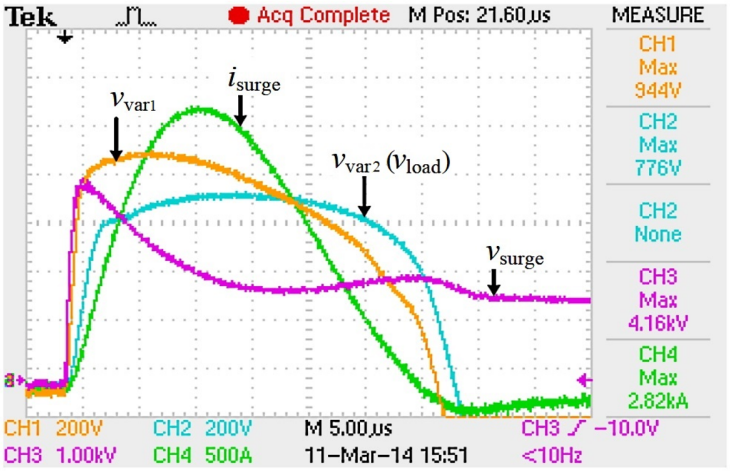

(a)

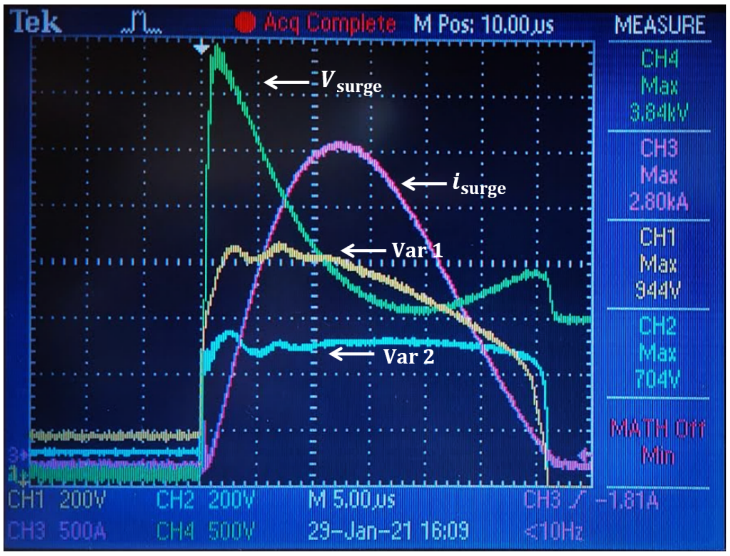

(b)

Figure 7.11: Oscilloscope waveforms for different commercial magnetic cores under a transient of 6 kV/3 kA: (a) Kool µu powdered-iron core (0077071A7); (b) air-gapped EER ferrite core (R43521A125)

to standard 1.2/50 μs transient pulses to evaluate the surge endurance. In order to facilitate surge generation, a lightning surge simulator (NoisenKen LSS-6230) and a digital oscilloscope (Tektronix TPS2014) were used as the main instruments. Figure 7.6 depicts the experimental setup implemented for 6 kV/3 kA combinational surge-waveform generation. As described previously in Section 5.6.2, using UL-1449 test procedure (Figure 5.15), oscilloscope waveforms were recorded for LSS peak settings across Varistor-1 and Varistor-2 for the SCASA prototype shown in Figure 7.10. Table 7.9 and Figure 7.11 demonstrate the clamping voltage improvements of varistor-2 with comparisons made to original (Kool µu powdered-iron core) SCASA design.

As surge protector devices (SPDs) are primarily characterized by their clamping-voltage level, lower clamping indicates better surge absorption, hence more protection. According to Table 7.9 (based on Figure 7.11), varistor-1 in both circuit designs yielded identical clamping voltages of 944 V. This is mainly due to the generation of similar surge conditions of 6 kV/3 kA

Table 7.9: Comparison of clamping level reduction by different SCASA prototypes based on commercial magnetic cores: Kool μu powdered-iron core (0077071A7) and air-gapped ferrite EER core (R43521A125)

Magnetic Core	Clamping voltage of Varistor 1 (V)	Clamping voltage of Varistor 2 (V)	Reduction percentage of Varistor 2 voltage
Kool μu Powdered-iron Toroid (0077071A7)	944	776	~ 17 %
Air-gapped EER core (R43521A125)	944	704	~ 25 %

Reduction percentage = $\frac{(776-704)\times 100}{776}$ = ~ 10 %

using LSS-6230 simulator. However, due to the impedance effects of connecting wires and surge simulator (described in Chapter 2), actual injected surge current i_{surge} slightly varied from 3 kA. But, as per Figure 7.11(a) and Figure 7.11(b), both circuits experienced approximately ∼2.8 kA maximum surge current. Out of the two varistors, varistor-2 is of greater concern for our analysis as it is directly connected to the load-end. Noticeably, the SCASA prototype designed using gapped EER core showed an encouraging clamping voltage of 704 V for varistor-2 which is ∼25 % reduction compared to the varistor-1. Conversely, the present SCASA design built using powdered-iron core recorded ∼17 % drop for the varistor-2 with 776 V clamping. Given the reduced varistor-2 voltage in EER core based prototype, we can infer that is superior to the present design in terms of surge absorption. More importantly, we can quantify the reduction percentage of varistor-2 clamping as ∼10 % (Table 7.9) which is a considerable improvement shown by the air-gapped prototype relative to present SCASA design.

Another important aspect of gapped EER core is the energy losses associated with air-gap: specially under transient operation when SCASA transformer becomes active, fringing losses can be significant. This gap effect drastically increase the total losses due to fringing and leakage flux around the air gap (More information is described in Chapter 5). The fringing flux in EER core intersects the copper windings, creating excessive eddy currents in the SCASA coupled-inductor coils. These unrestrained core losses facilitates the dissipation of surge energy and optimize the load-end characteristics as indicated by Table 7.9 and Figure 7.11. A detailed discussion about fringing losses due to eddy currents in SCASA circuit is beyond the scope of this thesis. However, more information about fringing flux patterns in air-gapped EER cores is found in Appendix E.

Furthermore, gapped ferrite cores have advantages over powder cores in terms of the manufacturing cost. With regard to the relatively easy production, gapped ferrites cost ∼40 % less compared to the complex manufacturing (air-bubble distribution) process of powdered-iron cores. The convenience of air-gap insertion in terms of trimming make these EER cores commercially affordable and mass-producible. A comparison of usability (based on surge reduction) and

Table 7.10: Comparison of performance level and relative cost of Kool μu powdered-iron core (0077071A7) and air-gapped ferrite EER core (R43521A125) used in SCASA prototype design

Magnetic Core	Material	Usability in SCASA surge protector	Relative Cost
Powdered-iron Toroid (0077071A7)	Kool μu	Usable	X
Un-gapped EER core (R43521)	R-Ferrite	Very Limited	~ 0.6 X
Air-gapped EER core (R43521A125)	R-Ferrite (Air-gapped)	Highly Usable	~ 0.6 X

relative cost of powdered-iron core (0077071A7) vs gapped EER core (R43521A125) is presented in Table 7.10. As described previously in Chapter 5, the suitability of ungapped ferrites is very limited even for R43521 due to poor energy storage capability.

Yet another benefit of using gapped ferrites is that they have much better tolerance limits than powdered-iron cores in transformer design. Gapped ferrites typically have a ±3% tolerance on inductance compared to powder cores' ±8% [118]. Since self-inductances of SCASA transformer windings lie in μH range, having a reduced tolerance is useful in determining optimum circuit parameters. Considering aforementioned factors, the discussion provided in this Section clearly indicates that the magnetic-permeance based core selection is highly relevant to our surge protection application, and the air-gapped ferrite EER core (R43521A125) results in a significant performance enhancement of SCASA surge suppression.

7.5 Chapter Summary

In this chapter, we investigated the possibility of optimizing SCASA technique by adopting commercially available magnetic cores. In deciding the optimum core under industry price constraints, we based our selection on maximum flux density and permeance coefficient of various powdered-iron toroids and low-cost EER type air-gapped cores. Improvement of the present design was highlighted as per clamping voltage reduction under repetitive surges.

In the next chapter, conclusions arising from this thesis are discussed with an emphasis on possible future research work.

Chapter 8

Conclusions and Future Research Work

The research objectives formulated during an early stage of this study were aimed at improving the patented SCASA surge protector developed and tested by the power electronics team at University of Waikato. Based on the investigations of surge withstanding capability of supercapacitors (SCs), our team has discovered the novel use of a SC sub-circuit inside a surge protector. Compared to traditional applications as energy storage elements, the use of SCs as a surge endurant element that facilitates transient energy circumvention is a remarkable implementation in SCASA design. First, I highlight key concepts arising from initial research work.

- Supercapacitors have a million times larger capacitance and extremely low ESR compared to electrolytic capacitors (ECs), thus greater energy density and larger time-constants than ECs. Also, due to low ESR, power density of SCs is much bigger than rechargeable batteries.
- Due to larger RC constant circuits, for a transient in the order of few microseconds, SCs develop only few milli-volts across the terminals, whereas ECs exceed their rated voltage leading to failure.
- Out of various SC types, only symmetric electrical dual layer capacitors (EDLCs) are suitable for transient suppression circuits. As transient surges can appear in both polarities, asymmetric hybrid capacitors (HCs) and pseudo-capacitors (PCs) are vulnerable to electrode damage.
- SCASA is a circuit topology designed to allow EDLCs to function inside a practical surge protector without exceeding the low DC rating of $\sim$2.7 V under 230 V AC operation, but facilitates surge dissipation for transient conditions.

The core of this thesis is based on the investigation of magnetic component utilized in present SCASA design; hence, chapter development and research outcomes are aimed towards predicting, validating and optimizing the properties of transformer core. Notably, the study of magnetic core selection problem (discussed in Chapter 3) of first SCASA version revealed the following important outcomes:

- Commercially available ferrite cores did not perform well in SCASA surge protector, while a powdered-iron toroid such as Kool μu 0077071A7 was able to perform satisfactorily.
- From the magnetic action of coupled-inductor, it was discovered that pure ferrites possess a relatively low energy storage capability than powdered-iron alloys, thus usability for surge absorption is highly limited.

- In addition, the dissimilarity of hysteresis behaviour and relative permeability between ferrite and powdered-iron materials were identified as key criteria for core selection in SCASA. Specially with a narrow B-H loop, it was found that ferrites reach magnetic saturation at a low flux density than powdered-iron leading to poor performance under high-current transients.
- Due to high permeability of magnetically soft ferrites, they are characterized to have very low core reluctance. But with the distribution of air gaps, powdered-iron has a high magnetic reluctance; this effect was recognized as a main factor for better energy absorption.

While present SCASA topology performs well for IEC-61000-4-5/IEEE-C62.45-2002 standard surge tests, the following limitations were identified with the study of Kool μu toroid's magnetic action.

- Although the powdered-iron core shows greater energy storage, it also accompanies an inductive energy release that transfers towards the load side in terms of a reversed voltage (negative surge) peak. This phenomenon was experimentally verified by disconnecting the SC sub-circuit loop of SCASA circuit.
- According to oscilloscope waveforms, the second metal oxide varistor (Var2) connected to load-side indicated an output clamping voltage between 780–800 V under a 6 kV/3kA surge pulse. As internal degradations may occur above 700 V (for repeated surges), the need for a clamping improvement emerged.

To address above limitations, I first came up with an analytical model based on magnetic permeance. Theory development during this research phase was aimed at explaining the operation of SCASA transformer under both 230 V AC and transient conditions. Following are the highlights of permeance model described in Chapter 4.

- Compared to the fundamental magnetic property of permeability which depends only on the material type, permeance has a dependency on material as well as core geometry (cross-section and path-length).
- SCASA magnetic core possess significant leakage flux due to the presence of air gaps inside the Kool μu powdered-iron toroid; hence deviate from ideal transformer behaviour.
- These non-ideal characteristics were modelled using magnetizing permeance (Λ_m) and leakage permeance (Λ_σ) to construct a comprehensive circuit model for the SCASA transformer.
- Model predictions for self-, mutual and leakage inductances were validated using LCR meter measurements with a $\sim$95% accuracy level. Furthermore, magnetic coupling between the SCASA transformer windings was estimated with $\sim$99% accuracy.
- Notably, our permeance based analytical approach predicted 50 Hz AC steady state and high-frequency transient state with a minimum disparity compared to empirical observations. As per clamp-meter current measurements, nearly 95% of the total RMS current passed through the transformer secondary, whereas only 5% flowed through the primary.

In moving towards SCASA optimization, I first experimented with modifying commercially available ferrite toroids (ZW43615TC) by introducing air gaps. Motivated by the reduction

effect of permeability due to air gaps, new theoretical models were developed in Chapter 5 for effective permeability, effective permeance and magnetic energy storage. Notably, air-gapped ferrite cores resulted in:

- a 95% depletion of the negative-surge effect that would otherwise pass to the load end
- lowering the self-inductances of primary and secondary SCASA windings compared to the pure ferrite core
- improving surge energy storage capability of the coupled-inductor
- a greater leakage of surge related magnetic flux leading to a better level of protection
- facilitating extra surge dissipation in terms of fringing flux and associated eddy current losses

The analytical work carried out in Chapter 6 to predict transient propagation became a complex task due to the high-frequency dependency of a standard surge pulse. Therefore, the following methods were adopted to theoretically validate SCASA operation in transient mode.

- Study of the frequency distribution of a 1.2/50 µs surge using Fourier transform.
- Adopting Laplace transforms to analyse LSS internal generation circuit and equivalent SCASA transformer in S-domain.
- Linearisation of metal oxide varistor states using a logarithmic relationship between current and varistor resistance.
- Fitting a model for the LSS-6230 to justify its output waveform in the presence of SCASA as EUT.

Outcomes emerged from above analytical methods were promising, and matched well with the LTSpice simulated waveforms. More importantly, I discovered;

- $\sim 92\%$ of the total transient current propagates through the primary winding of SCASA transformer, whereas only $\sim 8\%$ flow through the secondary
- majority of the surge energy ($\sim 49\%$) dissipates across Var1, while only $\sim 2.5\%$ of energy is lost across Var2
- inductive energy absorption is significant in primary winding where $\sim 20\%$ of surge gets stored; conversely, secondary coil stores only $\sim 2.5\%$ of total surge energy
- path resistance of connecting wires and leads is another key factor that is estimated to dissipate $\sim 22\%$ of the surge

Given the detailed energy estimation in various resistive and inductive components of SCASA circuit, I conclude that the coupled-inductor topology is successful in limiting the transient stress on two varistors that might otherwise fail with a minor surge endurance.

Final design optimizations were achieved by high performance magnetic cores manufactured using Kool μu, High-Flux and X-Flux type powdered-iron materials and low-cost air-gapped EER type ferrite. Optimum core material and shape within the industry price constraints were selected on the basis of permeance (inductance factor-A_L) of these commercial magnetic assortments. Overall performance improvements of SCASA technique can be summarized as:

- lifting saturation flux density of the coupled-inductor by $\sim 52\%$ with the use of X-Flux powdered-iron toroid. Compared to 10,500 gauss of Kool µu core, X-Flux core possessed

a high saturation level of 16,000 gauss. This allowed the surge protector to operate satisfactorily under high-magnitude transients with 55% greater saturation flux capacity

- R-ferrite based air-gapped EER core (R43521A125) rendered an effective-permeance (A_L) of 125 nH/turn^2 that is highly comparable to 61 nH/turn^2 of original Kool μu core
- increasing overall surge energy losses by means of greater leakage flux and fringing flux associated with the air-gapped EER core. The fringing effect around the air gap facilitated further surge dissipation in terms of eddy currents
- reduction of clamping voltage of Var2 by $\sim$ 10% with the use of air-gapped EER core. This resulted in optimizing load-side voltage characteristics of the SCASA device
- saving manufacturing cost by implementing commercial gapped EER cores in prototype development. Compared to the relatively expensive Kool μu powdered-iron toroids, air-gapped ferrites cost $\sim$40% less due to ease of production.

Overall, as the ultimate goal of this research, a better version of the SCASA surge protector was developed with reduced clamping and greater surge endurance that is highly suited as a low-cost commercial product.

8.1 Future Work

During different stages of this research, several subject matters that require an extended study were identified. A list of such topics which can be carried out to consolidate and expand the concepts presented in this thesis are discussed here according to the chapter order.

- In Chapter 3, the novel use of electrical double layer capacitors (EDLCs) for surge protection circuits was highlighted. However, due to the asymmetric electrode arrangement of hybrid capacitors and pseudo capacitors, it was realised that these supercapacitor types cannot be subjected to transient surges. Future experimental work can be conducted to substantiate this research idea using scanning electron microscopy (SEM). Such an attempt would validate the surface degradation of reduction-oxidation occurring chemical electrodes.
- The high-power resistor method I adopted in Chapter 4 to measure transient currents in SCASA transformer coils had some limitations due to extra 0.2 Ω resistive elements. This effect slightly modified the current sharing between the primary and secondary windings as predicted by Laplace solutions. However, to overcome this limitation, more accurate measurements can be carried out using a Rogowski coil current transducer which is well suited for high-frequency transient detection.
- Permeance model theorized in Chapter 4 is expandable to calculate transient induced voltages in primary and secondary windings of the couple-inductor. Magnetizing and leakage permeances (Λ_m and Λ_σ) of Kool μu powdered-iron toroid could be applied to this matter along with the first time-derivative of primary and secondary currents.
- Out of the various energy losses associated with air-gapped transformers (described in Chapter 5), leakage flux effect was experimentally confirmed for gapped toroid (ZW43615TC) and EER (R43521A125) core. However, the fringing flux loss (corresponding eddy current

dissipation) can be measured using a high-resolution infrared camera to justify our predictions. In addition, an investigation about the fringing effect could be carried out with a detailed theoretical model.

- By utilizing a larger cross-section toroid of X-Flux material or low-cost air-gapped ferrite EER core, SCASA topology can be advanced to a higher energy version (∼200 J or more). LSS-F03 lightning surge simulator could be used in evaluating the surge endurance of such a design with 15 kV standard transients.
- The present SCASA surge protector optimized during this research is only capable of suppressing differential-mode transient surges. However, a fully versatile SCASA can be developed to incorporate both differential-mode and common-mode surges. Such a circuit will require two coupled inductors (for live-neutral and live-earth) or four inductors coupled to a single transformer core. Moreover, this topology can be advanced into a 3-phase surge protector.

Appendix A

Commercial Implementation of SCASA as SMART TViQ

This appendix includes the brochure of patented commercial product (based on SCASA technique) known as SMART TViQ, developed and manufactured by Thor technologies, Australia in 2016.

SMART TViQ

ABSOLUTE PROTECTION
ULTIMATE FILTRATION

iQ3

MODEL: **STViQ/3**

POWER PROTECTION

23000
JOULES

NOISE FILTRATION

HIGH
EMI/RFI

WARRANTY

UP TO
$500K
FOR CONNECTED EQUIPMENT

REACTION TIME

1 NANO
0.000000001 SECOND

THOR
thortechnologies.com.au

MODEL: **STViQ/3**

SMARTTViQ iQ3

FEATURES

- PATENTED SC REGENERATION TECHNOLOGY
- IEC CONNECTOR
- 3 PIN ADAPTOR (CLOVER LEAF)
- SPACE SAVING FLAT HEAD PLUG
- 1.2M CABLE LENGTH
- FIRE RETARDENT
- 6 YEAR REPLACEMENT WARRANTY

PROTECTS

- FLATSCREEN TV
- PROJECTORS
- POS/CASH REGISTER
- COMPUTERS

SC REGENERATION TECHNOLOGY

ABSOLUTE PROTECTION ULTIMATE FILTRATION

The STViQ uses a patented technology that revolutionises power protection. A standard power board may survive 1 or 2 exposures to 6,600V. The STViQ was exposed to 100 strikes at 6,600V within 1 hour and was performing like new with absolutaley no signs of stress or damage.

1. Power indicator
2. IEC connector
2. 3 pin adaptor (clover leaf)
4. Space saving flat head plug

SMART BRAIN

The slimline design allows for in-line insertion behind space challenge wall mounts. Is ideal for attaching to these wall brackets with the whole product no larger than a 3 pin plug used to power these devices. Great for projectors, point of Sale equipment and even computers, Tablets and Laptops.

TECHNICAL SMARTS

Product Dimensions: 160mm (L) x 25mm (H) x 25mm (W) | Supply voltage 240/V AC 50Hz | Maximum current rating 5amps/1200 W (VA) | Clamping Voltage 275VAC | Reaction speed less than 1 nanosecond | EMI/RFI noise reduction filter | In-line protection application | Operating conditions Indoor AC/Mains | Operating temperature -10C/+60C | Cable lenght 1.2m | Model no. STViQ/3

INSIDE THE SMART BRAIN

SmartBrain entry level filter is a passive technology. Managing to cover a wider range of shielding to like competitors by "cleaning" a wider range of unwanted frequency noise. The filter works both ways. Stopping noise from robbing equipment performance as well as connected devices' noise contaminating power.

THOR Technologies Pty Ltd
PO Box 95, Karrinyup Western Australia 6921
thortechnologies.com.au

AUSTRALIAN DESIGNED AND ENGINEERED
Made in China

Appendix B

Data-sheets of Lightning Surge Simulator Models

This appendix accommodate selected pages of user manuals of Noiseken lightning surge simulator models (LSS-6230 and LSS-F03) developed by Noiseken Laboratories, Japan.

Lightning Surge Simulator

NoiseKen

Lightning Surge Simulator

LSS-6230

- Lightning Surge Simulator
- Conforming to IEC61000-4-5 ed2 Standard
- Ring wave conforming to ANSI/IEEE C62.45 available
- Max. voltage 6.6kV output focusing on the practical use
- Monitor terminal standard equipped so as for easy waveform pre-checking
- Interlock built-in as the emergency stop function for safety
- Remote control software from PC ready as the option besides the stand-alone operation
- AC/DC CDN standard equipped. Available up to 3-phase AC500V 50A as the option
- CDN for Telecom lines, CDN for interconnection lines, isolation transformer, etc. ready as the option

Specification

Parameter	Specification		
■ Common			
Polarity	Positive / Negative		
Interval	(Minimum charging time) ~999 sec. 1 sec. step		
No. of output setting	1~999 times 1 time step		
■ Surge generating unit			
1.2/50μs-8/20μs Combination waveforms	Voltage surge	Output voltage	0.5~6.0kV ±10%
		Front time	1.2μs±30%
		Duration	50μs±20%
	Current surge	Output current	250~3000A ±10%
		Front time	8μs±20%
		Duration	20μs±20%
	Minimum charge time		10 Sec.
	Output impedance		2Ω±10%
0.5μs-100kHz Ring wave	Voltage surge	Output voltage	0.5~6.0kV ±10%
		Rise time	0.5μs±0.15μs
		Frequency	100kHz±20kHz
	Current surge	2nd peak voltage	40-110% of 1st peak voltage
		3rd peak voltage	40-80% of 2nd peak voltage
		4th peak voltage	40-80% of 3rd peak voltage
	Minimum charge time		5 Sec.
	Output impedance		12 Ω±3 6 Ω at 12 Ω selection in interruptive resistance 30 Ω±8 Ω at 30 Ω selection in interruptive resistance
Coupling network	Line - Line : 18μF, Line - PE : 10Ω+9μF, Line - PE simultaneous coupling (L+N-PE) : 9μF/9μF		
Decoupling coil	1.5mH		
AC EUT power capacity	Single phase AC 240V 16A MAX (50/60Hz)		
DC Eat power capacity	DC125V/16A MAX		
Phase angle control	0~360°±10°, Based on set injection / return angle		
■ Surge generating unit for external CDN			
10/700μs-5/320μs Combination waveforms	Voltage surge	Output voltage	0.5~6.0kV ±10%
		Front time	10μs±30%
		Duration	700μs±20%
	Current surge	Output current	12.5~150A ±10%
		Front time	5μs±20%
		Duration	320μs±20%
	Minimum charge time		15 Sec.
	Output impedance		40Ω±10%
■ Other			
Voltage monitor	BNC output, 1/1000±10%		
Current monitor	BNC output, 1mV/A±10%		
External communication	RS-232C optical communication		
Power supply	AC100V ~120V±10%, AC200V ~240V±10%,50/60Hz Power consumption : Less than 300VA		
Dimension	W430×H515×D500 mm(Projection excluded)		
Mass	Approx. 65kg		

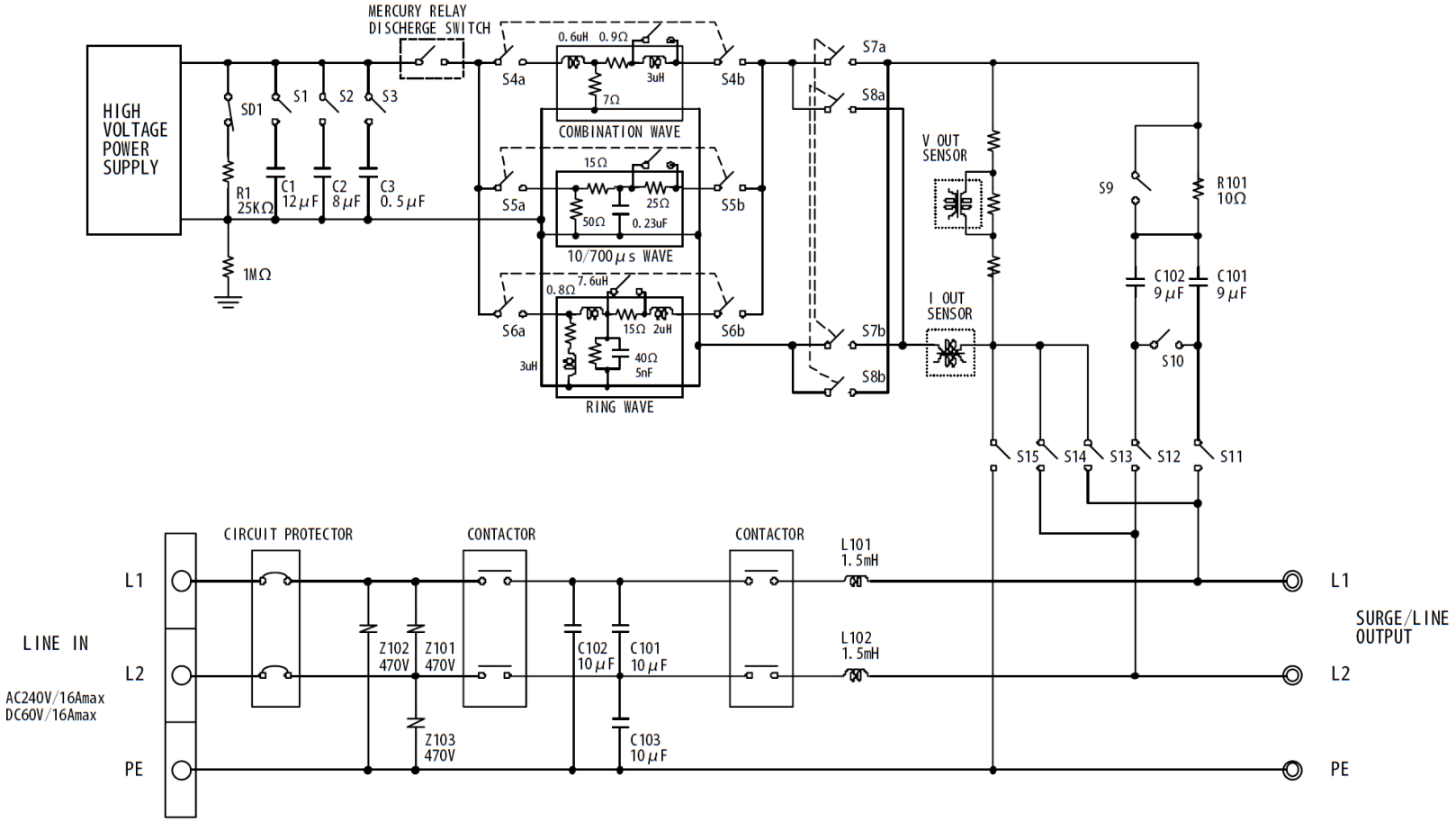

LSS-6130 BLOCK DIAGRAM

NoiseKen

Lightning Surge Simulator LSS-F03 series

Compliant with IEC61000-4-5 Edition 3 requirements

www.noiseken.com

NoiseKen NOISE LABORATORY

How to understand the model numbers

LSS-F03-□□
- 1 : Model for single phase EUT L/N/PE
- 3 : Model for 3-phase EUT L1/L2/L3/N/PE(Available both for single phase & 3-phase)
- A : 1.2/50μs-8/20μs (Totally 1 kind surge generates)
- C : 1.2/50μs-8/20μs、10/700μs-5/320μs (Totally 2 kinds)

Specification

Parameter	Specification		Note
Surge generating unit			
1.2/50μs-8/20μs Combination waveforms	Output voltage	0.5kV ~ 15kV ±10%	Common for the all models Voltage step : 0.1kV step The setting can be from 0kV
	Front time	1.2μs ±30%	
	Duration	50μs ±20%	
	Output current	250A ~ 7500A ±10%	
	Front time	8μs ±20%	
	Duration	20μs ±20%	
10/700μs-5/320μs Combination waveforms	Output voltage	0.5kV ~ 15kV ±10%	Models : C1/C3 Voltage step : 0.1kV step The setting can be from 0kV
	Front time	10μs ±30%	
	Duration	700μs ±20%	
	Output current	12.5A ~ 375A ±10%	
	Front time	5μs ±20%	
	Duration	320μs ±20%	
Output polarity	Positive / Negative		
Interval	10 sec.~989 sec., depending on the set voltage 10 sec. (< 6kV)		15 sec.~ in 10/700μs waveform
Output impedance	2Ω ±10%		1.2/50μs waveform
	40Ω ±10%		10/700μs waveform
AC/DC CDN			
Coupling surge waveform	1.2/50μs-8/20μs combination waveforms		
Max. coupling surge voltage / current	Up to the values which can be set		
Coupling network	18μF	Between LINE - LINE (10Ω +9μF selectable)	
Correspondent to IEC61000-4-5	10Ω ±9μF	Between LINE - PE (18μF selectable)	
Injection mode	Between LINE - LINE, Between LINE - PE		
Power supply lines structure for EUT	Single phase AC	: L/N/PE	Model : A1 / C1
	DC	: +/-/PE	
	3-phase AC	: L1/L2/L3/N/PE (Common for single phase and 3-phase)	Model : A3 / C3
	DC	: +/-/PE	
EUT power capacity	AC240V/20A MAX 50/60Hz DC125V/20A MAX		Model : A1 / C1
	AC500V/50A MAX 50/60Hz DC125V/50A MAX		Model : A3 / C3
Decoupling coil	1.5mH		
Phase angle control	0 ~ 360° ±10°		
CDN for Telecom lines (Only in model C1 and C3)			
Coupling surge waveform	1.2/50μs-8/20μs combination waveforms		
	10/700μs-5/320μs combination waveforms		
Max. coupling surge voltage / current	6 kV(Waveform specifications can be met up to 2kV for 1.2/50uS waveform and up to 4kV for 10/700 waveform)		
Impedance matching resistors	40Ω	80Ω per 1 line at 2 lines	1.2/50 μs waveform
		160Ω per 1 line at 4 lines	
	25Ω per line		10/700 μs waveform
Coupling mode	Common mode		
Coupling network	Gas arrestor : 90V		
Line for EUT	2 lines / 4 lines DC50V/100mA MAX		Selectable
Decoupling coil	20mH		
Others			
Voltage monitor	BNC output, 1/2000±10%		In open-circuit for SURGE OUT
Current monitor	BNC output, 1mV/A±10%		In short-circuit for SURGE OUT
External communication	RS-232C optical communication		
Power supply	AC100V ~ AC240V ±10%50Hz / 60Hz		
Dimension	W555×H1450×D790 mm(A1/A3), W555×H1800×D790 mm(C1/C3)		Projection excluded (in all models)
Mass	A1:Approx.290kg A3:Approx.300kg C1:Approx.325kg C3:Approx.340kg		

Standard accessory

Item	Specification / Function	Q'ty	Correspondent model
Surge output cable	HOT / COM	2 pcs.	Common
Output cable to power supply lines	For single phase : L / N / PE	3 pcs.	A1 / C1
	For 3-phase : L1 / L2 / L3 / N / PE	5 pcs.	A3 / C3
Output cable to telecom lines	For 1~4 lines and GND	5 pcs.	C1 / C3
Arrestor unit	For coupling : Equipped to main unit panel	4 pcs.	C1 / C3
	For input protection : Equipped to main unit panel	4 pcs.	
Cable for monitor	BNC-BNC cable	1 pc.	Common
External interlock connector	5P plug (Short between #1 - #3)	1 pc.	Common
Power supply cable	For AC100V, 3P equipped with G connector cable	1 pc.	Common
High voltage connector cap	Equipped to main unit panel	5 pcs.	A1 / C1
		7 pcs.	A3 / C3
FG cable	For grounding the body	1 pc.	Common
Instruction manual	-	1 volume	Common

- These products use parts containing mercury. Please comply with lows or regulation in countries or states the products are used for the disposal.
- Certain periodical inspection shall be recommended since consumable parts are contained in the products.
  In the test to 3-phase 5 lines (with PE) power supply lines, a message which alert the inspection per around 200 sets (in the test to single phase (with PE) power supply lines, it is done per around 800 sets).
  (1 set in this case means that the test shall be done with 2 levels (eg. 0.5kV and 1kV) for the test series according to IEC61000-4-5)

* Exchange timing of the parts may differed depending on the operative conditions and environment. Please contact us for the more details.

Appendix C

Manufacturer Specifications of Supercapacitors

This appendix contains industry data-sheets of Maxwell and Vinatech 5 F supercapacitors used in SCASA surge protector (SMART-TViQ) circuit.

DATASHEET HC SERIES ULTRACAPACITORS

FEATURES AND BENEFITS*

- Up to 500,000 duty cycles or 10 year life
- Low internal resistance
- High power density
- 1F to 150F capacitance range
- -40° to 85°C operating temperature range

TYPICAL APPLICATIONS

- Back-up power for cache-to-flash applications
- Smart Meters
- Automotive subsystems
- Consumer and industrial electronics
- Wireless transmitters

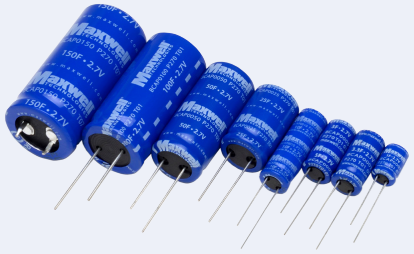

PRODUCT SPECIFICATIONS

ELECTRICAL	BCAP0001	BCAP0003	BCAP0005	BCAP0010 T01/T11/T12
Rated Capacitance[1]	1 F	3.3 F	5 F	10 F
Minimum Capacitance, initial[1]	0.8 F	2.6 F	4.0 F	8.0 F
Maximum ESR_{DC}, initial[1]	700 mΩ	290 mΩ	170 mΩ	75 mΩ
Test Current for Capacitance and ESR_{DC}[1]	0.1 A	0.33 A	0.5 A	1 A
Rated Voltage (65°/85°C)	2.70 / 2.30 V	2.70 / 2.30 V	2.70 / 2.30 V	2.70 / 2.30 V
Absolute Maximum Voltage[2]	2.85 V	2.85 V	2.85 V	2.85 V
Absolute Maximum Current	0.8 A	1.9 A	3.2 A	7.2 A
Leakage Current at 25°C, maximum[3]	0.006 mA	0.012 mA	0.015 mA	0.030 mA
TEMPERATURE				
Operating temperature range (Cell case temperature)				
Minimum	-40°C	-40°C	-40°C	-40°C
Maximum	65° / 85°C	65° / 85°C	65° / 85°C	65° / 85°C
Storage temperature range (Stored uncharged)				
Minimum	-40°C	-40°C	-40°C	-40°C
Maximum	70°C	70°C	70°C	70°C
PHYSICAL				
Mass, typical	1.1 g	1.7 g	2.3 g	3.5 g
Terminals	Wire Leads	Wire Leads	Wire Leads	Wire Leads
Vibration	-	-	-	-
Shock	-	-	-	-

Maxwell TECHNOLOGIES
Enabling Energy's Future™

2.7V 5F (0825)

Features

EDLC (Electric Double Layer Capacitor)

- High Power Density
- Over 500,000 cycle life (semi-permanent)
- Short-term Peak Power assist applications
- RoHS compliant
- Long-term reliability improved at high temperature and humidity

Drawing

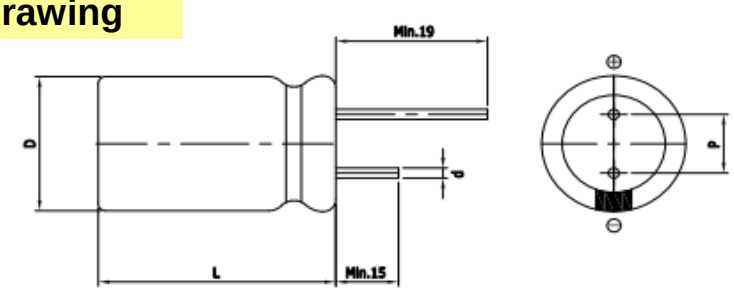

D (Φ)	8.0 +1.0 Max
L (㎜)	25.0 ±1.5
d (Φ)	0.6 ±0.1
P (㎜)	3.5 ±0.5

Specification

Item		Characteristics	
Product series		EDLC	
Rated Voltage (V_R)		2.7V	
Operating Temperature		-40 ~ +65℃	
Capacitance Tolerance		-10 ~ +30%	
High Temperature Load Life		After 1,000 hours at V_R loaded under +65℃, capacitors meet the following criteria.	
		Capacitance Change	≤ 30% of initial value
		ESR	≤ 2 times of specified value
		85°C Temperature	Max. 2.3V
Cycle Life Characteristics	Cycle	Over 500,000	
	△C	≤ 30% of initial value	
	ESR	≤ 2 times of specified value	
	Method	Cycle of Charge/discharge from V_R to $1/2V_R$	
Shelf Life		3 Years No Electrical Charge, Temperature below 25℃ (△C : ≤ 10% of initial value / △ESR : ≤ 50% of specified value)	

Part Number	Rated Voltage (V)	Capacitance (F)	ESR (mΩ)		Max. Current (A)	Leakage Current (㎃, 72hr)	Size (mm)
			AC(1㎑)	DC			D x L
WEC 2R7 505 QA	2.7	5	45	75	4.5	0.010	08 x 25

*** Max. Current** : 1 sec. discharge to $1/2V_R$

Version 1.3 2021.02.01.

VINATech Co., Ltd. **Tel : +82 63 715 3020** **E-mail : hycap@vina.co.kr** **Web : www.vina.co.kr**

Appendix D

Models for Metal Oxide Varistors

This appendix contains Littelfuse Pspice Ultra-MOV varistor models used for LTSpice circuit simulations of SCASA topology. In addition, the linearised relationship between varistor resistance and current is presented (In-Compliance Magazine).

```
******************************
*Varistor PSpice Model Netlist*
******************************
*
* ©    Littelfuse Inc.
*
*     March 25, 2003
*       version 4.2
*
* Representing typical characteristics for the following UltraMOV series
varistors:
*
*V20E130 V20E140 V20E150 V20E175 V20E200
*V20E230 V20E250 V20E275 V20E300
*V20E320 V20E385 V20E420 V20E440
*V20E460 V20E510 V20E550 V20E625
*
.SUBCKT UMOV  1 2 PARAMS: T=1 C=1pF L=1nH a1=1 a2=0 a3=0 a4=0 a5=0 a6=100u
a7=100u
E_non_lin       3 1     VALUE {T*(
+       10^(
+       +a1+a2*(log10(limit(v(4),a7,1g))-3)
+       +a3*2^(-log10(limit(v(4),a7,1g))+3)
+       +a4*exp(-log10(limit(v(4),a7,1g))+3)
+       +a5*exp(log10(limit(v(4),a7,1g))-3)
+       +a6*2^(log10(limit(v(4),a7,1g))-3)
+       )
+       -10^(
+       a1+a2*(log10(-limit(v(4),-1g,-a7))-3)
+       +a3*2^(-log10(-limit(v(4),-1g,-a7))+3)
+       +a4*exp(-log10(-limit(v(4),-1g,-a7))+3)
+       +a5*exp(log10(-limit(v(4),-1g,-a7))-3)
+       +a6*2^(log10(-limit(v(4),-1g,-a7))-3)
+       )
+       +limit(v(4)/a7*v(8),-v(8),v(8))
+       )}
L_series        5 6  {L}
H_H1            4 0  VH_H1 1k
VH_H1           5 70 0V
R_R2            0 4  1G
R_series        6 2  100u
V_V1            3 70  0V
E_x_zero        8 0     VALUE {10^(
+       a1+a2*(log10(a7/1e3))
+       +a3*2^(-log10(a7/1e3))
+       +a4*exp(-log10(a7/1e3))
+       +a5*exp(log10(a7/1e3))
+       +a6*2^(log10(a7/1e3))
+       )}
R_x_zero        8 0  1G
C_parallel      1 5 {C}
.ENDS
.SUBCKT V20E130 1 2 PARAMS: TOL=0
X1      1 2     UMOV PARAMS: T={1+TOL/100} L=12nH C=1.9nF a1=2.398 a2=4.817E-2
a3=1.273E-2 a4=-2.058E-3 a5=1.193E-2 a6=-2.71E-2
.ENDS
*
```

```
.SUBCKT V20E140 1 2 PARAMS: TOL=0
X1      1 2     UMOV PARAMS: T={1+TOL/100} L=12nH C=1.75nF a1=2.429 a2=4.817E-
2 a3=1.273E-2 a4=-2.058E-3 a5=1.193E-2 a6=-2.71E-2
.ENDS
*
.SUBCKT V20E150 1 2 PARAMS: TOL=0
X1      1 2     UMOV PARAMS: T={1+TOL/100} L=12nH C=1.6nF a1=2.467 a2=4.817E-2
a3=1.273E-2 a4=-2.058E-3 a5=1.193E-2 a6=-2.71E-2
.ENDS
*
.SUBCKT V20E175 1 2 PARAMS: TOL=0
X1      1 2     UMOV PARAMS: T={1+TOL/100} L=12nH C=1.4nF a1=2.518 a2=4.817E-2
a3=1.273E-2 a4=-2.058E-3 a5=1.193E-2 a6=-2.71E-2
.ENDS
*
.SUBCKT V20E200 1 2 PARAMS: TOL=0
X1      1 2     UMOV PARAMS: T={1+TOL/100} L=12nH C=1.3nF a1=2.558 a2=3.756E-2
a3=1.103E-2 a4=-1.894E-3 a5=8.026E-3 a6=-8.958E-3
.ENDS
*
.SUBCKT V20E230 1 2 PARAMS: TOL=0
X1      1 2     UMOV PARAMS: T={1+TOL/100} L=12nH C=1.1nF a1=2.649 a2=5.574E-2
a3=1.837E-2 a4=-3.412E-3 a5=1.362E-2 a6=-3.772E-2
.ENDS
*
.SUBCKT V20E250 1 2 PARAMS: TOL=0
X1      1 2     UMOV PARAMS: T={1+TOL/100} L=12nH C=1nF a1=2.683 a2=5.574E-2
a3=1.837E-2 a4=-3.412E-3 a5=1.362E-2 a6=-3.772E-2
.ENDS
*
.SUBCKT V20E275 1 2 PARAMS: TOL=0
X1      1 2     UMOV PARAMS: T={1+TOL/100} L=12nH C=900pF a1=2.726 a2=5.574E-2
a3=1.837E-2 a4=-3.412E-3 a5=1.362E-2 a6=-3.772E-2
.ENDS
*
.SUBCKT V20E300 1 2 PARAMS: TOL=0
X1      1 2     UMOV PARAMS: T={1+TOL/100} L=12nH C=800pF a1=2.764 a2=5.574E-2
a3=1.837E-2 a4=-3.412E-3 a5=1.362E-2 a6=-3.772E-2
.ENDS
*
.SUBCKT V20E320 1 2 PARAMS: TOL=0
X1      1 2     UMOV PARAMS: T={1+TOL/100} L=12nH C=750pF a1=2.8 a2=5.574E-2
a3=1.837E-2 a4=-3.412E-3 a5=1.362E-2 a6=-3.772E-2
.ENDS
*
.SUBCKT V20E385 1 2 PARAMS: TOL=0
X1      1 2     UMOV PARAMS: T={1+TOL/100} L=12nH C=700pF a1=2.885 a2=5.574E-2
a3=1.837E-2 a4=-3.412E-3 a5=1.362E-2 a6=-3.772E-2
.ENDS
*
.SUBCKT V20E420 1 2 PARAMS: TOL=0
X1      1 2     UMOV PARAMS: T={1+TOL/100} L=12nH C=600pF a1=2.925 a2=5.574E-2
a3=1.837E-2 a4=-3.412E-3 a5=1.362E-2 a6=-3.772E-2
.ENDS
*
.SUBCKT V20E440 1 2 PARAMS: TOL=0
```

```
X1      1 2     UMOV PARAMS: T={1+TOL/100} L=12nH C=500pF a1=2.947 a2=5.574E-2
a3=1.837E-2 a4=-3.412E-3 a5=1.362E-2 a6=-3.772E-2
.ENDS
*
.SUBCKT V20E460 1 2 PARAMS: TOL=0
X1      1 2     UMOV PARAMS: T={1+TOL/100} L=12nH C=400pF a1=2.967 a2=5.574E-2
a3=1.837E-2 a4=-3.412E-3 a5=1.362E-2 a6=-3.772E-2
.ENDS
*
.SUBCKT V20E510 1 2 PARAMS: TOL=0
X1      1 2     UMOV PARAMS: T={1+TOL/100} L=12nH C=350pF a1=3.006 a2=5.574E-2
a3=1.837E-2 a4=-3.412E-3 a5=1.362E-2 a6=-3.772E-2
.ENDS
*
.SUBCKT V20E550 1 2 PARAMS: TOL=0
X1      1 2     UMOV PARAMS: T={1+TOL/100} L=12nH C=300pF a1=3.051 a2=5.574E-2
a3=1.837E-2 a4=-3.412E-3 a5=1.362E-2 a6=-3.772E-2
.ENDS
*
.SUBCKT V20E625 1 2 PARAMS: TOL=0
X1      1 2     UMOV PARAMS: T={1+TOL/100} L=12nH C=250pF a1=3.092 a2=5.574E-2
a3=1.837E-2 a4=-3.412E-3 a5=1.362E-2 a6=-3.772E-2
.ENDS
*
*
```

Varistor Resistance R

Dividing the voltage by the current of each data point gives the point resistance value. Plots of resistance versus voltage (Figure 4) or current (Figure 5) can then be made. Figure 4 does not show any particular relationship between resistance and voltage. Remarkably, Figure 5 shows nearly a straight-line relationship between resistance and current of the form $r = 10^{(A + B \times \log(i))}$, where r is the resistance value, i is the current value and A and B are constants.

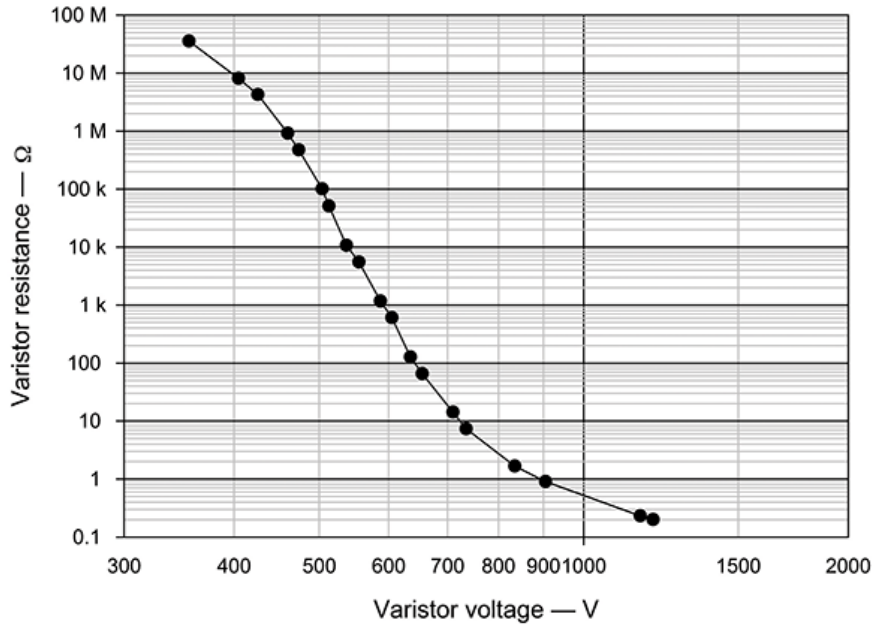

Figure 4: 14 mm 275 V rms varistor resistance versus voltage

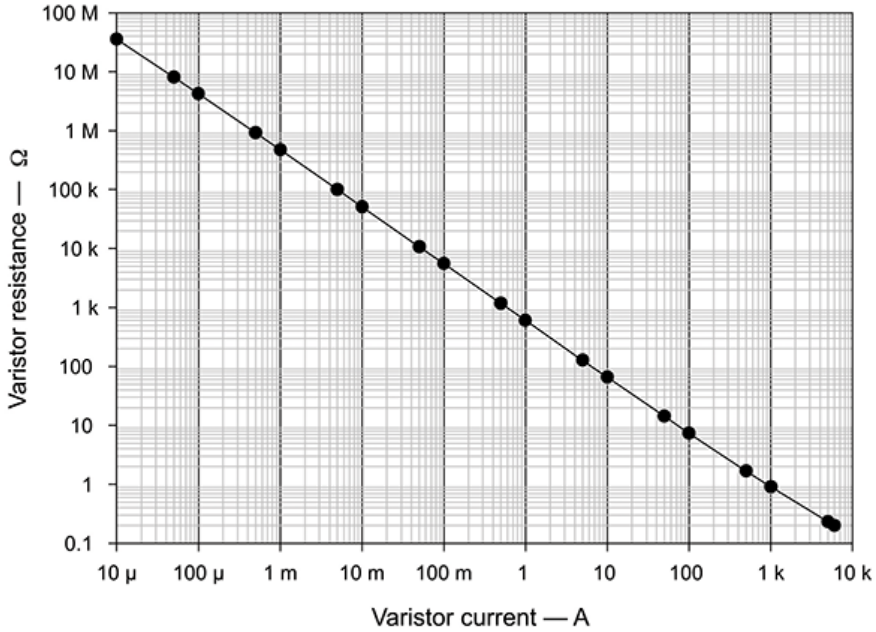

Figure 5: 14 mm 275 V rms varistor resistance versus current

Resistance-current Relationship

A straight-line equation fit to the data points is $r = 10^{(2.8-0.95 \times \log(i))}$, but the plot line shows a 16% error at the 5 kA and 6 kA points and the calculated resistance needs to be increased by 0.035 W. The resultant equation would then be $r = 0.035+10^{(2.8-0.95 \times \log(i))}$ and is shown in Figure 6. Although the equation has less than 5% error over most of the current range, in the 5 A to 100 A region there is about a 10 % error. These errors could be caused by incorrect data point values and the error may not matter if only the high impulse current operation is important.

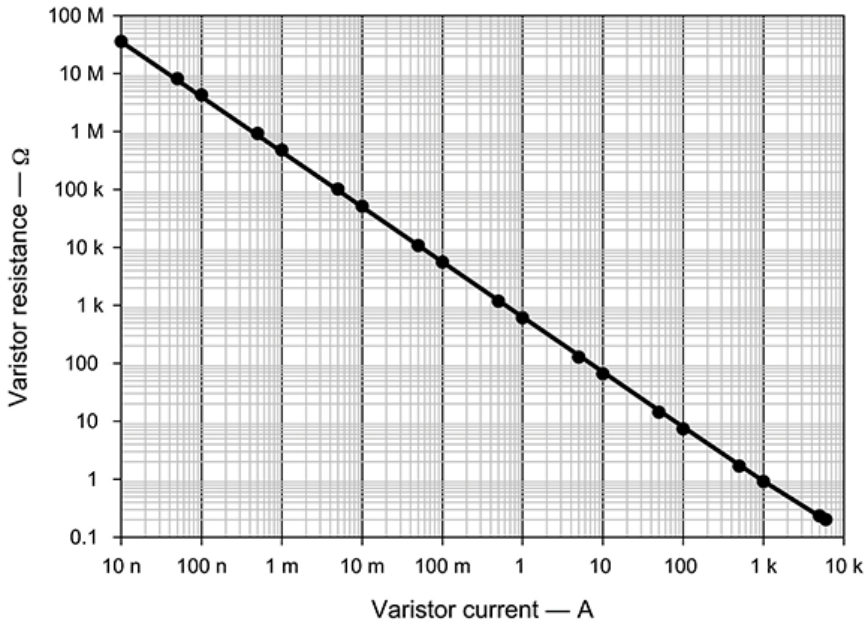

Figure 6: Figure 4 with r = 0.035+10^(2.8-0.95×log(i)) plot

Using curve-fitting software resulted in the more complex equation of $r = 5.793\times(i)^{-0.5} + (595.5 + 18\times LN(i))/i - 1/(1.953E-7 + 871\times((i)^2))$, which reduces the maximum error to 1%. One needs to be careful in using such software as outside the data current range some crazy results may occur that causes circuit simulations to fail. The fit quality of this equation (multiplied by current) to the data point set is shown in Figure 7.

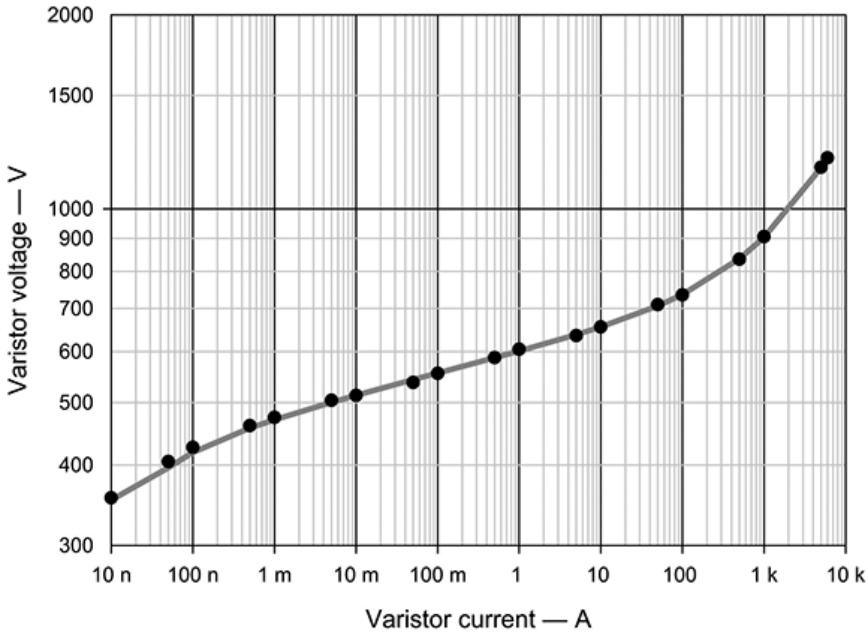

Figure 7: Figure 2 with curve-fitted equation plot

These results are not the full story as factors like di/dt have not been taken into account. Figure 8 shows the di/dt resistance effect on a 100 A peak current pulse initiating with di/dt applied values of 1.25A/µs, 12.5A/µs and 250A/µs. In Figure 8, the varistor resistance is normalised to the 12.5 A/µs value because the current rise time will be 8 µs and hence be similar to the virtual front time of an 8/20 impulse. Plotting di/dt on a logarithmic axis shows the measured values are in straight line with a relationship of $R_N = 0.9 + 0.4 \times LN(di/dt)$, where R_N is the resistance normalised to the 12.5 A/µs value. For the tested di/dt values the varistor R-I characteristic is modified by -9% and +12% depending on the di/dt limit values.

Appendix E

Manufacturer Specifications of Magnetic Core Assortments

This appendix contains industry data-sheets of various powdered-iron and ferrite core samples used in SCASA prototype design, Magnetics Inc. 2021.

0077071A7

110 Delta Drive
Pittsburgh, PA 15238
NAFTA Sales: (1)800-245-3984
HK Sales : (852)3102-9337
magnetics@spang.com
www.mag-inc.com

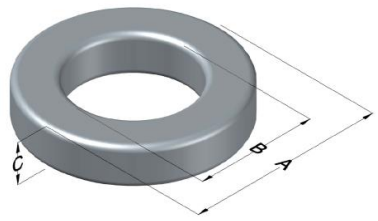

Kool Mμ Permeability (μ)	A_L (nH/T²)	Core Marking			Coating Color
		Lot Number	Part Number	Inductance Grade	
60	61 ± 8%	XXXXXX	77071A7	N/A	Black

Dimensions	Uncoated		Coated Limits			Packaging
	(mm)	(in)	(mm)	(in)		
OD (A)	32.80	1.291	33.66	1.325	max	Cardboard cut-outs Box Qty= 250 pcs
ID (B)	20.1	0.791	19.4	0.766	min	
HT (C)	10.7	0.420	11.5	0.450	max	

Electrical Characteristics			Physical Characteristics						
Watt Loss @ 100 kHz, 100mT max (mW/cm³)	DC Bias min (oersteds)		Voltage Breakdown wire to wire min (V_{AC})	Break Strength min (kg)	Window Area W_A(mm²)	Cross Section A_e (mm²)	Path Length L_e (mm)	Volume V_e (mm³)	Weight (g)
	80%	50%							
900	39.0	87.0	2000	79.0	297	65.6	81.4	5340	32

Winding Information							Temperature Rating
Winding Length Per Turn				Wound Coil Dimensions (mm)			Curie Temp: 500˚C
Winding Factor	(mm)	Winding Factor	(mm)	40% Winding Factor	OD	36.8	Coating Temp (Continuous up to): 200˚C
					HT	17.8	
				Completely Full Window	Max OD	46.7	Notes:
0%	37.4	40%	47.2		Max HT	28.0	
20%	42.4	45%	48.8	Surface Area (mm²)			
25%	43.5	50%	50.1				
30%	44.7	60%	53.2	Unwound Core		3,100	
35%	46.1	70%	56.7	40% Winding Factor		4,900	

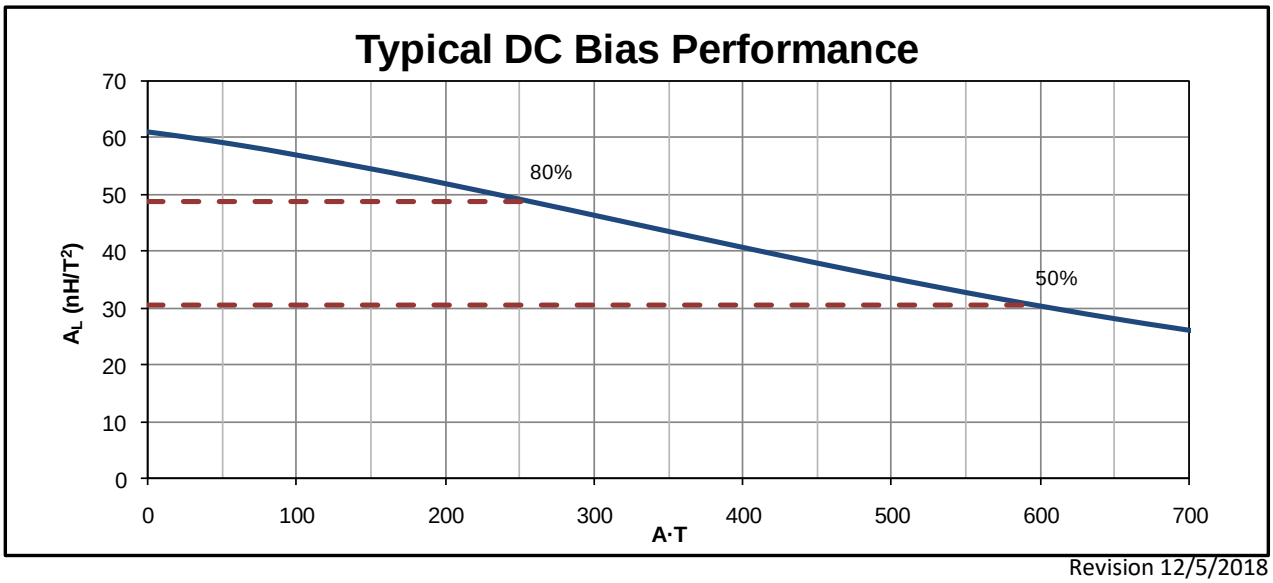

Revision 12/5/2018

0077083A7

110 Delta Drive
Pittsburgh, PA 15238
NAFTA Sales: (1)800-245-3984
HK Sales : (852)3102-9337
magnetics@spang.com
www.mag-inc.com

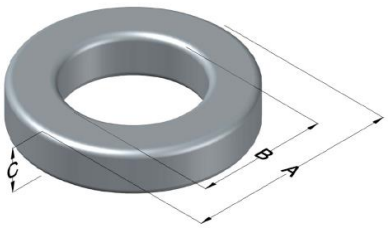

Kool Mμ Permeability (μ)	A_L (nH/T²)	Core Marking			Coating Color
		Lot Number	Part Number	Inductance Grade	
60	81 ± 8%	XXXXXX	77083A7	N/A	Black

Dimensions	Uncoated		Coated Limits			Packaging
	(mm)	(in)	(mm)	(in)		
OD (A)	39.90	1.570	40.77	1.605	max	Cardboard cut-outs Box Qty= 180 pcs
ID (B)	24.1	0.950	23.3	0.918	min	
HT (C)	14.5	0.570	15.4	0.605	max	

Electrical Characteristics			Physical Characteristics						
Watt Loss @ 100 kHz, 100mT max(mW/cm³)	DC Bias min (oersteds)		Voltage Breakdown wire to wire min (V_{AC})	Break Strength min (kg)	Window Area W_A(mm²)	Cross Section A_e (mm²)	Path Length L_e (mm)	Volume V_e (mm³)	Weight (g)
	80%	50%							
900	39.0	87.0	2000	126.0	427	107	98.4	10,600	61

Winding Information							Temperature Rating
Winding Length Per Turn				Wound Coil Dimensions (mm)			Curie Temp: 500˚C
Winding Factor	(mm)	Winding Factor	(mm)	40% Winding Factor	OD	44.3	Coating Temp (Continuous up to): 200˚C
					HT	22.4	
				Completely Full Window	Max OD	56.4	Notes:
					Max HT	35.2	
0%	48.2	40%	60.2	Surface Area (mm²)			
20%	54.3	45%	62.1				
25%	55.8	50%	63.7	Unwound Core	4,800		
30%	57.0	60%	67.3	40% Winding Factor	7,300		
35%	58.8	70%	71.5				

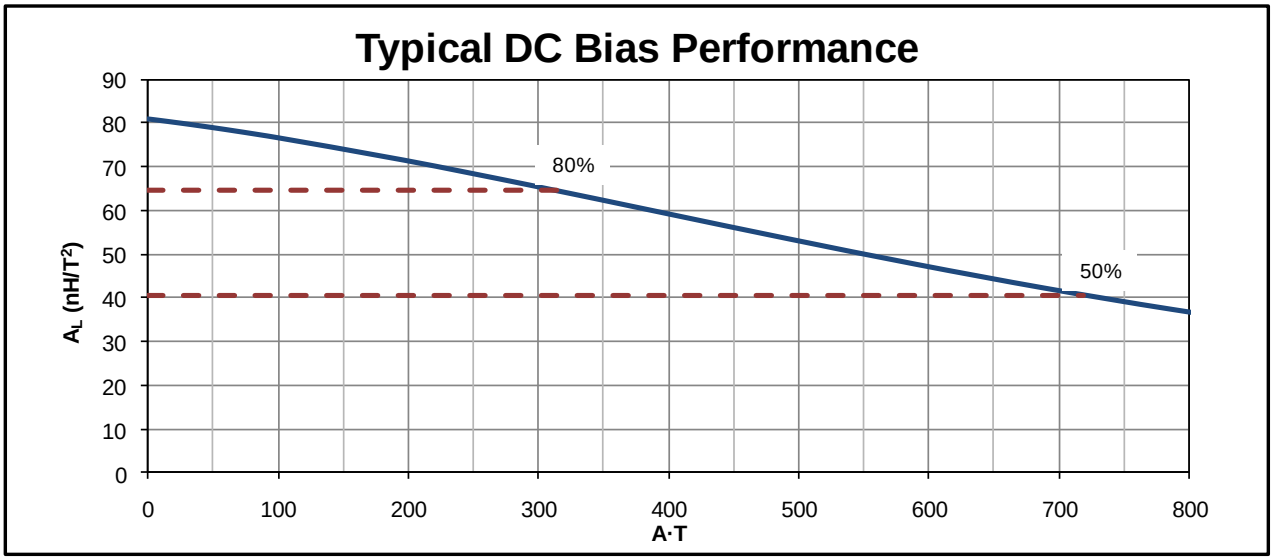

Revision 12/12/2018

C058071A2

110 Delta Drive
Pittsburgh, PA 15238
NAFTA Sales: (1)800-245-3984
HK Sales : (852)3102-9337
magnetics@spang.com
www.mag-inc.com

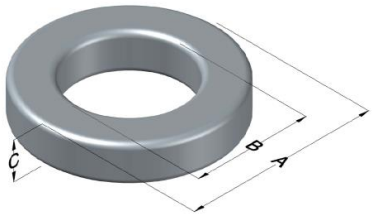

High Flux Permeability (μ)	A_L (nH/T²)	Core Marking			Coating Color
		Lot Number	Part Number	Inductance Grade	
60	61 ± 8%	XXXXXX	58071A2	X	Khaki

Dimensions	Uncoated		Coated Limits			Packaging
	(mm)	(in)	(mm)	(in)		
OD (A)	32.80	1.291	33.66	1.325	max	Cardboard cut-outs Box Qty= 250 pcs
ID (B)	20.1	0.791	19.4	0.766	min	
HT (C)	10.7	0.420	11.5	0.450	max	

Electrical Characteristics			Physical Characteristics						
Watt Loss @ 100 kHz, 100mT max (mW/cm³)	DC Bias min (oersteds)		Voltage Breakdown wire to wire min (V_{AC})	Break Strength min (kg)	Window Area W_A(mm²)	Cross Section A_e (mm²)	Path Length L_e (mm)	Volume V_e (mm³)	Weight (g)
	80%	50%							
900	90.0	170	2000	79.0	297	65.6	81.4	5340	41

Winding Information						Temperature Rating
Winding Length Per Turn				Wound Coil Dimensions (mm)		Curie Temp: 500˚C
Winding Factor	(mm)	Winding Factor	(mm)	40% Winding Factor	OD 36.8	Coating Temp (Continuous up to): 200˚C
					HT 17.8	
				Completely Full Window	Max OD 46.7	Notes:
0%	37.4	40%	47.2		Max HT 28.0	
20%	42.4	45%	48.8	Surface Area (mm²)		
25%	43.5	50%	50.1			
30%	44.7	60%	53.2	Unwound Core	3,100	
35%	46.1	70%	56.7	40% Winding Factor	4,900	

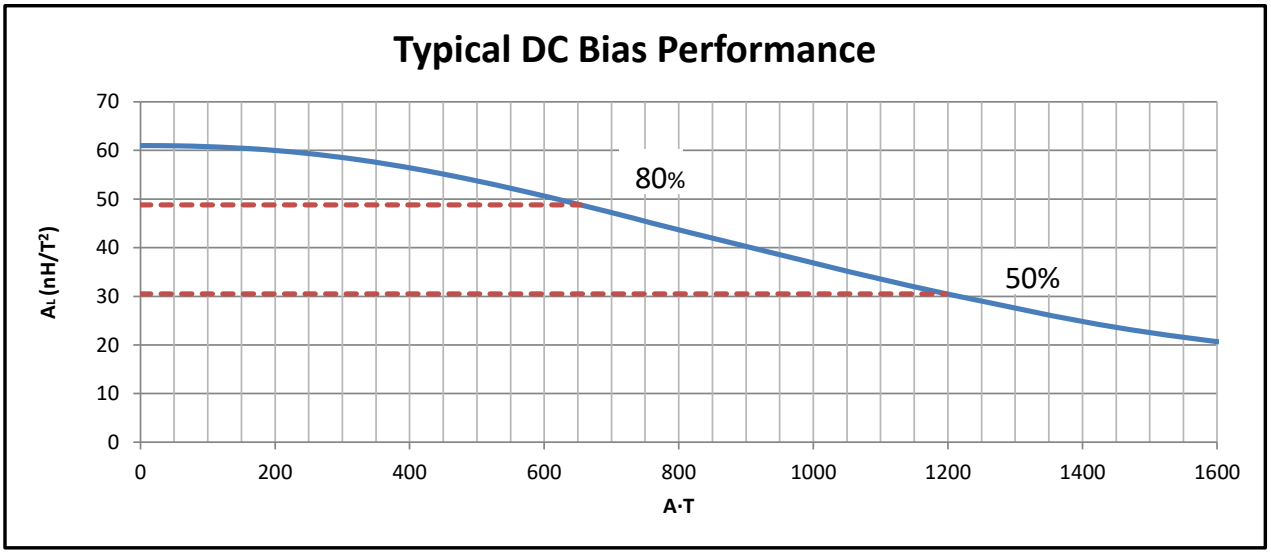

Revision 6/24/2019

0078550A7

110 Delta Drive
Pittsburgh, PA 15238
NAFTA Sales: (1)800-245-3984
HK Sales : (852)3102-9337
magnetics@spang.com
www.mag-inc.com

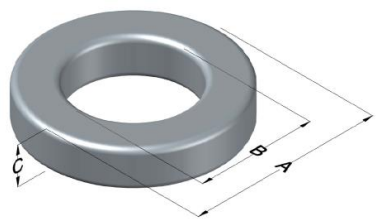

XFLUX Permeability (μ)	A_L (nH/T²)	Core Marking			Coating Color
		Lot Number	Part Number	Inductance Grade	
26	28 ± 8%	XXXXXX	78550A7	N/A	Brown

Dimensions	Uncoated		Coated Limits			Packaging
	(mm)	(in)	(mm)	(in)		
OD (A)	32.80	1.291	33.66	1.325	max	Cardboard cut-outs Box Qty= 250 pcs
ID (B)	20.1	0.791	19.4	0.766	min	
HT (C)	10.7	0.420	11.5	0.450	max	

Electrical Characteristics			Physical Characteristics						
Watt Loss @ 50 kHz, 100mT max (mW/cm³)	DC Bias min (oersteds)		Voltage Breakdown wire to wire min (V_{AC})	Break Strength min (kg)	Window Area W_A(mm²)	Cross Section A_e (mm²)	Path Length L_e (mm)	Volume V_e (mm³)	Weight (g)
	80%	60%							
850	185	320	2000	79.0	297	65.6	81.4	5,340	38

Winding Information							Temperature Rating
Winding Length Per Turn				Wound Coil Dimensions (mm)			Curie Temp: 700˚C
Winding Factor	(mm)	Winding Factor	(mm)	40% Winding Factor	OD	36.8	Coating Temp (Continuous up to): 200˚C
					HT	17.8	
				Completely Full Window	Max OD	46.7	Notes:
0%	37.4	40%	47.2		Max HT	28.0	
20%	42.4	45%	48.8	Surface Area (mm²)			
25%	43.5	50%	50.1				
30%	44.7	60%	53.2	Unwound Core	3,100		
35%	46.1	70%	56.7	40% Winding Factor	4,900		

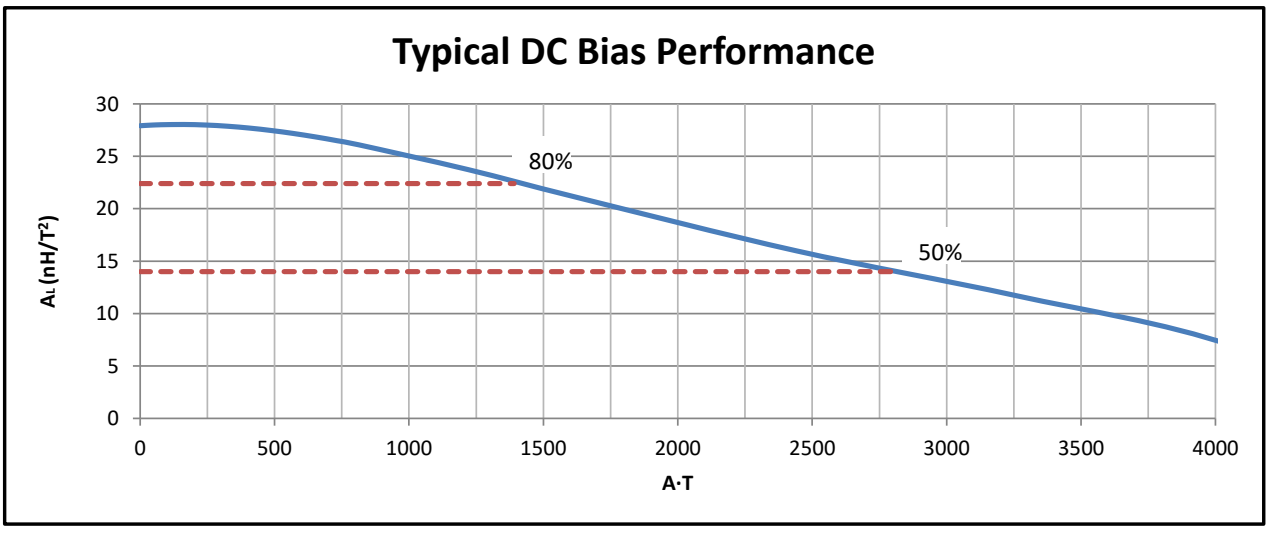

Revision 12/26/2018

MAGNETICS®
A Division of Spang & Company

Specification for:

ZW43615TC

110 Delta Drive
Pittsburgh, PA 15238
Phone: 412/696-1333
Fax: 412/696-0333
Email:magnetics@spang.com

DIMENSIONS

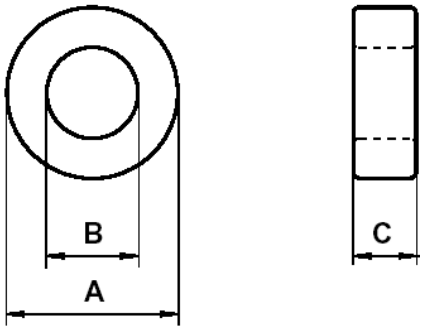

(mm)	Uncoated Nominal:	Coated Min:	Coated Max:
O.D. (A)	36	35.36	37.14
I.D. (B)	23	21.86	23.64
Ht. (C)	15	14.75	15.75

Eff. Parameters		
A_e mm^2	l_e mm	V_e mm^3
95.9	89.6	8596

INDUCTANCE

AL value (nH/T^2)	**Test conditions**
13400 ± 30%	10 kHz, 0.5 mT (For N = 5, use 0.42 mA), 25°C

ELECTRICAL LOSSES

tan δ / μ_i	**Production lot limit Average**	**Test conditions**	
≤ 4.1·10^{-6}	≤ 3.5 ·10^{-6}	10 kHz	0.5 mT, 25ºC
≤ 60·10^{-6}	≤ 50·10^{-6}	100 kHz	

COATING

Epoxy rated for 200°C continuous operation.
Voltage breakdown rating 2000 V Min Wire-to-Wire.

NOTE

Spec. Modifications	Previous	Revised
2005.11.08	Breakdown voltage > 1,000 V LF: General W material	Breakdown voltage > 2,000 V LF: Detail as indicated

Applications & Materials

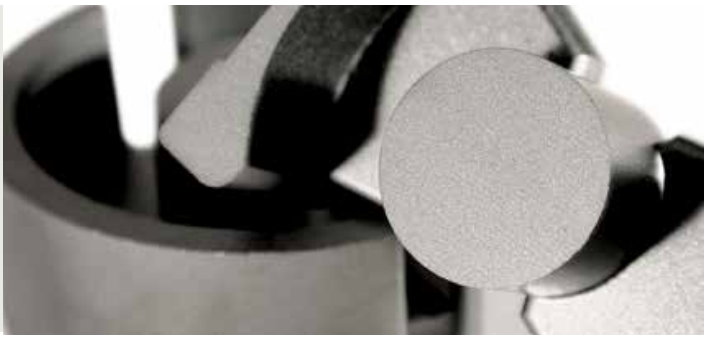

Ferrites are dense, homogenous ceramic structures made by mixing iron oxide with oxides or carbonates of one or more metals such as zinc, manganese, nickel or magnesium. They are pressed, then fired in a kiln at 1,000 - 1,500°C and machined as needed to meet various operational requirements. Ferrite parts can be easily and economically molded into many different geometries. A diverse set of materials, providing a range of desired electrical and mechanical properties, are available from Magnetics.

Magnetics' ferrite cores are manufactured for a wide variety of applications. Magnetics has the leading MnZn ferrite materials for power transformers, power inductors, wideband transformers, common mode chokes, as well as many other applications.

ADVANTAGES OF MAGNETICS' FERRITES

- The widest range of toroid sizes in power and high permeability materials
- Superior toroid coatings available in several options: epoxy, nylon and Parylene C
- Standard gapping to precise inductance or mechanical dimension: wide range of coil former and assembly hardware available
- The full range of standard planar E and I cores
- Rapid prototyping capability for new development

FERRITE APPLICATIONS

APPLICATIONS	DESIRED PROPERTIES	PREFERRED MATERIALS	AVAILABLE SHAPES
Broadband Transformers	Low loss, high μ. Good frequency response.	J, W	Pot cores, Toroids, E, U & I cores, RM cores, EP cores
Common Mode Chokes	Very high μ (permeability).	J, W	Toroids, E Cores
Converter and Inverter Transformers	Low losses, high saturation.	F, L, P, R, T	Toroids, E, U & I cores, Pot cores, RS cores, Planar cores
Differential Mode Inductors	Low losses, high temperature stability, good stability across load conditions.	F, P, R, T	Gapped Pot cores, EP cores, E cores, RM cores, Planar cores, PQ cores
Linear Filters and Sensors	Good loss factor, linearity and temperature linearity at low drive level.	C, E, V	Pot cores, Toroids
Narrow Band Transformers	Moderate Q, high μ, high stability.	F, J	Pot cores, Toroids, RM cores, EP cores
Noise Filters	High μ, good frequency response.	J, W	Toroids
Power Inductors	Low losses at high flux densities and temperatures. High saturation. Good stability across load conditions.	F, L, P, R, T	Pot cores, E cores, PQ cores, RM cores, Planar cores
Power Transformers	High μ and low losses at high flux densities and temperatures. High saturation. Low exiting currents.	F, L, P, R, T	Ungapped Pot cores, E, U & I cores, Toroids, EP cores, RS cores, DS cores, PQ cores, Planar cores
Pulse Transformers	High μ, low loss, high B saturation.	J, W	Toroids
Telecom Inductors	Low losses, high temperature stability, good stability across load conditions.	F, P, R, T	Pot cores, EP cores, E cores, RM cores, Planar cores

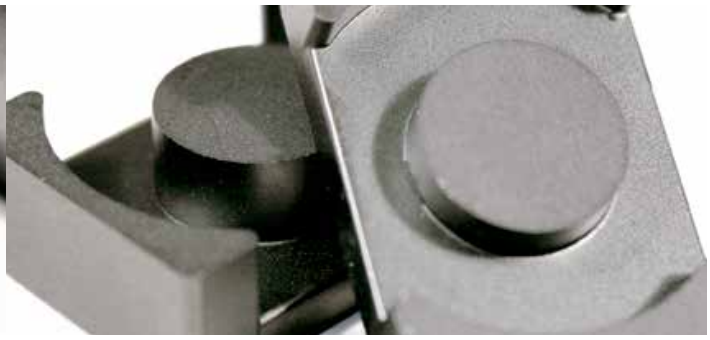

			INDUCTORS & POWER TRANSFORMERS					EMI/RFI FILTERS & BROADBAND TRANSFORMERS		LINEAR FILTERS & SENSORS		
MATERIAL			**L**	**R**	**P**	**F**	**T**	**J**	**W**	**C**	**E**	**V**
Initial Permeability	μ_i		900 ±25%	2,300 ±25%	2,500 ±25%	3,000 ±20%	3,000 ±25%	5,000 ±20%	10,000 ±30%	900 ±25%	2,000 ±25%	2,300 ±25%
Maximum Usable Frequency (50% roll-off)	f	MHz	≤6	≤1.8	≤1.8	≤1.5	≤1.5	≤0.7	≤0.5	≤8	≤3	≤1.5
Relative Loss Factor X 10^{-6} 25°C		tan δ/μ_{ioc}						≤15 100 kHz	≤7 10 kHz	≤10 300 kHz	≤3 100 kHz	≤5 100 kHz
Curie Temperature	T_c	°C	>300	>210	>210	>210	>220	>145	>135	> 200	>160	>170
Flux Density @ 1,194 A/m (15 Oe) 25°C	B_m 10 kHz	G mT	4,200 420	4,700 470	4,700 470	4,700 470	5,300 530	4,300 430	3,900 390	3,800 380	3,600 360	4,400 440
Remanence 25°C	B_r	G mT	1,500 150	1,600 160	1,600 160	1,500 150	1,500 150	1,000 100	800 80	1,500 150	700 70	1,500 150
Power Loss (PL) Sine Wave in mW/cm³ (typical)	25 kHz 200 mT (2,000 G)	@25°C		90	180	60	80					
		@60°C		65	110	55	75					
		@100°C		60	65	90	70					
		@120°C		65	110	125	75					
	100 kHz 100 mT (1,000 G)	@25°C		87	70	70	65					
		@60°C		64	50	65	57					
		@100°C		58	65	110	55					
		@120°C		64	45	150	58					
	500 kHz 50 mT (500 G)	@25°C	290									
		@60°C	150									
		@100°C	115	175	300		150					
		@120°C	130									
Resistivity	ρ	Ω-m	10	5	5	5	5	0.5	0.1	2	2	1
Density	δ	g/cm³	4.8	4.8	4.8	4.8	4.8	4.8	4.9	4.7	4.7	4.8

TYPICAL MECHANICAL PROPERTIES OF FERRITE MATERIALS

MECHANICAL DATA		UNITS	THERMAL DATA		UNITS
Bulk Density	4.85	gm/cm³	Coefficient of Linear Expansion	$10.5x10^{-6}$	°C^{-1}
Tensile Strength	$5.0, 7.0x10^3$	kgf.mm^{-2}, lbs.in^{-2}	Specific Heat (25°)	800	J/kgK
Compressive Strength	$45, 63x10^3$	kgf.mm^{-2}, lbs.in^{-2}	Thermal Conductivity (25-85°C)	3500-4300	μW.mm^{-1}.°C^{-1}
Youngs Modulus	$12.4x10^3, 1.8x10^7$	kgf.mm^{-2}, lbs.in^{-2}		35-43	mW.cm^{-1}.°C^{-1}
Hardness (Knoop)	650 Typical			.0083-.010	cal.s^{-1}.cm^{-1}.°C^{-1}
Resistivity	10^2-10^3	ohm-cm			

Powder Core and Gapped Ferrite Core Comparison

Although high grade ferrite core losses are lower than powder core losses, ferrite often requires low effective permeability to prevent saturation at high current levels. Ferrite, with its high initial permeability, requires a relatively large air gap to get a low effective permeability. This large air gap results in gap loss, a complex problem which is often overlooked when comparing material loss curves. Gap loss can drastically increase total losses due to fringing flux around the air gap (Figure 2). The fringing flux intersects the copper windings, creating excessive eddy currents in the wire.

The soft-saturation characteristics of powder cores are designed to exploit the controlled, partial roll-off of permeability in the material while having more than twice the flux capacity of ferrite. This slow roll-off also has the added benefit of improved fault tolerance. Additionally, flux capacity in powder cores stays relatively constant with temperature in comparison to ferrite.

Gapped ferrite cores do have advantages over powder cores. Gapped ferrites typically have a ±3% tolerance on inductance compared to powder cores' ±8%. Gapped ferrites are available in a wider selection of shapes. Since ferrite material can have a higher gapped effective permeability it is well suited for relatively low bias applications, such as feed forward transformers and low biased inductors.

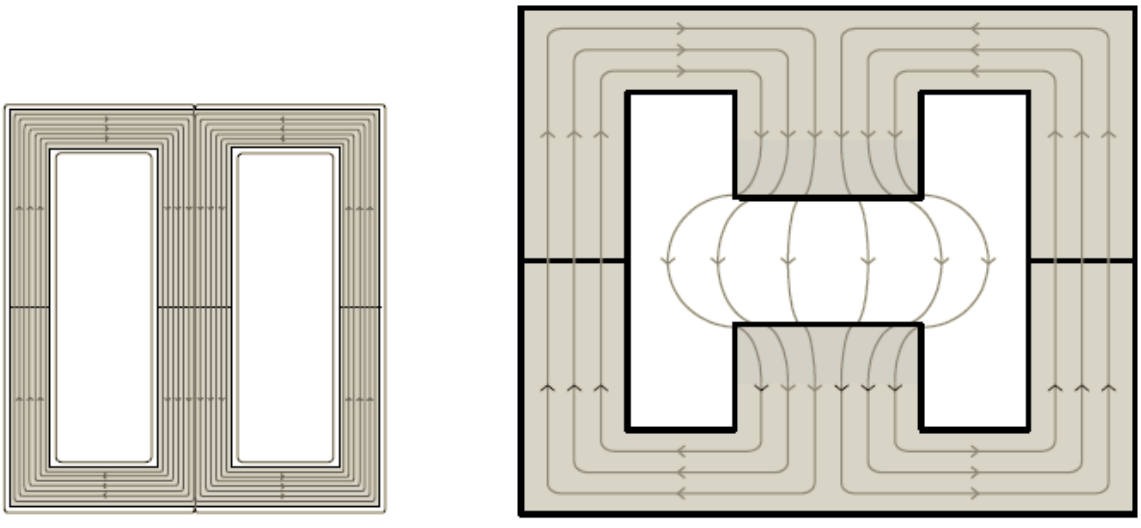

FIGURE 2

Appendix F

MATLAB Commands

This appendix includes selected MATLAB codes used in this thesis for graph plotting and analytical calculations.

MATLAB Commands

```
%%Open voltage: comparison of LSS waveforms (LTSpice, Analytical, LSS-Out
%%and EUT-Out


clear all;
A=1.037;
Vp=6050;
alpha = 1/(68.22e-6);
beta = 1/(0.407e-6) + 1/(68.22e-6);
N=A*Vp;
% Ls = 62e-6;
% Lp = 3.8e-6;
a=alpha;
b=beta;

t=(0:1:145)*1e-6;
t1 =(5:1:150)*1e-6;
t2 = (5:1:155)*1e-6;

v = N*(exp(-alpha*t)- exp(-beta*t));
v2 = importdata('ch6_sim_sadeesh_LSS_waveforms3.txt');

vv = xlsread('F0070CH4_N.xls','sheet1','D:E');
vv2 = xlsread('F0070CH1_N.xls','sheet1','D:E');


hold on; xlim([0 inf]);

plot(t1*1e6,v, '--o'); title('IEEE 1.2/50 us Standard Voltage Wave');
xlabel('Time T(us)'); ylabel('Voltage V(t)')  %analytical


plot(v2.data(:,1)*1e6,v2.data(:,2),'*'); title('IEEE 1.2/50 us Standard
Voltage Wave'); xlabel('Time T(us)'); ylabel('Voltage V(t)') %Ltspice


plot(5+vv(:,1)*1e6,vv(:,2),'.'); xlim([0 100]) %LSS-panel

plot(5+vv2(:,1)*1e6,vv2(:,2),'-'); xlim([0 100]) %EUT-injected

legend('Analytical Plot','Ltspice Plot','LSS Setting Out ','EUT Line Out')


grid on


%%Short-circuit current: comparison of LSS current waveforms (LTSpice,
%%Analytical, LSS-Out and EUT-Out


tau1= 28.1e-6;
tau2= 1e-6;
tau3=3.911e-6;
```

```
t=(0:1:95)*1e-6;
tt=(0:1:95)*1e-6;


Is = 4400* sin(0.126*1e6*tt).* exp(-tt/tau1) .*(1-exp(-tt/tau2));
%including the ring

Iss= 3000 * 1e18 * (0.01243).* t.^3 .* exp(-t/tau3);

II = xlsread('F0075CH3.csv','F0075CH3','D:E');
II2 = xlsread('F0077CH1.csv','F0077CH1','D:E');

I2 = importdata('ch6_sim_sadeesh_LSS_waveforms4.txt');


hold on

%plot(2+tt*1e6,Is,'--*'); title('IEEE 8/20 us Standard Current Wave');
xlabel('Time T(us)'); ylabel('Current-I(A)') %Practical current
(analytical)

plot(4+t*1e6,Iss,'--o'); title('IEEE 8/20 us Standard Current Wave');
xlabel('Time T(us)'); ylabel('Current - I(A)') % Analytical


plot(I2.data(:,1)*1e6,I2.data(:,2),'--*'); title('IEEE 8/20 us Standard
Current Wave'); xlabel('Time T(us)'); ylabel('Current - I(A)') %Ltspice


plot(5+II(:,1)*1e6,II(:,2),'.'); xlim([0 35]) % LSS-panel out


plot(5+II2(:,1)*1e6,II2(:,2)*1.26,'-'); xlim([0 35]) % EUT-injected out


legend('Analytical Plot','Ltspice Plot','LSS Setting Out','EUT Line Out')


grid on


% Non-ideal characteristics of SCASA transformer (Kool Mu, ungapped and
gapped Ferrite toroids)

% Self inductance of secondary

x = [1 3 5 7 9 11 13 15];
y1 = [56.65 56.6 56.5 56.5 56.5 56.5 56.5 56.45];
% y2 = [11600 11370 11260 11220 11200 11200 11200 11210];
% y3 = [169.6 169.5 169.5 169.5 169.4 169.4 169.35 169.32];
% y4 = [65.2 65.2 65.18 65.16 65.14 65.1 65.1 65];

y5 = [62.4 62.4 62.4 62.4 62.4 62.4 62.4 62.4]; %theory

plot(x,y1,'b--o','DisplayName','Powdered-core','LineWidth',1.6)
```

```
hold on
ylim([0 100])
grid minor
% semilogy(x,y2,'b--o','DisplayName','Ferrite core')
% semilogy(x,y3,'r--*','DisplayName','Single-gapped')
% semilogy(x,y4,'m-s','DisplayName','Double-gapped','LineWidth',0.8)

plot(x,y5,'r--','DisplayName','Model-prediction','LineWidth',1.6)

plot(x,y5-y1,'-.s','DisplayName','Model-prediction','LineWidth',1.6)


hold off

xlabel({'Frequency','(kHz)'})
ylabel({'Self inductance - secondary winding','(µH)'})

%legend('Powdered-core','Ferrite core','Single-gapped ferrite','Double-
gapped ferrite')

legend('Measurement','Model-prediction','Deviation')


%%
% Self inductance of primary

x = [1 3 5 7 9 11 13 15];
y1 = [3.36 3.3 3.2 3.2 3.1 3.1 3.1 3.05];
% y2 = [11600 11370 11260 11220 11200 11200 11200 11210];
% y3 = [169.6 169.5 169.5 169.5 169.4 169.4 169.35 169.32];
% y4 = [65.2 65.2 65.18 65.16 65.14 65.1 65.1 65];

y5 = [2.96 2.96 2.96 2.96 2.96 2.96 2.96 2.96]; %theory

plot(x,y1,'b--o','DisplayName','Powdered-core','LineWidth',1.6)
hold on
ylim([0 10])
grid minor
% semilogy(x,y2,'b--o','DisplayName','Ferrite core')
% semilogy(x,y3,'r--*','DisplayName','Single-gapped')
% semilogy(x,y4,'m-s','DisplayName','Double-gapped','LineWidth',0.8)

plot(x,y5,'r--','DisplayName','Model-prediction','LineWidth',1.6)

plot(x,y1-y5,'-.s','DisplayName','Model-prediction','LineWidth',1.6)


hold off

xlabel({'Frequency','(kHz)'})
ylabel({'Self inductance - primary winding','(µH)'})

%legend('Powdered-core','Ferrite core','Single-gapped ferrite','Double-
gapped ferrite')

legend('Measurement','Model-prediction','Deviation')
```

```
% Leakage inductance of secondary

x = [1 3 5 7 9 11 13 15];
y1 = [34.6 31.3 30.8 30.5 30.4 30.2 30.2 30.05];
% y2 = [11600 11370 11260 11220 11200 11200 11200 11210];
% y3 = [169.6 169.5 169.5 169.5 169.4 169.4 169.35 169.32];
% y4 = [65.2 65.2 65.18 65.16 65.14 65.1 65.1 65];

y5 = [27 27 27 27 27 27 27 27 ]; %theory

plot(x,y1,'b--o','DisplayName','Powdered-core','LineWidth',1.6)
hold on
ylim([0 50])
grid minor
% semilogy(x,y2,'b--o','DisplayName','Ferrite core')
% semilogy(x,y3,'r--*','DisplayName','Single-gapped')
% semilogy(x,y4,'m-s','DisplayName','Double-gapped','LineWidth',0.8)

plot(x,y5,'r--','DisplayName','Model-prediction','LineWidth',1.6)

plot(x,y1-y5,'-.s','DisplayName','Model-prediction','LineWidth',1.6)


hold off

xlabel({'Frequency','(kHz)'})
ylabel({'Leakage inductance - secondary winding','(µH)'})

%legend('Powdered-core','Ferrite core','Single-gapped ferrite','Double-
gapped ferrite')

legend('Measurement','Model-prediction','Deviation')

%%

% Leakage inductance of primary

x = [1 3 5 7 9 11 13 15];
y1 = [1.6 1.6 1.6 1.6 1.6 1.6 1.6 1.6];
% y2 = [11600 11370 11260 11220 11200 11200 11200 11210];
% y3 = [169.6 169.5 169.5 169.5 169.4 169.4 169.35 169.32];
% y4 = [65.2 65.2 65.18 65.16 65.14 65.1 65.1 65];

y5 = [1.2 1.2 1.2 1.2 1.2 1.2 1.2 1.2 ]; %theory

plot(x,y1,'b--o','DisplayName','Powdered-core','LineWidth',1.6)
hold on
ylim([0 10])
grid minor
% semilogy(x,y2,'b--o','DisplayName','Ferrite core')
% semilogy(x,y3,'r--*','DisplayName','Single-gapped')
% semilogy(x,y4,'m-s','DisplayName','Double-gapped','LineWidth',0.8)

plot(x,y5,'r--','DisplayName','Model-prediction','LineWidth',1.6)

plot(x,y1-y5,'-.s','DisplayName','Model-prediction','LineWidth',1.6)
```

```
hold off

xlabel({'Frequency','(kHz)'})
ylabel({'Leakage inductance - primary winding','(µH)'})

%legend('Powdered-core','Ferrite core','Single-gapped ferrite','Double-
gapped ferrite')

legend('Measurement','Model-prediction','Deviation')


% Percentage variations of leakage inductance: For secondary coil

x = [1 3 5 7 9 11 13 15];
y1 = [61.13 60.12 58.1 57.1 56.92 55 53.35 53.3];
y2 = [0.66 0.66 0.65 0.65 0.65 0.65 0.65 0.65];
y3 = [34.16 32.04 31.8 31.7 31.5 31.5 31.42 31.40];
y4 = [69.8 69 68.1 68.1 68 67.5 67.5  67.48];


plot(x,y1,'-o','DisplayName','Powdered-core','LineWidth',1)
hold on
grid minor
plot(x,y2,'-*','DisplayName','Ferrite core','LineWidth',1)
plot(x,y3,'-^','DisplayName','Single-gapped','LineWidth',1)
plot(x,y4,'-s','DisplayName','Double-gapped','LineWidth',1)

ylim([0 100])
hold off

xlabel({'Frequency','(kHz)'})
ylabel({'Leakage Percentage(%): secondary winding','(µH)'})

legend('Powdered-core','Ferrite core','Single-gapped','Double-gapped')

%%

% Percentage variations of leakage inductance: For primary coil

x = [1 3 5 7 9 11 13 15];
y1 = [55.2 55 55 55 55 54.8 53.84 53.24];
y2 = [0.56 0.56 0.55 0.55 0.54 0.54 0.53 0.53];
y3 = [30.26 30.24 30.18 30.17 30.15 30.15 30.12 30.12];
y4 = [66.13 66 65.66 65.66 65.4 65.2 65.18 65.16];


plot(x,y1,'-o','DisplayName','Powdered-core','LineWidth',1)
hold on
grid minor
plot(x,y2,'-*','DisplayName','Ferrite core','LineWidth',1)
plot(x,y3,'-^','DisplayName','Single-gapped','LineWidth',1)
plot(x,y4,'-s','DisplayName','Double-gapped','LineWidth',1)

ylim([0 100])
hold off
```

```
xlabel({'Frequency','(kHz)'})
ylabel({'Leakage Percentage(%): primary winding','(μH)'})

legend('Powdered-core','Ferrite core','Single-gapped','Double-gapped')



%Magnetic Fux Distribution_SCASA_Transient-Mode


k = 60;

l_c = 81.4*1e-3;
mu_o = 4*pi*1e-7;
N = 5;


tau1= 28.1e-6;
tau2= 1e-6;
tau3=3.911e-6;

t=(0:1:95)*1e-6;
tt=(0:1:95)*1e-6;


Is = 4400* sin(0.126*1e6*tt).* exp(-tt/tau1) .*(1-exp(-tt/tau2));
%including the ring

Iss= 3000 * 1e18 * (0.01243).* t.^3 .* exp(-t/tau3);

B = ( (k*mu_o*N) / l_c ) * Iss *0.9;


%plot(4+t*1e6,Iss,'--o'); title('IEEE 8/20 us Standard Current Wave');
xlabel('Time T(us)'); ylabel('Current - I(A)') % Analytical

plot(4+t*1e6,B,'r--o','LineWidth',1); title('Magnetic Flux generation
inside SCASA toroidal core'); xlabel('Time T(us)'); ylabel('Magnetic Flux
Density - Tesla') % Analytical


grid on

%Fint = int(B,t,[0 50e-6])

Iss2 = @(t) 3000 * 0.90 * 1e18 * (0.01243).* t.^3 .* exp(-t/tau3);

q1 = integral(Iss2,0,100e-6); %integrate Iss from 0 to 100 us


I_avg = q1/100e-6  % avg current;


%Average Flux

B_avg = ( (k*mu_o*N) / l_c ) * I_avg
```

Appendix G

LTSpice Circuit Models

This appendix contains LTSpice circuit models of LSS-6230 generation circuit and equivalent SCASA topology (non-ideal transformer core, metal oxide varistors and SC sub-circuit). Considering the accuracy of simulations, X- and Y-type filter capacitors, oscilloscope probe characteristics and path impedance of connecting cables are also included.

Note: Magnetizing and leakage inductances of SCASA transformer windings are characterized by coupling coefficients 0.74 and 0 respectively in the LTSpice simulation circuit.

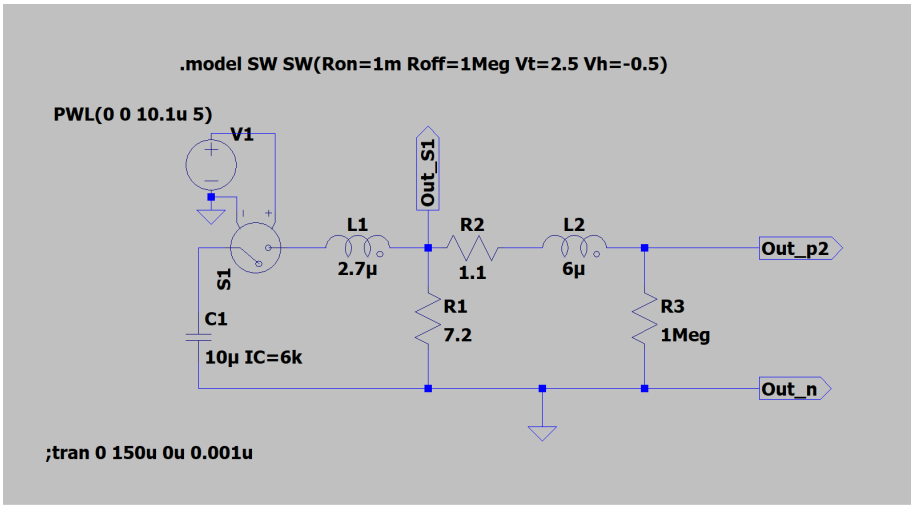

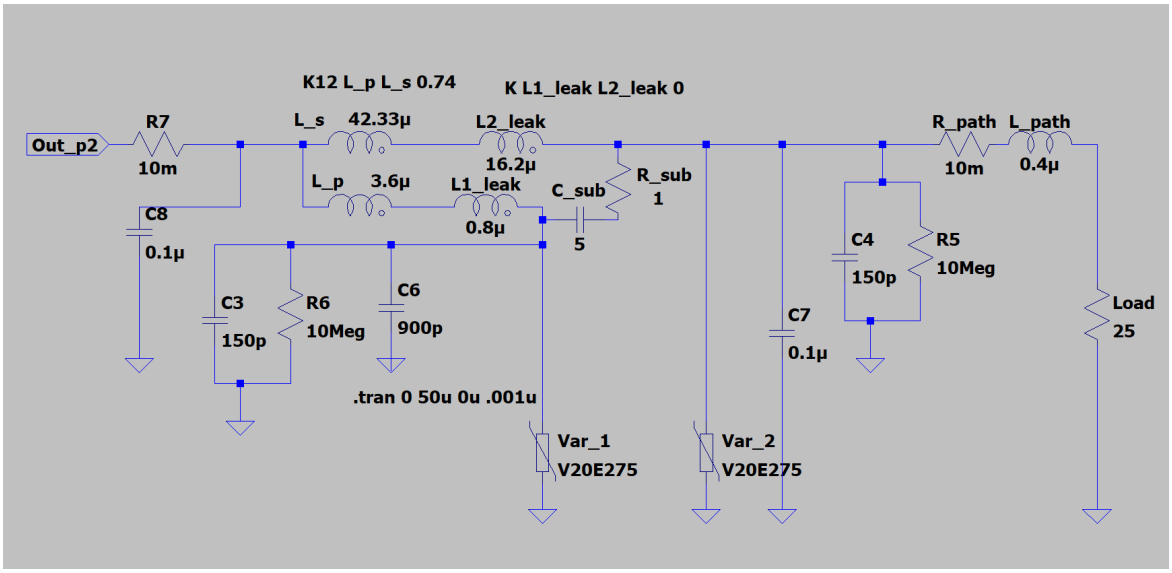

Appendix H

Standard Laplace Transforms

This appendix contains a standard Laplace transform table based on the book "Linear Control System Analysis and Design" by John Joachim D'Azzo and Constantine H. Houpis, McGraw-Hill Computer Science Series, 1988.

Laplace Transform Table

Largely modeled on a table in D'Azzo and Houpis, *Linear Control Systems Analysis and Design*, 1988

$F(s)$	$f(t) \quad 0 \le t$
1. 1	$\delta(t)$ unit impulse at $t = 0$
2. $\frac{1}{s}$	1 or $u(t)$ unit step starting at $t = 0$
3. $\frac{1}{s^2}$	$t \cdot u(t)$ or t ramp function
4. $\frac{1}{s^n}$	$\frac{1}{(n-1)!}t^{n-1}$ n = positive integer
5. $\frac{1}{s}e^{-as}$	$u(t-a)$ unit step starting at $t = a$
6. $\frac{1}{s}(1-e^{-as})$	$u(t)-u(t-a)$ rectangular pulse
7. $\frac{1}{s+a}$	e^{-at} exponential decay
8. $\frac{1}{(s+a)^n}$	$\frac{1}{(n-1)!}t^{n-1}e^{-at}$ n = positive integer
9. $\frac{1}{s(s+a)}$	$\frac{1}{a}(1-e^{-at})$
10. $\frac{1}{s(s+a)(s+b)}$	$\frac{1}{ab}(1-\frac{b}{b-a}e^{-at}+\frac{a}{b-a}e^{-bt})$
11. $\frac{s+\alpha}{s(s+a)(s+b)}$	$\frac{1}{ab}[\alpha-\frac{b(\alpha-a)}{b-a}e^{-at}+\frac{a(\alpha-b)}{b-a}e^{-bt}]$
12. $\frac{1}{(s+a)(s+b)}$	$\frac{1}{b-a}(e^{-at}-e^{-bt})$
13. $\frac{s}{(s+a)(s+b)}$	$\frac{1}{a-b}(ae^{-at}-be^{-bt})$

$F(s)$	$f(t) \qquad 0 \le t$
14. $\frac{s+\alpha}{(s+a)(s+b)}$	$\frac{1}{b-a}[(\alpha-a)e^{-at}-(\alpha-b)e^{-bt}]$
15. $\frac{1}{(s+a)(s+b)(s+c)}$	$\frac{e^{-at}}{(b-a)(c-a)}+\frac{e^{-bt}}{(c-b)(a-b)}+\frac{e^{-ct}}{(a-c)(b-c)}$
16. $\frac{s+\alpha}{(s+a)(s+b)(s+c)}$	$\frac{(\alpha-a)e^{-at}}{(b-a)(c-a)}+\frac{(\alpha-b)e^{-bt}}{(c-b)(a-b)}+\frac{(\alpha-c)e^{-ct}}{(a-c)(b-c)}$
17. $\frac{\omega}{s^2+\omega^2}$	$\sin \ \omega t$
18. $\frac{s}{s^2+\omega^2}$	$\cos \ \omega t$
19. $\frac{s+\alpha}{s^2+\omega^2}$	$\frac{\sqrt{\alpha^2+\omega^2}}{\omega}\sin(\omega t+\phi) \qquad \phi=\text{atan2}(\omega,\alpha)$
20. $\frac{s\sin\theta+\omega\cos\theta}{s^2+\omega^2}$	$\sin(\omega t+\theta)$
21. $\frac{1}{s(s^2+\omega^2)}$	$\frac{1}{\omega^2}(1-\cos\omega t)$
22. $\frac{s+\alpha}{s(s^2+\omega^2)}$	$\frac{\alpha}{\omega^2}-\frac{\sqrt{\alpha^2+\omega^2}}{\omega^2}\cos(\omega t+\phi) \qquad \phi=\text{atan2}(\omega,\alpha)$
23. $\frac{1}{(s+a)(s^2+\omega^2)}$	$\frac{e^{-at}}{a^2+\omega^2}+\frac{1}{\omega\sqrt{a^2+\omega^2}}\sin(\omega t-\phi)$ $\phi=\text{atan2}(\omega,\alpha)$
24. $\frac{1}{(s+a)^2+b^2}$	$\frac{1}{b}e^{-at}\sin(bt)$
24a. $\frac{1}{s^2+2\zeta\omega_n s+\omega_n{}^2}$	$\frac{1}{\omega_n\sqrt{1-\zeta^2}}e^{-\zeta\omega_n t}\sin(\omega_n\sqrt{1-\zeta^2}t)$
25. $\frac{s+a}{(s+a)^2+b^2}$	$e^{-at}\cos(bt)$

References

[1] National Aeronautics and Space Administration (NASA). Lightning Data at GHRC DAAC - Lightning Research, 2010. Available at: `https://ghrc.nsstc.nasa.gov/lightning`, Accessed: 2020-10-20.

[2] ITRS 2.0. The International Technology Roadmap for Semiconductors 2.0. Technical report, European Semiconductor Industry Association, 2015. Executive summary report.

[3] I. Batarseh and A. Harb. *Power Electronics: Circuit Analysis and Design*. Springer International Publishing, 2017.

[4] IEC 60038:2009 Standard. IEC Standard Voltages. Technical report, International Electrotechnical Commission, 2009. ISBN 978-2-88910-024-8.

[5] M.A. Laughton and D.F. Warne. *Electrical Engineer's Reference Book*. Elsevier Science, 2002.

[6] Crosby, N. and Huang, T.Y. and Rycroft, M.J. *Coupling of Thunderstorms and Lightning Discharges to Near-Earth Space: Proceedings of the Workshop*. AIP Conference Proceedings. American Inst. of Physics, 2009.

[7] Atmosphere and Climate — Stats NZ. Atmosphere and climate: Stats NZ, 2018. Available at: `https://www.stats.govt.nz/topics/atmosphere-and-climate`, Accessed: 2018-10-20.

[8] J.R. Barnes. *Robust Electronic Design Reference Book: no special title*. Robust Electronic Design Reference Book. Kluwer Academic, 2004.

[9] Lee, B. US Patent 4,901,183: Surge protection device, 1990. Available at: `https://www.google.com/patents/US4901183`, Accessed: 2019-11-04.

[10] N. Kularatna, J. Fernando, A. Pandey, and S. James. Surge Capability Testing of Supercapacitor Families Using a Lightning Surge Simulator. *IEEE Transactions on Industrial Electronics*, 58(10):4942–4949, 2011.

[11] J. Fernando and N. Kularatna. A supercapacitor based enhancement technique for standalone surge protection circuits. In *2013 IEEE International Symposium on Industrial Electronics*, pages 1–6, 2013.

[12] J. Fernando, N. Kularatna, H. Round, and S. Tálele. Implementation of the supercapacitor-assisted surge absorber (SCASA) technique in a practical surge protector. In *IECON 2014 - 40th Annual Conference of the IEEE Industrial Electronics Society*, pages 5191–5195, 2014.

[13] J. Fernando and N. Kularatna. Supercapacitor assisted surge absorber (SCASA) technique: Selection of supercapacitor and magnetic components. In *2014 IEEE Energy Conversion Congress and Exposition (ECCE)*, pages 1992–1996, 2014.

[14] Thor Technologies. Thor Technologies : STViQ/3 SMART TViQ, 2018. Available at: `https://www.thortechnologies.com.au/product/stviq3/`, Accessed: 2019-11-22.

[15] Underwriters Laboratories. UL Standard for Safety for Surge Protective Devices: UL 1449. Technical report, Underwriters Laboratories Inc., 2006. UL-1449 3rd Edition.

[16] S.Khalid and Bharti Dwivedi. Power quality issues, problems , standards & their effects in industry with corrective means. *International journal of advances in engineering & technology*, 1:1–11, May 2011.

[17] R.B. Standler. *Protection of Electronic Circuits from Overvoltages*. Dover Books on Electrical Engineering Series. Dover Publications, 2002.

[18] N. Kularatna. *DC Power Supplies: Power Management and Surge Protection for Power Electronic Systems*. CRC Press, 2018.

[19] N. Kularatna, A.S. Ross, J. Fernando, and S. James. *Design of Transient Protection Systems: Including Supercapacitor Based Design Approaches for Surge Protectors*. Elsevier Science, 2018.

[20] M.F. Hordeski. *Emergency and Backup Power Sources: Preparing for Blackouts and Brownouts*. Fairmont Press, 2005.

[21] J.A. Martinez-Velasco. *Transient Analysis of Power Systems: A Practical Approach*. Wiley - IEEE. Wiley, 2020.

[22] C.A. Vergers. *Handbook of Electrical Noise: Measurement and Technology*. TAB professional and reference books. Tab Professional and Reference Books, 1987.

[23] A. Baggini. *Handbook of Power Quality*. Wiley, 2008.

[24] F.C. De La Rosa. *Harmonics and Power Systems*. Electric Power Engineering Series. CRC Press, 2006.

[25] Dranetz Technologies. *The Dranetz Field Handbook for Power Quality Analysis*. Dranetz Technologies, Incorporated, 1991.

[26] T. Mueller and J. C. Thompson. The use of surge protection devices in the pulp and paper industry. In *Conference Record of 1998 Annual Pulp and Paper Industry Technical Conference (Cat. No.98CH36219)*, pages 58–66, 1998.

[27] J.C. Das. *Transients in Electrical Systems: Analysis, Recognition, and Mitigation*. McGraw-Hill Education, 2010.

[28] P. Kundur, N.J. Balu, and M.G. Lauby. *Power System Stability and Control*. EPRI power system engineering series. McGraw-Hill Education, 1994.

[29] F.F. Mazda. *Power Electronics Handbook*. Electronics & Electrical. Elsevier Science, 1997.

[30] John R. Barnes. *Robust electronic design reference book*, volume 1. Springer science & business media, 2004.

[31] IEEE Guide for the Application of Component Surge-Protective Devices for Use in Low-Voltage [Equal to or Less than 1000 V (ac) Or 1200 V (dc)] Circuits. *IEEE Std C62.42-2005 (Revision of IEEE C62.42-1992)*, pages 1–105, 2006.

[32] T.N. McManus. *Management of Hazardous Energy: Deactivation, De-Energization, Isolation, and Lockout*. CRC Press, 2016.

[33] United States. Federal Aviation Administration. *Fundamental Considerations of Lightning Protection, Grounding, Bonding, and Shielding*. Fundamental Considerations of Lightning Protection, Grounding, Bonding, and Shielding. Department of Transportation, Federal Aviation Administration, 1978.

[34] IEEE recommended practice on surge testing for equipment connected to low-voltage (1000 V and less) AC power circuits. *IEEE Std C62.45-2002 (Revision of IEEE Std C62.45-1992)*, pages 1–85, 2003.

[35] IEEE Standard Test Specifications for Surge-Protective Devices (SPDs) for Use on the Load Side of the Service Equipment in Low-Voltage (1000 V and Less) AC Power Circuits. *IEEE Std C62.62-2018 (Revision of IEEE Std C62.62-2010)*, pages 1–61, 2018.

[36] J. T. Pauley and G. D. Gregory. North american codes and standards: a global challenge. In *Conference Record of 1998 IEEE Industry Applications Conference. Thirty-Third IAS Annual Meeting (Cat. No.98CH36242)*, volume 3, pages 2372–2378 vol.3, 1998.

[37] Joseph DeGregoria. UL 1449 and the 2008 NEC significant changes have been made in the requirements for identifying and evaluating surge protective devices. `http://ecmweb.com/power-quality/ul-1449-and-2008-nec`, June 2008. Accessed: 05-04-2016.

[38] Citel Inc. Surge protection. Technical report, CITEL, 2013. General catelog 9th edition.

[39] IEC 61000-4-5. Electromagnetic compatibility (EMC) - Part 4-5: Testing and measurement techniques - Surge immunity test. Technical report, International Electrotechnical Commission, 2014. International Standard.

[40] IEEE Recommended Practice on Characterization of Surges in Low-Voltage (1000 V and Less) AC Power Circuits. *IEEE Std C62.41.2-2002*, 2003.

[41] V.N.K.S. R. *Power System Switchgear and Protection*. S. Chand Publishing, 2009.

[42] IEEE Guide for the Application of Surge-Protective Devices for Use on the Load Side of Service Equipment in Low-Voltage (1000 V or Less, 50 Hz or 60 Hz) AC Power Circuits. *IEEE Std C62.72-2016 (Revision of IEEE Std C62.72-2007)*, pages 1–110, 2016.

[43] Underwriters Laboratories. UL Standard for Safety for Surge Protective Devices: UL 1449. Technical report, Underwriters Laboratories Inc., 2014. UL-1449 4th Edition.

[44] NoiseKen Laboratories. Lightning Surge Simulator LSS-6230A . Technical report, NoiseKen Laboratory Co. LTD, 2012. Compliant with IEC61000-4-5 Edition-3 requirements.

[45] NoiseKen Laboratories. Lightning Surge Simulator LSS-F03 series. Technical report, NoiseKen Laboratory Co. LTD, 2014. Compliant with IEC61000-4-5 Edition-3 requirements.

[46] NoiseKen Laboratories. Lightning Surge Simulator LSS-6230. Technical report, NoiseKen Laboratory Co. LTD, 2012. User Manual.

[47] Electrical group. Eaton's guide to surge suppression. Technical report, Eaton Corporation, 2009. Application note.

[48] Franklin Bohac. Ul 1449-3rd edition effects on lightning protection systems. Technical report, GE Industrial Solutions, 2010. Available at: `http://apps.geindustrial.com/publibrary/checkout/UL-1449`.

[49] P. Hasse and Institution of Electrical Engineers. *Overvoltage Protection of Low Voltage Systems*. IEE Publication Series. P. Peregrinus, 1992.

[50] *Ham Radio Magazine*. Number v. 11, nos. 7-12. Communications Technology, Incorporated, 1978.

[51] J. Whitaker. *AC Power Sys Hdbk*. Design, Installation & Operation of Electronic Systems. CRC-Press, 1991.

[52] J. He. *Metal Oxide Varistors: From Microstructure to Macro-Characteristics*. Wiley, 2019.

[53] AN9767.1. Littelfuse Varistors - Basic Properties, Terminology and Theory. Technical report, Littlefuse Co-operation, 1999. Application Note.

[54] Mick Maytum. THERE'S AN "R" IN "VARISTOR", 2020. Available at: `https://incompliancemag.com/article/theres-an-r-in-varistor/`, Accessed: 2020-11-24.

[55] S. James. *Investigation of surge propagation in transient voltage surge suppressors and experimental verification*. Doctoral thesis, 2014.

[56] Hongcai Chen and Ya-ping Du. A comprehensive study on the nonlinear behavior of metal oxide varistors. In *2016 33rd International Conference on Lightning Protection (ICLP)*, pages 1–5, 2016.

[57] H. R LEVINSON, L. M; PHILIPP. Zinc oxide varistors — a review. *American Ceramic Society bulletin*, 1986.

[58] C.A. Harper. *Handbook of Components for Electronics*. McGraw-Hill handbooks. McGraw-Hill, 1977.

[59] ON Semiconductor Industries. ESD Protection Diode Micro Packaged Diodes for ESD Protection, 2017. Available at: `https://www.onsemi.com/pdf/datasheet/esdm3551-d.pdf`, Accessed: 2018-11-24.

[60] D. Weston. *Electromagnetic Compatibility: Principles and Applications, Second Edition, Revised and Expanded*. Electrical and Computer Engineering. Taylor & Francis, 2001.

[61] R.L. Ozenbaugh and T.M. Pullen. *EMI Filter Design, Third Edition*. Taylor & Francis, 2011.

[62] J.D. Walker and R.L. Ozenbaugh. *Surge Protection, Design, and Applications*. Taylor & Francis.

[63] Waseem Raza, Faizan Ali, Nadeem Raza, Yiwei Luo, Ki-Hyun Kim, Jianhua Yang, Sandeep Kumar, Andleeb Mehmood, and Eilhann E. Kwon. Recent advancements in supercapacitor technology. *Nano Energy*, 52:441–473, 2018.

[64] Ioannis Hadjipaschalis, Andreas Poullikkas, and Venizelos Efthimiou. Overview of current and future energy storage technologies for electric power applications. *Renewable and Sustainable Energy Reviews*, 13(6):1513–1522, 2009.

[65] A.K. Samantara and S. Ratha. *Materials Development for Active/Passive Components of a Supercapacitor: Background, Present Status and Future Perspective*. SpringerBriefs in Materials. Springer Singapore, 2017.

[66] J. Fernando. *Supercapacitor-Assisted Surge Absorber (SCASA) and Supercapacitor Surge Modelling*. Doctoral thesis, 2016.

[67] B.E. Conway. *Electrochemical Supercapacitors: Scientific Fundamentals and Technological Applications*. Springer US, 2013.

[68] Lu Wei and Gleb Yushin. Nanostructured activated carbons from natural precursors for electrical double layer capacitors. *Nano Energy*, 1(4):552–565, 2012.

[69] M. Lu, F. Beguin, and E. Frackowiak. *Supercapacitors: Materials, Systems, and Applications*. New Materials for Sustainable Energy and Development. Wiley, 2013.

[70] Martin G. Bakker, Rachel M. Frazier, Susan Burkett, Jason E. Bara, Nitin Chopra, Scott Spear, Shanlin Pan, and Cailing Xu. Perspectives on supercapacitors, pseudocapacitors and batteries. *Nanomaterials and Energy*, 1(3):136–158, 2012.

[71] Qi Lu, Jingguang G. Chen, and John Q Xiao. Nanostructured electrodes for high-performance pseudocapacitors. *Angewandte Chemie International Edition*, 52(7):1882–1889, 2013.

[72] K.K. Kar. *Handbook of Nanocomposite Supercapacitor Materials II: Performance*. Springer Series in Materials Science. Springer International Publishing, 2020.

[73] Yanwu Zhu, Shanthi Murali, Meryl D. Stoller, K. J. Ganesh, Weiwei Cai, Paulo J. Ferreira, Adam Pirkle, Robert M. Wallace, Katie A. Cychosz, Matthias Thommes, Dong Su, Eric A. Stach, and Rodney S. Ruoff. Carbon-based supercapacitors produced by activation of graphene. *Science*, 332(6037):1537–1541, 2011.

[74] Nihal Kularatna, Jayathu Fernando, Amit Pandey, and Sisira James. Surge capability testing of supercapacitor families using a lightning surge simulator. *IEEE Transactions on Industrial Electronics*, 58(10):4942–4949, 2011.

[75] Maxwell Technologies. Product guid- boostcap® ultracapacitors. Technical report, Maxwell Technologies, 2009.

[76] Mag-inc.com. Magnetics Powder-Core Kool Mu: 0077071A7, 2018. Available at: `https://www.mag-inc.com/Media/Magnetics/Datasheets/0077071A7.pdf`, Accessed: 2018-12-22.

[77] Mag-inc.com. Magnetics - W Material, 2017. Available at: `https://www.maginc.com/Products/Ferrite-Cores/W-Material`, Accessed: 2019-11-30.

[78] Mag-inc.com. Magnetics Ferrite-Core Catalog: 2017, 2017. Available at: `https://www.mag-inc.com/Design/Technical-Documents/Ferrite-Core-Documents`, Accessed: 2020-10-22.

[79] Mag-inc.com. Magnetics Powder-Core Catalog: 2020, 2020. Available at: `https://www.mag-inc.com/Design/Technical-Documents/Powder-Core-Documents`, Accessed: 2020-11-30.

[80] S. T. Sadeeshvara Udayanga, N. Kularatna, and D. A. Steyn-Ross. Investigating the impact of ferrite magnetic cores on the performance of supercapacitor assisted surge absorber (SCASA) technique. In *2019 IEEE 28th International Symposium on Industrial Electronics (ISIE)*, pages 130–135, 2019.

[81] Mag-inc.com. Magnetics Ferrite-Core R-Ferrite: 0R43521EC, 2017. Available at: `https://www.mag-inc.com/File%20Library/Product%20Datasheets/Ferrite/New%20Ferrite%20data%20sheets/0R43521EC.pdf`, Accessed: 2020-12-28.

[82] V.C. Valchev and A. Van den Bossche. *Inductors and Transformers for Power Electronics*. CRC Press, 2018.

[83] C.W.T. McLyman. *Transformer and Inductor Design Handbook, Third Edition*. Taylor & Francis, 2004.

[84] C. Heck. *Magnetic Materials and Their Applications*. Elsevier Science, 2013.

[85] Satoshi Hirosawa, Masamichi Nishino, and Seiji Miyashita. Perspectives for high-performance permanent magnets: applications, coercivity, and new materials. *Advances in Natural Sciences: Nanoscience and Nanotechnology*, 8(1):013002, mar 2017.

[86] H. Pender. *Electricity and Magnetism for Engineers: Electric and magnetic circuits*. Electricity and Magnetism for Engineers. McGraw-Hill book Company, Incorporated, 1918.

[87] K.M. Krishnan. *Fundamentals and Applications of Magnetic Materials*. OUP Oxford, 2016.

[88] B.D. Cullity and C.D. Graham. *Introduction to Magnetic Materials*. Wiley, 2011.

[89] W.J. Duffin. *Electricity and Magnetism*. McGraw Hill Book Company, 1980.

[90] F.N. Bradley. *Materials for Magnetic Functions*. Hayden series in materials for electrical and electronic design. Hayden Book Company, 1971.

[91] H. Pender and W.A.D. Mar. *Handbook for Electrical Engineers: A Reference Book for Practicing Engineers and Students of Engineering*. J. Wiley & Sons, Incorporated, 1922.

[92] R.D. Vecchio, R.M.D. Vecchio, B. Poulin, P.T. Feghali, D.M. Shah, and R. Ahuja. *Transformer Design Principles, Third Edition*. CRC Press, 2017.

[93] Massachusetts Institute of Technology. Department of Electrical Engineering. *Magnetic Circuits and Transformers: A First Course for Power and Communication Engineers, by Members of the Staff of the Department of Electrical Engineering. Massachusetts Institute of Technology*. Principles of electrical engineering series. M.I.T. Press, 1965.

[94] Magnetics Inc. Magnetics powder-core catalog-2021. Technical report, Magnetics Headquarters' Technology Center, Pittsburgh, 2021.

[95] Francois D. Martzloff and Harold A. Gauper. Surge and high-frequency propagation in industrial power lines. *IEEE Transactions on Industry Applications*, IA-22(4):634–640, 1986.

[96] Littelfuse Inc. Ultra MOV Varistor Series: Radial Lead Varistors, 2019. Available at: `https://www.littelfuse.com/~/media/electronics/datasheets/varistors/littelfuse_varistor_ultramov_datasheet.pdf.pdf`, Accessed: 2019-12-28.

[97] S. T. S. Udayanga, N. Kularatna, and D. A. Steyn-Ross. Permeance based model for the coupled-inductor utilized in the supercapacitor assisted surge absorber (scasa) and its experimental validation. In *2020 2nd IEEE International Conference on Industrial Electronics for Sustainable Energy Systems (IESES)*, volume 1, pages 267–272, 2020.

[98] C.W.T. McLyman. *Magnetic Core Selection for Transformers and Inductors: A User's Guide to Practice and Specifications, Second Edition*. Taylor & Francis, 1997.

[99] Martin H. Weik. *magnetic reluctance*, pages 960–960. Springer US, Boston, MA, 2001.

[100] W.G. Hurley and W.H. Wölfle. *Transformers and Inductors for Power Electronics: Theory, Design and Applications*. Wiley, 2013.

[101] Richard Clarke. Air gapped magnetic cores, 2011. Available at: `http://info.ee.surrey.ac.uk/Workshop/advice/coils/gap/index.html`, Accessed: 2019-09-30.

[102] B. Bilgin, J.W. Jiang, and A. Emadi. *Switched Reluctance Motor Drives: Fundamentals to Applications*. CRC Press, 2019.

[103] M.K. Kazimierczuk. *High-Frequency Magnetic Components*. Wiley, 2013.

[104] W.M. Flanagan. *Handbook of Transformer Design and Applications*. McGraw-Hill Education, 1993.

[105] Circuit Globe.com. Leakage Flux and Fringing, 2017. `https://circuitglobe.com/at-is-leakage-flux-and-fringing.html`, Accessed: 2020-11-30.

[106] Illinois Institute Technology. *Proceedings of the American Power Conference*. Number v. 58, pt. 1. Illinois Institute of Technology., 1996.

[107] M.K. Kazimierczuk. *High-Frequency Magnetic Components*. John Wiley & Sons, 2009.

[108] J. Fletcher, B. Williams, and M. Mahmoud. Airgap fringing flux reduction in inductors using open-circuit copper screens. *Electric Power Applications, IEE Proceedings* -, 152:990 – 996, 08 2005.

[109] R. Kasikowski and B. Wiecek. Ascertainment of fringing-effect losses in ferrite inductors with an air gap by thermal compact modelling and thermographic measurements. *Applied Thermal Engineering*, 124:1447–1456, 2017.

[110] J.T. Humphries and L.P. Sheets. *Industrial Electronics*. Delmar Publishers, 1993.

[111] Transient voltage surge suppressors. Standard, Underwriters Laboratories, Northbrook, IL, 2014.

[112] J.L. Schiff. *The Laplace Transform: Theory and Applications*. Undergraduate Texts in Mathematics. Springer New York, 2013.

[113] W.R. LePage. *Complex Variables and the Laplace Transform for Engineers*. Dover Books on Electrical Engineering. Dover Publications, 2012.

[114] Inc MathWorks. *Symbolic Math Toolbox for Use with MATLAB: User's Guide*. MATLAB handbooks. MathWorks, Incorporated, 2001.

[115] Credson de Salles, Thiago Arantes Nogueira, Estácio Tavares Wanderley Neto, Manuel Luís Barreira Martinez, and Alvaro Antonio Alencar de Queiroz. Effects of operation temperature in artificially aging of zinc oxide varistors by high current short impulses. *Electric Power Systems Research*, 134:145–151, 2016.

[116] Mag-inc.com. Magnetics Powder-Core Kool Mu: 0077083A7, 2018. Available at: `https://www.mag-inc.com/Media/Magnetics/Datasheets/0077083A7.pdf`, Accessed: 2018-12-22.

[117] E.C. Snelling and A.D. Giles. *Ferrites for Inductors and Transformers*. Electronic & Electrical Engineering Research Studies. Research Studies Press, 1983.

[118] Mag-inc.com. Powder Core and Gapped Ferrite Core Comparison, 2018. Available at: `https://www.mag-inc.com/Products/Powder-Cores/Learn-More-about-Powder-Cores/Gapped-Ferrite-Comparison`, Accessed: 2020-09-28.